UNIVERSITY OF GENOA
POLYTECHNIC SCHOOL

DIME – Department of Mechanical, Energy, Management and Transport Engineering

PhD in Marine Science and Technologies
Curriculum Machines and Energy Systems for the Sea

PhD Thesis
XXXVI Course

Optimal energy management techniques for island applications

Supervisor:
Prof. Ing. Mario Luigi Ferrari
Co-Supervisor:
Prof. Ing. Aristide Massardo

Candidate:
Lorenzo Gini

June 2024

Contents

Abstract

The global imperative to address climate change and pollution has catalysed the development of innovative and environmentally sustainable energy systems, with poly-generation microgrids emerging as a leading technology due to their high energy conversion efficiencies and low emissions. This thesis focuses on the integration of electrical and thermal technologies in isolated maritime environments, an area of increasing interest in both academia and industry. The primary challenge addressed herein is the development of an energy management system capable of optimizing power flows and storage operations while ensuring robustness.

Drawing from practical experience, this thesis aims to advance the current understanding of energy management systems and control for microgrids, particularly in maritime applications such as islands and ships. The central objective is to conceptualize and test an energy management system tailored to these environments, considering operational constraints and optimizing overall system performance. These efforts are supported by simulation tools and cyber-physical tests conducted in the Innovative Energy System laboratory of the Thermochemical Power Group at the University of Genoa.

The methodology begins with the introduction of the isolated microgrid layout, incorporating industrial symbiosis principles. Dynamic models of each component are then developed and validated using Matlab-Simulink®. These models serve as the basis for designing and fine-tuning the Energy Management System, which controls each prime mover to fulfil the customer demand meeting operational constraints and minimizing costs. Comparative analyses are conducted between scenarios with and without the EMS, utilizing both simulations and real-world tests over typical operational periods. Additionally, the robustness of the EMS is thoroughly tested and validated, ensuring its efficacy in practical applications.

In conclusion, this thesis highlighted the great potential of microgrids with EMS, showing high energy conversion efficiencies in a wide operative range in terms of load and ambient

conditions. It also showed that the proper operation of the system is possible during various transient scenarios, implementing proper control strategy in order to face each scenario.

Acknowledgements

I would like to thank all the people I had the pleasure to work with during all these years. Mario, Alberto, Loredana and Aristide Fausto gave me the opportunity to work on various challenging projects, and their mentorship was a fundamental contribution to my professional growth. I would have never thought to work on so many different topics at the beginning of this journey!

Working at TPG I met a lot of wonderful colleagues and friends, and it would be hard to make a list. I just want to say it was great to spend these years with all of them, and that I will always remember our time together at the office, at the bar, at the restaurant, on the football field.

Finally, I would like to my family for their love and support. Your faith in me made every obstacle much easier to overcome.

This project has received funding from the European Union's Horizon 2020 research and innovation program under grant agreement No 957752. This thesis reflects only the authors' view and the Research Executive Agency and the European Commission are not responsible for any use that may be made of the information it contains.

Nomenclature

Abbreviations and Acronyms

AD-BES	Anaerobic Digestor
ASME	American Society of Mechanical Engineering
BoP	Balance of Plant
CHP	Combined Heat and Power
DoE	Department of Energy
DG	Distributed Generation
DHN	District Heating Networks
EMS	Energy Management System
ESS	Energy Storage Systems
ETN	European Turbine Network
GDP	Gross Domestic Product
GHG	Greenhouse Gas
HDI	Development Index
HIL	Hardware in the Loop
HOB	Heat-Only Boilers
ICE	Internal Combustion Engines
IEA	International Energy Agency
IES	Innovative Energy System
LCOH	Levelized Cost of Heating
LHV	Lower Heating Value
mGT	micro Gas Turbines
MIL	Model in the Loop
MPC	Model Predictive Control
ORC	Organic Rankine Cycles
PV	Photovoltaic
RES	Renewable Energy Sources
TES	Thermal Energy Storages

UNIGE	University of Genoa
WT	Wind Turbine

Variables

A	Area [m^2]
c	cost
E	Energy
h	enthalpy
J	cost function
k	current discrete time
l	part load
m	mass
$\dot{m}$	mass flow
P	power
R	weight matrix
Q	weight matrix, thermal flow
T	time, temperature
u	control signal
x	state of the system, mass title
ε	expansion ratio
η	Efficiency [-]

Subscripts and Superscripts

c	receding control horizon
el	electric
in	inlet
nom	nominal
out	outlet

p	prediction horizon
th	thermal

1 Introduction

1.1 Energy Scenario

Since the industrial revolution, energy has become an indispensable commodity supporting various human endeavours. Its diverse forms serve fundamental purposes such as sustaining human well-being, powering industries, facilitating production of consumer goods, enabling transportation, and catering to the rising energy needs linked to services and internet data. Over recent decades, primary energy consumption has consistently risen, barring periods of economic downturn like the 2020 COVID-19 pandemic. Figure 1 vividly illustrates this upward trajectory, primarily fuelled by regions experiencing recent development or ongoing growth from economic and demographic standpoints.

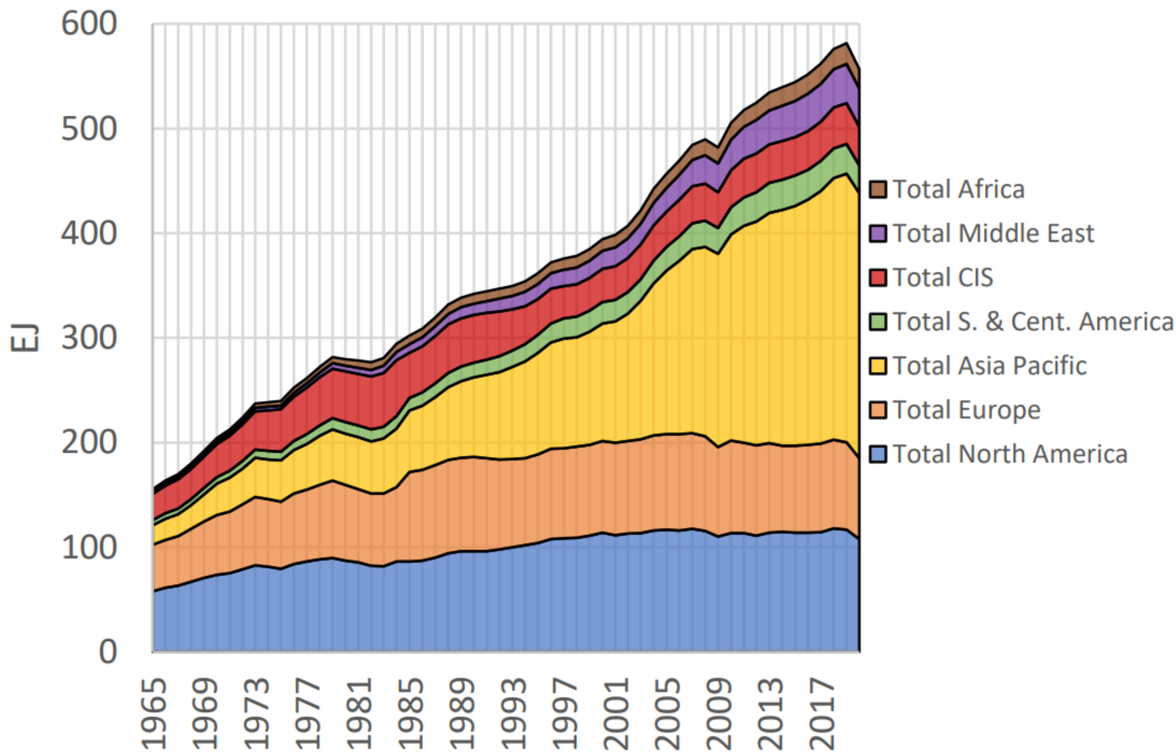

Figure 1 - Word's primary energy consumption trend by region, elaboration of data reported by BP [1]

The heightened awareness of climate change has spotlighted the energy issue, yet there remains no set target, either adopted or in discussion, regarding a cap or decrease in energy demand. Numerous policies have been implemented with the goal of reducing energy intensity (i.e., the average energy required to produce a unit of Gross Domestic Product) or enhancing the environmental quality of energy production. This stems from the strong correlation between a country's prosperity, human well-being, and energy consumption. Figure 2 and Figure 3 depict the correlation between Gross Domestic Product (GDP) and the Human Development Index (HDI) with primary energy consumption. These charts make it evident that global energy demand is poised to rise further as heavily populated developing nations like China and India continue to progress.

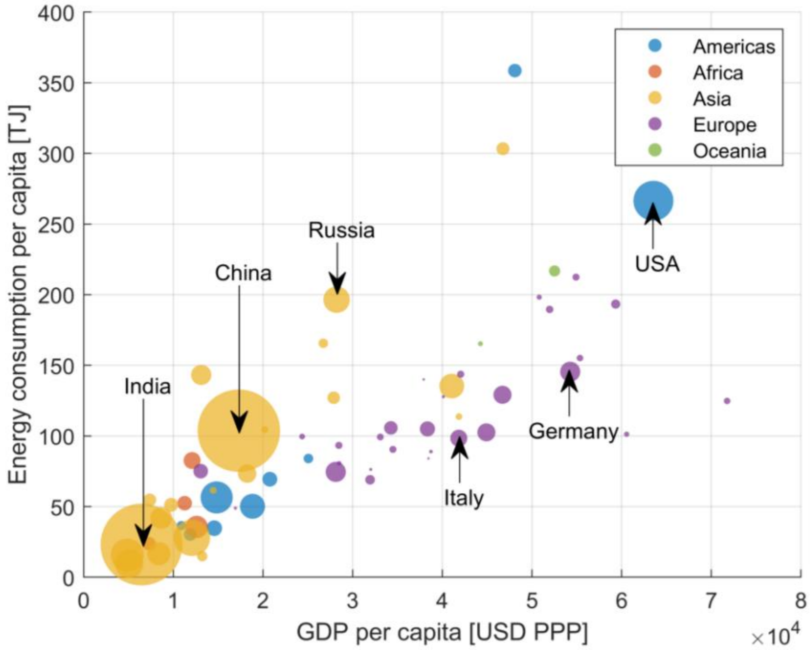

Figure 2 - Yearly energy consumption versus pro capita GDP, all the data are referred to 2020. The size of the markers is proportional to the country's population. elaboration of data reported by BP and the World Bank [1,2]

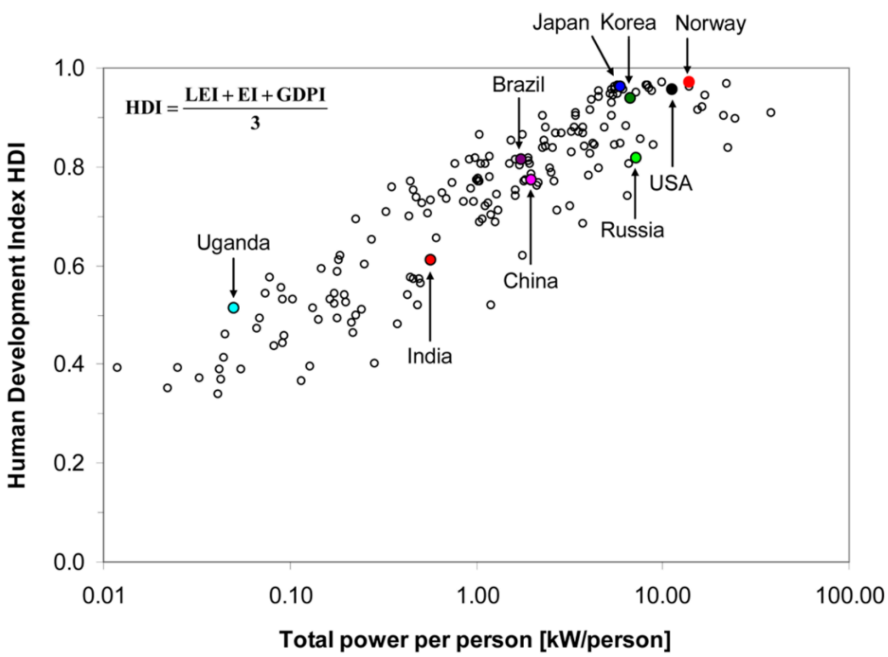

Figure 3 - HDI correlation to energy consumption [3].

However, the pressing concern of climate change and its impending repercussions is expected to wield significant human and economic costs if left unchecked. The anticipated rise in extreme weather events, sea-level elevations, desertification, and more necessitates serious consideration of future scenarios. Despite the pivotal role of energy access and availability in human well-being and economic growth, the energy sector stands as the primary contributor to Greenhouse Gas (GHG) emissions, which have substantial climate change potential. This poses a dilemma for governments and policymakers torn between global development rights, the pursuit of adequate living standards (defined as energy equity), and environmental sustainability.

Energy equity encompasses concerns regarding the affordability and accessibility of energy. In 2019, an estimated 761 million people lacked access to the electricity grid, mainly in sub-Saharan African countries [2,4]. Yet, affordability remains an issue even in developed nations. In Italy, for instance, the Observatory on Energy Poverty reported that 8.8% of families faced energy poverty conditions in 2019 [5], with similarly significant figures across Europe [6]. Striking a balance between energy equity and environmental sustainability becomes complex as often the most affordable energy sources tend to induce considerable local environmental pollution or high emissions of carbon dioxide and other GHGs.
Resolving this dilemma might involve investing in cleaning up the energy mix and formulating policies that consider these costs through a lens of social equity. However, this endeavour must tread cautiously to avoid jeopardizing energy system security. Policies that overlook this aspect may result in excessive reliance on foreign energy sources or an inadequate grid despite a surplus of Renewable Energy Sources (RES), leading to price volatility or potential electricity shortages.
The Global Energy Institute of the US Chamber of Commerce evaluates an energy security index based on various measures across nine categories, including global fuels, energy expenditures, environmental factors, and more [7]. These energy security issues transform the previous dilemma into a "trilemma," as termed by the World Energy Council [8], which

evaluates how each country manages the competing demands of energy equity, environmental sustainability, and energy security.

Engineering and technology confront these three main challenges: Energy Equity, Environmental Sustainability, and Energy Security. These targets were officially adopted by UN member states in 2015 as part of the 2030 agenda for sustainable development, encapsulated in the seventh and thirteenth goals: "Ensure access to affordable, reliable, sustainable, and modern energy for all" and "Take urgent action to combat climate change and its impact," respectively [4].

This thesis delves into proposing and assessing technological solutions to address these challenges, particularly focusing on electricity and heating sectors for a specific focus on maritime application. It endeavours to explore heat and power poly-generation micro-grid configurations to cater to the needs of both sectors simultaneously. The overarching aim is to tackle the requirements for flexible, programmable microgrids, power generation, and decarbonization in the electrical and heating sectors.

The activities described in this thesis have been part of projects (ROBINSON, PUMPHEAT, and ENVISION) in Horizon 2020 program. The main focus is on ROBINSON, an H2020 EU-funded initiative coordinated by the European Turbine Network involving a diverse consortium of industrial and academic partners across the European Union [9]. The project will be concluded in 2024 after four years of investigating optimal coupling for microgrids with industrial symbiosis on islands. Consequently, this thesis centres on the conceptual development and application of an optimized Energy Management System for isolated microgrids showing the application of the concept even for other case studies (PUMPHEAT and ENVISION).

1.2 Current Heating supply context decarbonization strategies

The heating share of global final energy consumption was about 50% in 2021 [10], then the sector decarbonization is very important within the energy transition scenario. While cooling is highly coupled with the electricity sector, since electricity is the main source to drive the air conditioning and chiller devices, heating is often defined as a sector hard to decarbonize because most of the heat today relies directly on fossil sources and it is often de-centrally generated by small units. So, the shift to decarbonized technologies is complicated since the owner of the dislocated small units must be persuaded to adopt an alternative low (or free) carbon technology, within a market-based economy these alternatives are supposed to be cheaper to be adopted on a large scale. The German trend of RES implementation can give an idea about how different are the results achieved within the electricity and the heating sectors, comparable developments can be observed in other industrialized countries. In 2016 the share of renewables in gross power generation was nearly 32% in Germany, up from around 3% in the early 1990s. In contrast, concerning final energy demand for heating and cooling the RES share was only around 13% in 2016, up from 2% in 1990 [11].
The strategies mostly adopted to reduce the environmental impact of heating are:

- Sector coupling and heating electrification.
- Efficient heat generation, distribution, and use, including condensing boilers, solar collectors, Combined Heat and Power (CHP) generation, waste heat recovery, and District Heating Networks (DHNs) for distribution.

According to the IEA to reach carbon neutrality by 2050 the share of heat pumps, low carbon district heating, and renewables-based heating must exceed 80% of sales in 2030.

Figure 4 points out how after years of slow but steady decline, the share of coal, oil, and natural gas boilers in global heating equipment sales fell under 50% [10].

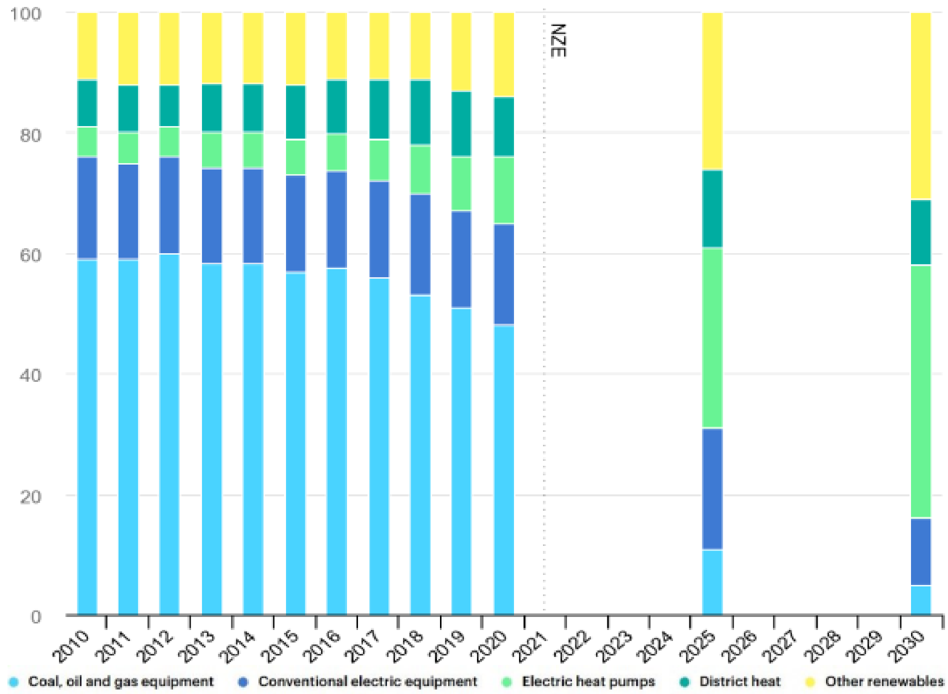

Figure 4 - Percentage heating technologies sold globally for residential and service buildings 2010- 2030, 2025, and 2030 values are simulated according to the scenario towards the 2050 carbon neutrality [10] .

Generally speaking, it is common to refer to "sector coupling" to indicate the interconnection of the sector, which has traditionally relied on other sources (such as heating or transport), to the power sector. It may be defined also as "power to heat" or heat electrification. The process is considered to be essential for a deep decarbonization of heating [12],[13]. Moreover, power to heat technologies may provide elasticity to the electrical demand [14],[15], this is today a debated issue since if not properly managed the massive electrification of the heating systems may increase the demand for electricity within some time of the day since the need for heating is almost simultaneous for most of the residential buildings. It would require a lot of power capacity to be installed, but then this capacity may be unused when there is no demand for heating (during low demand hours or warm seasons), and it may be reflected in the risk of not paying back the new capacity investment or in very high electricity price during the peak demand hours. However, if the power to heat system is carefully implemented and managed, including energy storage or exploiting the building thermal inertia as storage itself, and the market has an effective design able to provide proper price signals to the final user, the heating sector coupling may be beneficial also for a deep RES penetration in the electricity generation. Section 1.1 outlined how the growing penetration of renewable energy sources, mostly non-programmable and inverter-based, requires more and more demand for services and demand response, under this perspective poly-generation technologies, smart grids, and advanced power management strategies could give a substantial contribution to the decarbonization of bot electricity and heating sectors [16]. The complete array of technologies available to convert the electricity to heat has been well revied by Bloess et al. [12], but heat pumps are the most promising [10],[17]. The benefits of heating electrification in terms of carbon intensity are of course correlated to the average carbon intensity of the power generation. If all current fossil-fuelled heat generation technologies were replaced by heat pumps overnight, the combined emissions of the heat and power sector would be reduced, but the benefit quantification depends on the local electricity grid. If the heat is generated by and heat pump with a COP of 2-3, reasonable for air sourced HP in a cold climate, and the heat pump is fed with the electricity of a coal-based power plant with a 30-35% efficiency, then the results are comparable or even worse than what a condensing gas boiler emits to supply the same amount of heat. The Joint Research Centre of the European Union assesses that the benefits would be about a decrease in carbon dioxide emission by 16% on average in the EU but reports heterogeneous results among the member states. The biggest potential is found in France, a strongly nuclear-based electricity system, with 65%, and the lowest potential in PL and EE, coal-based economies, with 4%. Without additional "clean" capacity additions the additional electricity demand for heating will be mainly generated by dispatchable sources which usually have a higher emission rate than the average electricity generation mix and the environmental potential of heating electrification may be reduced.

Many purposes for which large amounts of heat are required, especially in the industry sector, need it at high-temperature levels. When the heat has utilized its potential at some level and the temperature falls below the value required by the specific application, unless the heat can be supplied to other users at a lower thermal level at the site, it will be wasted and dumped into the environment. The interest in recovering such waste has been strong for decades [18] but in the last year, the growing fuel prices and the effort in reducing global GHG emissions boost the research and the applications. Additionally, in the last years, the exponential growth of demand for data centres cooling has been observed, the cooling medium exits the data centre at a warm temperature with a relevant heat potential if the vastity of the source is considered [19]. The waste potential is normally divided between the high-temperature waste heat recovery (>400°C), medium-range (100-400°C), and low-temperature (>100°C). Usually, most of the waste heat in the high-temperature range comes from direct combustion processes, in the medium range from the exhaust of combustion units, and in the low temperature range from parts, products, and the equipment of process units [20]. The waste can be exploited for three different purposes. (i) Heating purpose, so the heat is redirected to the new user, if required, improving its thermal level by heat pumps. (ii) Mechanical or electrical purpose, utilizing the technology which best suits the waste temperature, the heat can be recovered in form of mechanical and electrical energy. Organic Rankine Cycles (ORC) are a fast-developing technology that meets this demand [21. (iii) For refrigeration or cryogenic purpose exploiting adsorption refrigerators. The highest is the temperature the easiest is the recovery for all the aforementioned purposes. Jouhara et al. [22] reviewed all the available technologies for waste heat to heat and waste heat to power recovery, highlighting that the selection of heat recovery methods and techniques largely depends on key factors such as the quality, quantity, and the nature of heat source in terms of suitability and effectiveness. However, it is also shown that heat pumps best suits medium and large amounts of low-temperature waste heat recovery, as it gives the capability to upgrade waste heat to a higher temperature and quality. Since heat pumps intrinsically imply the heating sector coupling, the use of this technology for low temperature waste heat recovery is particularly interesting because it may allow combining the benefits presented by the previous subsection with a deep energy efficiency improvement which would follow a systematic recovery and exploitation of low-temperature heat sources. In order to quantify the described potential Forman et al. [23] systematically applied a novel top-down approach for the estimation of waste heat in the most common sectors of end-use (transportation, industrial, commercial and residential) including electricity generation on a global scale. The results pointed out that 72% of the global primary consumption is wasted, and transportation and electricity reported the highest values (81% and 61% respectively). Moreover, on average 63% of wasted heat is classified as low temperature, within the electricity sector the low-temperature share reaches 88%.

The waste heat recovery potentialities have been explained by the previous subsection, however, these wasted resources are often far from the residential areas [24,25]. Moreover, the integration of flexible and clean energy sources into the energy mix could be challenging at the individual building level in urban dense areas. For this reason the centralizing of the heat generation is generally considered auspicial, furthermore, a centralization would reduce the number of stakeholders that newly designed policies would involve, and it will make easier their implementation. Centralizing the heat generation also implies developing networks to transfer that amount of heat from the generator to the user, such networks are commonly defined ad District Heating Networks (DHN) which is a technology implemented since the 1870s than could today play a pivotal role in the sector decarbonization [26]. China, Russia, and Europe are responsible for more than 90% of global DHN production, and therefore critically influence the current average carbon intensity of district heating. The International Energy Agency has defined the DHNs as an important part of heating sector decarbonization but today the sector is classified as “not on track” to reach the 2050 targets [10]. The combined share of renewable sources and electricity in global district heat supplies together should rise from 8% today to about 35% in the current decade, China DHN carbon intensity is the highest, 29% higher than the world average. Moreover, the share of DHN on the overall heating demand is almost constant since 2000, although building area has increased by 65% over the same period. It means that DHN adoption for new buildings does not increase despite the effort in reducing GHG emissions. The countries with the highest growth rate are China and Korea, with +7% each in 2020, In Northern China especially DHN is considered essential to improve the air quality during the heating season [27]. Usually, DHNs rely on a combination of several generators together, most of them are fossil fuel-based today. In particular, cogeneration plants (e.g., Combined Cycle, Internal Combustion Engine, and Steam power plant) are usually adopted to cover the base of the thermal load while Heat-Only Boilers (HOBs), whose Levelized Cost of Heating (LCOH) is normally higher, cover demand peaks or supply back-up generation. Thermal Energy Storages (TES) are commonly integrated within the networks as well for effective demand management. Even centralized heat generation, using larger combustion units with higher energy efficiency and more advanced control over air pollution is a benefit itself the DHN potentialities are not limited to this. Many networks have successfully integrated renewable energy sources. RES with the highest potential to be employed in district heating systems are solar thermal, geothermal, and bioenergy. Bioenergy currently accounts for the largest share of renewable district heat supplies, especially for use as a conversion fuel in old plants or areas with high biofuel availability (e.g., biomass-rich mountain areas). Copenhagen covers 95% of the demand by bioenergy (biomass and waste) [28], while Silkeborg, Denmark, has a relevant percentage of demand covered by solar thermal production, up to 20%, with 110 MWth installed capacity [29,30]. DHN technology has been improved for more than a century since its first application, Lund et al. [31] reviewed the development of the networks concerning the supply temperature, piping insulation, energy sources, management strategies, and ability to be used also as a cooling network. Based on these features they identify four different DHN generations, as illustrated in Figure 5. The division into four generations is widely accepted and used, even if the concept for the fifth generation has been presented such as a network operating at ambient temperature and using distributed heat pumps [32]. In the end, low-temperature DHNs are appreciated for their low carbon intensity potential achievable through RES integration, heat losses reduction and the potential for large heat pumps efficient operations [33].

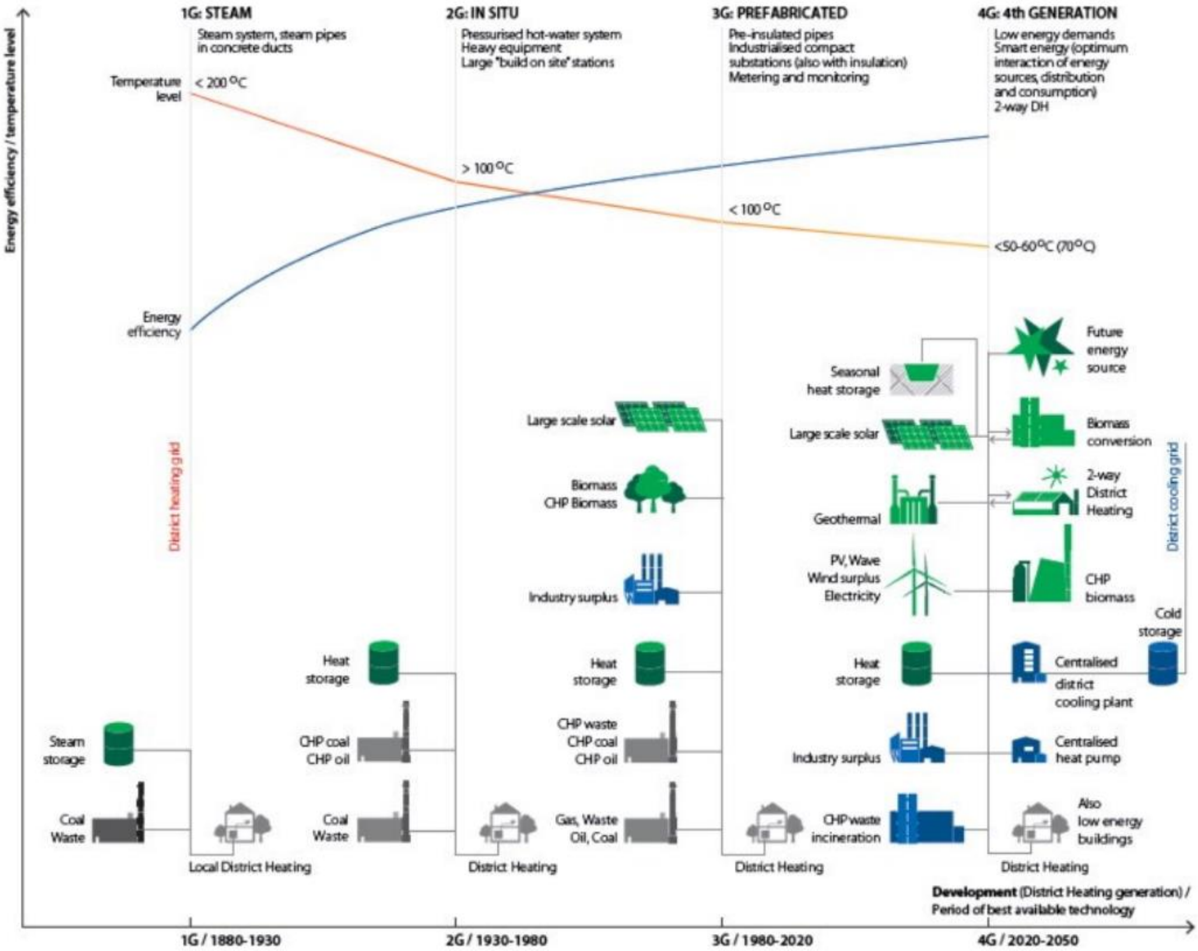

Figure 5 - Illustration of the concept of DHN generation.

1.3 PhD microgrid optimization challenge

In recent years, escalating environmental concerns [34] and the rising cost of energy [35] have compelled transportation, industrial and residential sectors to explore innovative power generation solutions. Exploring the potential and limitations of alternative, non-programmable renewable sources [36], integrating technology into smart grids [37] emerges as a viable solution with significant promise in reducing CO_2 emissions, ensuring energy security, and maintaining acceptable costs [38]. Advanced grids utilizing distributed generation technology from diverse energy sources offer enhanced flexibility, reducing dependence on conventional fuel [39] (in particular, natural gas). Moreover, aligning with the EU Green Deal objectives [40] and international CO_2 emission reduction agreements, the utilization of energy storage systems becomes imperative [41]. Among various technologies, hydrogen generation and storage [42] emerge as promising solutions, including options like high-pressure vessels, metal hydrides, or ammonia [43]. Yet, selecting the appropriate energy storage technology and managing it over time pose critical challenges due to numerous variables involved in the process [44]. This includes system choice and sizing, which impacts costs, energy security, reliability, and more [45] for maritime applications. Subsequently, post-installation management becomes crucial to prevent energy shortage and minimize operational costs [46].

In light of this scenario, developing real-time software for optimizing a poly-generation grid [47] becomes imperative for integrating smart grids into the energy transition. This tool should operate seamlessly in real-time while possessing optimization capabilities. Termed as the Energy Management System (EMS), this technology varies from simplistic solutions (such as if/else cases combined with a prime mover ranking [48]) to complex approaches employing optimizers [49] or agent-based calculations [50]. Building on previous successful outcomes, this work employs EMS based on a market function block (incorporating a minimization algorithm and if/else cases) coupled with a Model Predictive Control (MPC) tool that considers generator dynamics without imposing a rigid connection between the optimizer and physical systems, reaching TRL 7 [51].

The primary innovation in this thesis lies in the robust EMS managing diverse integrated generation technologies in maritime environment, including industrial symbiosis for waste resource recycling.

2 Distributed Generation Technologies

Distributed Generation employs small-scale technologies to generate power in proximity to end-users, ensuring cost reduction, enhanced reliability, and a smaller environmental footprint compared to conventional power generation methods. In the past, large coal, gas, or hydroelectric power stations produced electricity centralized through a grid. While effective in a less electrified era with predictable demand, the reliability of the supply has become a concern in many developed economies due to the increasing demands of a more electrified world. Energy security is sometimes tied to diversifying primary energy supplies and, in other interpretations, to ensuring the reliability of the electricity system.

In the first context, diversifying primary energy supplies, including renewables, inherent in distributed generation, offers evident advantages. However, exploring the second perspective introduces complexities regarding the potential benefits of DG. According to the IEA (2002) as summarized in [52], distributed generation can mitigate blackout risks and costs. Hence, it is considered as a mean to decrease private costs and risks for electricity consumers during system failures. Conversely, CIRED (1999) contends that distributed generation does not enhance system security; instead, it could have adverse effects, particularly when non-dispatchable generation capacity, such as wind turbines or photovoltaic systems closely tied to heat demand, increases. Their natural power supply variability prevents centralized control, necessitating increased backup power regulation. These challenges concerning the rise of non-programmable units in the grid persistently confront Regulatory Authorities.

Various definitions of Distributed Generation exist, some based on size, energy sources, or proximity to end-users. The European Union in Deliberation 2009/72/CE [53] concisely defines DG as electricity-generating plants connected to distribution networks, distinct from transmission networks. Previously, the Italian Authority defined DG based on generation

plants with nominal capacities below 10 MVA, considering historical treatment of such plants as "irrelevant" in overall electricity system management. However, from 2012, the Italian Authority aligned with the DG definition provided by 2009/72/CE.
Distributed generation encompasses diverse technologies tied to the distribution grid, like solar panels and combined heat and power systems. It can serve individual structures or integrate into microgrids within larger electricity delivery systems, benefiting places like industrial sites, military bases, or campuses. Consequently, DG aids in supplying clean, dependable power to more users, while reducing electricity losses along transmission and distribution lines [54]. The environmental impact of Distributed Generation can be positive when its use reduces the need for centralized power plant electricity generation, subsequently lessening environmental impacts.
Detailed benefits include cost-effective distributed generation technologies at homes and businesses utilizing renewable resources like solar and wind, utilization of wasted energy, such as through combined heat and power systems, reduction or elimination of "line loss," which is wasted energy during transmission and distribution within the electricity delivery system, by leveraging local energy sources.
However, distributed generation also presents potential adverse environmental effects [93] despite their single efficiency is generally lower than high size power plant:

- The physical space requirements ("footprint") of distributed generation systems, being closer to end-users, may raise aesthetic or land-use concerns.
- Certain technologies like waste incineration, biomass combustion, and combined heat and power might necessitate water for steam generation or cooling.
- Environmental issues may arise at the end of the useful life of distributed energy technologies during replacement or removal.
- Some distributed generation systems, particularly combustion-based ones, might be less efficient compared to centralized power plants due to scale efficiencies.

- Technologies involving combustion, especially those burning fossil fuels, can produce similar impacts to larger fossil-fuel-fired plants, like air pollution, albeit potentially on a smaller scale but closer to populated areas.

However, addressing pollutant emissions could be achievable by integrating distributed generation into a smart grid. Proper management of interconnected technologies within the distribution grid might enhance overall efficiencies, consequently reducing emissions.

Further advantages associated with leveraging Distributed Generation are outlined in [55]:

- Reduced reliance on major power plants, obviating the need for new large-scale generation and deferring new capacity construction.
- Diminished dependence on long-distance national transmission grids, freeing up transmission line capacities, curbing installation costs, and easing congestion in existing lines.
- Mitigation of price volatility in energy markets.
- Improved or sustained system reliability with backup generation, coupled with increased flexibility for system operators.
- Drive towards an innovative system by expediting the retirement of older, more polluting units.
- Enhanced energy security through diversified energy sources and reduced reliance on intricate large systems.
- Boost in personal, business, and regional self-sufficiency.
- Reduced environmental impact and greenhouse gas emissions due to the prevalence of renewable or low-emission generators in DG units.

This emphasis on lower environmental impact from DG leads to a deeper examination of the technologies employed, elucidating the primary sources involved and their respective characteristics.

In the Italian context, distinguishing between installed power and the number of installed plants is crucial when assessing Distributed Generation penetration. Solar fields typically exhibit smaller, locally based installations at the building scale, while wind farms, hydro systems, and distributed thermal plants, often used in Combined Heat and Power (CHP) units, tend to have larger installed power. Thermal plants, in terms of installed power, significantly contribute to the distributed generation share.

Recent trends in DG, as depicted in Figure 6, indicate a decrease in the share connected to conventional thermal sources and a concurrent rise in solar PV installations.

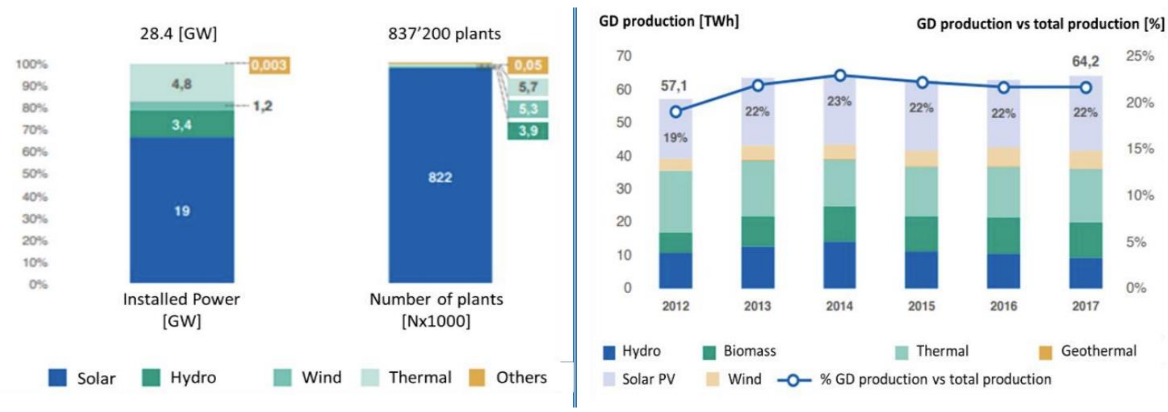

Figure 6 - Installed power and number of plants per primary source (ITA), (b) DG production overall trend (ITA) [56]

As seen in Figure 6, Terna categorizes the DG technologies depending on the primary energy source used. Following this scheme, a brief description of the technologies involved in DG are reported in Figure 7. The traditional generators are the common thermal power plant, fuelled by Natural Gas or Diesel; while among the non-traditional generators are included renewable devices, batteries and Fuel Cells.

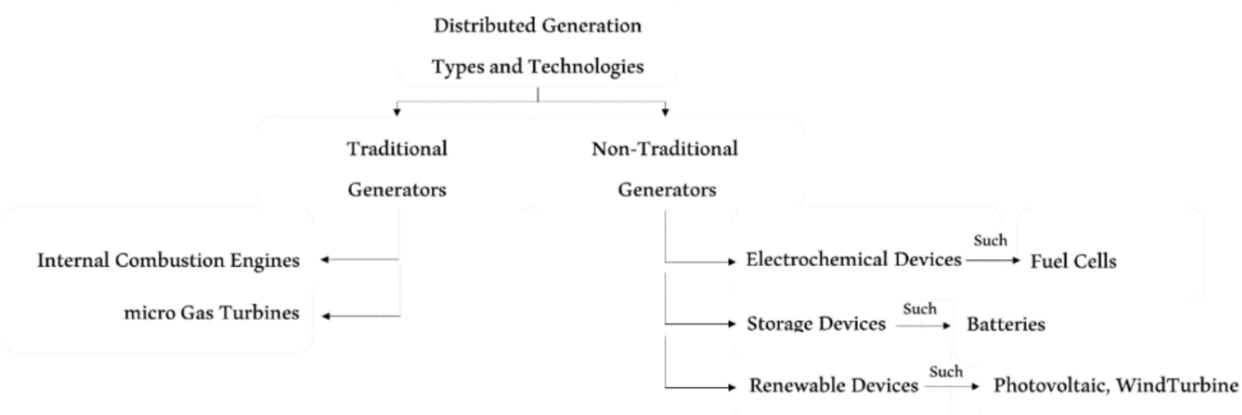

Figure 7 - Distributed Electrical Generation Technologies Classifications [57]

2.1 Traditional generators

Traditional generators are energy systems that convert primary energy into profitable electric and/or thermal energy via combustion. The large majority of this kind of plants is not feasible for the small sizes related to DG; therefore steam power plants, combined cycles and large gas turbine power systems will not be treated in this part. While the most interesting applications for DG, considering their power size and dimensions, are Internal Combustion Engines (ICEs) and micro–Gas Turbines (mGTs). The interest in these generators consists mainly on their application as Combined Heat Power (CHP) units; producing simultaneously thermal and electrical power the overall efficiency of the unit increase dramatically, making interesting the application of these traditional generators also in a small scale, especially for residential purpose.

2.1.1 Internal Combustion Engine

Internal Combustion Engines (ICEs) stand as the most technologically mature units within DG [58]. Although recognized for their role in transportation (like automotive and maritime applications), there is a growing interest in utilizing stationary engine/generator setups for power generation. ICEs, combined with heat recovery methods, form the fundamental components of Combined Heat and Power (CHP) systems across all scales [59]. In various sectors like universities, hospitals, data centres, and municipal utilities, ICE technology predominantly serves as the go-to for providing backup power in case of electric utility failure.

These engines come in diverse sizes, ranging from 5 kWe for small residential use to several MW, and can be paired with different fuels. Functionally, an internal combustion engine converts fuel energy into mechanical power, subsequently turning a shaft within the engine. A generator is then employed to convert this rotational motion into power.

Regarding emission reduction, ongoing exploration involves innovative fuels such as biogas, methanol and ammonia. These investigations aim to mitigate pollutants, particularly in the maritime sector, an aspect that will receive detailed scrutiny in the maritime section of this study.

2.1.2 Micro Gas Turbine

Microturbines, spanning a power range of 15 to 500 kW, are compact energy generators renowned for their efficiency. Their optimal fuel choice, minimizing emissions, predominantly remains natural gas, hence the common reference as micro Gas Turbines (mGT) in small business settings. Typically, these turbines require the compression of natural gas to ambient pressure at the compressor inlet. Operating at nominal pressures of three to four atmospheres, they align with open cycle gas turbines, but feature distinct characteristics: variable speed, compactness, ease of installation and maintenance, low NOx emissions, and often incorporate a recuperator to enhance overall system performance [60].

The initial utilization of microturbines dates back to the automotive sector between 1950 and 1970, gaining prominence in the energy market during the 1980s and 1990s with the burgeoning demand for DG.

Key features of mGTs include:

- Variable rotation speed ranging between 30,000 and 120,000 rpm depending on the size.
- High-frequency electric alternators functioning via a converter for AC/DC, also serving as the engine starter.
- Demonstrated reliability with some units reaching 30,000 operational hours, though the expected lifespan is around 10 years.
- Simplified construction and maintenance due to the generator integration within the turbine shaft, facilitating potential for cost-effective mass production.
- Compact design for straightforward installation and upkeep.
- Higher noise levels during operation, necessitating specific acoustic systems, particularly relevant in residential settings.
- Use of air-cooled bearings to prevent lubricant contamination by combustion products, extending equipment life and reducing maintenance expenses.
- Enhanced efficiency through heat recovery from exhaust gases, achieving a typical thermal efficiency of 30%.

Certain microturbines exhibit flexibility in operating with diverse fuels, apart from natural gas, enabled by embedded digital control software that allows this adaptation without significant hardware alterations. Like other power generation units, microturbines generate substantial heat during fuel-to-electricity conversion, with over two-thirds of the input fuel energy content converted into heat. Unlike conventional power plants that discard this waste heat, distributed generation technologies, owing to their size and location, facilitate its recovery [61].

Combined Heat and Power (CHP) plants utilizing microturbines produce heat and electricity at or near the load side, boasting an efficiency of up to 85% and lower operating costs compared to other applications. The recovered heat, usually from the hot exhaust gas, finds application in heating hot water (especially in residential contexts) or low-pressure steam purposes. Schematically depicted in Figure 8, the recuperator functions as a pre-heater, minimizing fuel combustion and augmenting system efficiency, while a water-gas heat exchanger is integrated in CHP configurations to absorb heat from exhaust gases.

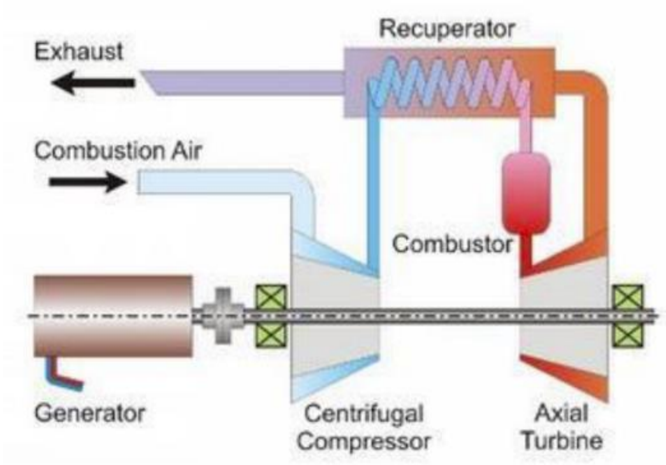

Figure 8 - Microturbine scheme [98]

2.2 Not-traditional generators

Innovative generation units are getting more and more relevance due to their potential in the increasing of energy savings and pollutant emissions. These technologies are generally characterized by their high efficiency and very low pollutant emissions. The size of non-traditional generators is commonly quite small, therefore they fit perfectly with DG applications. Innovative generation units can be classified depending on the primary energy source; renewables are certainly the large majority of these technologies, but a relevant role is represented also by Fuel Cells and Batteries.

2.2.1 Renewables

Among renewables, the main technologies employed in DG are bases on solar and wind. Especially solar power fits perfectly with the small scale required for DG; while wind power generation is basically at large scale and therefore connected to the transmission lines, but several applications of small wind generators are already installed.

Wind turbine technology has evolved significantly, transitioning from its historical use in agricultural windmills to modern setups generating electricity. Presently, expansive wind farms featuring large, modern wind turbines constitute the backbone of electricity production, while smaller turbines cater to localized energy needs in residential settings. Horizontal-axis wind turbines, particularly medium to large grid-connected ones with capacities surpassing 2 MW, currently dominate the market and are anticipated to continue their prominence in future developments [58]

The design of aerodynamic rotor diameters depends on the installation environment, aiming to maximize annual energy harvest. In high-wind speed areas, smaller rotor diameters with specific aerodynamic profiles achieve maximum efficiency between 14–16 m/s. Conversely, low-wind sites utilize larger rotors, reaching peak efficiency between 12–14 m/s. Capital and maintenance costs are significant considerations for wind applications. Presently, three-bladed wind turbines are prevalent in the market due to their manageable rotor inertia, better visual aesthetics, and lower noise levels compared to two-bladed variants. These factors are crucial for deploying wind turbines in densely populated regions. Additionally, three-bladed turbines exhibit suitability across a wider wind velocity range, leading to enhanced efficiency and stability. However, two-bladed turbines offer lighter tower tops, resulting in lighter supporting structures and reduced costs.

The industry trend leans towards larger wind turbines, reaching the multi-megawatt range, as manufacturers focus on their development [58].

In contrast, solar technologies encompass both thermal (Solar thermal panels) and electricity production (Photovoltaic panels), offering options for distributed electricity generation and local thermal production, potentially connecting to District Heating Networks. While thermal distributed production will receive dedicated analysis in a separate section, this introduction emphasizes Photovoltaic (PV) technology. Solar electric production through PV cells emerges as a promising avenue aligned with future energy sustainability requirements [58]. Initially based on silicon wafers akin to those in microelectronics, PV panels have transitioned toward the second generation of thin-film technology, driving cost reduction. This shift, combined with increased residential rooftop applications, has propelled market growth and subsequently slashed PV panel prices, rendering electricity production on a large scale increasingly competitive, as depicted in Figure 9.

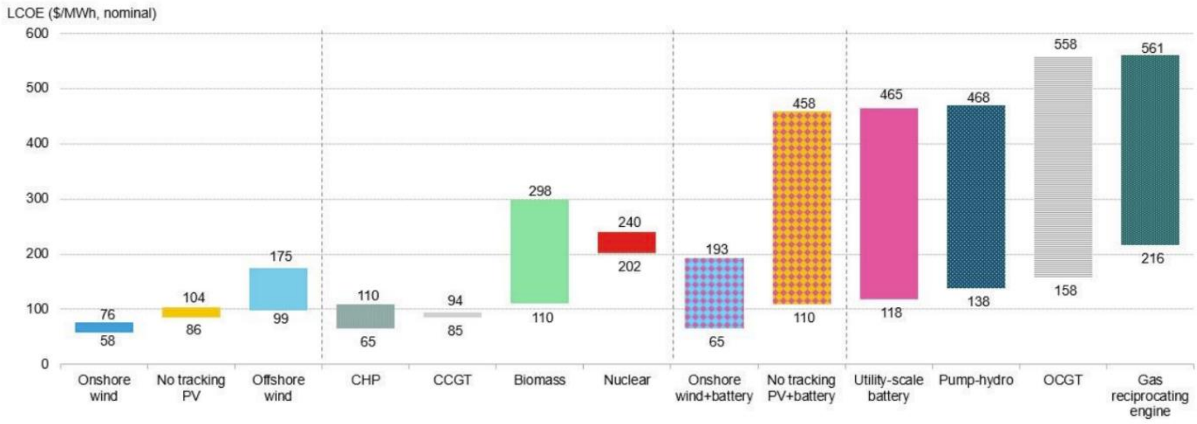

Figure 9 - Electricity cost by source [62]

2.2.2 Fuel Cell

A Fuel Cell (FC) stands as an energy conversion device, generating electricity and heat via an electrochemical process merging a gaseous fuel (often hydrogen-based) and an oxidant gas (oxygen from the air) across electrodes and an ion-conducting electrolyte, resulting in water as the sole exhaust. Distinguishing itself by converting chemical energy directly into electrical energy without combustion, a fuel cell boasts significantly higher overall conversion efficiency (approaching 50%) than conventional thermomechanical systems. Notably, these cells operate almost silently due to the absence of moving parts.

To generate electrical power, a fuel cell stack requires auxiliary components collectively known as the balance of plant (BoP). This encompasses various components facilitating fuel and oxidant supply to the stack, including pumps, blowers, compressors, and in the case of high-temperature fuel cells, burners to initiate system heating during startup. High-temperature fuel cells typically employ cathode air for cooling, while low-temperature fuel cells necessitate separate cooling systems due to insufficient temperature gradients.

Given that fuel cells produce variable voltage and current in DC power, power conditioning equipment like DC/AC inverters is deployed to convert the electricity to grid-compatible voltage and frequency. Noise related to fuel cell applications is primarily attributed to these BoP components.

Fuel cells present notable technical advantages such as modularity, favourable partial load characteristics, and swift dynamic response. However, their widespread adoption faces hurdles due to high costs, primarily associated with hydrogen usage. The production and delivery expenses of hydrogen, coupled with the intricate management requirements (high-pressure tanks or cryogenic storages), limit their widespread application. The US Department of Energy (DOE) published a market report in 2016 illustrating these aspects, as depicted in Figure 10.

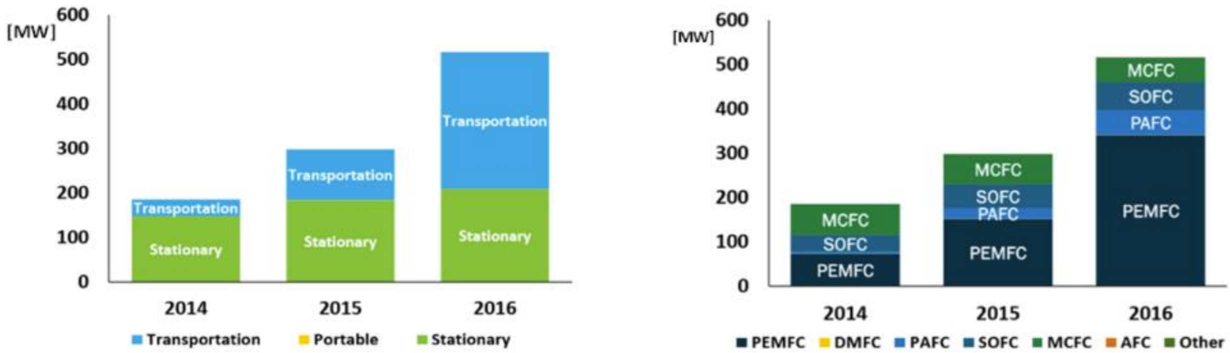

Figure 10 - Evolution of fuel cell installed power in terms of applications (left) and type (right) [63]

A significant increase in installed power by fuel cells is occurring in these years, mainly in the transportation sector. This increase is mainly related to the great exploitation of PEMFCs in the transport sector. Although, a variety of fuel cell types with distinct characteristics is currently present in the market. The most relevant are the Low and High-Temperature

Polymer Electrolyte Membrane Fuel Cell (LT/HT-PEMFC), Phosphoric Acid Fuel Cell (PAFC), Molten Carbonate Fuel Cell (MCFC) and Solid Oxide Fuel Cell (SOFC), Figure 11.

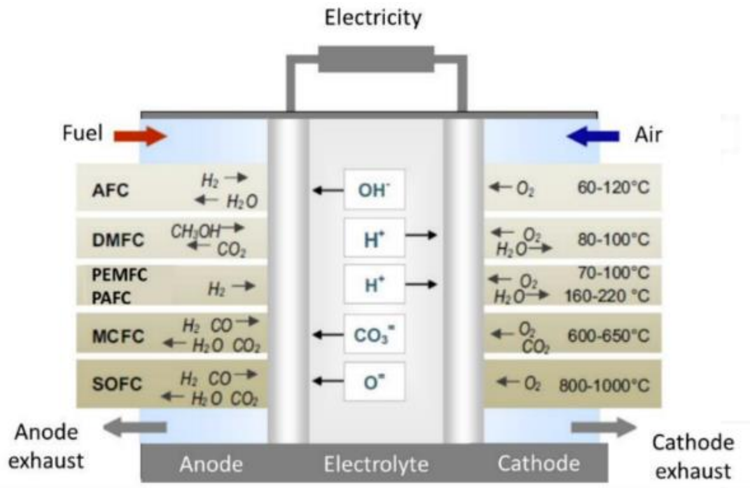

Figure 11 - Different Fuel Cell types, operational scheme [64]

- PEMFC: this fuel cell uses as electrolyte a polymeric membrane with high proton conductivity and operates in a temperature range between 70 and 100 °C; they are mainly developed for traction and small generation/cogeneration (1-250 kW). They can be divided in Low-Temperature PEMFC (LT-PEMFC) and High Temperature PEMFC (HT-PEMFC). The LT-PEMFC has known rapid development in the last decades and achieved high power densities and good transient performance. Its membrane consists of a proton-conducting wetted polymer (commonly Nafion). The need for a wet membrane, while the gas-diffusion pores have to remain dry, dictates an operational temperature of 65 and 85 °C, in order to do not vaporize the water. Considering the relatively low-temperature range, the use of platinum is required to catalyse the electrochemical reaction [65]. Another important disadvantage of the low operating temperature is the limited tolerance to fuel impurities. In particular, carbon monoxide (CO) deactivates the catalyst, because of its strong surface adsorption at low temperatures. A membrane that combines a polymer electrolyte with a phosphoric acid has been developed in order to operate in a higher temperature region (over 100°C). These PEMFCs are known as High-Temperature PEMFC (HT-PEMFC). In this configuration, platinum can be replaced with cheaper catalysts, such as nickel, in the high temperature fuel cell classes. Furthermore, the sensitivity to fuel impurities has strongly decreased. Another advantage is the opportunity to use high-temperature waste heat and steam, for example in a bottoming cycle or for fuel processing. On the other hand, the main drawback of this solution is related to their slow dynamics and low durability [66], not really performant in case of transport applications.

- PAFC: the membrane of Phosphoric Acid Fuel Cell consists of a silicon carbide matrix saturated with liquid phosphoric acid; working in a temperature range between 140 to 200°C, the required platinum loading decreases, while the CO tolerance increases. The low power density and durability issues have so far limited the commercial success of the PAFC [65].
- MCFC: Molten Carbonate Fuel Cell uses as electrolyte a solution of alkaline carbonates melted at the operating temperature of the cell (650-700°C) and contained in a porous ceramic matrix; they are mainly suitable for the generation of electricity and cogeneration from few hundred kW to several MW. This technology represents a relatively mature solution among high-temperature fuel cell. Indeed, MCFCs are commercially available but still struggle with high cost, limited lifetime and low power density (particularly an issue for transport applications) [63].
- SOFC: Solid Oxide Fuel Cells operate at very high temperature (about 600-1000°C) to guarantee a sufficient conductivity to the electrolyte, made of ceramic material (zirconium oxide doped with yttrium oxide). These cells are particularly promising for electricity generation and cogeneration from a few kW to several MW. The lower temperature classes are mainly applied in stand-alone fuel cell products, with electrical efficiencies up to 60% [63], while the high-temperature SOFCs are designed for combined operation with gas turbines, where efficiencies over 70% are projected [63]. Their high operating temperature allows the internal reforming of fuels,

eliminating the need for an external reforming unit and allowing the units to be used with a certain variety of fuels, mostly Natural Gas. They are also relatively resistant to small amounts of sulphur in the fuel, when compared to other types of fuel cells, and can therefore be used with hard coal gas. An additional advantage due to the high operating temperature is that the reaction kinetics is improved, eliminating the need for a catalyst. Although SOFC represents a promising solution, their current limited development state is mainly related to their mechanical vulnerability (ceramic material is particularly sensitive to vibrations) and high costs. Furthermore, there are some disadvantages related to their high temperatures: these cells require more time to be heated up to their operating temperature, it is also necessary to build this technology with robust and heat- 40 resistant materials and must be shielded to prevent heat loss (especially during start-up), besides they present control issue due to slow transients.

Table 1 summarizes the main peculiarities of the mentioned Fuel Cells technologies.

Table 1 - Main Fuel Cells characteristic

Fuel Cell Type	Temperature range [°C]	Fuel	Poisonous substances	Internal reforming	Efficiency
LT-PEMFC	65-85	H_2	S, CO>10 ppm	No	40-60 % with H_2
HT-PEMFC, PAFC	140-200	H_2	S, CO>3%	No	40-60 % with H_2
MCFC	650-700	H_2, CO	S	Yes	40-55 % with NG
SOFC	500-1000	H_2, CO	S	Yes	45-60% with NG

2.2.3 Energy storage systems

Energy storage systems are considered enabling technologies for different DG functionalities such as active management of network assets, network flexibility, improve power quality, self-healing, and resiliency. In addition, energy storage systems are essential components for integrating the non-dispatchable renewable energy resources. Other applications for energy storage systems include micro-grids and electrification of remote areas, in which energy storage systems are used to minimize dependence on the main grid supply. Energy Storage Systems (ESS) can be classified depending on the energy form they are using in the storage process. There are five main categories, as reported in Figure 12.

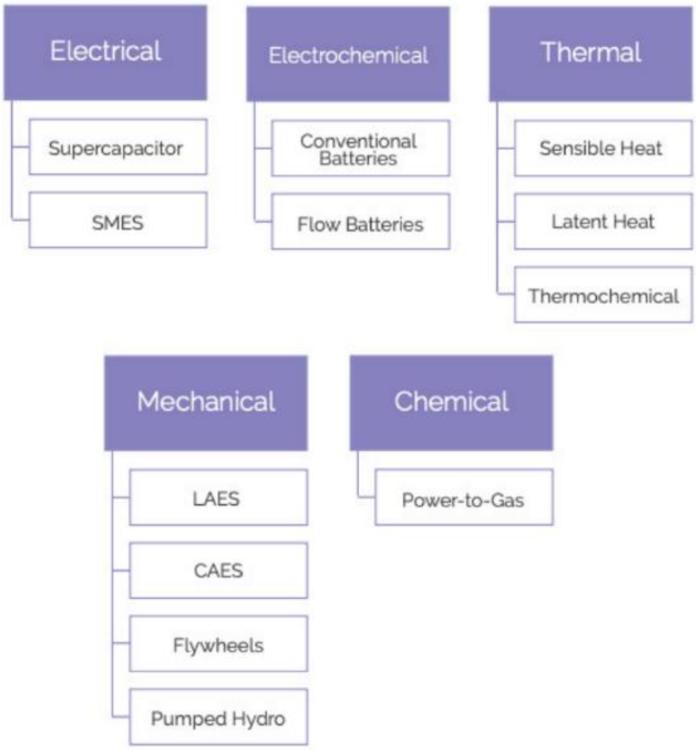

Figure 12 - Energy storages categories [67]

The main used technologies in DG scenario are electrochemical storages and thermal storages. The presence of storages gives to the system manager one degree of freedom more to perform the optimized management of the generation units. In the case of CHP units, as an example, the presence of a storage guarantees to decouple electrical and thermal demands. Therefore, it is possible to manage the system tracking one demand or the other considering economic and/or environmental aspects. Usually, in this case, thermal storage (more economic) is preferable. On the other hand, the use of electrochemical energy storages is getting more and more interesting considering the electric vehicle increasing share (Figure 13). The presence of these units in connection to the distribution grids is expected to have a huge impact on the grids and environment. Batteries contain a number of heavy metals and toxic chemicals. The disposing of them by the same process as regular household waste has raised concerns over soil contamination and water pollution. The Basel Convention on the Control of Trans-boundary Movements of Hazardous Wastes and their Disposal is the most comprehensive global environmental agreement on hazardous and other wastes. The Convention includes parties and aims to protect human health and the environment against the adverse effects resulting from the generation, management, transboundary movements and disposal of hazardous and other wastes, including batteries. Battery recycling aims to reduce the number of batteries being disposed of as municipal solid waste. Recycling plants in Europe have to comply with Directive 2006/66/EC, which requires a minimum recycling quota of 50%. From an economic point of view, the main drivers for recycling are cobalt (31,440 US$/t, 99.8%) and nickel (15,914 US$/t, 99.8%), followed by copper (6451 US$/t, grade A, LME) and lithium (6439 US$/t lithium carbonate, average prices June 2014–May 2015) [68].

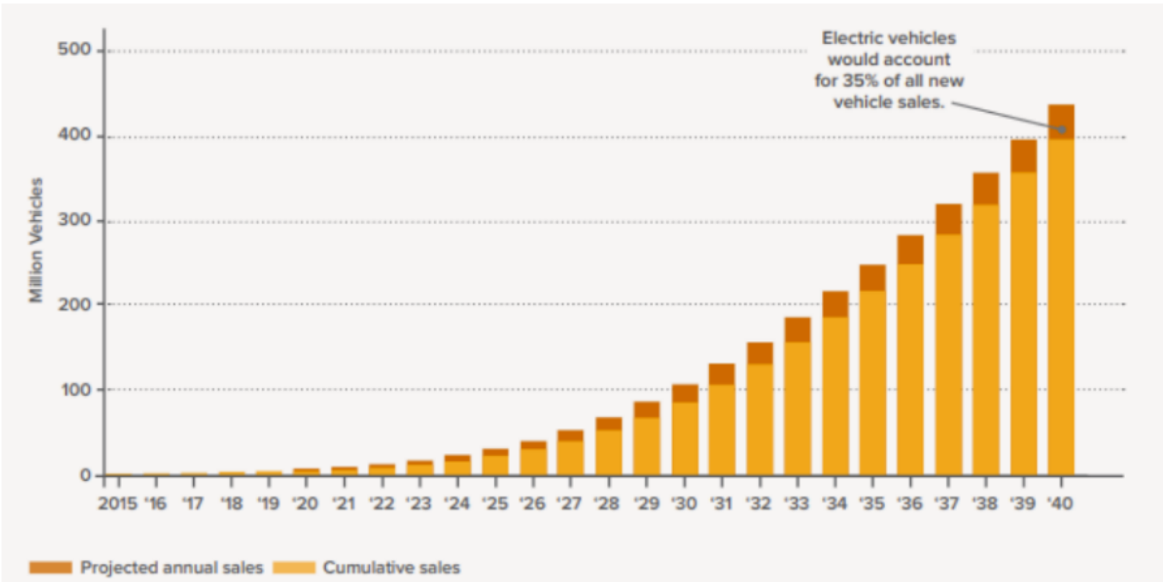

Figure 13 - Electric Vehicles selling projection [69]

2.3 Energy scenario summary

In this introduction, we have described the current and the foreseen energy scenario. In this context, where renewables will have an increasing role, the Distributed Generation approach looks like a necessity considering the currently available size for these systems. Furthermore, the trend towards wider use of DG shows an interesting potential with many benefits, such as size optimization and waste reduction. It is also worth notice that some critical aspects related to the management of the electrical grids have to be considered and properly managed in order to guarantee a reliable and safe massive introduction of these technologies in the energy market. Therefore, moving to the DG paradigm, the available fuelled technologies for Distributed Generation are reported in Figure 14 in comparison with standard centralized plants.

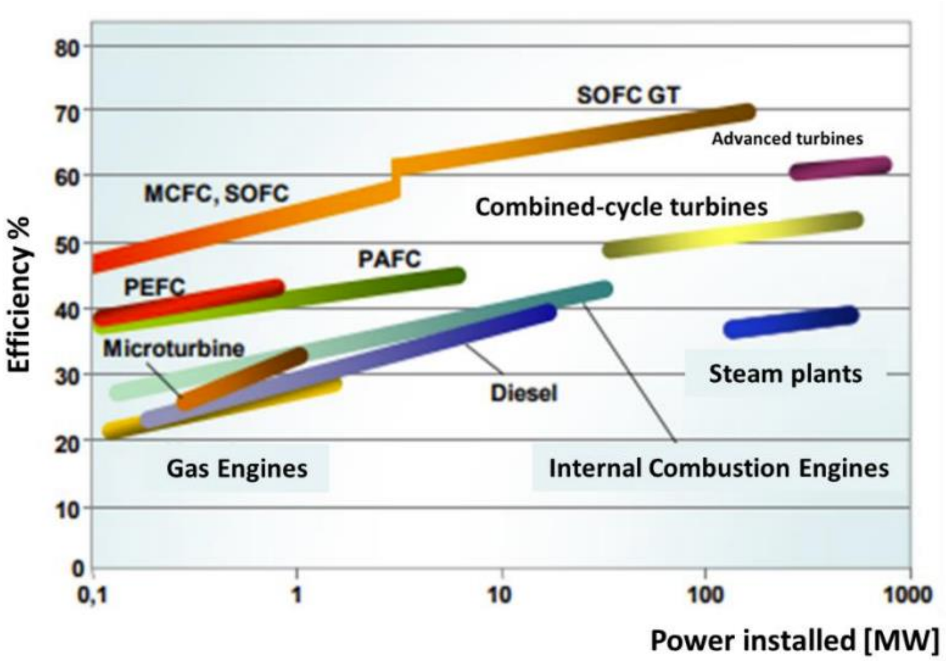

Figure 14 - Generation units' efficiency, comparison between DG technologies and centralized ones

Among DG technologies, the most promising in terms of energy efficiency are the Fuel Cells that still present drawbacks in terms of costs and life cycle. Most mature technologies such as Internal Combustion Engines and micro Gas Turbine, represents a good compromise solution since that, accepting their lower efficiencies, are very competitive in terms of cost and system management.

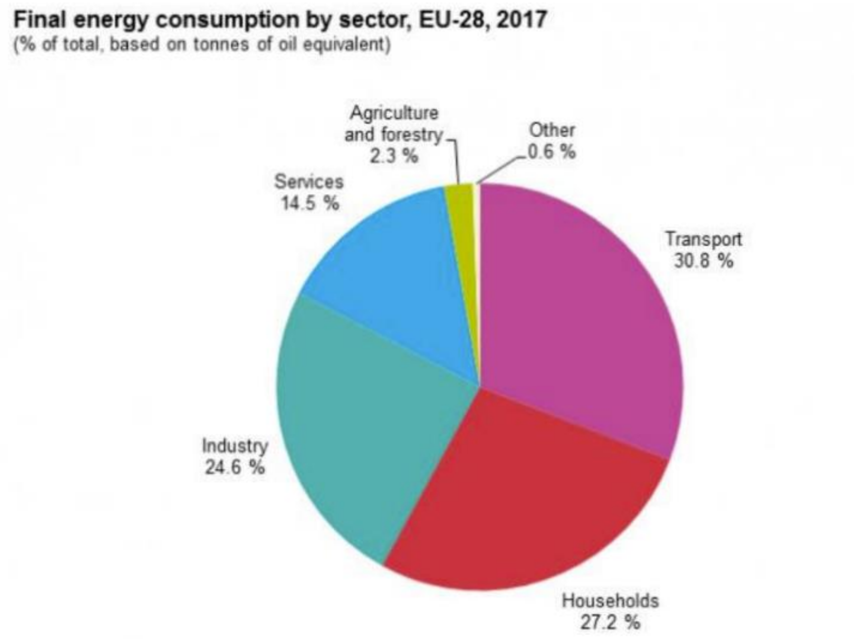

Figure 15 - Energy consumption by sector in EU-28

As reported in Figure 15, referring to Eurostat and IEA [70], the main energy consumptions in Europe are related maritime sector with industrial symbiosis and buildings sector. Therefore, the study presented in the next chapters of this thesis is focused on the development of the distributed generation approach in these two energy sectors. The use of micro Gas Turbines is studied in residential and transport sectors with the aim of evaluating their viability considering the different constrains set by the two sectors. In detail, the household application is related to the development of an energy hub in interaction with a poli-generation Smart Grid. In this case study the author has developed the design of the system (necessary for the proper selection of all the necessary components) and the management strategies with the aim of guaranteeing efficient and economic operations. For what concerns the transport application, the author has focused on the maritime sector, in particular the application of a DG approach onboard cruise ships. This has been possible via evaluating the most suitable technologies for this application considering the limitations in terms of weights and volumes when facing this kind of applications.

Figure 16 - ROBINSON demo-site in Eigerøy, Norway

2.4 Energy Research funding programs

Funding programs aimed at advancing new energy solutions, such as Horizon 2020 (H2020), Horizon Europe (currently on-going) and its counterparts worldwide, play a pivotal role in propelling innovation, sustainability, and technological breakthroughs in the energy sector.
Horizon 2020, a flagship initiative by the European Union, exemplifies a collaborative effort that nurtures groundbreaking energy projects. It offers a substantial budget to support research and innovation across various fields, including renewable energy, energy efficiency, and sustainable development. The program provides grants, competitive funding, and partnerships to foster cross-border collaboration among researchers, businesses, and institutions.
Similarly, other global initiatives echo this commitment to drive progress in the energy landscape. Programs in countries like the United States, Japan, and China allocate

substantial resources to foster innovation in clean energy technologies. These initiatives encourage the development of smart grids, renewable energy sources, energy storage solutions, and efficient consumption models.

The significance of these funding programs extends beyond financial support. They act as catalysts, nurturing a dynamic ecosystem for researchers, startups, and established companies to ideate, collaborate, and bring transformative energy solutions to fruition. These programs often emphasize not only technological advancements but also social, economic, and environmental impacts, ensuring a holistic approach towards a sustainable energy future. Moreover, these initiatives promote knowledge sharing, international cooperation, and the exchange of best practices. By fostering partnerships between academia, industry, and governments, they facilitate the transfer of cutting-edge research into real-world applications, accelerating the adoption of innovative energy solutions globally.

In conclusion, funding programs like Horizon 2020 and similar endeavours worldwide serve as vital engines for driving the development and deployment of new energy solutions. They empower stakeholders to pioneer advancements that are crucial in addressing pressing energy challenges, promoting sustainability, and steering us towards a cleaner, more resilient energy future.

2.5 Off-shore microgrid & island with industrial symbiosis

On islands, providing energy is difficult and expensive. Most islands have relied on diesel, and given the fuel logistics, storage, and other issues, many islands pay high rates for electricity [71].

Many islands have already, and many others are looking into switching from primarily diesel generators (DGs) to microgrids with significant amounts of renewable energy sources such as wind and solar. In fact, the US Navy has set a goal for 25% renewable energy sources [72]. Microgrids are system solutions to the energy generation and distribution problem because it involves the design of sufficient energy generation, storage, and controls to deal with the intermittent generation of renewable sources as well as balancing load and supply across the network [73]. The diversification away from diesel should also make the energy infrastructure more resilient to natural as well as man-made disasters. Resilience is the ability of a system to withstand external disruptions and, if damaged, to recover quickly from the damage. Resilience is especially important to the military because of the need for energy to sustain operations. Additionally, military installations are not only concerned with disruptions due to natural events but to attacks on the infrastructure from adversaries.

The military uses the resilience concept to describe a system that is trusted and effective in a wide range of mission contexts, is easily adapted to operational and environmental changes through reconfiguration and/or replacement and has predictable and graceful degradation of function [74]. The Navy designs microgrid systems using a top-down, multiphase process of architecture design followed by detailed design [72]. The microgrid architecture describes the structure of the microgrid in terms of its components, how they are configured and related to each other as well as the environment, and how the microgrid balances the competing stakeholder requirements. The microgrid architectural decisions include the type and quantity of distributed energy resources and energy storage systems in the microgrid to meet the loads' power demands. The subsequent detailed design phase addresses the power and electrical engineering issues of microgrid control, frequency regulation, voltage regulation, and so forth.

The industrial symbiosis refers to the collaboration between industries, where the waste or by-products of one industry become the resources for another. This concept holds particular significance for islands due to their unique challenges and limitations.

1. Resource Optimization: Islands often have limited resources, such as land, water, and energy. Industrial symbiosis allows for the efficient use of these resources by creating closed-loop systems where one industry's waste becomes another's input. For

instance, excess heat from a power plant can be utilized by a nearby greenhouse for agriculture.

2. Waste Reduction and Environmental Sustainability: Islands typically face challenges in waste management and disposal due to limited space and environmental concerns. By implementing industrial symbiosis, industries can minimize waste generation and promote recycling and reusing materials. This reduces the strain on the island’s environment and helps maintain its ecological balance.
3. Economic Benefits: Industrial symbiosis can lead to cost savings and new revenue streams for industries. By exchanging resources and materials, businesses can reduce production costs, optimize processes, and create new business opportunities. This can be especially crucial for islands, where importing resources can be expensive.
4. Community Resilience and Self-Sufficiency: Islands are often vulnerable to disruptions in supply chains due to their isolation. Industrial symbiosis fosters a more self-sufficient and resilient community by reducing dependence on external resources. When industries collaborate and share resources, it can mitigate the impact of supply chain disruptions.
5. Innovation and Collaboration: Encouraging collaboration among different industries promotes innovation and knowledge sharing. This can lead to the development of new technologies and solutions tailored to the island's specific needs, such as renewable energy sources or sustainable waste management practices.

In essence, industrial symbiosis on islands fosters sustainability, resilience, and economic development by optimizing resource use, reducing waste, fostering innovation, and strengthening local communities. It is a powerful concept that addresses the unique challenges islands face in a resource-constrained environment.

Due to these reasons, the islands with industrial symbiosis stand as the primary environment for the implementation of optimized Energy Management System in microgrid, main object of in this thesis (Figure 17). The figure below shows energy vector flows (electricity, heat, fuel) in island configuration for the ROBINSON case study, connecting generator and users.

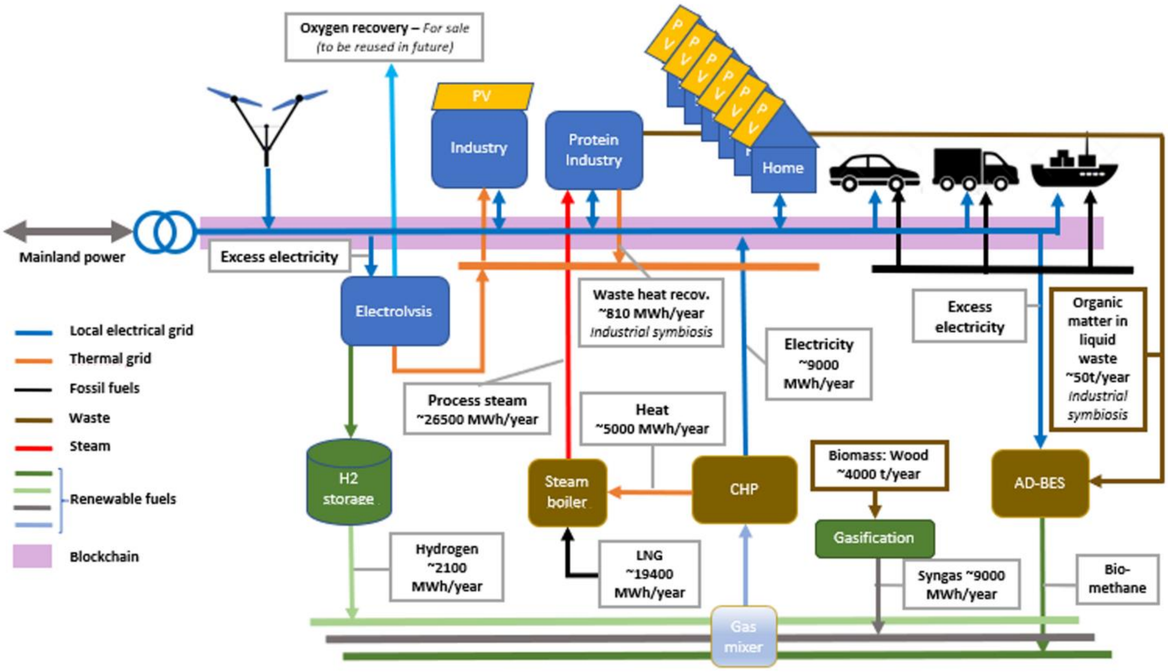

Figure 17 - The concept of ROBINSON project for the Eigerøy island

3 EMS concept for optimization in islands

This chapter presents the updated innovative EMS concept for micro-grid applications, developed by the PhD candidate after bibliographic analysis and learning research group know-how.

EMS should manage power fluxes, controlling system. Figure 18 shows it for general case, splitting EMS into three parts:

- Daily scheduling
- Market function
- Model Predictive Control

The daily or weekly scheduling provides a first guess off-line optimization scheduling, proving storage optimization management, according to the forecasted energy demand. The on-line Market function defines optimum reference value (r) for each controllable prime mover, minimizes target function and satisfying users demands, considering system operating condition. Real-time Model Predictive Control defines optimum control signal (u), respecting constraints of each prime mover.

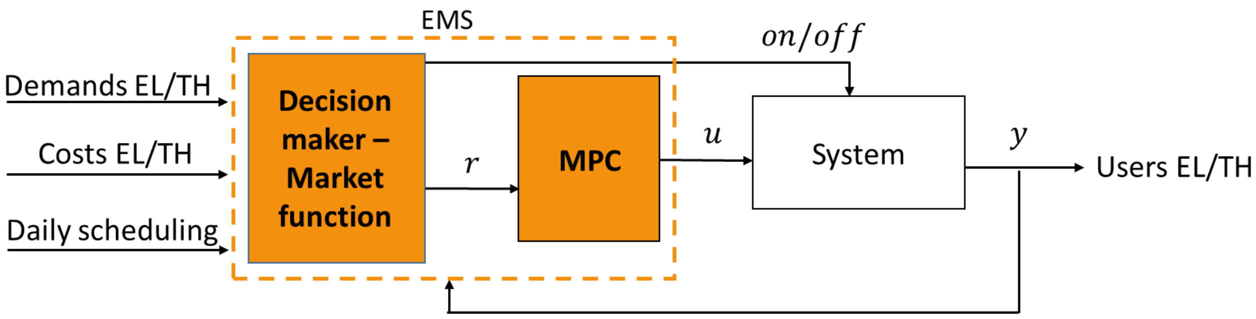

Figure 18 - EMS micro-grid concept

This innovative concept has been tested in the laboratories of the University of Genoa for three different case studies, all of the correlated to a specific project in H2020 program; the ROBINSON project represent the main EMS concept application of this thesis.

3.1 The ROBINSON project

The ROBINSON project, that has been started in October 2020 and will last to the end of September 2024 (except extensions), is part of the EU H2020 program [75]. It involves 18 partners, under the coordination of the European Turbine Network (ETN) including research centres, universities, companies (also SMEs) and local authorities. Although the project is quite complex with several objectives to be reached [9], in few words the main ROBINSON target is the demonstration in a real plant of a smart component integration for satisfy the local energy needs. Special attention is devoted to the integration of the renewable sources and to the industrial symbiosis (utilization of industrial waste for the local generation process). Although the demonstration is planned in the Norwegian island of Eigerøy involving the industrial symbiosis with the Prima Protein company, the project includes detailed analyses and experiments in the IES laboratory for the concept replication, starting from energy districts in Crete (Greece) and in the Western Islands (United Kingdom). However, the simulation tool and the related results included in this thesis refer just to the Eigerøy island considering further publication opportunities for the other cases. Figure 17 shows the general layout of the ROBINSON concept applied to the Eigerøy island. The system includes different grids for electricity, heat, hydrogen, steam and other fuels (syngas and biogas). The demands regard electrical and thermal needs of houses, industries and vehicles. Moreover, the grid is mainly equipped with these technology: (i) 400 kW (electrical power) microturbine (CHP), (ii) 22 MW (steam) boiler, (iii) two 500 kW (consumed electrical power) electrolyzers, (iv) a very small anaerobic digester (<0.25 Nm^3/day of biogas) based on bio-electrochemical system (AD-BES) for using the industrial waste, and (v) a wood gasifier sized for about 70% of the fuel needed by the CHP, (vi) a 100 kW wind turbine, (vii) PV panels. Moreover, the grid includes a 40 m^3 pressure vessel for hydrogen storage, and a gas mixer for generating the proper fuel mixture for the microturbine. To complete the configuration, it is important to highlight that the thermal power produced by the microturbine (an A400 machine working in CHP mode [76]) is used to pre-heat the water for the steam generation. This layout solution was defined during the proposal submission to give the priority to the industrial symbiosis. So, no connection between the CHP thermal generation and the grid was included, to exploit all the CHP thermal energy for the boiler water pre-heating. However, since the ROBINSON project includes a workpackage on business cases and design improvement, it could be possible to have a different configuration on the thermal side for the demonstration (this is an ongoing activity). The component sizes were defined on the basis of these aspects: (i) the boiler was already present in the site (it was designed and installed in the past to satisfy the steam needs by Prima Protein), (ii) the CHP and the wind turbine sizes were chosen to cover an average electrical district demand (with several hours including an important grid charging), (iii) the electrolyzers were chosen considering the available sizes on the market and the hydrogen needs (as shown in these simulations the chosen size is able to generate the necessary EMS flexibility to maintain a minimum energy safety margin- 6 hours of autonomy with the CHP at maximum load plus a further margin from the empty condition), (iv) the hydrogen storage vessel size was chosen depending on the available space and the needs of guaranteeing at least 12 h of CHP autonomy at full charged condition).

This is the configuration that was considered in this work, as defined in the initial part of the project. So, although the results shown here will be significant for the EMS development and testing, the further project development can produce significant changes in the layout (also considering other ongoing analyses in the project) moving the demonstration to a different configuration.

3.2 ROBINSON model development

The details related to the modelling activities are reported in this section for the case of the Eigenrøy island. However, the structure of the component models presented here is valid also for the other cases for replication issues. All the simulation models developed are presented here, including the related calculated results. In general, all the components have been modelled with dynamic approach except for the AD-BES. This choice is due to the purpose of developing the EMS. So, since the fuel mass flow rate produced by the AD-BES is negligible (the AD-BES produces a fuel flow lower than 3 order of magnitudes of the other fuel flows), the impact on the EMS operations is negligible. However, for the replication issues, the EMS will include the possible integration with the AD-BES technology considering the related dynamic issues (due to the low dynamic response the related produced gas will be a system input without any modelling and control on the AD-BES side).

This section presents in detail each single prime mover model, considering the Eigerøy scale.

3.2.1 CHP

The Aurelia A400 CHP model integrates part-load curves correlation and dynamic manufacturer details to emulate transients and off-design behavior. The model Figure 19 computes and monitors the main global performance operating parameters, not considering the thermodynamic internal process (e.g. pressures and temperatures between the components shown in Figure 20). The CHP exhaust mass flow (thermal power) heats the air at steam boiler inlet, decreasing the steam boiler fuel consumption.

The CHP input model parameters are:

- Electrical power set-point
- Temperature of the water at intercooler inlet
- Ambient temperature
- LHV

- Nominal efficiency
- Nominal electrical Power

The CHP output model parameters are:

- Electrical power
- Thermal power (Eq.2)
- Fuel mass flow (Eq. 3)
- Electrical efficiency (Eq. 1)
- CHP efficiency (Eq. 4)

$$\eta_{CHP} = \eta_{CHP\_max}(\eta_{CHP_n}, T_{amb}, T_{In_{IC}}) * (p_{3a_{1(1)}} * P_{\%}{}^{2} + p_{3a_{1(2)}} * P_{\%} + p_{3a_{1(3)}}) \quad (1)$$

$$Pth = p_{2_{1(1)}} * Pel + p_{2_{1(2)}} \quad (2)$$

$$m_{fuel} = P_{el}/LHV * \eta_{CHP} \quad (3)$$

$$\eta_{CHP\_t} = (P_{el} + P_{th})/LHV * \eta_{CHP} \quad (4)$$

Figure 19 presents the CHP Matlab-Simulink model, highlighting inputs on the right and outputs on the left, while Figure 20 shows the A400 machine (optimized layout that allows to achieve 40% efficiency).

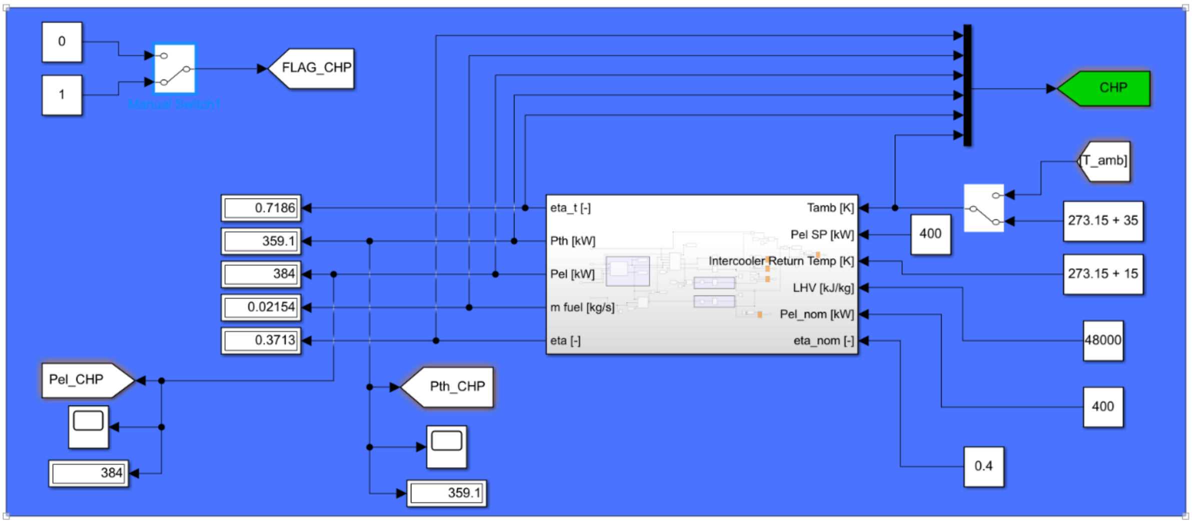

Figure 19 - A400 CHP model

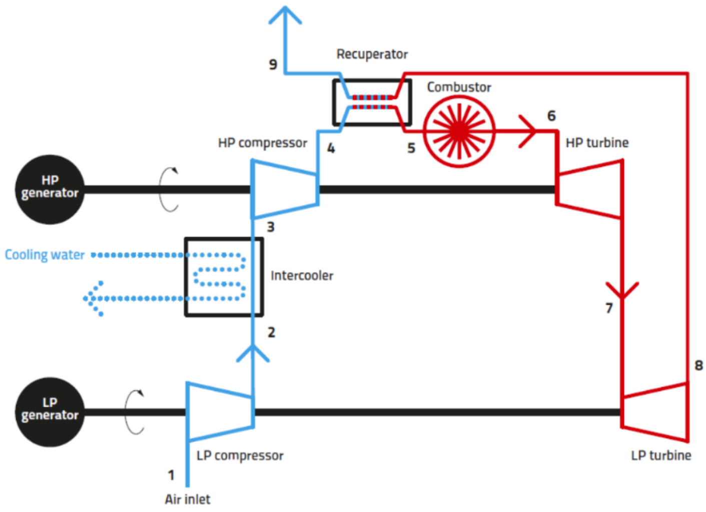

Figure 20 - Intercooled and recuperated, generator on both shafts, process layout

3.2.2 Steam Boiler

The steam boiler model emulates both transients and part-load operations using Prima Protein data and literature off-design characteristic curves. The equation below defines the efficiency at part-load operations according to UNIGE in-house tool (Eq. 5).

$$\eta = \eta_{nom} * \sqrt{(1 + l_{\%})/2} \tag{5}$$

Starting from efficiency and LHV the model computes the fuel mass flow. Figure 21 presents the steam boiler model in Matlab-Simulink environment.

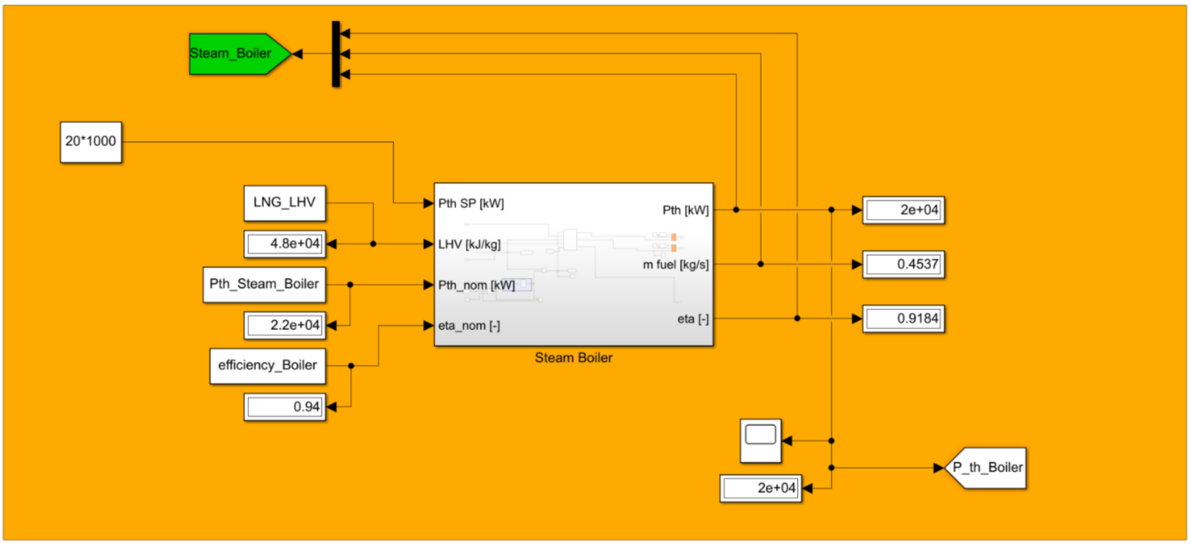

Figure 21 - Steam boiler model

The transients data (e.g., start-up, shutdown) of the manufacturer provided time characterization that has been modelled using first order delay.

The CHP input model parameters are:

- Thermal power set-point
- LHV
- Nominal efficiency
- Nominal thermal Power

The CHP output model parameters are:

- Thermal power
- Fuel mass flow
- Efficiency

The steam boiler (Figure 22) is regulated on the basis of the steam pressure. Considering a desired pressure set-point (normally 8.0-8.5 bar), the burner operates the start-up as soon as the pressure gets below that set point (some hysteresis of course is present).

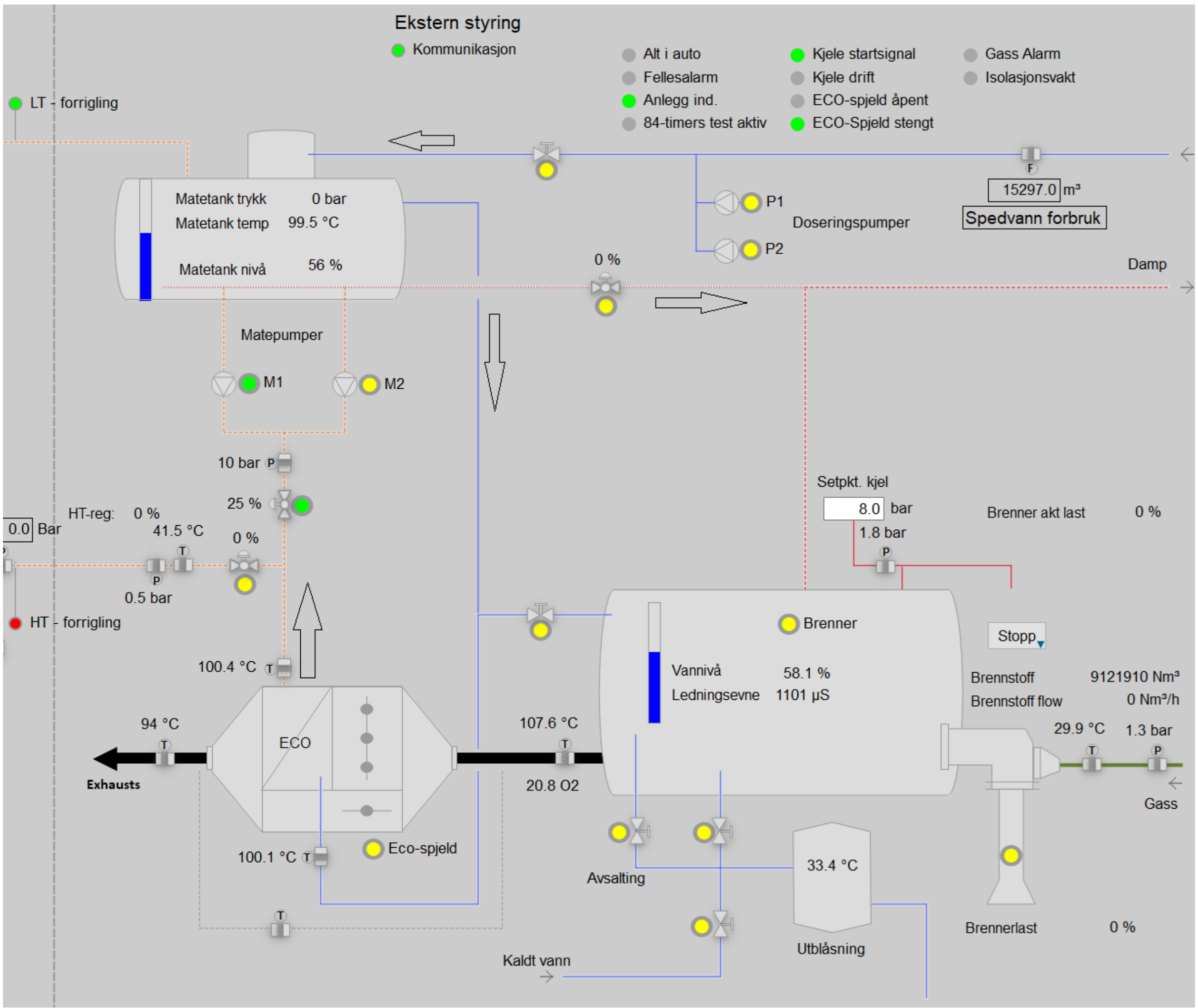

Figure 22 - Screen shot of the steam boiler from PC, in control room

The high-level modelling approach presented does not include technical process details, but allows to simulate the global system (main inputs/outputs) for EMS set-up and test (MIL, HIL).

3.2.3 Wind turbine

The wind turbine model computes the power generation using the manufacturer performance curve. The model input is the wind speed [m/s], while the output is the generated electrical power.

The overall model couples the characteristic curve (look-up-table from manufacturer data) with a first order delay transfer function, emulating both part-load operation and transient rotating inertia. The wind speed is the input, while the electrical power generated is the output. The picture below (Figure 23) shows the estimated power generation, considering a typical wind speed profile in Eigerøy.

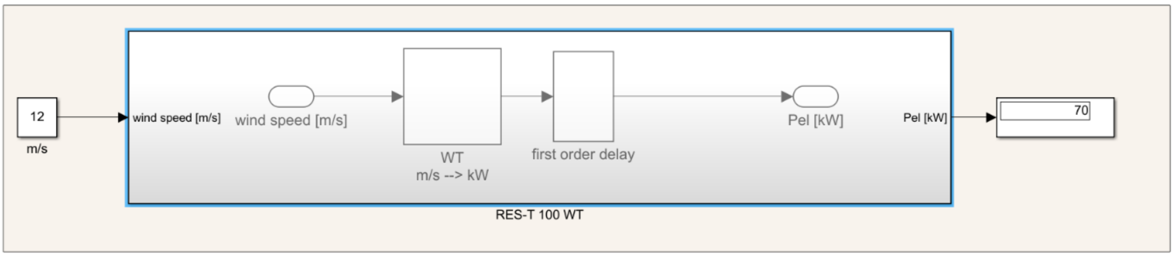

Figure 23 - Wind turbine model

3.2.4 Gasifier

The gasifier is meant to provide syngas to the CHP. The modelling work was the innovation and the update of the gasifier model present in the TRANSEO library (TPG UNIGE tool) [77]. To achieve the gasifier model a generic "Thermal Network Library" based in MATLAB-Simulink was developed, and relying mainly on embedded MATLAB functions originally developed for this purpose. Such a library is composed of the following three main components:

1) Solid domain, simulating a 2D solid matrix with internal conductive heat transfer.
2) Fluid domain, simulating a quasi 2D reacting flow of solid/liquid/gas.
3) Heat linker, defining the heat exchange relationships between the boundaries of solid and fluid domains.

Such components use a finite-difference formulation of the thermal problem, which is resolved with an implicit time integration scheme. Figure 24 presents the generic reaction scheme.

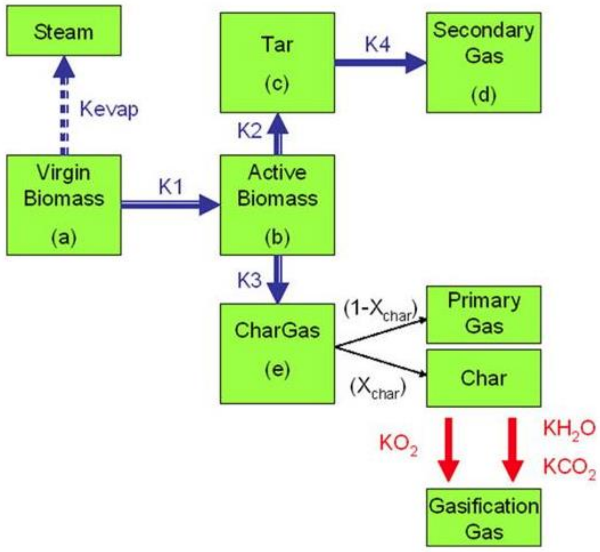

Figure 24 - Generic reaction scheme used to model cellulose, hemicellulose, and lignin pyrolysis (blue and black arrows). Red arrows regard char gasification.

The real-time application of the model constrained the developers to avoid the inclusion of some real effects that may occur in a gasifier. The main phenomena not represented at the moment are:

- Mass accumulation; the level of solid is predefined, as well as the surface available for the vapor phase. Thus, start-up phenomena cannot be captured.
- Tar condensation; tar is considered to be always in the vapor phase, together with the incondensable gases and steam.
- Diffusion and heat resistance; diffusion and heat resistance within the solid particles is not considered (intrinsic apparent kinetics should be used), thus particle size has no influence on results.

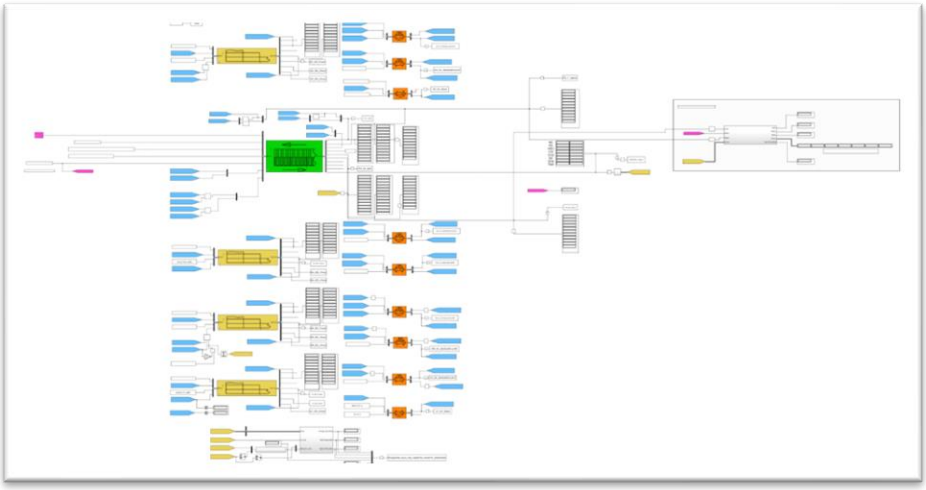

Figure 25 - Gasifier model screenshot

Despite the 2D approach, the present low computational cost makes it (Figure 25) real-time runnable for cyber-physical tests. Further clarification on the gasifier model could be available in paper by Alberto Traverso et all [78], in collaboration with the National Energy Technology Laboratory (US Department of Energy, Morgantown West Virginia).

The specification features of the biomass composition are presented in Figure 26 below.

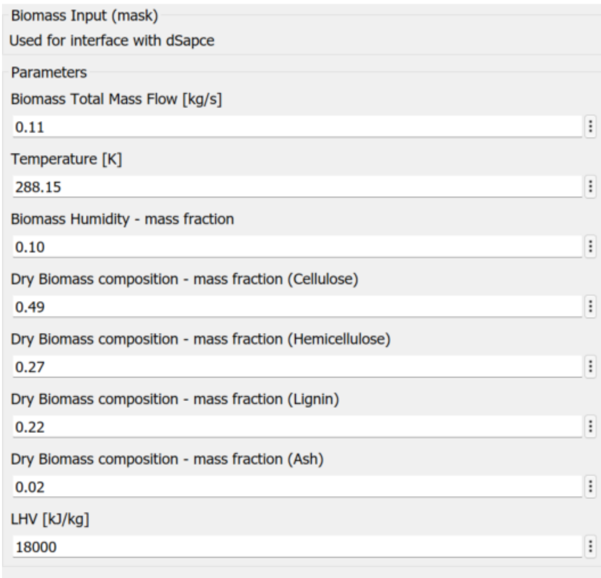

Biomass Input (mask)
Used for interface with dSapce

Parameters

Biomass Total Mass Flow [kg/s]
0.11

Temperature [K]
288.15

Biomass Humidity - mass fraction
0.10

Dry Biomass composition - mass fraction (Cellulose)
0.49

Dry Biomass composition - mass fraction (Hemicellulose)
0.27

Dry Biomass composition - mass fraction (Lignin)
0.22

Dry Biomass composition - mass fraction (Ash)
0.02

LHV [kJ/kg]
18000

Figure 26 - Biomass composition guess, gasifier model inputs from its mask

3.2.5 Electrolyzer

The alkaline electrolyzer model computes the hydrogen and oxygen mass flow, while the input is the total power to the electrolyzer system (compression power included). The model uses the following manufacturer parameters to compute the outlet mass flows:

- Ratio between the compression energy and the stack electrolyzer energy
- Minimum input power percentage
- Nominal power electrolyzer stack
- Nominal efficiency (normalized efficiency curve)

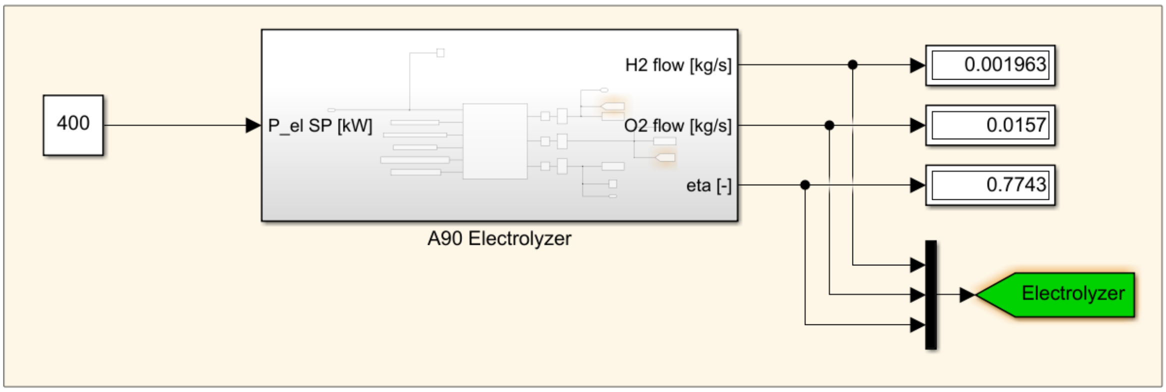

Figure 27 - Electrolyzer model

If the electrical power input (Figure 27) would be lower than the minimum input power, the model considers the electrolyzer in hot stand-by operation.

The model includes part-load performance curves (Eq. 6, Eq. 7, Eq. 8) and dynamic behaviour literature data [4], integrating the characteristics curves and the dynamic feature to emulate the transients and the steady state operations. The electrolyzer dynamic response could be modelled as a first order delay, as confirmed by the A90 manufacturer.

$$Y = P_{in\_electr} / P_{N\_in\_El\_\&\_C} \quad (6)$$

$$Y_{\eta} = p_1 * Y^3 + p_2 * Y^2 + p_3 * Y + p_4 \quad (7)$$

$$\dot{m}_{H2} = (P_{n\_elec} * Y) * (\eta_n * Y_\eta)/(142 * 10\text{^}3) \quad (8)$$

3.2.6 H_2 storage

The H_2 storage tank has been developed starting from the TRANSEO plenum model [77], and integrating the real gas properties by REFPROP library [77].

The plenum is assimilated to a rigid volume, which changes its pressure and temperatures with the upstream and downstream components according to the mass and enthalpy exchanges. The user selects the volume and the fluid and the number of input/output stream flows. The plenum receives the incoming and exiting gaseous mass flows as known input. So, it just needs to explicitly integrate the continuity and energy equation, to provide the components themselves with the boundary conditions for the next time step. In the plenum, the total temperature is maintained (unless there is thermal exchange with the environment) while the total pressure is assumed to be equal to the static pressure (Figure 28). This means that a plenum carries out an adiabatic transformation where the flow kinetic energy is dissipated: as a consequence, plena should be inserted where velocity is negligible, while the real kinetic-pressure transfers should be managed within each component (however, this is not mandatory: the user only needs to be aware that the kinetic energy is dissipated into the plenum).

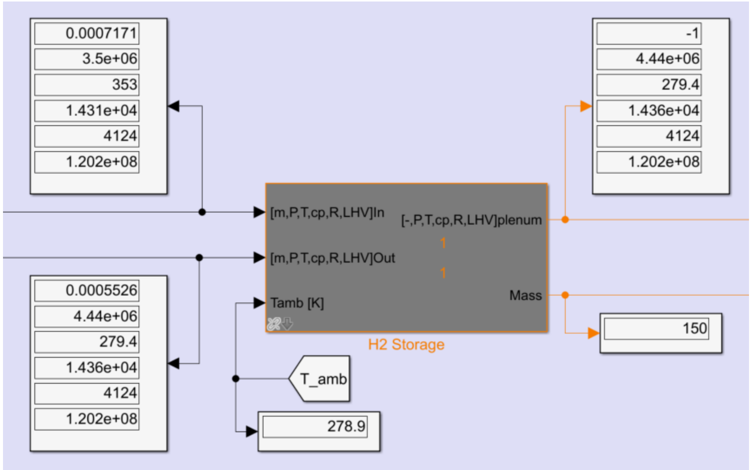

Figure 28 - H_2 Storage model screenshot

The plenum model computes the property of the flow inside it, but not the mass flow at the outlet, then the UNIGE group decided to use the value "-1" for highlighting it.

3.2.7 Gas mixer

The gas mixer model represents an innovation of the basic plenum component, integrating the volumetric composition computation in the gas volume component. It calculates the outlet composition (of the fuel gas mixture) as well as physical (pressure & temperature) and chemical properties (heating value). The user can set-up in the mixer mask the heat exchange coefficient with external ambient temperature. So, it can be in thermal balance with the surrounding environment or not, depending on the physical situation (including possible thermal insulation).

Starting from inlet flow condition of the individual fuel gas sources (LPG, bio-methane, syngas) at the current time [k] and outlet flow at the previous instant [k-1], the gas mixer model computes the fuel gas mixture properties at the mixing tank outlet (Figure 29):

- pressure
- temperature
- specific heat
- R

- LHV
- composition

As there are currently still limits set for the H_2 content (max. 30%vol. of H_2) of the fuel gas mixture delivered to the CHP unit, optional addition of hydrogen from a separate H_2 source (water electrolyzer), is subsequently determined by the EMS.

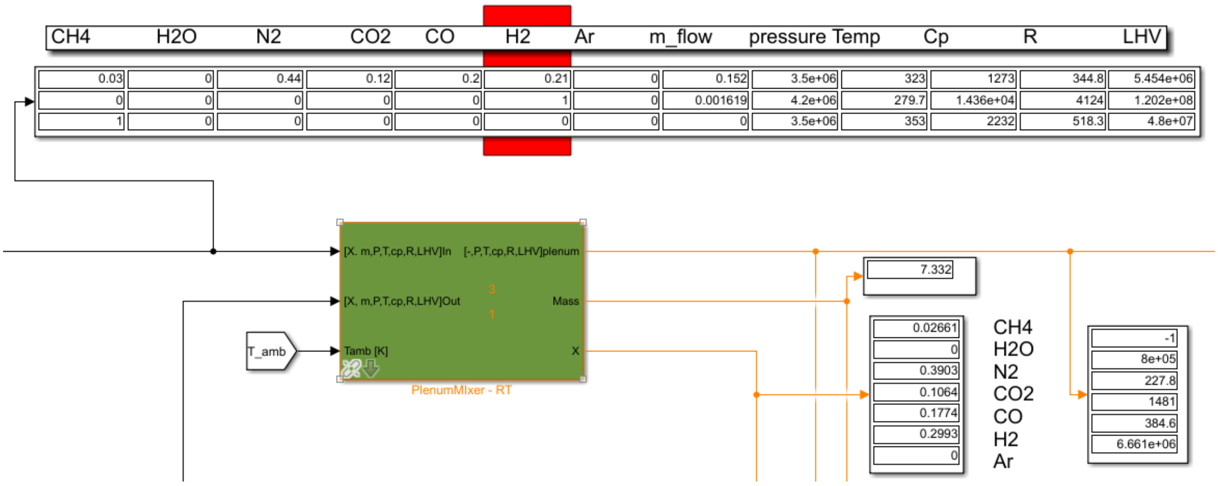

Figure 29 - Mixer model screenshot

3.3 Single component model validation

UNIGE gained wide experience in the dynamic modelling, simulation and validation of different energy systems since 2005 [77]. In ROBINSON, each model has been validated according to the available data, and considering their structure approach. Table 2 sums up the data source and the references for the validation each component models in steady-state and transient operations. The validation could be achieved using:

- manufacturer data
- in-house data
- previous work validation data
- literature data

Table 2 - Details related to the model validation activity

MODEL	*VALIDATION DATA AND REFERENCE*
CHP	Manufacturer data and in-house data
Steam boiler	Manufacturer data and in-house data
Wind Turbine	Manufacturer data
Gasifier	Traverso A., Tucker D., Haynes C., 2012, Preliminary Experimental Results of Integrated Gasification Fuel Cell Operation Using Hardware Simulation, Journal of Engineering for Gas Turbines and Power, Vol. 134, pp. 071701/1-10.
Electrolyzers	Manufacturer data
H_2 storage	Traverso A., 2005, TRANSEO Code for the Dynamic Performance Simulation of Micro Gas Turbine Cycles, ASME Paper GT2005-68101, ASME Turbo Expo 2025.
Mixer	Traverso A., 2005, TRANSEO Code for the Dynamic Performance Simulation of Micro Gas Turbine Cycles, ASME Paper GT2005-68101, ASME Turbo Expo 2025.

3.3.1 CHP

The data-driven approach (manufacturer data) makes the CHP model validated in steady-state operations. The A400 transient and dynamic data are not available yet since the CHP is still in the development and design process, they will be accessible when the CHP will be tested in the Aurelia facility or when it will be installed in the Prima Protein micro-grid. Then, the in-house transient behaviour data considered of the AE T100 for preliminary validation; when the Aurelia A400 step response will be available has been considered for the time constant. The picture below (Figure 30) shows T100 model validation that provided the time constant for preliminary characterization of the A400 dynamic behaviour, as first guess. Following a load demand step (from 20 kW to 60 kW) performed at time zero, the model is able to match with good accuracy the experimental results.

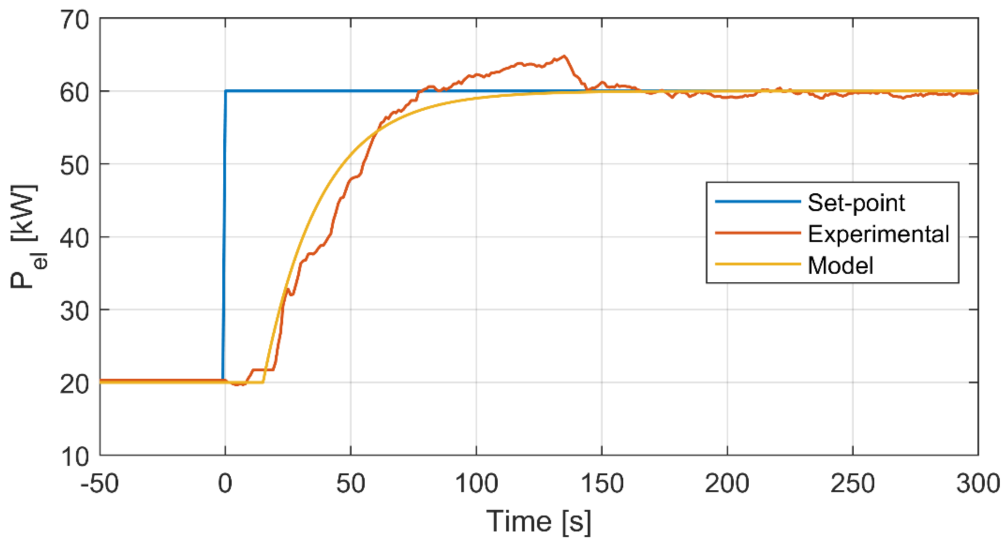

Figure 30 - T100 model validation with in-house experimental data

3.3.2 Steam Boiler

The steady part-load performance curve has been estimated using the proper correlation, coming from the validated in-house tool W-ECOMP for steady-state off-design analysis in polygeneration micro-grid. The dynamic behaviour of the steam boiler model has been validated on the experimental data presenting the transient from stand-by to production. In details, Figure 32 shows a good agreement between the model results and the experimental data related to a step response.

3.3.3 Wind Turbine

The data-driven approach (manufacturer data) makes the wind turbine model validated in steady-state operations. The rotor speed variation allows the WT to maximize the efficiency according to wind speed presenting a transient dynamic behaviour, as during start-up and shut-down.

3.3.4 Gasifier

The gasifier system model validation refers to a previous work [78].

3.3.5 Electrolyzer

The steady part-load performance curve has been estimated using the manufacturer data, for computing H_2 and O_2 mass flows. The electrolyzer dynamic response is very fast (few seconds), and it is extremely difficult getting reliable data. The model has been validated on the experimental data available in the paper “Proton exchange membrane water electrolysis: modelling for hydrogen flow rate control” by Rebah Maamouri et all [79].

3.3.6 H_2 storage and Mixer

The H_2 storage and mixer models belong to the TRANSEO in-house library [77], and they have already been validated in previous works [80].

3.4 Simulation results: step responses

The current section presents the simulation results of each component model, considering the dynamic characteristics and proposing transient behaviours.

3.4.1 CHP

Figure 31 presents a first order system step response for the A400 model. For emulating the transient operation, assuming the same time characterization of the AE T100, as in Figure 30. The model presents a time constant equal to 23 s (this value will be update for A400 when the experimental data will be available). The maximum power rate is 2 kW/s.

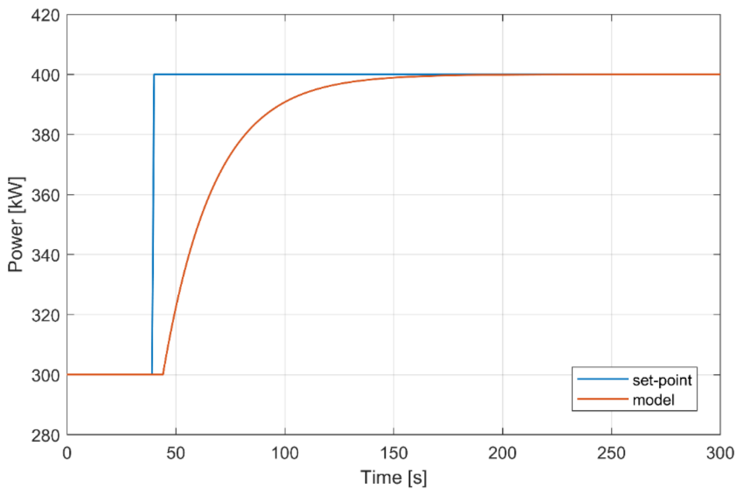

Figure 31 - Step response of the A400 model

3.4.2 Steam Boiler

The Figure 32 shows the comparison between the steam boiler experimental data by Prima Protein and the results by the model. It presents the typical first order system step response behaviour. The estimated time constant is equal to 9000 s. The steam boiler takes almost ten hours to switch from standby condition to production.

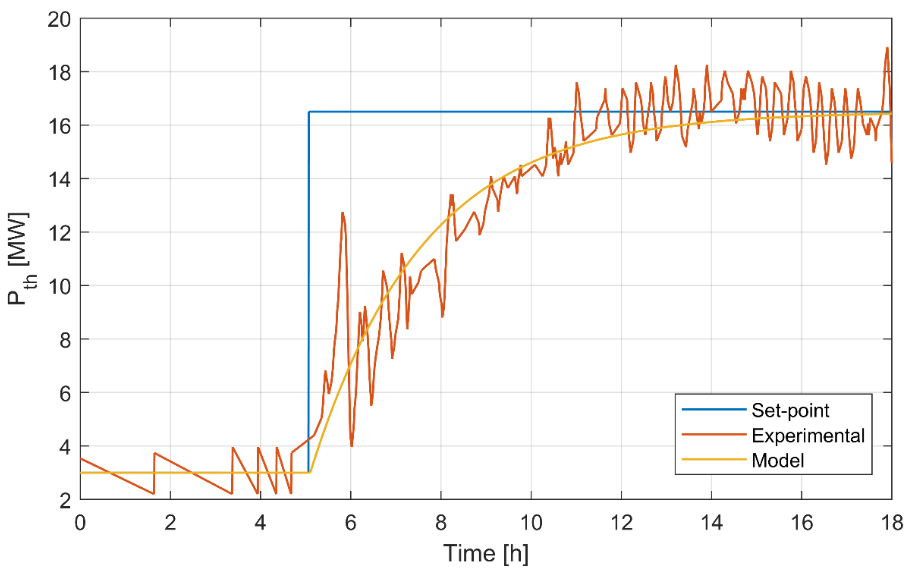

Figure 32 - Steam boiler step response and model validation

3.4.3 Wind turbine

The RES-T V 100 WT presents cut-in speed equal to 2.5 m/s, while the cut-off speed is 20 m/s. Figure 33 show the model results for the WT operation during a typical operation day in Prima Protein (in Eigerøy).

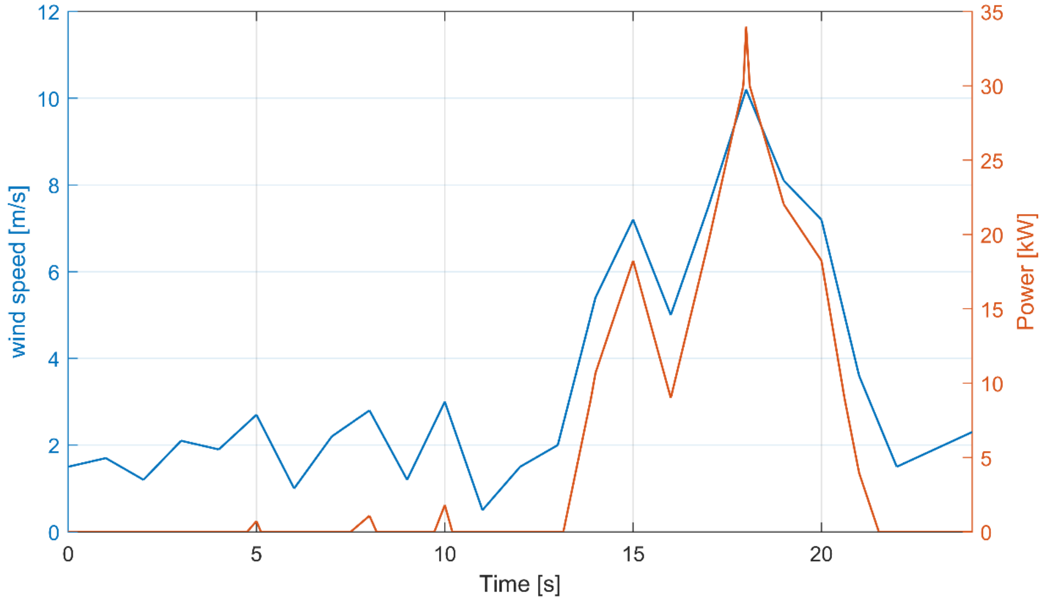

Figure 33 - RES-T V 100 WT daily simulation

3.4.4 Gasifier

Figure 34 and Figure 35 present the gasifier mass flow and composition dynamic response for the biomass composition (Figure 26). These results regard the dynamic effect of a step in the biomass inlet.

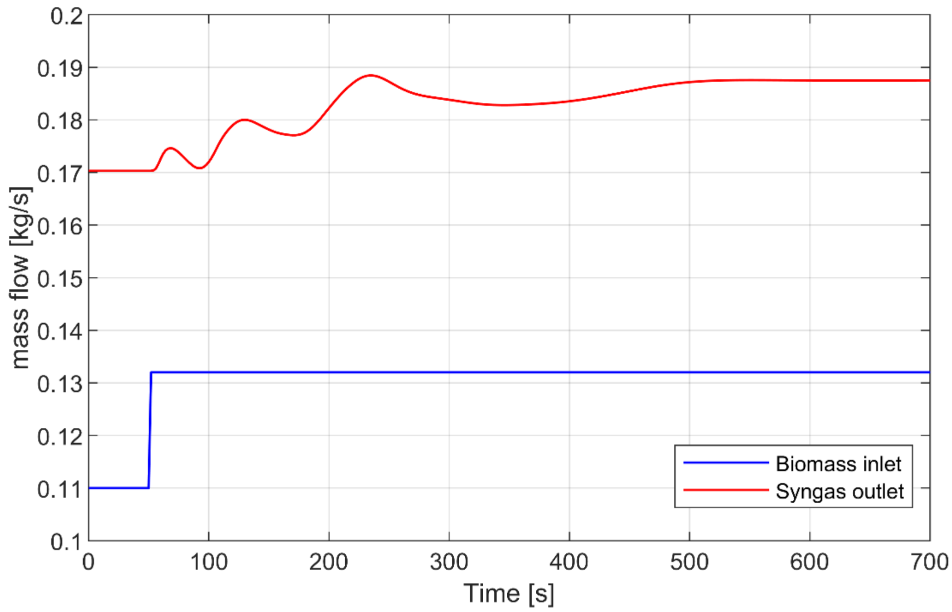

Figure 34 - Gasifier model step response, mass flow

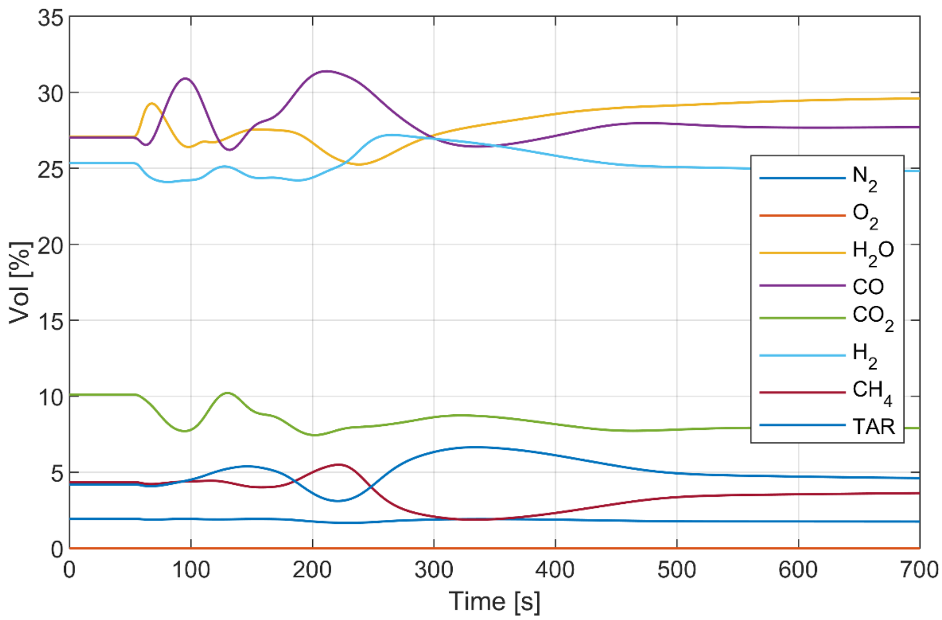

Figure 35 - Gasifier model step response, composition

3.4.5 Electrolyzer

The Figure 36 shows the part-load and transient behaviour of the A90 Green Hydrogen System electrolyzer, highlighting the fast electrochemical dynamic reaction of it. The first order time constant is equal to 2 s, as it has been preliminary calibrated according to the literature. This value will be updated according to new data from the R&D section of Green Hydrogen System.

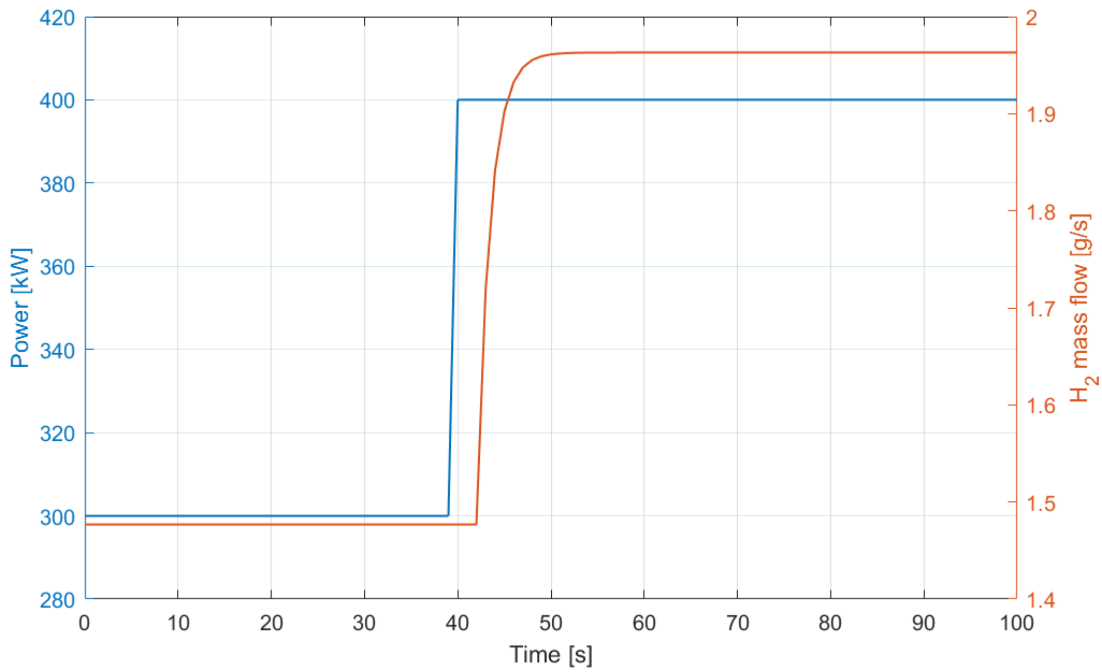

Figure 36 - Step response of the A90 electrolyzer model

The electrtolyzer transient time scale from hot standby to operation is approximated 5 s, while from cold standby to operation approximated 7 min (according to the manufacturer).

3.4.6 H_2 storage

The Figure 37 shows hydrogen storage pressure response to the inlet and outlet mass flow steps. When the mass flow at the inlet is equal to the mass flow at the outlet, the pressure is constant; decreasing the inlet mass flow, the storage pressure decreases until such time as the outlet mass flow decreases.

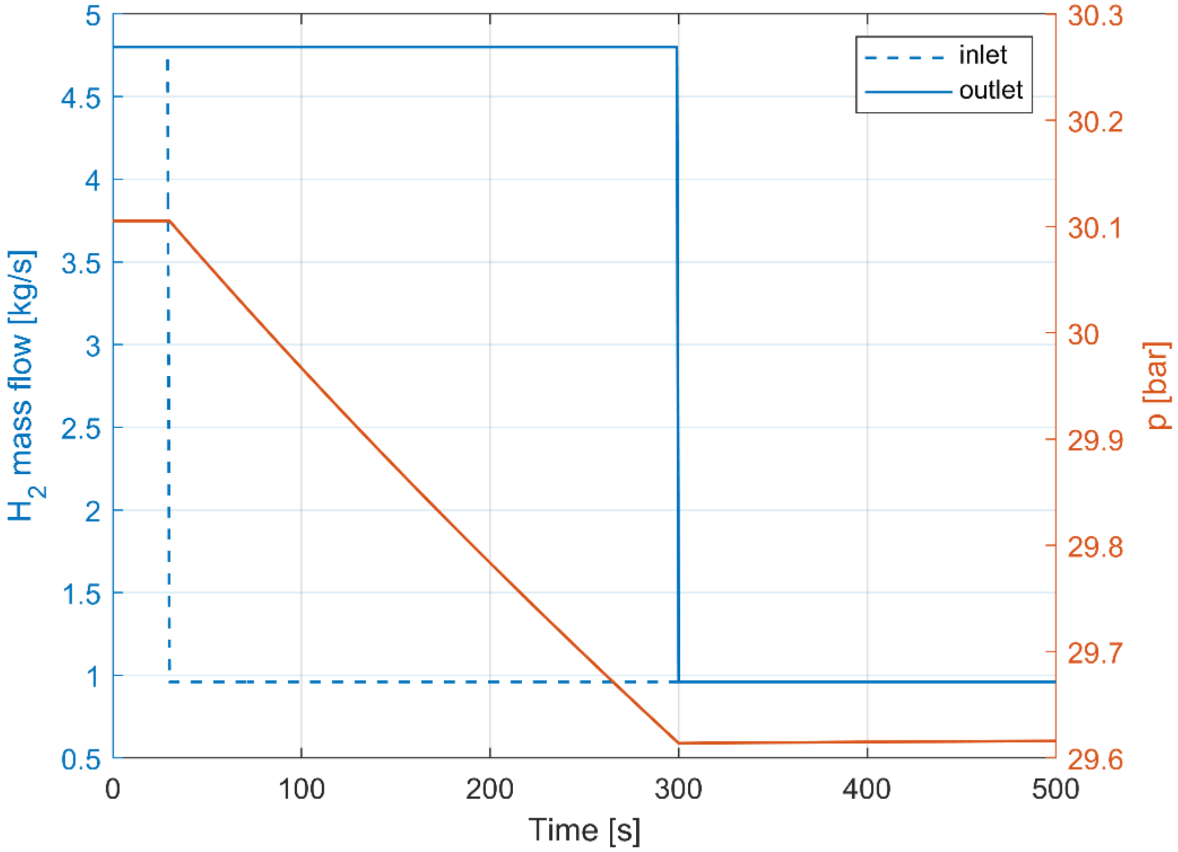

Figure 37 - Double step response of the H_2 storage model

3.4.7 Mixer

The Figure 38 shows the step response transient analysis for the mixer. The H_2 mass flow step down effects on the fuel outlet composition, decreasing H_2 % volume from 30% to 28% and increasing the other gases % (in particular N_2).

The CHP fuel mass flow control loop will define the gas mixer outlet that would be an input of the plenum mixer model.

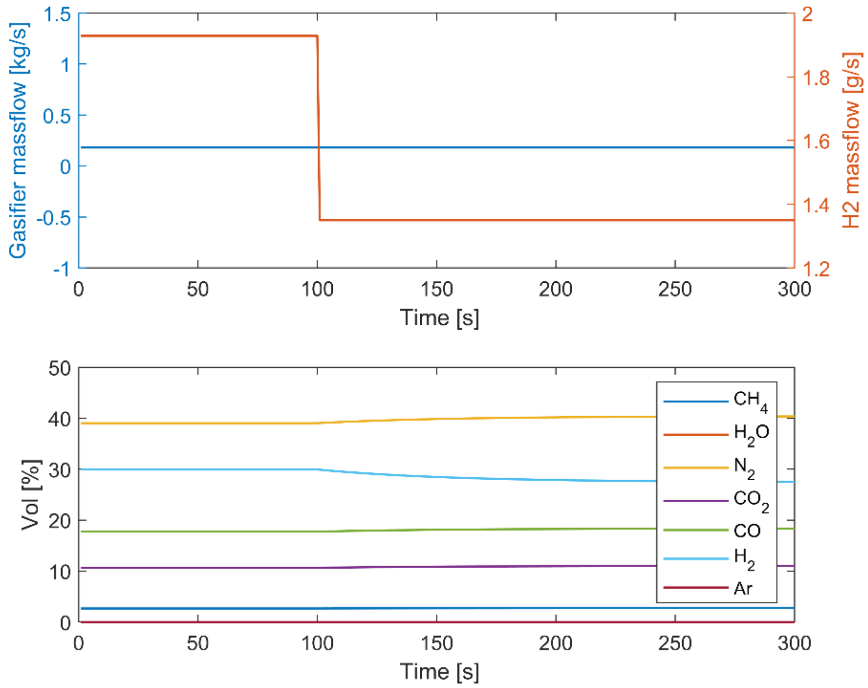

Figure 38 - H_2 mass flow step response for the mixer model

3.5 The EMS developed for the ROBINSON project

The Energy Management System (EMS) developed for the ROBINSON project needs to control the smart grid system in a robust way, integrating the inputs from other sources around it while aiming at the minimization of the costs, considering also the management of the hydrogen storage vessel. The EMS is basically constituted by a decision maker (Figure 18) and an MPC. The necessary inputs are the power demands (also in real-time mode), the cost curves for the electricity market and the fuel costs. It is possible to consider also the hourly scheduling in case these data will be known.

Basing on the demand curves, the Decision maker calculates the best strategy with a 15 minutes time step, defining the set points (r) for the system in order to minimize the operational cost. This is done using an optimizer, described in the following section. Moreover, the Decision maker produces the Boolean on/off signals for the following system components: the CHP, the boiler and the electrloyzers. This is to perform component switch-off in case this operation would be calculated as effective from cost minimization point of view. In case of "off" signals, the involved components are immediately switched off because the approach bypasses the MPC tool. The set point signals computed by the Decision maker then needs to be used by a controller and passed to the system as actuators signals (u, in Figure 18). The system output (the generation for the users – y, in Figure 18) is the feedback for the EMS. These three vectors (r, u, and y) include in this work the following power set-points or measurements: the CHP electrical power, the boiler thermal power, and the electrical power of the electrolyzers.

In the final application, the controlled system (in Figure 18) will be the real energy generators of the ROBINSON demo. However, in order to set up the controller, it is fundamental to study it in a simulation environment, and this requires a model as accurate as possible. This is made through the development of data-driven models of each component of the system. These models are used to set up and test the EMS in the simulation environment, and then followed by an implementation in cyber-physical mode (future activity planned in the IES laboratory). The controller is constituted by an MPC, which itself is split in the actual discrete-time MPC and an observer, that provides information on the system. A predictive control needs to have a model of the system itself in order to accurately predict the response of the real system and tune the best set point signals. So, it is necessary to know the actual state of the system. However, usually it is not possible to know every parameter of the system, thus an observer is used to estimate the state of the real system, using the measured outputs of it (y, in Figure 18). Thus, with information on the 15 min set points from the optimizer and the measured output of the system, the MPC is then able to communicate the actuator signals with a time step of 1 s (it is the global sample time of the simulation).

The interactions between the EMS and the simulated components are shown in Figure 39. As discussed in previous section, the AD-BES and the gasifier are not directly interacting with the EMS because (due to their very slow response) they are supposed to be controlled to maintain constant the pressure in their gas outlet buffers.

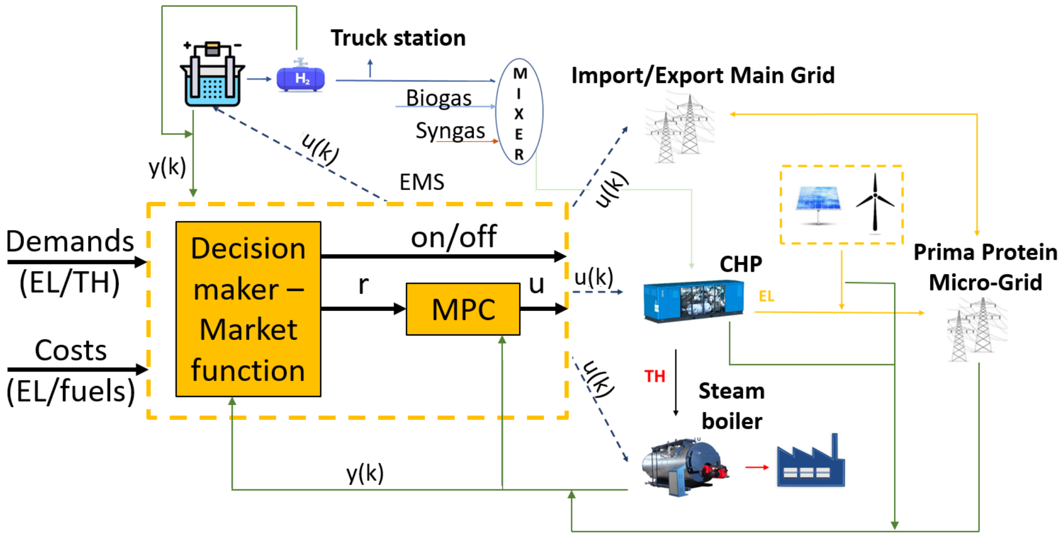

Figure 39 - Interaction between the EMS and the simulated components

3.5.1 Decision Maker – Optimizer

The decision maker is an on-line scheduler which implements an optimizer in order to find the best set point values given the state of the system and the demand and costs.

As previously introduced, the decision maker aims to minimize the total operational cost (J_{cost}) needed to satisfy the electrical and thermal demand, leading to an optimized curve of the set points every 15 minutes (decision maker prediction horizon). To do that, the optimizer receives the electrical and thermal demands, the renewable energy production, the electricity and fuel costs, together with the characteristics of the boiler and the CHP. The optimization variables (the decision variables) are the electrical power exchanged with the grid ($P_{el_{grid}}$) and the electrical power produced by the CHP ($P_{el_{CHP}}$). The objective function is fully presented by Eqs. 9, 10 and 11 that are necessary to show how the different parts are calculated. The Operation & Maintenance costs and the start-up operation impact are included in Eq. 9. Finally, no thermal energy cost is included in Eq. 9 because it is considered as an internal production and consumption, not generating any cost.

The fuel mass flow needed to achieve a certain CHP electrical power is computed, starting from the rated values, using the consumption curves of the specific device. If power is purchased from the grid, the cost is based on the purchasing price, otherwise if the power is sold to the grid, the electrical power is multiplied by the selling price value (purchasing price per the selling-buying ratio). So, with this approach it is possible to use a selling price lower than the buying one (as it happens in some electricity contracts). The optimization is based on the constrains of Table 3. Moreover, the tool receives also the constraint related to the electrical power balance: the electrical power bought (or sold) from the grid is the difference between the electrical demand and the electrical production by the CHP (all values as power). If the sign is positive the system is buying electrical energy from the grid, while in case of negative values, the system is selling electrical energy to the grid (obtaining an economic income that is taken into account).

$$J_{cost} = (c_{el} + c_{O\&M}) \cdot P_{el_{grid}} + c_{fuel_{CHP}} \cdot m_{fuel_{CHP}} + c_{st} \cdot N_{st} \tag{9}$$

$$m_{fuel_{CHP}} = f\left(P_{el_{CHP}}, LHV_{CHP}, \eta_{CHP}, T_{amb}\right) \tag{10}$$

$$c_{el} = \begin{cases} c_{el} & if\ P_{el_{grid}} > 0 \\ c_{el} * Sell & if\ P_{el_{grid}} < 0 \end{cases} \tag{11}$$

Since the problem is nonlinear (due to the CHP efficiency curve shape), the optimization algorithm is nonlinear. In details, it is the "patternsearch" Matlab function [81],[82] operated with the following parameters: initial state vector array, linear equalities, linear inequalities and lower/upper bounds of the two decision variables. The initial state is zero for both variables, the linear equalities regard the link between the electrical power values (CHP generation, grid and CHP maximum), the inequalities express that the sum of these variables must be lower than the maximum (CHP+grid) and the lower/upper bounds are reported in Table 3. This optimization function was chosen because it was the best one to calculate the global minimum avoiding risks of obtaining local solutions. This decision comes from result comparison with other algorithms based on the gradient method that fit with the monotone functions used in this application.

The result of the optimization is thus the 15-minutes interval scheduling (prediction horizon), resulting in a Boolean indication whether it is convenient to produce electricity with the CHP and sell it to the grid, if the optimal power of the CHP is higher than its minimum value, or if it is convenient to buy the electricity from the grid, in case the optimal power of the CHP is lower than its minimum value.

This is then applied in a logic which objective is to follow the thermal demand of the system, as shown in Figure 40. There are three possible behaviours for the CHP: if the thermal power demand is lower than the minimum provided by the CHP, if the thermal power demand is between the minimum and maximum that can be provided by CHP, and the case in which an integration with a boiler is necessary to satisfy the thermal load.

Table 3 - Constraints of the system, used by the decision maker

Parameter	Min value	Max Value	Unit
CHP EL Power	70	400	kW
Grid EL Power	-2000	2000	kW
Boiler TH Power	2200	22000	kW

The process begins by comparing the thermal and electrical power demands with the minimum and maximum power capacities of the Combined Heat and Power (CHP) system. If the CHP can meet the demands, an economic evaluation compares it with available electricity to determine operating conditions, considering various combinations of grid and

CHP power. If the thermal demand exceeds the CHP's capacity, the decision maker initiates the boiler to supplement it. Economic analysis (Eq. 9, Eq. 10, Eq. 11) continues to optimize operational expenses and determine the power distribution between the prime movers. The optimization function makes the economic analysis and defines the optimum power split between the prime movers.

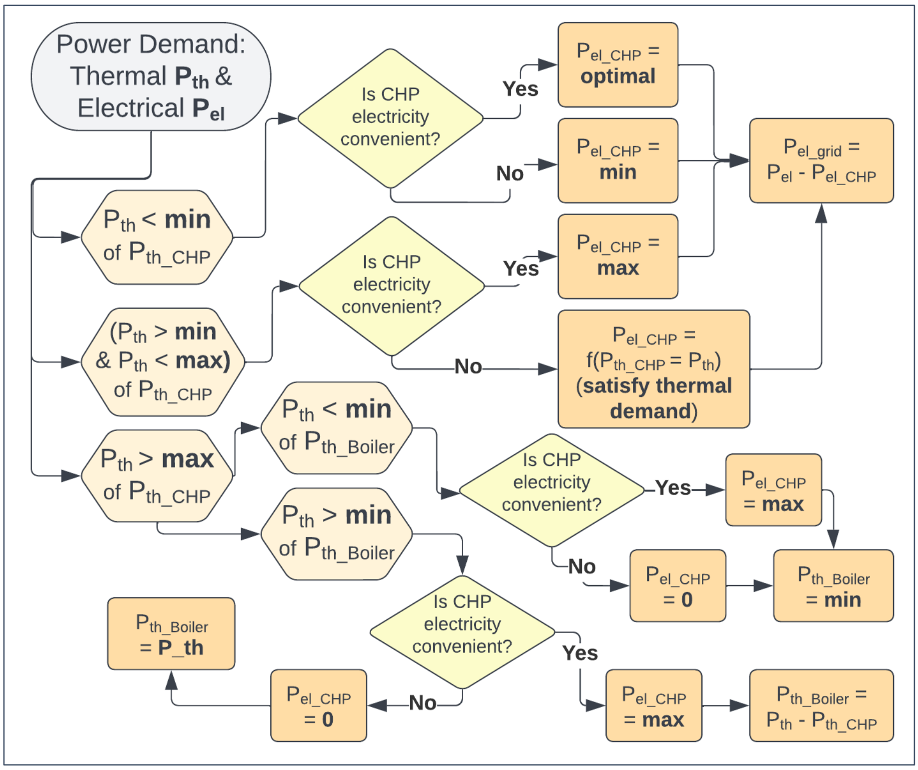

Figure 40 - Flowchart logic of the decision maker

3.5.2 Model Predictive Control

The model predictive control (MPC) system was developed following the procedure suggested in the book by Wang [83]. This controller is a constrained multi-input multi-output MPC, constituted by the actual discrete-time MPC and the integrated observer, used to estimate the state of the system. Its role is to control the system, by computing the values of the actuator variables, given the information on the setpoints from the decision maker, and the state of the system from feedback of measured values of the system.

The initialization consists in the definition of the time windows for the prediction horizon (in this work, N_P = 40 steps) and for the receding control horizon (N_C = 1 step), together with the definition of the sample time of the discrete system (Ts = 1 s). The prediction horizon was set equal to the number of steps (1 step = 1 second in this case). It was set equal to 150% of the bigger characterization time constant; then the controller could predict the operations of all prime movers considering their transients. The receding horizon was set equal to 1 step. Then, the information on the controlled plant, constituted by the CHP turbine and the steam boiler, is needed. A linearized state-space representation of the plant is then used, and passed to the observer; then, it is transformed into an augmented state-space model (matrices A,B,C): it can be based on the differences of the state variables (Δx) and of the input variables (Δu), as shown in the Eq. 12. After that, the knowledge of the augmented state-space system, as described, is reordered to be parametrically passed to the actual MPC, together with the constraints on the variables.

$$\begin{cases} \begin{bmatrix} \Delta x(k+1) \\ y(k+1) \end{bmatrix} = A \begin{bmatrix} \Delta x(k) \\ y(k) \end{bmatrix} + B\Delta u(k) \\ y(k) = C \begin{bmatrix} \Delta x(k) \\ y(k) \end{bmatrix} \end{cases} \quad (12)$$

When running the code, the controller receives the set points from the decision maker, and the measured values ($y(k)$) from the plant, giving the control signal as an output. Inside the controller, the observer receives the control output from the actual MPC, the estimated state of the system, and the measured values from the plant, to which it applies a Kalman filter. From this information, together with the knowledge of the state-space representation of the system, the observer computes a new estimate of the state of the system. This is received by the actual MPC, which computes a new value for the control variables, which are then passed to the plant and sent in feedback to the MPC and the observer too, to be used in the next step.

In this work, the MPC architecture is based on two functions: one for the discrete model predictive control (DMPC) and one for the observer, according to the velocity form presented here [84]. The model developed for the control is based on augmented state-space representation, i.e. Non-Minimal State Space (NMSS) (Eq. 12) [83]. The observer is used to estimate the state of the system at each time step, to be fed back to the DMPC dynamic model for the following iteration. This non-minimal representation is detectable and stabilizable if the original model is detectable and stabilizable and has no transmission zeros on the unit circle. The integration within the MPC is performed through the application of the Laguerre network. It is used to simplify MPC computation by adding tuneable parameters. In literature, Laguerre functions were used to describe the pulse response of dynamic systems – it is possible to describe dynamic behaviour of target system through this method. One of the advantages of MPC is linked to the possibility to tune controller response based on weights associated to control variables. Here, cost function is based on Discrete Linear Quadratic Regulator (DLQR) architectures, which are used to be as Eq. 13, with Q and R weight matrices, x is the state of the system, and u is the control signal. DMPC algorithm includes constraints on absolute value of plant inputs u and their rate of change Δu.

$$J = \frac{1}{2} x^T Q x + u^T R u \qquad (13)$$

The MPC technology has been developed both in Matlab-Simulink and in LabView environment, and tested in IES Laboratory.

In this work, the MPC represents an innovative control system for managing real-time the prime movers, avoiding instabilities and predicting dynamic and transients. The fine tuning of the MPC has been performed in MATLAB Simulink, using the validated models of the prime movers.

3.5.3 Scheduling - Hydrogen management

The hydrogen production depends mainly on the electricity price, thus the main schedule of the production is made off-line, and it results in a daily scheduling with an 1 hour time span, with two possible behaviours, as it can be seen in Figure 41. If the electricity price is lower than the average one, the electrolyzers will run at design point (flag 1), otherwise the electrolyzers will run at part-load (flag 2). In details, Figure 41 reports the electricity cost variation for a day in the month of November 2021 for the Eigerøy island. This approach was chosen for the management of the electrolyzers due to the necessity to have a scheduling based on the electricity cost values of the entire day (these can be forecasted on the basis of the previous day data and on other information, such as the day type) [51]. So, when the electricity cost is low, the electrolyzers at maximum load exploit the price situation trying to recharge the storage vessel. On the other hand, when the electricity cost is high the electrolyzers are managed by a devoted controller to reach the minimum pressure set-point, because it is not convenient to do the vessel full re-charging.

Given the scheduling based on price, the actual hydrogen management will follow the pressures of the storage, using an on-line scheduler and a dedicated MPC. In particular, the target pressures for the hydrogen storage can be 40 bar (in case of low electricity price) or 22 bar (in case of high electricity price), while the maximum and minimum values are 42 bar and 10 bar. These numbers were chosen on the basis of the data provided by the proposed manufacturer (design and maximum pressure values) and to ensure a good energy safety margin (22 bar set-point guarantees 6 hours of autonomy with the CHP at maximum load plus a further minimum margin for a further safety from the empty condition). For sure different values could be used depending on the energy safety level that is necessary to guarantee on the hydrogen storage side.

The control of the electrolyzers is structured with this approach: an on-line scheduler receives the off-line daily scheduling and the target pressure of the H_2 storage, and computes the set points of the absorbed electrical power. In case of flag 1 (low electricity price), if the pressure of the storage is lower than 90% of the maximum value, the electrolyzers work at design point; instead, if the pressure is between 90% and 96% of the maximum value, the power of the electrolyzers is controlled by the dedicated MPC; finally, if the pressure is higher than 96%, the electrolyzers are switched off (the 90%, 96% values were proposed after trials with the objective to avoid risks of pressure values higher than the maximum constraints). Instead, in case of flag 2 (high electricity price), the target pressure will be equal to 22 bar, and if the pressure of the storage is higher than this value, the electrolyzers are switched off; otherwise, the power of the electrolyzers is controlled by a dedicated MPC.

The models of the electrolyzers, two identical working in parallel, receive an electrical power set point and compute the efficiency, and the production in terms of H_2 and O_2 mass flow rates, with a dynamic first-order delay. The mass flow rates are then used by the hydrogen storage model, to compute the pressure of the storage itself, having assigned a certain volume (40 m^3). The outlet mass flow rates from the storage are determined by the utilization for transportation and by the need of the gas mixer to satisfy the desired percentage of hydrogen in the CHP fuel composition. On the transportation side, trucks using H_2 as fuel are charged, and the tank of the trucks can hold up to 32 kg of H_2; a further constraint is that the charging process must not lead to a pressure in the storage lower than the minimum allowable. Thus, the outlet mass flow rates of hydrogen are computed and the MPC takes them into account to regulate the absorbed powers of the electrolyzers to achieve the target pressures of the storage vessel.

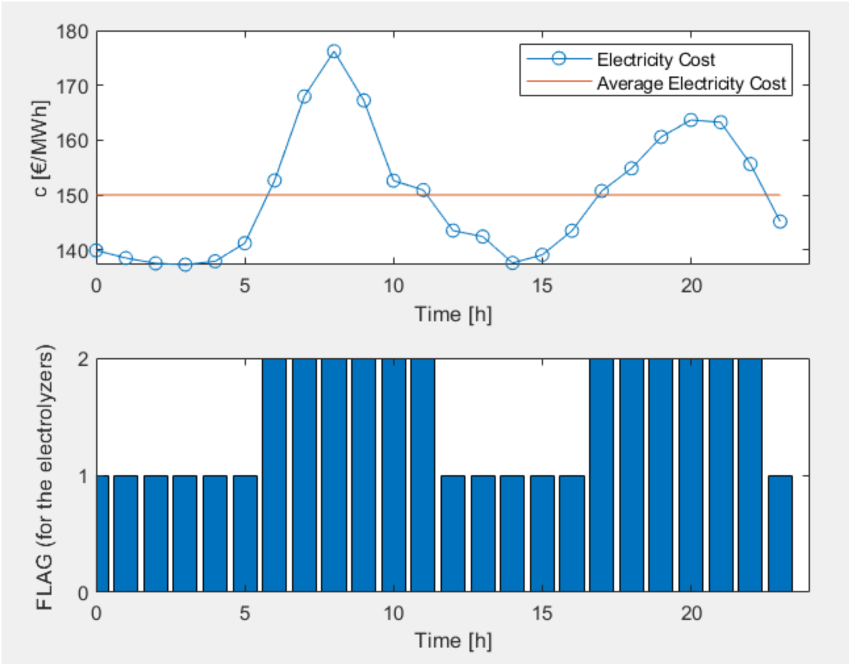

Figure 41 - Electricity cost and hydrogen production (daily scheduling)

3.6 Simulation results

The EMS integration with the components was performed considering the data from previous sections. In details, the EMS was connected to input blocks that include the component sizes and main constraints (e.g., minimum and maximum power values). Moreover, the EMS receives other parameters to properly calculate the cost function (in this case this is linked with the A400 efficiency off-design curve) and to set-up the decision boundary values (e.g., the coefficients to calculate the maximum and the minimum thermal power values produced by the A400). As shown in Figure 42, the EMS receives in input (in real-time mode) also the demands, the power generation by the renewable sources, the costs (for fuels and electricity). The integration with the component models was developed as presented in the following points:

- the set-point values and the on/off commands for the component models are the EMS outputs and the input of each power generator model;

- the calculated power (or storage vessel pressure for the hydrogen generation) by the components is collected in real-time mode provided as input to the EMS.

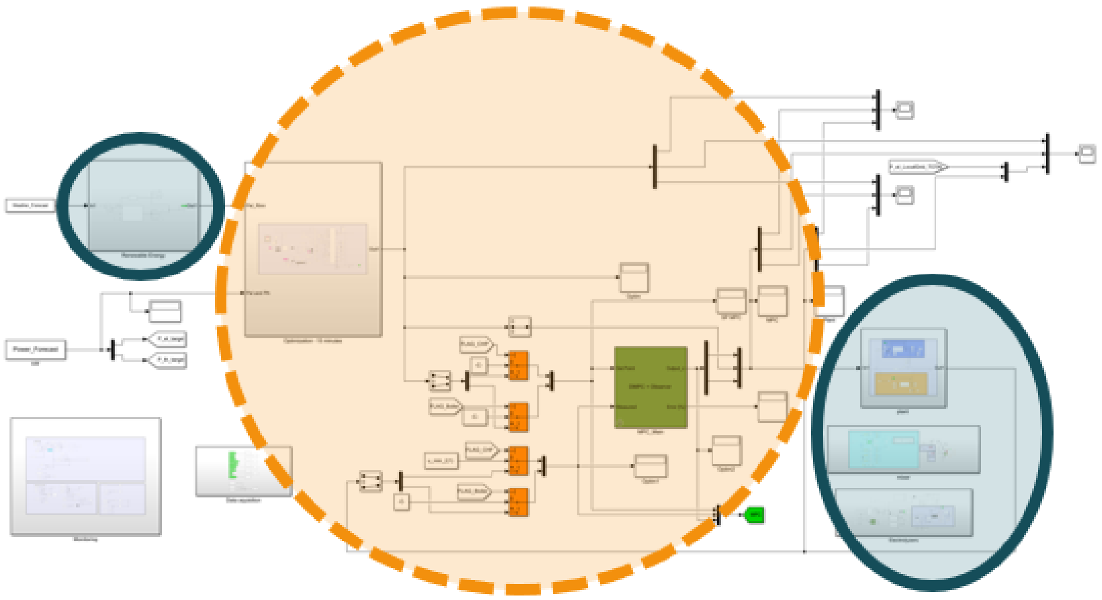

Figure 42 - EMS integration with the component models

Although this is a general integration approach for all the cases, Figure 42 shows the simulation tool for the Eigerøy case. The EMS (with the decision maker and the MPC) is in the dotted ellipse, while the other two ellipses highlight the component models (the PV and the turbine models on the left side – the CHP, the boiler, the fuel mixer, the electrolyzers and the grid connection on the bottom right side).

No models and no direct integration were considered for the AD-BES and the gasifier because they are very slow response devices. So, they are supposed to be controlled to maintain constant the pressure in their gas outlet buffers (devices installed to compensate the system slow dynamic response and to be able to deliver to the mixer all the gas needed for the CHP). So, at the moment, these systems are not managed by the EMS because the mentioned controllers are supposed to be installed in the PLCs of the gasifier and the AD-BES.

The simulation results included in this section were obtained with the component models presented and validated and interacting, as in Figure 42, with the EMS. The analysis was performed for the data (electricity costs, weather conditions and demands) related to a day of November 2021 for the Eigerøy island (Prima Protein grid including the connection to the distribution grid). The electricity cost trend was already presented in Figure 41 (the sell/buy ratio was set to 1), while for the syngas a cost 5 €/MWh was considered (it is mainly related to the wood cost). For the LNG (the fuel for the boiler) a cost of 150 €/MWh was implemented in the tool. For the hydrogen flow used for filling H_2-truk/trailer storage, N.2 13.3 g/s demand periods were included for a duration of 2400 s each. The first charging event is implemented at 5 a.m. while the second one at 11:15 a.m. (to simulate a possible future real situation). Another assumption regards the hydrogen percentage in the CHP fuel. Although different compositions are possible, this was fixed to 30% in volume for all the simulations. So, depending on the CHP load (and its fuel consumption calculated by the model) this fixed percentage allows to calculate the amount of hydrogen for the CHP to be taken from the storage vessel.

3.6.1 EMS performance against a standard management

An initial result regards the comparison of the system management: operation with the EMS against an operation with a standard management approach. This reference approach (named “No EMS” in the following figures) means that the system is managed in the following way: (i) the CHP is operated to satisfy the electrical demand, (ii) the boiler is used when the thermal demand is higher than the CHP maximum thermal generation (since the boiler is a low response device with 2.2 MW of minimum load, the set-point signal is calculated with a PI controller), (iii) the two electrolyzers are maintained at minimum load for the entire simulation.

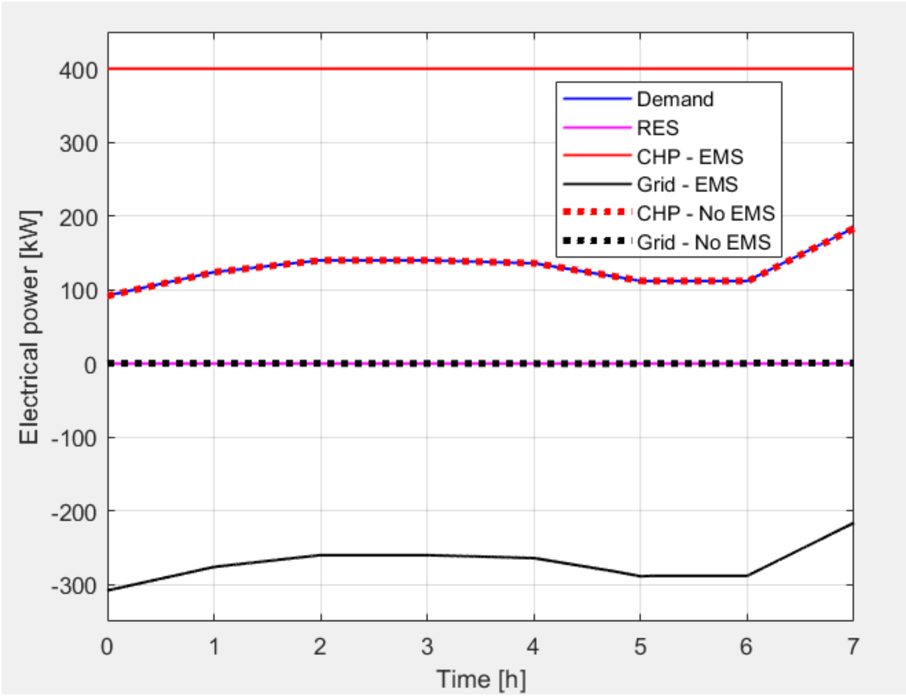

Figure 43 - EMS vs No EMS: electrical power

Due to the system sizes (a 400 kW CHP with a 22 MW boiler), instead of simulating an entire day (performance mainly driven by the boiler) attention was devoted on the initial 7 hours (from midnight to 7:00 a.m.). This is the factory (Prima Protein) start-up period including an important simulation part with the electrical demand lower than the CHP maximum and the boiler ignition. Due to the chosen hours, no PV generation was present. Moreover, due to low wind condition, also the wind turbine contribution was null (as shown in Figure 43). Since the syngas cost is very low (in comparison with the electricity one), the EMS maintained the CHP at its maximum for all the 7-hours. This was a good solution for obtaining profit from the electrical energy (not consumed and so sold to the grid). Moreover, Figure 43 shows that in the no EMS case, the CHP simply matched the electrical demand.

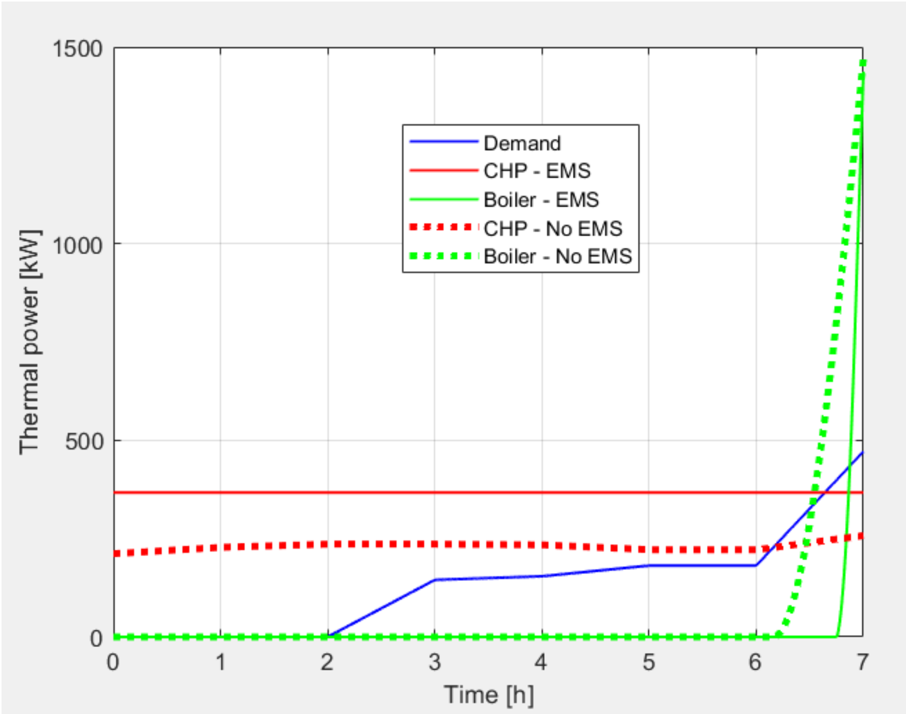

Figure 44 - EMS vs No EMS: thermal power

On the thermal side (Figure 44), the CHP produced the necessary power for more than 6 hours (since, at the moment, the system does not include a thermal storage, the generation excess was dissipated). The excess of thermal power was more significant in the EMS case because the CHP is at maximum load condition. Finally, when the CHP was not able to satisfy the thermal demand, the boiler was activated: due to the MPC tool the optimized case was more effective because the boiler switch on was delayed of about 30 minutes (with significant fuel saving) and presented a faster increase trend (in comparison with the no EMS simulation).

For the hydrogen side (Figure 45), in both cases the pressure decreased during these 7 hours due to the charging of the trucks/trailers (as presented before). While the EMS increased the set-point of the electrolyzers (because the electricity cost was lower than the average value), the no EMS case did not exploit this cost benefit. On the other hand, since the no EMS case was not able to switch off the electrolyzers, the pressure vessel showed a slow recharging trend (started at the end of the truck charging). In both cases, the hydrogen pressure vessel remained in the 22-40 bar range maintaining a good energy security margin (no risk of empty condition).

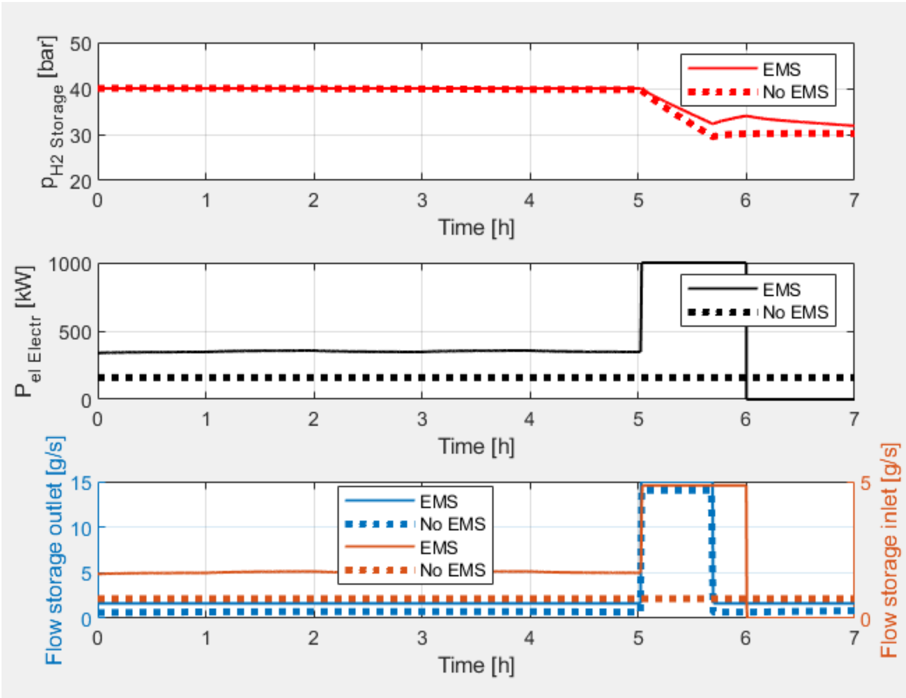

Figure 45 - EMS vs No EMS: H_2 generation, storage and utilization

After the details about electrical, thermal power and hydrogen system, a global comparison was performed for different parameters. Since cost minimization is the EMS objective, Figure 46 shows the variable cost comparison related to this 7-hour simulation. Due to no available specific data for the component O&M costs, literature values were implemented: 0.015 €/kWh for the CHP [86], 1.5% of the capital costs for the electrolyzers [87]. It shows a cost decrease (-30.1%) obtained with the EMS application. This comes from the EMS choice to operate the CHP at its maximum load (cost saving from selling some electrical energy). Moreover, the delayed boiler activation produced a significant fuel saving.

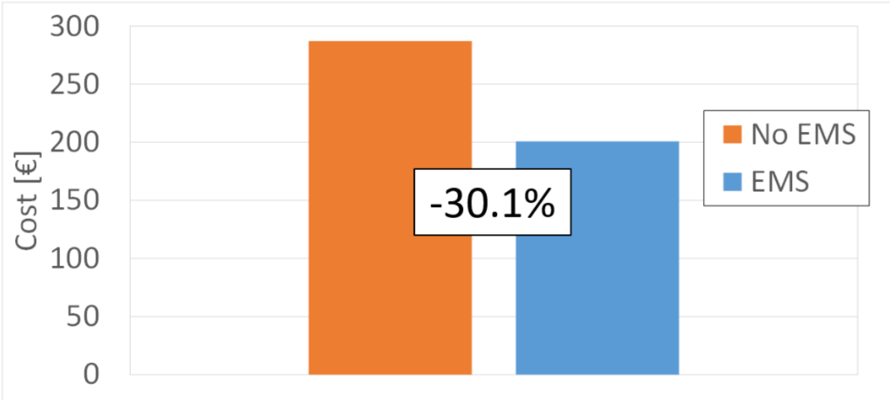

Figure 46 - EMS vs No EMS: variable cost comparison

Although the optimization objective is the cost minimization, this global analysis shows positive effects on other parameters, such as the efficiency values (Figure 47). Attention is focused on the electrical side because on the thermal efficiency is driven by the boiler one because this device is 1-2 orders of magnitude larger than the other components. So, the first-principle total efficiency remains close to the boiler thermal one when this device is used (variation lower than 1.5% in this case). So, two types of electrical efficiencies are compared here (in Eqs. 13 and 14). They are expressed in terms of the energy values (produced, consumed or stored) in these 7-hours. The fuel energy (at the denominator in both equations) is calculated doing the sum (for every simulation second) of the products of the fuel mass flow rate per the mixture lower heating value (at the mixer outlet). Eq. 14 shows that this system electrical efficiency includes also the consumed hydrogen for the truck/trailer charging ("users" subscript) and the related storage balance (in case of pressure decrease in the hydrogen vessel, this term would be negative to take into account that the consumed hydrogen needs to be produced in the following hours or days).

$$\eta_{el_{CHP}} = \frac{E_{el_{CHP}}}{E_{fuel_{CHP}}} \qquad (13)$$

$$\eta_{el_{system}} = \frac{E_{el_{CHP}} + E_{H2_{users}} + \Delta E_{H2_{storage}}}{E_{fuel_{CHP}} + E_{el_{grid}}} \qquad (14)$$

The electrical efficiency comparison is shown in Figure 47. Due to the EMS utilization (it operated the CHP at the nominal condition), the microturbine worked at higher electrical efficiency, with an increase of 35.3%. Moreover, Figure 47 shows a system electrical efficiency increase of 41.6%.

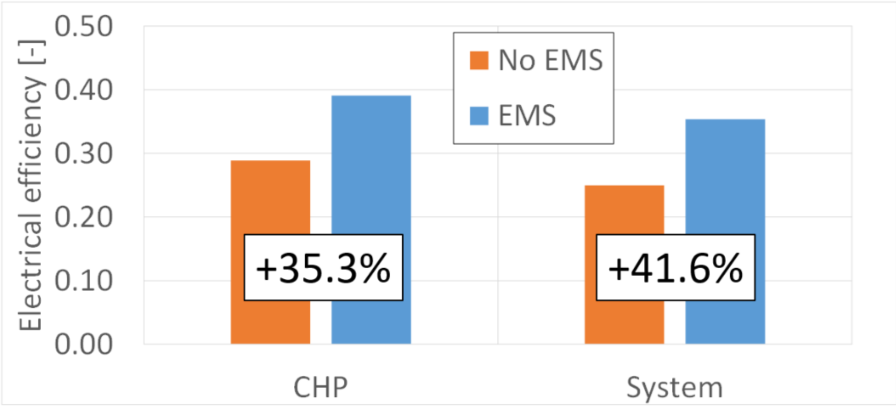

Figure 47 - EMS vs No EMS: electrical efficiency comparison

Considering the environmental issues, it is important to highlight that the EMS has an important impact on the CO_2 emission side (for this 7-hour calculation). These emissions are based on (Eq. 15) the sum of the mass of CO_2 produced by: boiler combustion, electrolyzer operations, energy generation bought from the grid (in case of energy purchase), change in the state of charge of the hydrogen pressure vessel. The CO_2 emitted from the syngas/biogas combustion is considered null. This is a typical approach considering that it was produced from a renewable source (in case of missing utilization it would produce the same amount of CO_2 as in a rubbish dump). Moreover, since the grid electricity from fossil fuel is just the 2% of the entire amount, the CO_2 generation is mainly driven by the boiler that is operated using LNG as fuel.

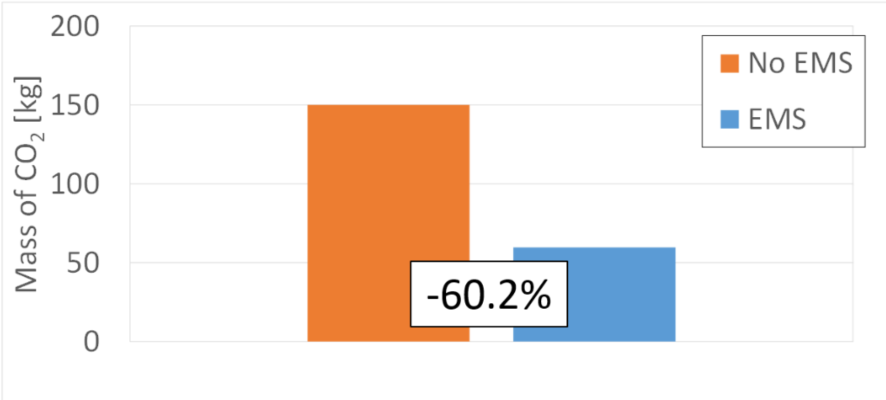

Figure 48 - EMS vs No EMS: CO_2 emission comparison

$$M_{CO2_{system}} = M_{CO2_{boiler}} + M_{CO2_{electrolyzers}} + M_{CO2_{grid}} + \Delta M_{CO2_{H2\ storage}} \quad (15)$$

Figure 48 shows the comparison for the emitted CO_2 during this simulation. The EMS produced a positive effect also in this case, obtaining a CO_2 emission decrease (-60.2% for these 7-hours).

3.6.2 EMS robustness simulations

Considering the same inputs and boundary conditions, simulations were performed to demonstrate the EMS robustness. So, errors in the input data were implemented starting from the measurements related to the electrical power generated by the turbine (Figure 49), the CHP thermal power (Figure 50) and the generation by the boiler (Figure 51). Since no data are available on measurement errors, the simulations implemented the worst cases. In these preliminary simulations 9-hours were considered and the impact on the management of the other properties was null or negligible. Moreover, no instabilities in the EMS or in the system were generated.

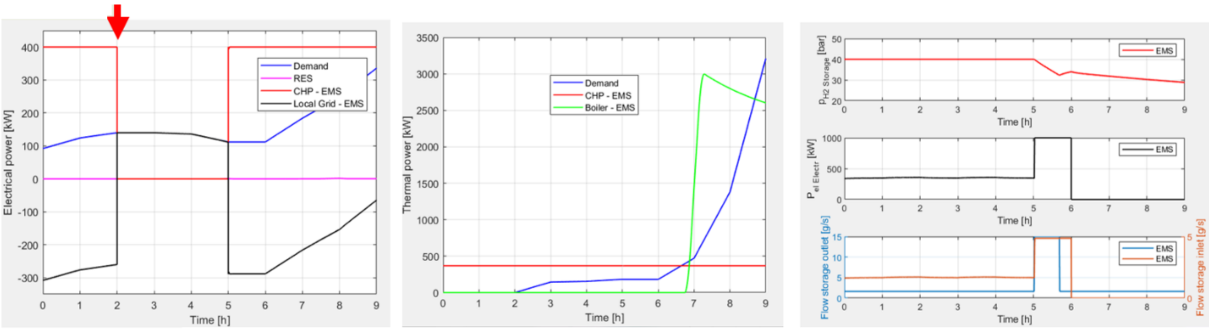

Figure 49 - CHP electrical power measurement (-50 kW – limited to 0 kW - instead of 400 kW, for 3 hours)

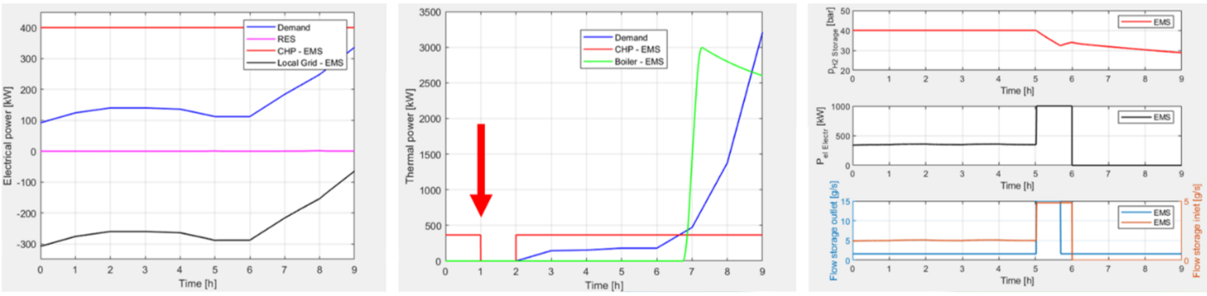

Figure 50 - CHP thermal power measurement (-50 kW – limited to 0 kW - instead of 365 kW, for 1 hour)

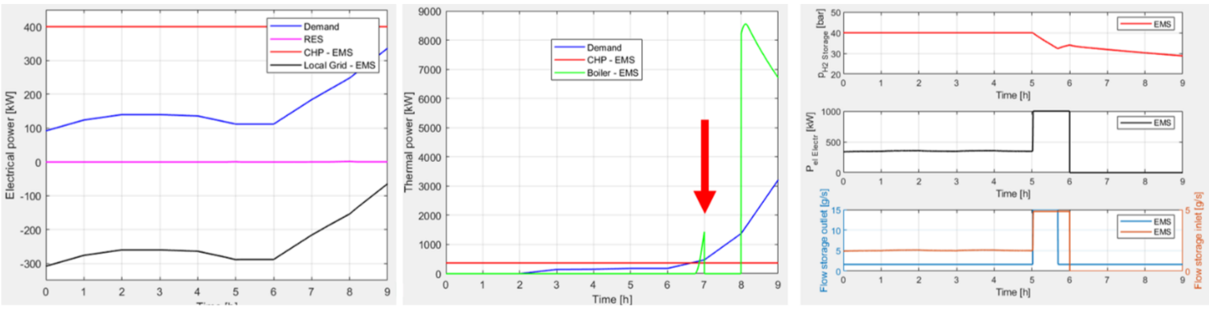

Figure 51 - Boiler thermal power measurement (-1000 kW – limited to 0 kW, for 1 hour)

A further simulation was a calculation for 24 h, using the entire data of Figure 52. This was another calculation to assess the EMS robustness. As example of wrong measurements (due to probe errors or cyberattacks) the following events were simulated: (i) measured CHP thermal power of-50 kW for 1 h (event started at 4:00), (ii) measured boiler thermal power of-1.0 MW for 1 h (event started at 9:00), and (iii) measured pressure in the hydrogen vessel of 1 bar for 1 h (event started at 16:00). Saturation blocks were also included for an initial data check and to exclude not-physical values. So, the measurements of both CHP and boiler thermal power values were limited to 0 kW and the hydrogen vessel pressure to 1 bar (absolute).

The EMS operated the CHP at the maximum load (400 kW) for the all the 24-hours (Figure 52). So, the EMS was able to calculate the solution (already described for the initial 7 hours) for all the 24 h. During the afternoon the system obtained some electrical power from the renewable sources (the wind turbine), up to 33.6 kW. This reduced the electrical energy needs (bought from the grid). Moreover, Figure 52 shows that the mentioned measurement errors had no influence for the CHP management and this assess the related tool robustness. The measurement errors (or cyberattack effects) are visible also for the the thermal side (Figure 53). Although these problems produce errors in global parameters, no problems were reported in the system management. The only impact regards the boiler: it was moved to a very high power generation following the measurement error due to the set-point (it was increased too much to try to compensate the missing thermal generation). However, in about 1 hour the EMS reduced the produced power to values in good agreement with the demand (Figure 53 after 12:00).

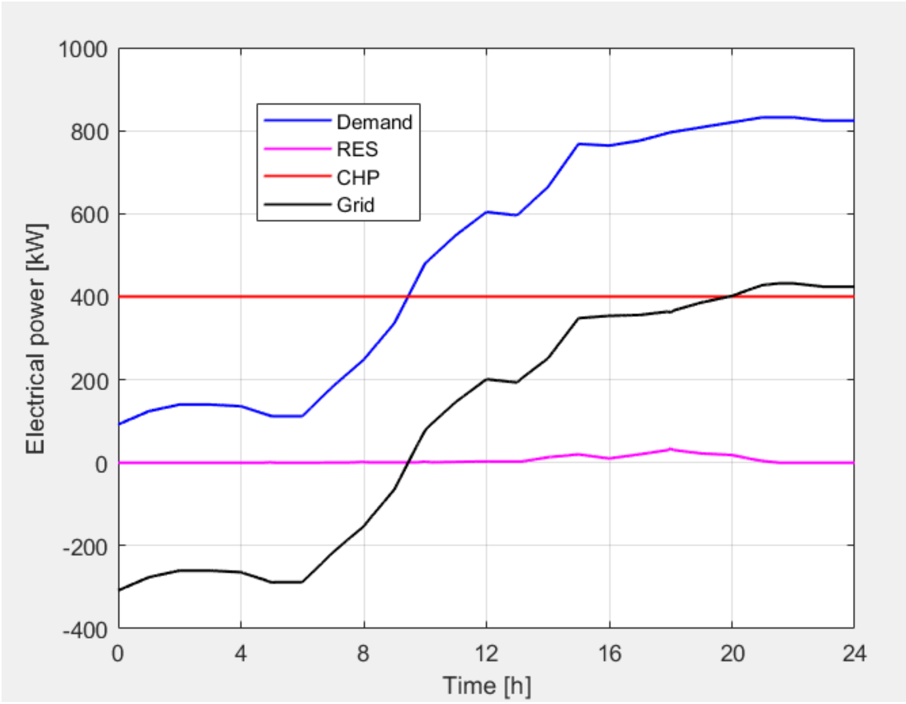

Figure 52 - EMS robustness evaluation (electrical power)

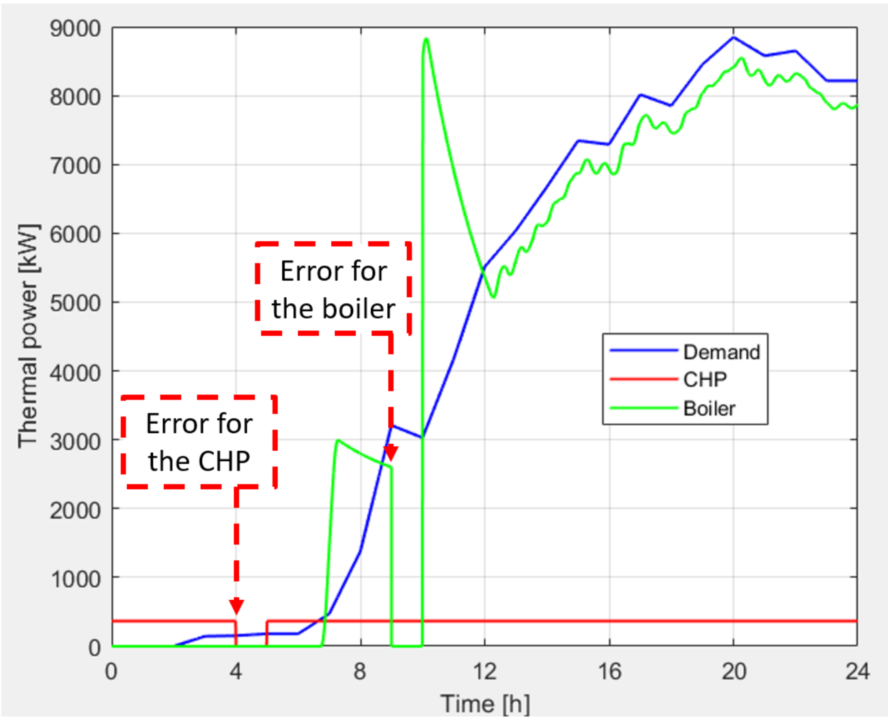

Figure 53 - EMS robustness evaluation (thermal power)

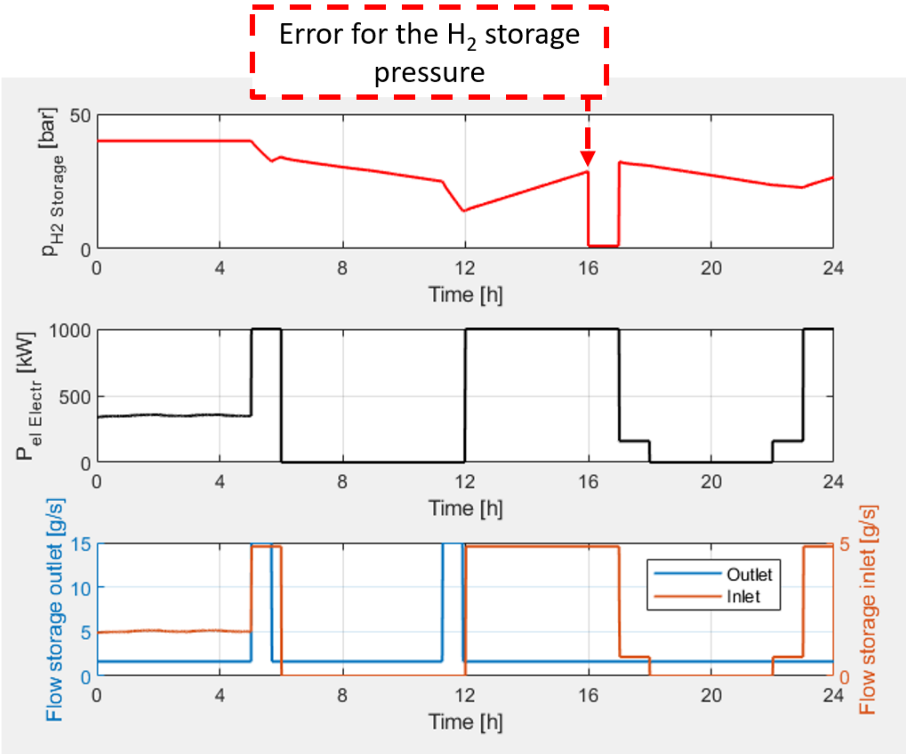

Figure 54 - EMS robustness evaluation (hydrogen system)

Figure 54 shows the tool robustness also on the hydrogen system side. While these errors on measurements on the thermal side had no effects on the results, also large errors in pressure measurements for the hydrogen storage vessel did not produced problems. While before the error the vessel pressure was low (about 23.4 bar), the electorlyzers continued to be operated at the maximum (2 X 500 kW) without any discontinuity.

3.7 Laboratory preparation for the tests in cyber-physical mode

Since the IES laboratory is not equipped with all the grid components, the tests are proposed to be performed in cyber-physical mode. As demonstrated in previous works [88], this is an effective approach at half-way between model results and demonstration activities with a complete plant. This intermediate approach is important to introduce experimental aspects and problems in the activities, without the critical aspects, costs and risks of a complete prototype. In this case, the cyber-physical approach allows having experimental tests for improving the EMS before moving to the demonstrator, to reduce time, costs and problems. In this part of the work, a test bench available at the UNIGE laboratory, located in Savona, and developed in previous activities [89] was prepared for the tests of the ROBINSON EMS. This bench is a local grid (with both electrical and thermal components) including: a T100 microturbine working in CHP mode, a 20 kW heat pump, thermal solar panels, 1.1 kWp PV panels, a 102 kW absorption chiller, two 5000 l thermal energy storage tanks (for hot water), a local thermal grid based on two distribution pipes and equipped with fan coolers for local load generation, a local electrical grid and the connection of both grids to the University campus systems. In this work, since some components are not included in the ROBINSON project, the planned tests are organized to involve the following components: (i) the CHP microturbine, (ii) the PV panels, (iii) the electrical local grid, (iv) the thermal local grid with the related thermal components (the fan coolers).

Although the activities started from an existing facility, it was necessary to perform some laboratory preparation before doing the tests. These activities included simple ordinary component maintenance of the device manufacturers or the substitution/installation of additional devices, such as new probes. This is the list of the main laboratory preparation:

- Fire sensor maintenance
- Air compressor maintenance
- Piping modifications
- New mass flow probe
- New temperature probes and substitution of damaged components
- New ethernet communication device
- New control valve
- Flanges for pipes
- New air dryer

- Accelerometers and microphone for vibration acquisition (T100 safety)
- Re-calibration of some mass flow probes
- Substitution and maintenance of other components

Due to the complexity of the planned tests (EMS + software models + real components) the laboratory experience in energy harvesting technologies. In details, the following activities were performed:

(i) development of the UDP communication between the hardware (controlled by LabView – see Figure 55) and the software in Matlab-Simulink,

(ii) activation of the data acquisition from the PV panels,

(iii) software development in LabView for the integration of the PV panels.

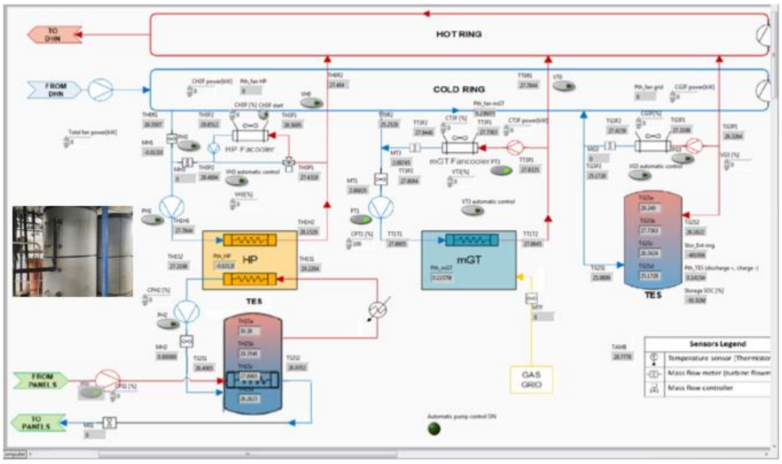

Figure 55 - Main part of the front panel in LabView for the test rig management and picture of the thermal grid

The communication between the software (in Matlab-Simulink) and the hardware (controlled by LabView) was obtained implementing the blocks in Figure 56. The boxes in red include the components necessary to transfer data from Matlab-Simulink to LabView, while the reverse communication is highlighted with the blue boxes.

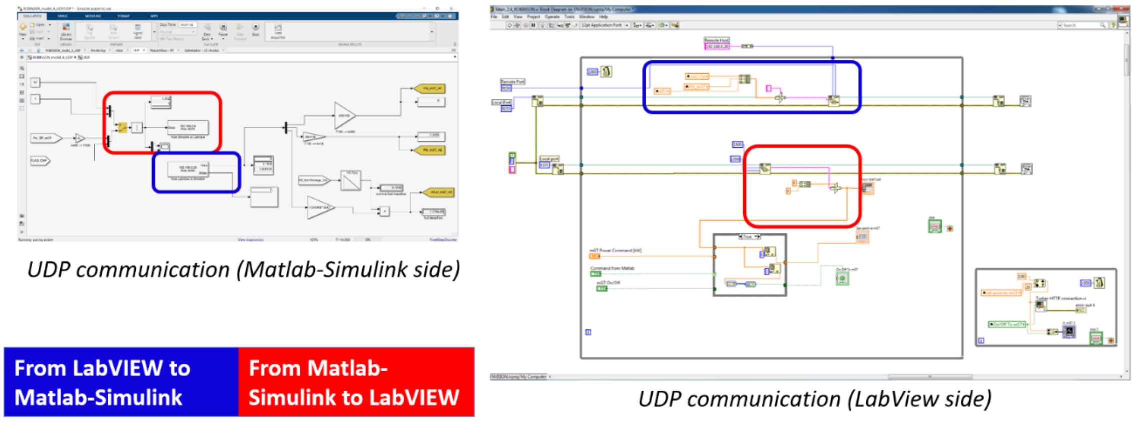

Figure 56 - UDP communication between Matlab-Simulink and LabView

The final communication result is shown in Figure 57. The software receives four measurement values from the field: CHP produced electrical power, CHP produced thermal power, CHP fuel mass flow rate, and produced power by the PV panels. On the other side, the hardware receives two calculated values from the software: the CHP on-off signal and the related set-point. Moreover, since the hardware includes a 100 kW microturbine while the software performs calculations with a 400 kW machine, a data conversion system was included: lookup tables to scale the signals in both communication senses. For the T100 machine, the operations were constrained in the 30 kW – 90 kW range to avoid problems in case of significant ambient temperature change. Also, for the PV panels a signal re-scaling was included to take into account the different installed panel areas in the laboratory (in comparison with Eigerøy.

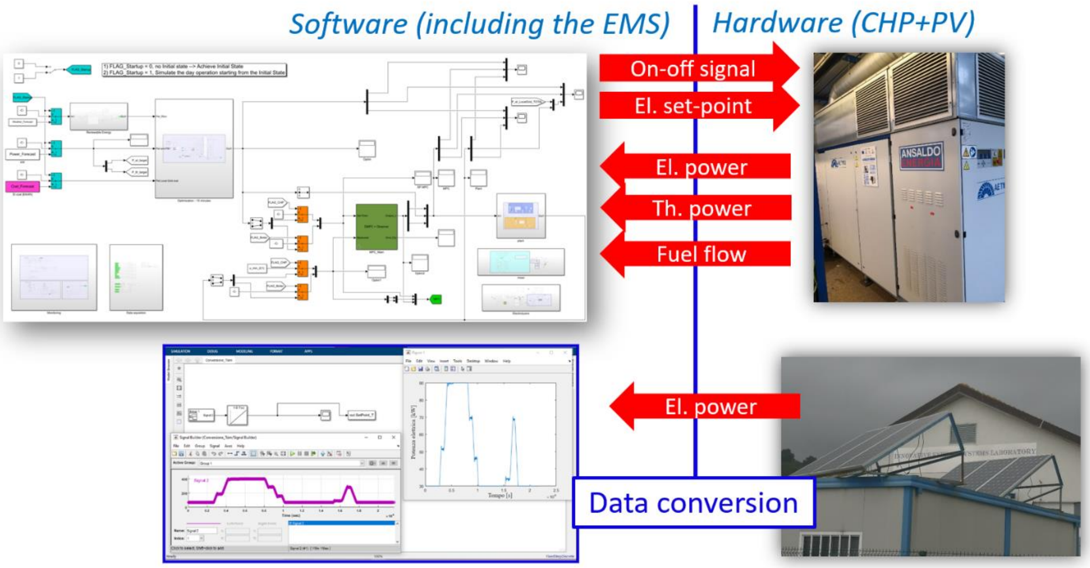

Figure 57 - Details for the software-hardware communication

3.8 Experimental results in cyber-physical mode

In spite of the long duration of the experimental tests (26 hours plus the start-up/shutdown phases), two different 26-hour tests were performed in the laboratory. It is important to highlight that the results reported here were obtained after preliminary tests that highlighted the necessity to stabilize better the tool. So, this shows the importance of tests because although the EMS was stable in just simulation mode Figure 53 oscillations coming from the measurements required improvements to have a stable behavior. Moreover, since the amount of produced biogas is negligible (<0.25 Nm^3/day) in comparison with the other fuels, it was neglected as performed Figure 54 [90].

Due to a completely different behavior depending on the syngas cost values, these results were performed considering two cases for the cost of syngas produced by the gasifier: 80 €/MWh and 5 €/MWh. Although the 80 €/MWh case is not realistic for a local syngas production, it is an opposite case of the 5 €/MWh test to validate the EMS in very different conditions. As performed in Figure 47 [90], in both syngas cost conditions, the results obtained with the EMS are compared with the related “No EMS” case. This reference is obtained with simulations considering a simple approach that does not require any intelligence or optimization. So, in the “No EMS” curves: the CHP is operated to satisfy the electrical missing demand (electricity demand minus the production by the RES that is significantly present mainly due to wind turbine operations in the late afternoon hours), the boiler is controlled through a Proportional-Integral- (PI) tool to produce the missing thermal power, and the electrolyzers are maintained at the minimum load for the entire test. Since there are no specific results or simulations for reference case (or cases), this approach has been chosen to have something simple and reasonable considering the necessity to satisfy the demands.

Finally, it is important to highlight that the selling/buying ratio was equal to 1 because, due to the preliminary condition of the Eigerøy site, no data are available for this aspect at the current development status.

3.8.1 80 €/MWh syngas cost

The 80 €/MWh case for the syngas cost was chosen because, in the 26 hours, this produced different conditions: situations when it is profitable to reduce or switch off the CHP due to low electricity price for selling and conditions that moved the EMS to operate the CHP at maximum load for producing earnings from electricity selling to the grid. In details, this aspect is clear in Figure 58 for the electrical power management. While in the “No EMS” case the CHP followed the demand trend and the missing power was provided by the grid, the EMS decided to maintain the CHP at low load when electrical selling was not profitable and increased the load at high electricity costs. Moreover, when the electricity selling was not profitable and the boiler was active (close to the hour number 14 in Figure 58) the CHP was switched off (a minimum negative power regards the ventilation or the start-up consumptions of the CHP).

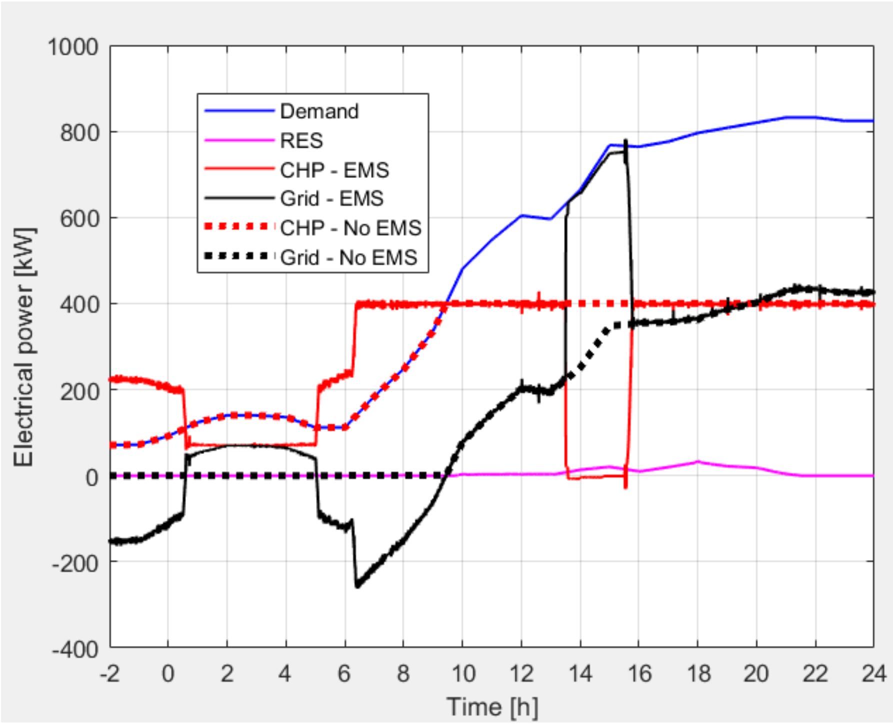

Figure 58 - Electrical power comparison (EMS against no EMS cases) for the 80 €/MWh syngas cost

For the thermal generation point of view, Figure 59 shows that the boiler was activated when the thermal demand started to be significant and higher than the maximum thermal generation by the CHP. While the predictive performance of the MPC was able to properly manage the boiler to cover the thermal demand, the PI tool produced significant oscillations with missing or excessive power situations. The gap between the demand and the boiler generation was the thermal power produced by the CHP. So, a demand-boiler matching was present when the CHP was switched off

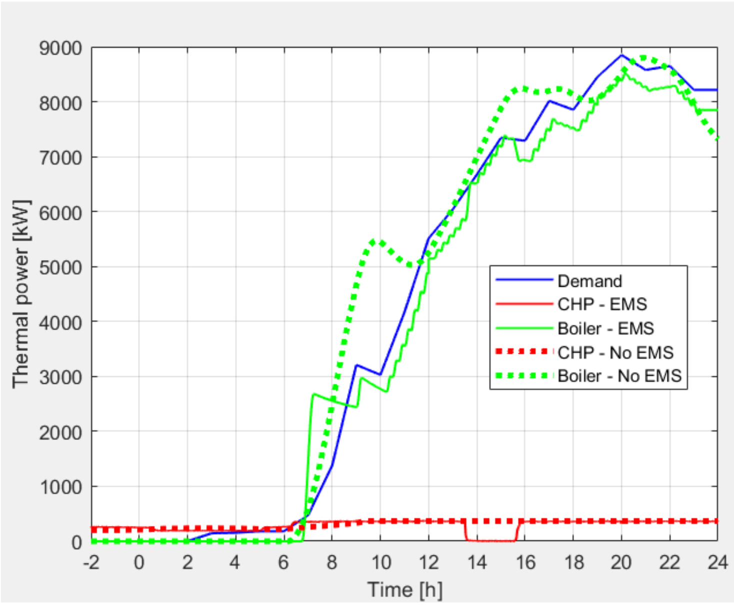

Figure 59 - Thermal power comparison (EMS against no EMS cases) for the 80 €/MWh syngas cost

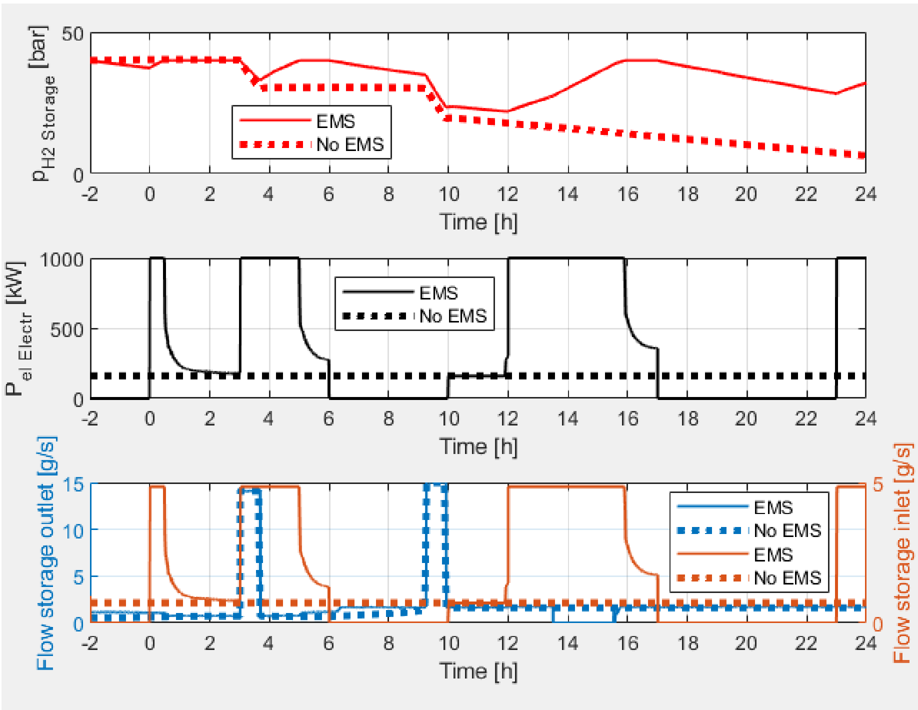

Figure 60 - Comparison (EMS against no EMS cases) for the hydrogen generation, storage and utilization (80 €/MWh syngas cost)

For the hydrogen management side, Figure 60 shows the vessel pressure, the electrolyzer power and the inlet/outlet flows. While a base hydrogen consumption is present due to the CHP need, two truck charging phases of 13.3 g/s are visible (2400 s duration in both cases). The initial charging operation is at 3:00 a.m., while the second one is at 9:15 a.m. Since no data are available for such hydrogen consumption because this will be related to future operations in the Eigerøy site, this could be representative of a typical consumption for large vehicles. Different operations could be implemented in future works also considering statistic data.

The results reported in Figure 60 show that the EMS was able to manage the electrolyzers performing proper charging operations during the FLAG = 1 situations. So, the EMS was able to re-charge the hydrogen vessel obtaining a final pressure close to the initial one. On the other hand, a non-managed approach (e.g., the "No EMS" case) produced a final hydrogen tank pressure that could be significantly lower than the initial one. Since this is linked with missing stored energy at the end of the period, this is taken into account in the result comparison section for the calculation of the global system performance.

3.8.2 5 €/MWh syngas cost

This second case, although more realistic for cost point of view, is less significant for laboratory operations because for the EMS it is always profitable to operate the CHP at maximum load for selling the possible electricity excess to the grid. So, while Figure 61 shows the same behavior of Figure 58 for the "No EMS" case, the application of the EMS tool produced a CHP behavior at 400 kW (electrical power) for the entire 26-hour test.

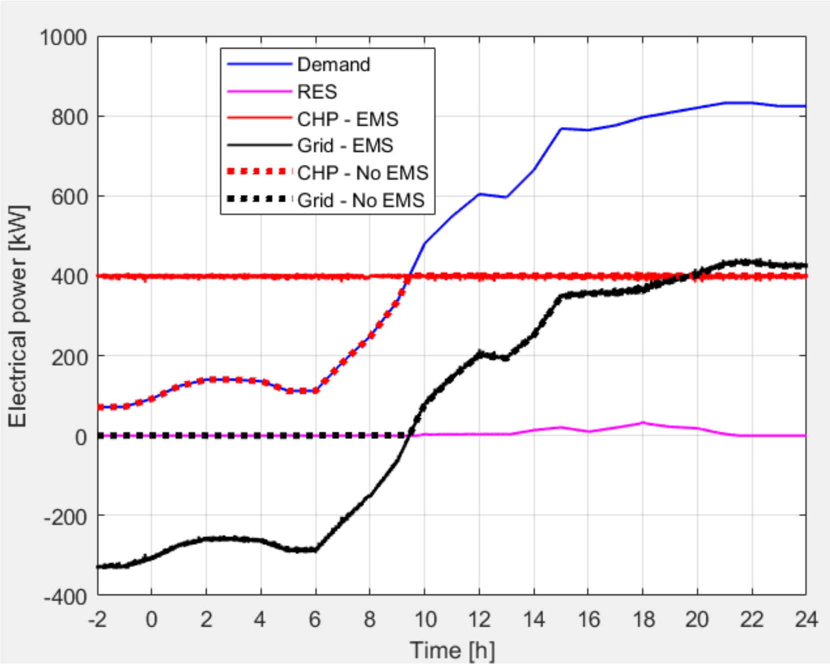

Figure 61 – Electrical power comparison (EMS against no EMS cases) for the 5 €/MWh syngas cost

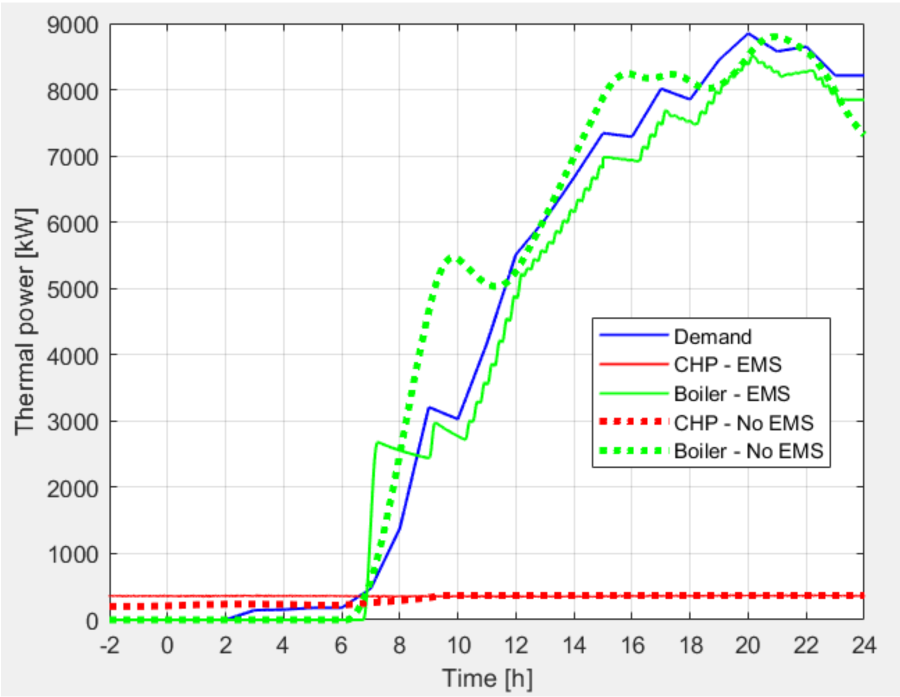

Figure 62 - Thermal power comparison (EMS against no EMS cases) for the 80 €/MWh syngas cost

On the thermal side, this test with 5 €/MWh syngas cost produced a constant thermal generation at the CHP maximum. As in the previous case, the EMS was able to manage the boiler to properly cover the thermal power demand.

For the hydrogen management point of view, Figure 63 shows similar aspects, as what presented and discussed for Figure 60. However, it is visible a constant outlet hydrogen flow (except for the truck charging phases) due to the constant 400 kW set-point on the electrical side.

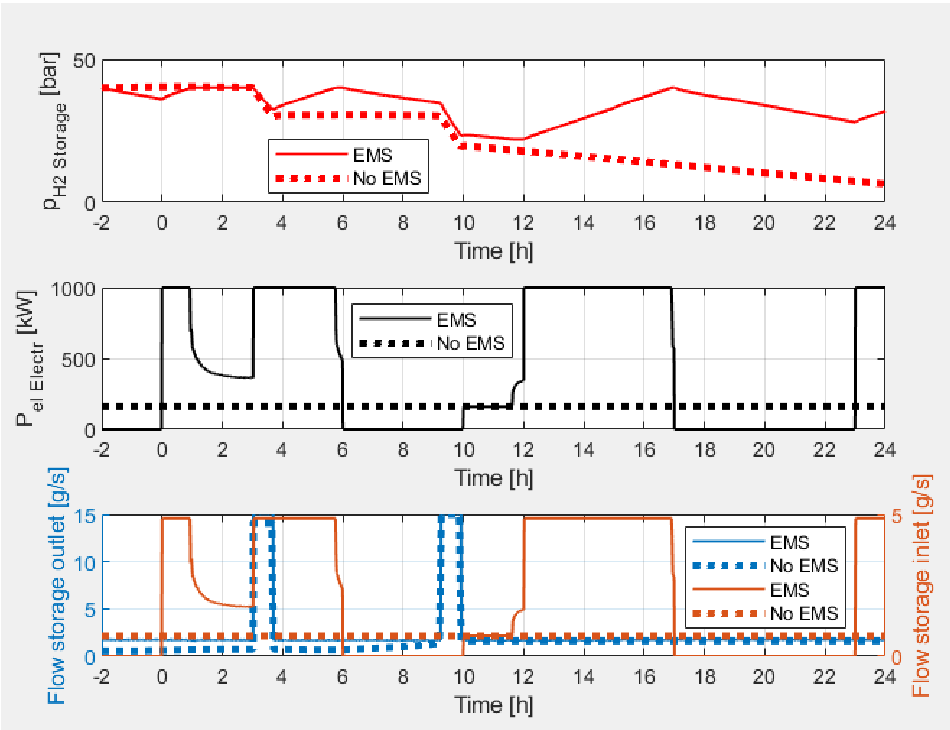

Figure 63 - Comparison (EMS against no EMS cases) for the hydrogen generation, storage and utilization (5 €/MWh syngas cost)

3.8.3 Comparison of global parameters

To finalize the EMS validation in cyber-physical mode, a comparison of global parameters was performed for all the 26 hours. The variable costs significantly decreased in comparison with the "No EMS" cases (Figure 64) due to the fact that the cost minimization is the objective chosen here. In Figure 64, it is important to include the two different costs of the "No EMS" cases due to different syngas costs. The bars for the 5 €/MWh case show, obviously, a lower global cost in comparison with the results obtained with 80 €/MWh in respective conditions. The cost decrease performance was significant due to the utilization of the EMS tool: -6.8% for the test with 80 €/MWh syngas cost and -8.3% for the 5 €/MWh case.

A second parameter discussed here and reported in Figure 65 is the electrical efficiency for the CHP alone and the integrated system. For the CHP electrical efficiency no benefits were obtained because it decreased (-7.6%) for the syngas cost value of 80 €/MWh (due to the fuel consumption during the restart phase) and the increase obtained for 5 €/MWh syngas cost was not significant (+0.9%). However, the benefits obtained for the system electrical efficiency are more important and significant: +13.6% for the 80 €/MWh syngas cost and +29.7% for the other case.

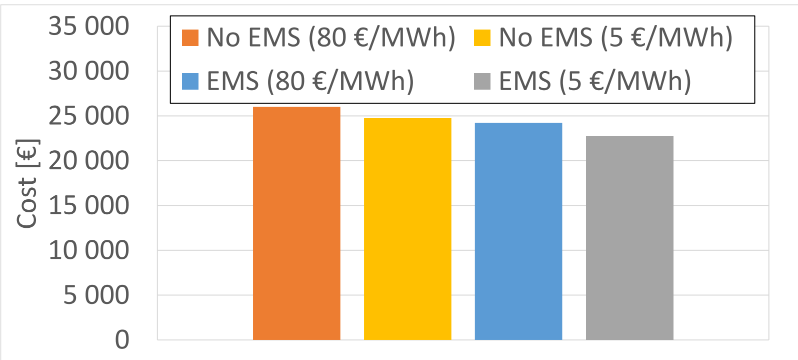

Figure 64 - Comparison of global variable costs for the cases discussed in this thesis (full 26-hour duration)

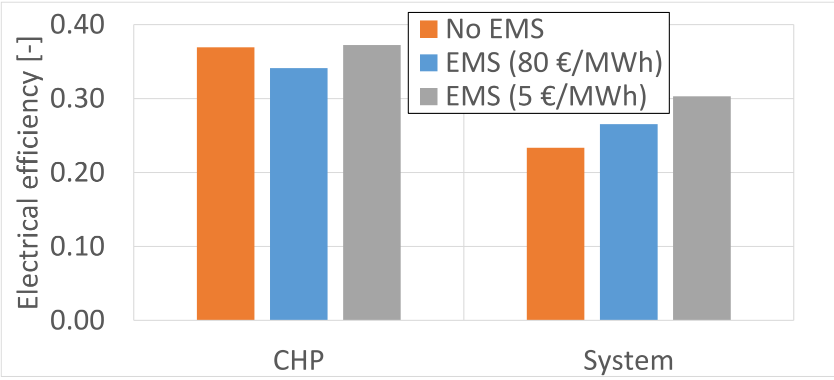

Figure 65 - Comparison of system electrical efficiency for the cases discussed in this thesis (full 26-hour duration)

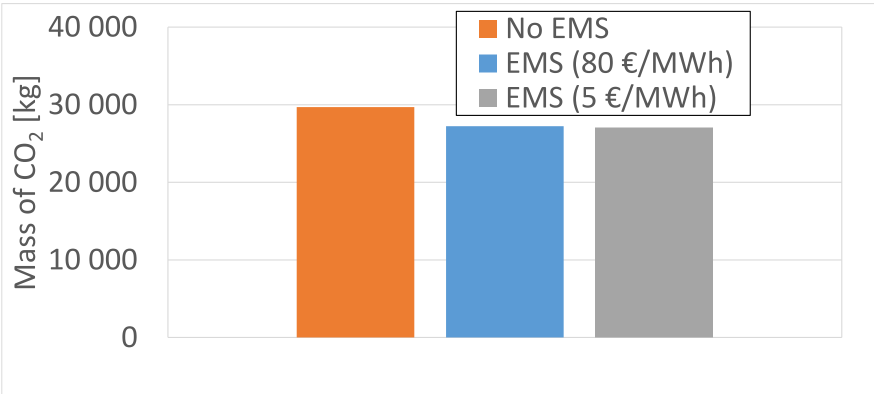

Figure 66 - Comparison of CO_2 emissions for the cases discussed in this thesis (full 26-hour duration)

Although not optimized by the EMS, it is important to report also the comparison of mass of CO_2 emitted for these 26-hour tests. The values reported in Figure 66 were calculated using the equations already presented. For these 26-hour tests, significant emission decrease was obtained with the EMS application: -8.3% for the syngas cost equal to 80 €/MWh case and -8.9% for the second test.

The experimental results (in cyber-physical mode) obtained in this work validated the proposed EMS for polygeneration grid operations. Following the simulation results in Figure 46, this experimental campaign was essential to confirm the software robustness and its performance considering the Eigerøy island (the demo site for the ROBINSON project). So, this innovative approach for these kinds of smart grid applications was considered for two 26-hour tests producing the following performance results:

- Significant cost decrease (the objective of this optimization tool) for both syngas cost scenarios (-6.8% for 80 €/MWh and-8.3% for the 5 €/MWh case).
- Due to an important link with cost decrease and efficiency increase the EMS produced also important system efficiency increase for the electrical side: +13.6% for the 80 €/MWh syngas cost and +29.7% for the other case.
- The efficiency increase generated also a positive impact on the CO_2 emissions:-8.3% for the syngas cost equal to 80 €/MWh case and-8.9% for the second test.

Considering the positive results of this work, this EMS is ready for the application in the real demo site and for its replication in the follower sites proposed by the ROBINSON project

4 Replication section

An important part of the work regards the concept replication for further applications. These analyses were performed at simulation level adapting the EMS tool for two other different cases: the Western Isles (WI) (Creed site) and Creta ("The Manna" district). So, the EMS and the component models were adapted considering the data reported in the project and further input data collected from the involved partners. Although in both WI and Crete cases there are important basic aspects similar to Eigerøy (e.g., the presence of a CHP microturbine, the integration with renewable sources, a hydrogen generation/storage/utilization system, etc.), the presence of some differences requires the analysis differentiation in the following two different sub-sections.

4.1 Western Isles

An example of the WI system management with the EMS is reported in Figure 67. Except the initial 30 minutes when the software performed the necessary iterations to be aligned with the system initial conditions, the EMS was able to manage the system to satisfy the load demands. The initial oscillation, although different from the previous cases where the simulation started from a stable condition, demonstrated the EMS robustness and the possible easy connection with the system. In comparison with the previous results for the Eigerøy case, here the contribution of renewable sources is very important. Moreover, the system includes also a thermal storage that was managed to uncouple the electrical generation (the CHP was operated to minimize the costs) with the thermal demand matching. On the hydrogen side, the simulation included a truck/trailer recharging operation (as described for the Eigerøy case) that generated the vessel pressure decrease. This is due to an important amount of hydrogen discharged from the pressure vessel (as in Figure 2 for the truck/trailer recharging). This was followed by the 40 bar restoring thanks to the operation of the electrolyzer.

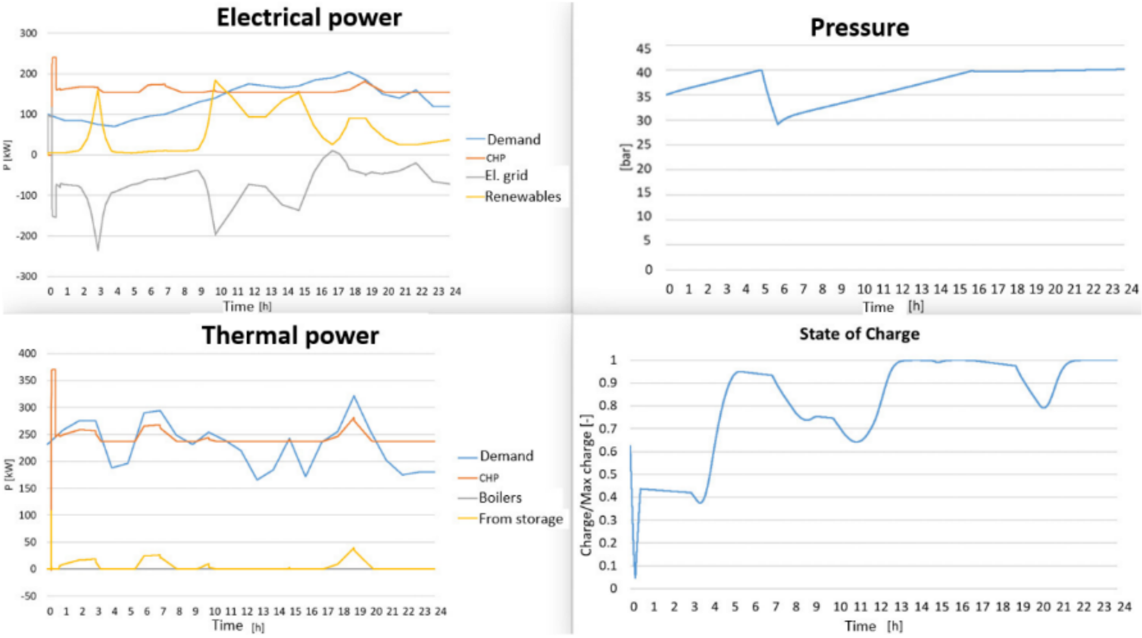

Figure 67 - EMS system management in the WI case (simulation results)

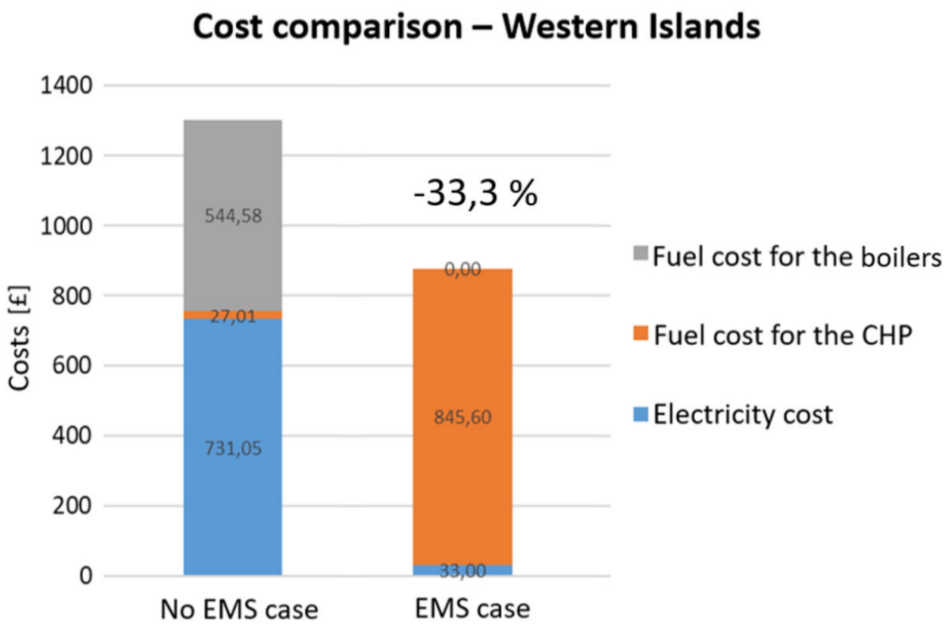

Figure 68 - Generation cost comparison for the WI case

As performed for Eigerøy, the results obtained with the EMS were compared with the no EMS simulations in terms of global variable costs. Also in this case the cost saving is significant (-33.3% as shown in Figure 68) thanks to a CHP utilization increase that allowed to avoid the switch on of the boilers.

4.2 Crete

For the Crete case, the daily demands were selected considering a typical working day for the 2021 year. As shown in Figure 69, in this case the electricity production from the renewable sources is very important. Although the wind turbine includes some production also overnight, the main contribution regards the PV panels that in the central part of the day increased the generation from renewables to values higher than 200 kW. The CHP is managed by the EMS to satisfy the thermal load when this operation is cost effective. When the CHP operations were not producing the optimal profit, some part of the thermal demand was covered by the boiler or the CHP was switched off. This event happened during this highest production from the renewables. For the electrolyzers point of view, Figure 69shows an important increase in the storage vessel pressure during the initial day hours, due to the electricity cost being lower than the average value. Then, due to the truck charging (at 5:00) the pressure significantly decreased. After an almost balanced period, at 10:30 the electricity cost decreased to values lower than the average one producing a further important pressure increase in the H2 storage vessel. Following this condition, the pressure decreased again for the second truck charging event. Then, the economic conditions changed and the EMS completed the vessel charging. The operations continued with this management: in the 16:00-22:00 the vessel was discharged due to the CHP operations and high energy cost condition, in the period of 22:00-24:00 it was recharged due to low energy costs.

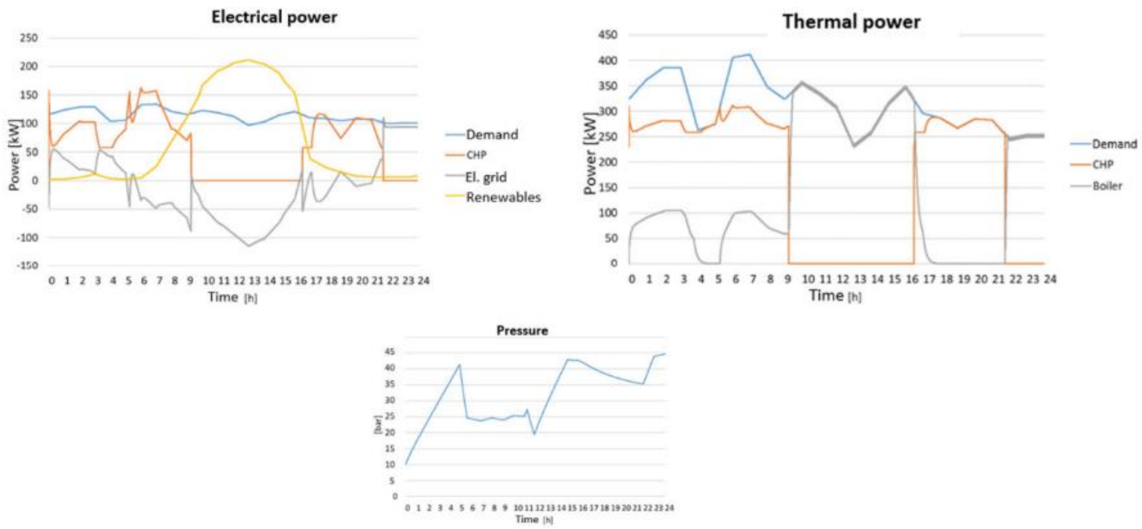

Figure 69 - EMS system management in the Crete case (simulation results)

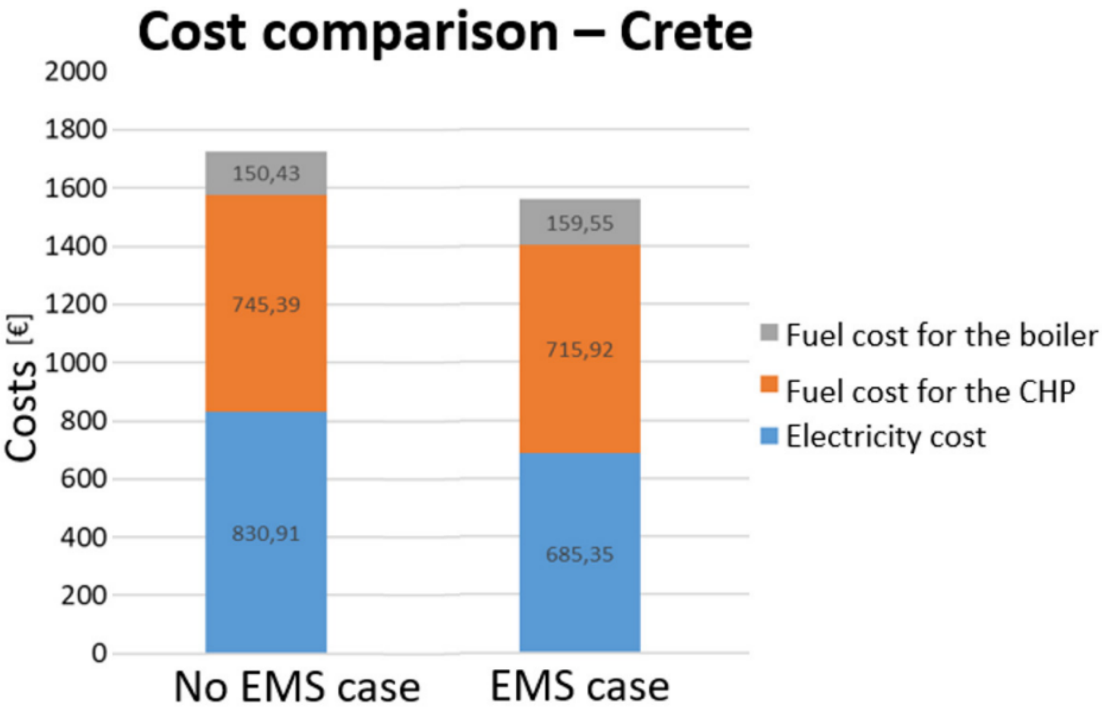

Figure 70 - Generation cost comparison for the Crete case

As performed before, the results obtained with the EMS were compared with the no EMS simulations in terms of global variable costs. Also, in this case the cost saving is significant (-9.4% as shown in Figure 70).

5 Conclusions

In conclusion, this thesis has successfully expanded the knowledge surrounding the Energy Management System (EMS) of maritime microgrids, with a specific focus on an innovative three-level concept. Over the course of three years, all the research questions posed at the outset have been thoroughly addressed. The utilization of simulation tools and cyber-physical tests played a pivotal role in achieving this milestone, given the novelty of the approach and the diverse array of prime movers involved.

The research methodology involved the development of dynamic models for each prime mover within the microgrid, followed by the design and integration of the EMS with these models to establish a closed feedback loop. Subsequently, experimental validation in a cyber-physical mode confirmed the efficacy of the proposed EMS for polygeneration grid operations. These experiments not only validated the software's robustness but also demonstrated its performance capabilities.

The results of the experimental campaigns, conducted over two 26-hour tests, were highly encouraging. The EMS led to significant cost reductions in both syngas cost scenarios, with decreases of 6.8% and 8.3% for the respective cases. Furthermore, notable increases in system efficiency were observed on the electrical side, resulting in efficiency gains of 13.6% and 29.7% for the two scenarios. Importantly, these efficiency improvements translated into reduced CO_2 emissions, with reductions of 8.3% and 8.9% recorded for the respective tests.

Given the positive outcomes of this research, the EMS is deemed ready for real-world applications and replication. Moreover, there is potential for further development and long-term applications of the proposed concept, including the integration of innovative cyber-physical approaches.

Bibliography

[1] BP, 2021, Statistical Review of World Energy Globally Consistent Data on World Energy Markets. and Authoritative Publications in the Field of Energy.

[2] The World Bank, "World Development Indicators" [Online]. Available: https://datacatalog.worldbank.org/search/dataset/0037712. [Accessed: 20-Feb-2024]

[3] Fragaszy, R. J., Santamarina, J. C., Amekudzi, A., Assimaki, D., Bachus, R., Burns, S. E., Cha, M., Cho, G. C., Cortes, D. D., Dai, S., Espinoza, D. N., Garrow, L., Huang, H., Jang, J., Jung, J. W., Kim, S., Kurtis, K., Lee, C., Pasten, C., Phadnis, H., Rix, G., Shin, H. S., Torres, M. C., and Tsouris, C., 2011, "Sustainable Development and Energy Geotechnology - Potential Roles for Geotechnical Engineering," KSCE J. Civ. Eng., 15(4), pp. 611–621

[4] United Nations, 2015, "Transforming Our World: The 2030 Agenda for Sustainable Development."

[5] Osservatorio Italiano sulla Povertà Energetica, 2019, Rapporto Sullo Stato Della Povertà Energetica in Italia

[6] Bouzarovski, S., Thomson, H., and Cornelis, M., 2021, "Confronting Energy Poverty in Europe: A Research and Policy Agenda," Energies, 14(4), pp. 1–19

[7] Global Energy Institute, 2018, "International Index of Energy Security Risk.

[8] World Energy Council, 2020, World Energy Trilemma Index 2020, London.

[9] ROBINSON project website: https://www.robinson-h2020.eu/ , [Accessed: 20-Feb-2024]

[10] IEA, 2021, Heating, Paris

[11] Bauermann, K., 2016, "German Energiewende and the Heating Market – Impact and Limits of Policy," Energy Policy, 94, pp. 235–246.

[12] Bloess, A., Schill, W.-P., and Zerrahn, A., 2018, "Power-to-Heat for Renewable Energy Integration: A Review of Technologies, Modeling Approaches, and Flexibility Potentials," Appl. Energy, 212, pp. 1611–1626.

[13] Kavvadias, K., Jimenez Navarro, J., and Thomassen, G., 2019, Decarbonising the EU Heating Sector: Integration of the Power and Heating Sector, Luxembourg.

[14] Gjorgievski, V. Z., Markovska, N., Abazi, A., and Duić, N., 2021, "The Potential of Power-to-Heat Demand Response to Improve the Flexibility of the Energy System: An Empirical Review," Renew. Sustain. Energy Rev., 138, p. 110489.

[15] Kohlhepp, P., Harb, H., Wolisz, H., Waczowicz, S., Müller, D., and Hagenmeyer, V., 2019, "Large-Scale Grid Integration of Residential Thermal Energy Storages as Demand-Side Flexibility Resource: A Review of International Field Studies," Renew. Sustain. Energy Rev., 101, pp. 527–547.

[16] Wang, J., Zhong, H., Ma, Z., Xia, Q., and Kang, C., 2017, "Review and Prospect of Integrated Demand Response in the Multi-Energy System," Appl. Energy, 202, pp. 772–782.

[17] Zhang, H., Zhou, L., Huang, X., and Zhang, X., 2019, "Decarbonizing a Large City's Heating System Using Heat Pumps: A Case Study of Beijing," Energy, 186, p. 115820.

[18] Al-Rabghi, O. M., Beirutty, M., Akyurt, M., Najjar, Y., and Alp, T., 1993, "Recovery and Utilization of Waste Heat," Heat Recover. Syst. CHP, 13(5), pp. 463–470.

[19] Wahlroos, M., Pärssinen, M., Manner, J., and Syri, S., 2017, "Utilizing Data Center Waste Heat in District Heating – Impacts on Energy Efficiency and Prospects for Low-Temperature District Heating Networks," Energy, 140, pp. 1228–1238.

[20] Brückner, S., Liu, S., Miró, L., Radspieler, M., Cabeza, L. F., and Lävemann, E., 2015, "Industrial Waste Heat Recovery Technologies: An Economic Analysis of Heat Transformation Technologies," Appl. Energy, 151, pp. 157–167.

[21] Mahmoudi, A., Fazli, M., and Morad, M. R., 2018, "A Recent Review of Waste Heat Recovery by Organic Rankine Cycle," Appl. Therm. Eng., 143, pp. 660–675.

[22] Jouhara, H., Khordehgah, N., Almahmoud, S., Delpech, B., Chauhan, A., and Tassou, S. A., 2018, "Waste Heat Recovery Technologies and Applications," Therm. Sci. Eng. Prog., 6, pp. 268–289.

[23] Forman, C., Muritala, I. K., Pardemann, R., and Meyer, B., 2016, "Estimating the Global Waste Heat Potential," Renew. Sustain. Energy Rev., 57, pp. 1568–1579.

[24] Connolly, D., Lund, H., Mathiesen, B. V, Werner, S., Möller, B., Persson, U., Boermans, T., Trier, D., Østergaard, P. A., and Nielsen, S., 2014, "Heat Roadmap Europe: Combining District Heating with Heat Savings to Decarbonise the EU Energy System," Energy Policy, 65, pp. 475–489.

[25] Kavvadias, K. C., and Quoilin, S., 2018, "Exploiting Waste Heat Potential by Long Distance Heat Transmission: Design Considerations and Techno-Economic Assessment," Appl. Energy, 216, pp. 452–465.

[26] Sipilä, K., 2016, Advanced District Heating and Cooling (DHC) Systems.

[27] Zhang, L., Li, Y., Zhang, H., Xu, X., Yang, Z., and Xu, W., 2021, "A Review of the Potential of District Heating System in Northern China," Appl. Therm. Eng., 188, p. 116605

[28] 2020, "Danish District Heating – The Heat of the Moment," ICIBSE J.

[29] SDH Solar District Heating, 2016, "Silkeborg Gets the World Largest Solar Thermal Plant" [Online]. Available: https://www.solar-district-heating.eu/silkeborg-gets-theworld-largest-solar-thermal-plant/#:~:text=In the Danish city of,front of the city's gate. [Accessed: 16-Jan-2022].

[30] Weiss, W., and Spörk-Dür, M., 2021, Solar Heat World Wide

[31] Lund, H., Werner, S., Wiltshire, R., Svendsen, S., Eric, J., Hvelplund, F., and Vad, B., 2014, "4th Generation District Heating (4GDH) Integrating Smart Thermal Grids into Future Sustainable Energy Systems," Energy, 68, pp. 1–11.

[32] Lund, H., Østergaard, P. A., Nielsen, T. B., Werner, S., Thorsen, J. E., Gudmundsson, O., Arabkoohsar, A., and Mathiesen, B. V., 2021, "Perspectives on Fourth and Fifth Generation District Heating," Energy, 227, p. 120520

[33] David, A., Mathiesen, B. V., Averfalk, H., Werner, S., and Lund, H., 2017, "Heat Roadmap Europe: Large-Scale Electric Heat Pumps in District Heating Systems," Energies, 10(4), pp. 1–18

[34] Green, R., Gill, E., Hein, C., Couturier, L., Mascarenhas, M., May, R., Newell, D., Rumes, B., International assessment of priority environmental issues for land-based and offshore wind energy development. Global sustainability, 5 (2022) article n. 14.

[35] Muñoz, P., Franceschini, E.A., Levitan, D., Rodriguez, C.R., Humana, T., Correa, P.G. Comparative analysis of cost, emissions and fuel consumption of diesel, natural gas, electric and hydrogen urban buses. Energy Conversion and Management, 257 (2022) article n. 115412

[36] Rivarolo, M., Freda, A., Traverso, A., Test campaign and application of a small-scale ducted wind turbine with analysis of yaw angle influence. Applied Energy, 279 (2020) 115850_1-9

[37] Giourka, P., Apostolopoulos, V., Angelakoglou, K., Kourtzanidis, K., Nikolopoulos, N., Sougkakis, V., Fuligni, F., Barberis, S., Verbeek, K., Costa, J.M., Formiga, J., The nexus between market needs and value attributes of smart city solutions towards energy transition. An empirical evidence of two european union (EU) smart cities, evora and alkmaar. Smart Cities, 3 (2020) 604-641

[38] Ferrari, M.L., Traverso, A., Pascenti, M., Massardo, A.F., Plant management tools tested with a small-scale distributed generation laboratory. Energy Conversion and Management, 78 (2014) 105–113.

[39] Senyel Kurkcuoglu, M.A., Analysis of the energy justice in natural gas distribution with Multiscale Geographically Weighted Regression (MGWR). Energy Reports, 9 (2023) 325-337.

[40] Cassetti, G., Boitier, B., Elia, A., Le Mouël, P., Gargiulo, M., Zagamé, P., Nikas, A., Koasidis, K., Doukas, H., Chiodi, A., The interplay among COVID-19 economic recovery, behavioural changes, and the European Green Deal: An energy-economic modelling perspective. Energy, 263 (2023) 125798.

[41] Amirthan, T., Perera, M.S.A., The role of storage systems in hydrogen economy: A review. *Journal of Natural Gas Science and Engineering, 108 (2022) 104843.*

[42] Gadducci, E., Lamberti, T., Bellotti, D., Magistri, L., Massardo, A.F., BoP incidence on a 240 kW PEMFC system in a ship-like environment, employing a dedicated fuel cell stack model. International Journal of Hydrogen Energy, 46 (2021) 24503-24317.

[43] Bellotti, D., Rivarolo, M., Magistri, L., A comparative techno-economic and sensitivity analysis of Power-to-X processes from different energy sources. Energy Conversion and Management, 260 (2022) 115565_1-15.

[44] Reboli, T., Ferrando, M., Traverso, A., Chiu, J.N.W., Thermal energy storage based on cold phase change materials: Charge phase assessment. Applied Thermal Engineering, 217 (2022) 119177_1-12

[45] Zhou, J., Xu, Z., Optimal sizing design and integrated cost-benefit assessment of stand-alone microgrid system with different energy storage employing chameleon swarm algorithm: A rural case in Northeast China. Renewable Energy, 202 (2023) 1110-1137.

[46] Akpinar, K.N., Gundogdu, B., Ozgonenel, O., Gezegin, C., An intelligent power management controller for grid-connected battery energy storage systems for frequency response service: A battery cycle life approach. Electric Power Systems Research, 216 (2023) 109040.

[47] Barberis, S., Rivarolo, M., Bellotti, D., Magistri, L., Heat pump integration in a real poly-generative energy district: A techno-economic analysis. Energy Conversion and Management: X, 15 (2022) 100238_1-10.

[48] Terlouw, T., AlSkaif, T., Bauer, C., Mazzotti, M., McKenna, R., Designing residential energy systems considering prospective costs and life cycle GHG emissions. Applied Energy, 331 (2023) 120362.

[49] Bouakkaz, A., Mena, A.J.G., Haddad, S., Ferrari, M.L., Efficient energy scheduling considering cost reduction and energy saving in hybrid energy system with energy storage. Journal of Energy Storage, 33 (2021) 101887_1-13.

[50] Rossi, I., Banta, L., Cuneo, A., Ferrari, M.L., Traverso, A.N., Traverso, A., Real-time management solutions for a smart polygeneration microgrid, Energy Conversion and Management, 112 (2016) 11-20.

[51] Reboli, T., Ferrando, M., Mantelli, L., Gini, L., Source, A., Garcia, J., Guedez, R., Gas Turbine Combined Cycle Range Enhancer – Part 1: Cyber-Physical Setup, ASME Paper GT2022-82494, ASME Turbo Expo 2022, Rotterdam, The Netherlands (2022).

[52] I. Benoit, “DISTRIBUTED GENERATION : DEFINITION , BENEFITS AND ISSUES Pepermans G ., Driesen J ., Haeseldonckx D ., D ’ haeseleer W ., Belmans R . secretariat : DISTRIBUTED GENERATION : DEFINITION , BENEFITS AND ISSUES,” Energy, vol. 32, no. 0, pp. 0–21, 2003.

[53] IRETTIVA 2009/72/CE.” https://eur-lex.europa.eu/legalcontent/IT/TXT/PDF/?uri=CELEX:32009L0072&from=EN (accessed Jan. 15, 2024).

[54] “Distributed Generation of Electricity and its Environmental Impacts | Energy and the Environment | US EPA.” https://www.epa.gov/energy/distributed-generation-electricityand-its-environmental-impacts (accessed Nov. 24, 2020).

[55] E. F. El-Saadany, H. H. Zeineldin, and A. H. Al-Badi, “Distributed Generation : Benefits and Challenges,” International Conference on Communication, Computer & Power, pp. 115–119, 2007.

[56] Terna s.p.a, “Contesto ed evoluzione del sistema elettrico,” pp. 42–45, 2019.

[57] W. El-Khattam and M. M. A. Salama, “Distributed generation technologies, definitions and benefits,” Electric Power Systems Research, vol. 71, no. 2, pp. 119–128, 2004, doi: 10.1016/j.epsr.2004.01.006.

[58] A. Poullikkas, “Implementation of distributed generation technologies in isolated power systems,” Renewable and Sustainable Energy Reviews, vol. 11, no. 1, pp. 30–56, 2007, doi: 10.1016/j.rser.2006.01.006.

[59] T. Phelps, S. David Wrightsman, and B. Development Manager, “INTERNAL COMBUSTION ENGINES Combined Heat and Power,” 2017. Accessed: Feb. 20, 2024. [Online].

[60] M. A. R. do Nascimento, L. D. O. Rodrigues, E. E. B. G. E. C. Dos Santos, F. L. G. Dias, E. I. G. Velásques, and R. a. M. Carrillo, “Micro Gas Turbine Engine: A Review,” Progress in Gas Turbine Performance, no. June 2019, pp. 108–142, 2013.

[61] “EMEA Bunker Prices - Ship & Bunker.” https://shipandbunker.com/prices/emea (accessed Dec. 30, 2023)

[62] AEEG, “Costi di produzione di energia elettrica da fonti rinnovabili.” https://www.autorita.energia.it/allegati/docs/13/RappPolitecnicoRinn.pdf (accessed Dec. 30, 2023)

[63] “» Natural Gas and the Environment NaturalGas.org.” http://naturalgas.org/environment/naturalgas/ (accessed Jan. 02, 2021).

[64] D. Rattazzi, M. Rivarolo, T. Lamberti, and L. Magistri, “A design tool for the performances comparison of innovative energy systems for naval applications,” in E3S Web of Conferences, Aug. 2019, vol. 113, doi: 10.1051/e3sconf/201911302005

[65] L. van Biert, M. Godjevac, K. Visser, and P. v. Aravind, “A review of fuel cell systems for maritime applications,” Journal of Power Sources, vol. 327, no. X, pp. 345–364, 2016, doi: 10.1016/j.jpowsour.2016.07.007.

[66] R. E. Rosli et al., “A review of high-temperature proton exchange membrane fuel cell (HTPEMFC) system,” International Journal of Hydrogen Energy, vol. 42, no. 14, pp. 9293–9314, Apr. 2017, doi: 10.1016/j.ijhydene.2016.06.211.

[67] “Market Review of Energy Storage Systems.” https://www.victanis.com/market-review-ofenergy-storage-systems (accessed Dec. 03, 2023).

[68] S. Al-Thyabat, T. Nakamura, E. Shibata, and A. Iizuka, “Adaptation of minerals processing operations for lithium-ion (LiBs) and nickel metal hydride (NiMH) batteries recycling: Critical review,” Minerals Engineering, vol. 45, pp. 4–17, Mar. 2013, doi: 10.1016/j.mineng.2012.12.005.

[69] D. Rattazzi, M. Rivarolo, and A. F. Massardo, “An innovative tool for the evaluation and comparison of different fuels and technologies onboard ships,” pp. 1–6, 2020.

[70] “ENERGY-EFFICIENT BUILDINGS PPP MULTI-ANNUAL ROADMAP AND LONGER TERM STRATEGY.” Accessed: Dec. 04, 2020. [Online]. Available: http://ec.europa.eu/research/research-eu.

[71] K. Bunker, S. Doig, K. Hawley and J. Morris, "Renewable microgrids: Profiles from islands and remote communities across the globe", 2015.

[72] "Installation energy resilience strategy", 2020.

[73] R. E. Giachetti, C. J. Peterson, D. L. Van Bossuyt and G. W. Parker, "Systems engineering issues in microgrids for military installations" in INCOSE Int. Symp., vol. 30, no. 1, pp. 731-746, 2020.

[74] S. R. Goerger, A. M. Madni and O. J. Eslinger, "Engineered resilient systems: A DoD perspective", *Procedia Comput. Sci.*, no. 28, pp. 865-872, 2014.

[75] https://cordis.europa.eu/programme/id/H2020-EC

[76] Jaatinen-Värri, A., Nerg, J., Uusitalo, A., Ghalamchi, B., Uzhegov, N., Smirnov, A., Malkamäki, M., Design of a 400 kW Gas Turbine Prototype. ASME Turbo Expo 2016, Paper No: GT2016-56444 (2016)

[77] Traverso, A., 2005, “TRANSEO Code for the Dynamic Performance Simulation of Micro Gas Turbine Cycles,” Proceedings of the ASME Turbo Expo, **5**, pp. 45–54

[78] Traverso, A., 2011, “TRANSEO Code for the Dynamic Performance Simulation of Micro Gas Turbine Cycles,” Proceedings of the ASME Turbo Expo, GT2011-45369, pp. 91-104; 14 pages

[79] Maamouri, R 2021, “Proton exchange membrane water electrolysis: Modeling for hydrogen flow rate control” International Journal of Hydrogen Energy, Volume 46, Issue 11, 11 February 2021, Pages 7676-7700.

[80] Traverso, A, Barberis, S, Lima, D, & Massardo, AF. "Dynamic Analysis of Concentrated Solar Hybridised Gas Turbine." Proceedings of the ASME Turbo Expo 2014: Turbine Technical Conference and Exposition. Volume 3A: Coal, Biomass and Alternative Fuels; Cycle Innovations; Electric Power; Industrial and Cogeneration. Düsseldorf, Germany. June 16–20, 2014. V03AT07A005. ASME. https://doi.org/10.1115/GT2014-25225

[81] Audet, C., Dennis J.E., Analysis of Generalized Pattern Searches. *SIAM Journal on Optimization*, 13 (2003) 889–903.

[82] Lewis, R.M., Shepherd, A., Torczon, V., Implementing generating set search methods for linearly constrained minimization. *SIAM Journal on Scientific Computing*, 29 (2007) 2507–2530.

[83] Wang, L., Model Predictive Control System Design and Implementation Using MATLAB®, Springer London, UK (2009)

[84] Wang, L., Young, P.C., An improved structure for model predictive control using non-minimal state space realization. Journal of Process Control, 16 (2006) 355-371

[85] Hang, T., Energy Forecasting: A Review and Outlook, 09 October 2020,IEEE Open Access Journal of Power and Energy (Volume: 7)

[86] Reboli, T., Ferrando, M., Traverso, A., Chiu, J.N.W., Thermal energy storage based on cold phase change materials: Charge phase assessment. Applied Thermal Engineering, 217 (2022) 119177_1-12

[87] Zhou, J., Xu, Z., Optimal sizing design and integrated cost-benefit assessment of stand-alone microgrid system with different energy storage employing chameleon swarm algorithm: A rural case in Northeast China. Renewable Energy, 202 (2023) 1110-1137

[88] Reboli, T., Ferrando, M., Mantelli, L., Gini, L., Sorce, A., Garcia, J., Guedez, R., Gas turbine combined cycle range enhancer – part 1: cyber-physical setup. ASME Turbo Expo 2022, ASME Paper GT2022-82494, Rotterdam, The Netherlands (2022)

[89] M.L. Ferrari, A. Traverso, M. Pascenti, A.F. Massardo, Plant management tools tested with a small-scale distributed generation laboratory. Energy Conversion and Management, 78, 105-113 (2014)

[90] Ferrari, M.L., Gini, L., Maccarini, S., Energy Management System for Smart Grids Including Renewable Sources and Industrial Symbiosis. *Proceedings of the ASME Turbo Expo* 2023, 5 (2023) 1-14.

[91] M. A. Ancona, M. Bianchi, F. Melino, and A. Peretto, "Power Augmentation Technologies: Part I — Literature Review," *Proc. ASME Turbo Expo*, vol. 3, Aug. 2015, doi: 10.1115/GT2015-43159.

[92] J. N. W. C. Vasilis G. Gkoutzamanis, Anastasia N. Chatziangelidou, Theofilos G. Efstathiadis, Anestis I. Kalfas, Alberto Traverso, "Thermal Energy Storage For Gas Turbine Power Augmentation," *GPPS Conf.*, vol. 3, pp. 1–11, Jul. 2019, doi: 10.33737/JGPPS/110254

[93] A. H. Lefebvre and D. R. Ballal, *Gas Turbine Combustion Alternative Fuel and Emissions*, 3rd editio., vol. 141, no. 2. CRC Press, 2010

[94] M. Cioffi, S. Piola, E. Puppo, A. Silingardi, and F. Bonzani, "Minimum Environmental Load Reduction in Heavy Duty Gas Turbine by Bleeding Lines," *Proc. ASME Turbo Expo*, vol. 3A, Sep. 2014, doi: 10.1115/GT2014-25438

[95] A. Gunschera, "High Efficiency Solutions Solutions for your power plant optimization."

[96] "Pump-Heat project." https://www.pumpheat.eu/ (accessed Dec. 18, 2023).

[97] A. Sorce, A. Giugno, D. Marino, S. Piola, R. Guedez, and R. G. A.Sorce, A.Giugno, D.Marino, S.Piola, "Analysis of a combined cycle exploiting inlet conditioning technologies for power modulation," in *ASME Paper GT2019-91541*, Nov. 2019, vol. 3, doi: 10.1115/GT2019-91541

[98] W. Mantilla, R. Guédez, J. García, and A. Sorce, “Short-term optimization of a combined cycle power plant integrated with an inlet air conditioning unit,” in *Proceedings of the ASME Turbo Expo*, 2020, vol. 5, doi: 10.1115/GT2020-15162

[99] A. Giugno, A. Sorce, A. Cuneo, and S. Barberis, “Effects of market and climatic conditions over a gas turbine combined cycle integrated with a Heat Pump for inlet cooling,” *Appl. Energy*, vol. 290, no. February, p. 116724, 2021, doi: 10.1016/j.apenergy.2021.116724

[100] Pump-Heat Project, “D4 . 6 – ‘ Validation results in Energy -Hub of MPC with cold thermal storage ,’” 2021. Accessed: Dec. 18, 2021. [Online]. Available: www.pumpheat.eu

[101] A. Rohr and C. Jauch, “Software-in-the-Loop Simulation of a Gas-Engine for the Design and Testing of a Wind Turbine Emulator,” *Energies 2021, Vol. 14, Page 2898*, vol. 14, no. 10, p. 2898, May 2021, doi: 10.3390/EN14102898

[102] J. Duquette, D. O’Sullivan, S. Ceballos, and R. Alcorn, “Design and Construction of an Experimental Wave Energy Device Emulator Test Rig,” 2009

[103] J. Agrawal and M. Aware, “Photovoltaic system emulator,” *PEDES 2012 - IEEE Int. Conf. Power Electron. Drives Energy Syst.*, 2012, doi: 10.1109/PEDES.2012.6484360

[104] S. Tan, W. Z. Song, S. Yothment, J. Yang, and L. Tong, “ScorePlus: An integrated scalable cyber-physical experiment environment for Smart Grid,” *2015 12th Annu. IEEE Int. Conf. Sensing, Commun. Networking, SECON 2015*, pp. 381–389, Nov. 2015, doi: 10.1109/SAHCN.2015.7338338

[105] M. L. Ferrari, I. Rossi, A. Sorce, and A. F. Massardo, “Advanced Control System for Grid-Connected SOFC Hybrid Plants: Experimental Verification in Cyber-Physical Mode,” *J. Eng. Gas Turbines Power*, vol. 141, no. 9, Sep. 2019, doi: 10.1115/1.4044196

[106] M. L. Ferrari, M. Pascenti, and A. Abrassi, “Test Rig for Emulation of Turbocharged SOFC Plants,” *E3S Web Conf.*, vol. 113, p. 02001, 2019, doi: 10.1051/e3sconf/201911302001

[107] Y. Watanabe and A. Traverso, “Dynamic Simulation of Steam Bottoming System in a Combined Cycle Power Plant with Modelica,” 2019

[108] I. Rossi, A. Sorce, and A. Traverso, “Gas turbine combined cycle start-up and stress evaluation: A simplified dynamic approach,” *Appl. Energy*, vol. 190, pp. 880–890, Mar. 2017, doi: 10.1016/j.apenergy.2016.12.141

[109] T. Reboli, M. Ferrando, L. Gini, L. Mantelli, A. Sorce, and A. Traverso, “Gas Turbine Combined Cycle Range Enhancer - Part 2: Performance Demonstration (to be published),” 2022.

[110] W. Mantilla, R. Guédez, J. García, and A. Sorce, “Short-term optimization of a combined cycle power plant integrated with an inlet air conditioning unit,” in *Proceedings of the ASME Turbo Expo*, 2020, vol. 5, doi: 10.1115/GT2020-15162.

[111] A. Gupte, S. Ahmed, M. S. Cheon, and S. Dey, “Solving Mixed Integer Bilinear Problems Using MILP Formulations,” *http://dx.doi.org/10.1137/110836183*, vol. 23, no. 2, pp. 721–744, Apr. 2013, doi: 10.1137/110836183.

[112] A. Vannoni, J. A. Garcia, W. Mantilla, R. Guedez, and A. Sorce, “Ancillary Services Potential for Flexible Combined Cycles,” *Proc. ASME Turbo Expo*, vol. 4, Sep. 2021, doi: 10.1115/GT2021-59587

[113] E. K. P. Chong and S. H. Zak, *An Introduction to Optimization*. 2004

[114] N. M. Abbasi, “Basic Matlab implementation of the Simplex matrix algorithm,” 2020.

[115] J. G. Ziegler and N. B. Nichols, “Optimum settings for automatic controllers,” *J. Dyn. Syst. Meas. Control. Trans. ASME*, vol. 115, no. 2B, pp. 220–222, Jun. 1993, doi: 10.1115/1.2899060

[116] Mario L., et al, Real-time tool for management of smart polygeneration grids including thermal energy storage, Applied Energy, Volume 130, 2014

[117] Y. Bulut, D. Smeulders, C. de Keizer; “Performance Assessment of Colored Façade Integrated Solar Collectors and Numerical Analysis of Solar Collector-Heat Pump System with TRNSYS”; 2018

6 Appendix 1 - EMS concept application for GTCC

Highly flexible programmable power plants are crucial to guarantee the stability of the electrical network. Gas turbine combined cycles (GTCC), will bridge the EU towards a decarbonized scenario, thanks to their reduced carbon footprint and fast response in terms of grid stabilization. To achieve this goal, GTCCs should have a minimum impact on the grid when running at minimum load (constrained by pollutant emissions) and produce at least the full nominal capacity when required. An extension of the operative range of these power plants in both directions results in an increased chance of providing ancillary services, acting as a reserve for the non-programmable generators. The EMS would play a key role even in GTCC when the integration of technologies allow the performance enhancement.

Industry has adopted several methods to increase the maximum production of GTCCs. These methods can be classified as inlet air cooling methods, combustion improvement methods or combustion chamber injection systems (e.g., steam or humid air injection [91]). This work focuses on the former power augmenting techniques, which rely on evaporating cooling systems (e.g., with wetted media, fogging, overspray) or continuous cooling systems, in a closed cycle (e.g., with absorption or compression chiller). This study also considers solutions where a thermal energy storage can be used to decouple the production and the use of energy, storing it below ambient temperature. Thermal energy storages include sensible heat storages (usually water) or latent heat storages, using the so-called Phase Change Materials (PCM). Not requiring a special material, ice storages are a particularly interesting solution. Their application for gas turbine power augmentation has been already tested by Vasilis et al. [92].

The reduction of the minimum power of a GTCC is usually related to the management of its CO emissions. In fact, for high air-to-fuel ratios, which are typical of low load conditions, the amount of CO generated is often too high for the current environmental regulations [93]. To decrease the amount of air entering the combustion chamber, several solutions were proposed by OEM. Some of the most interesting techinques are:

(i) By-pass of the combustion chamber [94].

(ii) Partial recirculation of the compressor outlet air flow to the compressor intake. This solution also increases the intake temperature, reducing the air density and thus further decreasing the air mass flow.

(iii) Installation of a heat exhanger to heat the intake air [95].

A solution called “Power Oriented”, focusing on the conditioning of the GTCC gas turbine intake, and devoted to following just the electrical market requests, was presented within the PUMP-HEAT H2020 project [96]. Inlet conditioning has a high impact on the power generation, enhancing the operative range of the GTCC. Moreover, the effectiveness of this solution is guaranteed by the invariancy of the GTCC efficiency with the intake temperature. The proposed layout integrates the GTCC with a heat pump (HP) and a cold thermal energy storage (TES), in an approach that is OEM-independent.

Even if the HP can be used for both cooling and heating, the presence of a cold TES greatly enhances the performance of the plant. In fact, thanks to the TES it is possible to decouple the refrigeration of the inlet air flow from the operation of the HP, avoiding electric consumptions when the prices are high. Then, the TES can be charged during low electrical price periods, when the HP is being used to heat the air flow and reduce the minimum environmental load of the GTCC.

Therefore, to fully exploit the capacity of the power plant, it is necessary to design an integrated conditioning system, regulated by an advanced control system [92]. This conditioning system is expected to increase the operation flexibility of GTCC in terms of [97]:

1) power augmentation: useful during high electricity price periods (peak periods), to increase the GTCC power output (+14% during TES discharging);

2) minimum environmental load reduction (-16%);

3) off-design efficiency enhancement (ca. +1%).

The economical perfomance assessment of such system was carried out relying on a mixed-integer linear problem (MILP) optimization strategy [98], an approach that is adopted in the experimental activity to schedule the daily operation of the plant. The optimal sizing of the HP, even for a simpler integration without the TES, is highly dependent on both market and meteorological conditions [99]. However, it can be stated that an air-cooled heat pump, with an electrical consumption of 1% of the electrical combined cycle capacity (4 MWe over 400 MWe F-Class GTCC), is enough to maximize the power production in a region with temperate climate (i.e. humid subtropical climate and hot summer mediterranean climates).

Beside the system sizing, a crucial aspect of the range enhancer is related to its practical realization under the hardware and software point of view. The proposed test-rig is equipped with a complex control architecture, designed to operate within the typical time frames of electrical system services: hourly on the day ahead schedule, 15 minutes for the production profile refinements (ancillary services), and real-time for the balancing actions performed by a model predictive control (MPC).

Integrating the control system with the test-rig, it is possible to test and emulate the response of the GTCC to the electricy grid requests.

6.1 Concept and test rig description

Within the framework of the PUMP-HEAT project, the Thermochemical Power Group (TPG) of the University of Genoa, built a facility to study innovative solutions to increase flexibility of GTCCs through compressor inlet conditioning via HP (inlet heating/cooling) and coupled with a dedicated cold TES [100].

The test rig facility includes two main parts: real hardware installed in the lab and simulation software. The integration of hardware and software constitutes the cyber-physical emulator of GTCC and range enhancer.

Cyber-physical systems are widely used in academia to study complex, expensive and large energy systems in a laboratory. It is possible to find examples of cyber-physical systems devoted at emulating wind turbines [101], wave energy converters [102], photovoltaic plants [103] or even whole smart grids [104]. Over the past two decades, the TPG has gained great experience on cyber-physical systems, designing, building and operating two different fuel cell hybrid system emulators [105], [106]. On these premises, the cyber-physical approach was chosen to study the GTCC range enhancer and test its control system.

Regarding the installed hardware, it consists of a micro gas turbine (mGT), a HP, a TES, several valves, pumps and heat exchangers (HXs), as illustrated at the bottom of Figure 72. The real hardware is integrated with a data acquisition and control system, which is developed in NI Labview environment.

The top of Figure 71 displays a schematic representation of the real-time software, which emulates the GTCC. Figure 71 also shows the points where information is exchanged between software and real facility. The real-time steam bottoming cycle dynamic model [107] [108] and the control system are developed in Matlab-Simulink. The NI Labview system and the model share information in real-time through a dedicated UDP communication system (Figure 77).

The Figure 72 shows the layout of the test-rig facility, including all the components installed in the laboratory, which will be described in the next paragraph.

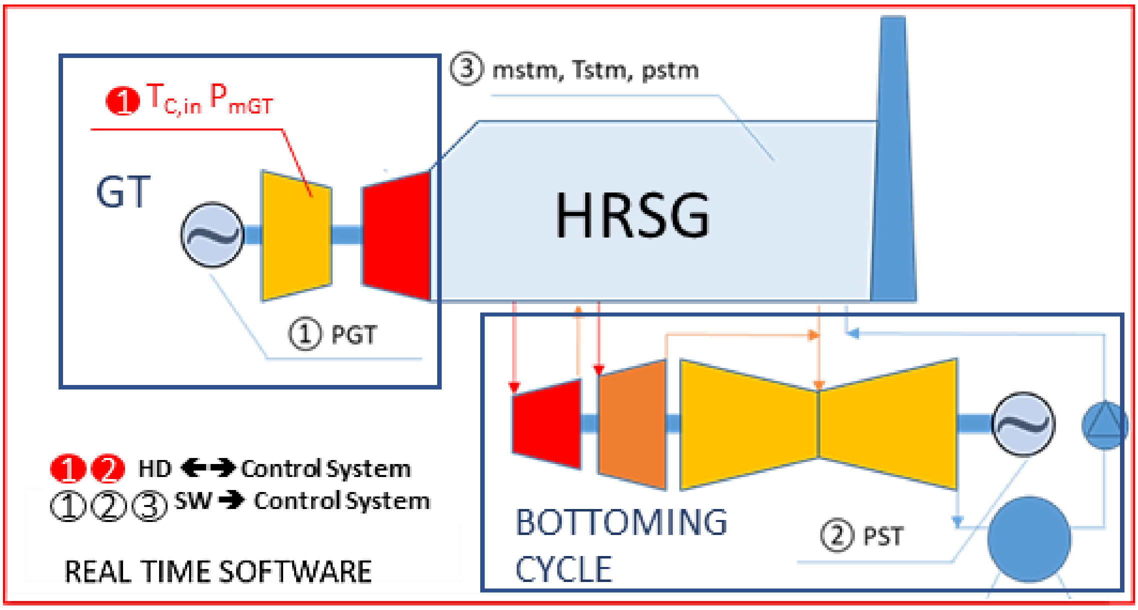

Figure 71 - THE real-time model, and exchange of information between them.

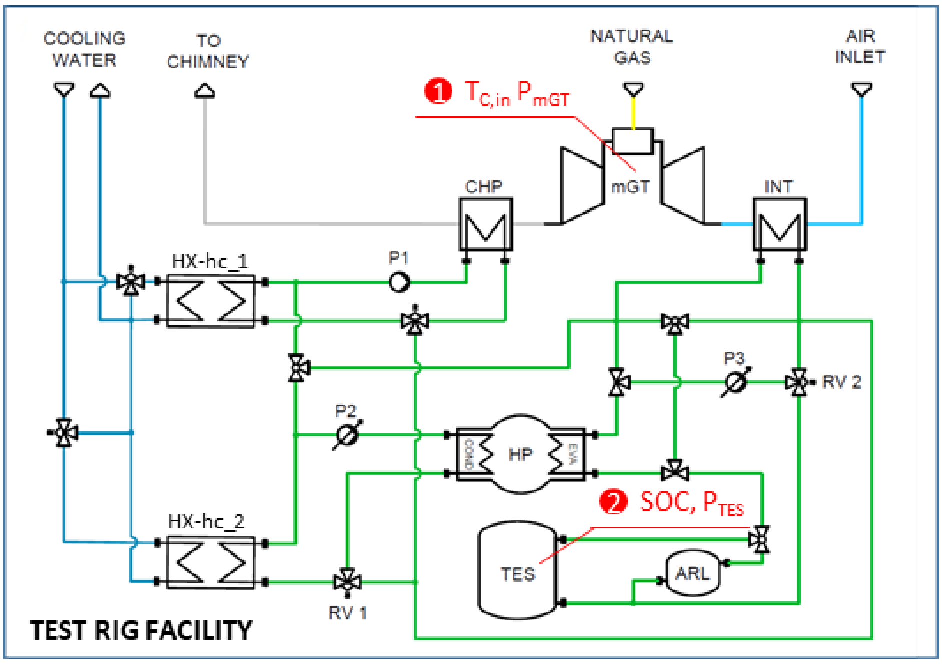

Figure 72 – THE test rig plant layout

6.2 Hydraulic circuit and operative configurations

A closed hydraulic circuit thermally connects all the hardware components installed in the laboratory. The circuit is filled with a water-glycol mixture (40%) as HTF, which would make it possible to operate at temperatures down to -30°C. However, this value is significantly lower than the real operating conditions, since the nominal temperature of the HP EVA is -6°C.

Keeping in mind the schematic layout shown in Figure 72, each operative configuration corresponds to a precise setup of all the plant components. The possible configurations of the GTCC range enhancer are identified by a FLAG parameter, which assumes the values reported here below:

- FLAG 1 – mGT only
- FLAG 2 – Continuous Cooling
- FLAG 3 – TES Discharging
- FLAG 4 – TES Charging

Each configuration is described in detail below.

6.2.1 FLAG 1 – mGT only

This configuration (Figure 73) corresponds to standard operation of the mGT, without any conditioning of the compressor intake temperature. The HP is turned off, and the TES is not involved in the operation of the plant.

The control system sends an electric power set point (SP) to the mGT, which is elaborated by the Physical Level Control System (PLCS) responsible for direct control of the mGT load. The role of the PLCS is shown in Figure 77.

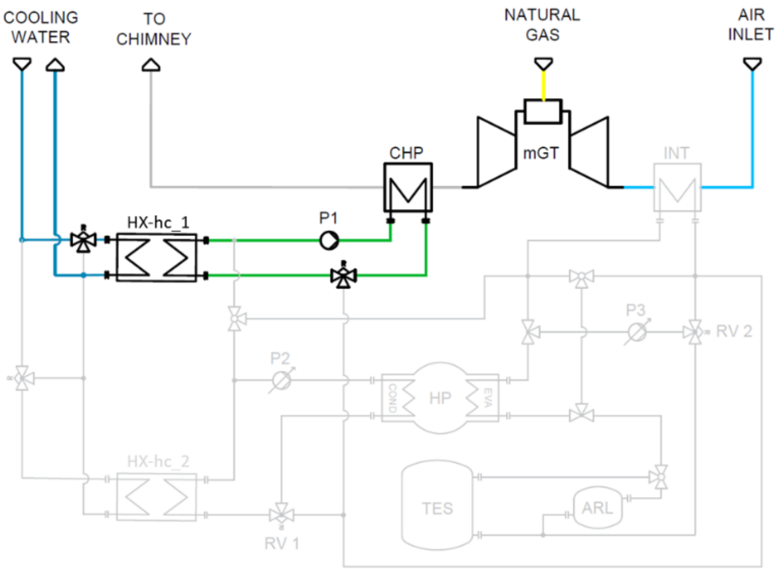

Figure 73 – mGT only configuration.

6.2.2 FLAG 2 – Continuous Cooling

In this configuration (Figure 74) the HP is turned on, as well as the mGT.

The cold thermal power generated by the HP is sent to the mGT intake in order to cool down the air entering the compressor. This configuration occurs only when it is necessary to increase the power of the mGT (e.g., when the price of electricity is high) by cooling down the compressor temperature, but the TES is empty.

Sorce et al. theoretically demonstrated that the increase of power generated by the GTCC due to the inlet temperature reduction is higher than the electric power consuption of the HP, resulting in a positive net effect [97]. This result guarantees the effectiveness of this configuration. The same behavior was observed during the experimental campaign presented in the 2nd part of this study [109].

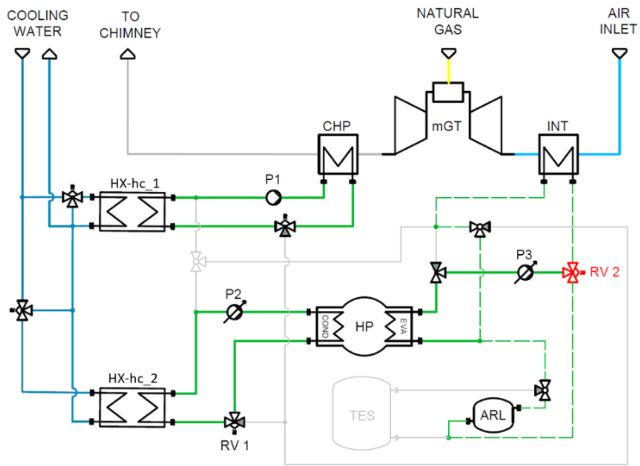

Figure 74 – Continuous cooling configuration.

The control system determines an electric power SP for both mGT load and HP load. Since the electric load of the HP is not directly controllable, the PLCS controls the proportional valve RV_2 to distribute the HTF mass flow at the HP EVA outlet. One part of the flow is sent to the compressor intake, and the other is sent to the auxiliary resistive load (ARL). In this configuration, the ARL is turned off and is only used as a thermal buffer. By regulating this proportional valve, it is possible to vary the HP EVA temperature to make the HP follow the load, while varying the mGT inlet temperature.

6.2.3 FLAG 3 – TES Discharging

In this configuration (Figure 75) the HP is turned off, while the mGT is turned on, and the $T_{C,in}$ is cooled down thanks to the circulation of water-glycol from the TES to the INT. This configuration is useful when it is necessary to increase the mGT power and the TES is not empty.

In this case, the control system sets an electric power SP for the mGT and a thermal power SP for the TES. To determine the TES thermal power SP, the control system takes into account the influence of ambient temperature at the INT on the thermal load of the TES. To provide the thermal power required by the TES, the PLCS adjusts the FT-P3 mass flow through a dedicated proportional–integral–derivative (PID) controller.

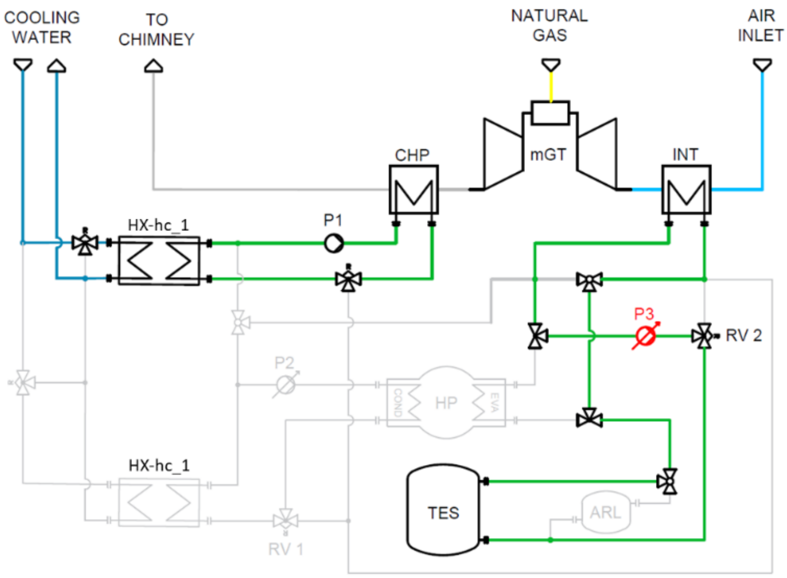

Figure 75 - TES discharging configuration.

6.2.4 FLAG 4 – TES Charging

In this configuration (Figure 76), both the mGT and the HP are turned on. The HP releases cold thermal power from the evaporator to the TES, while providing hot thermal power from its condenser to the INT. In this way, the compressor inlet temperature increases, reducing the mGT power under its nominal lower limit. This solution is expected to cause a reduction of mGT efficiency. However, as observed during the experimental tests presented in the 2nd part of this study [108], this effect is quite limited.

The control system determines an electric power SP for both mGT load and HP load. As already mentioned, the electric load of the HP is not directly controllable. The PLCS adjusts the FT-P3 mass flow to regulate the cold thermal power absorbed by the TES. This directly influences the HP evaporator temperature and, consequently, the electric load of the HP. In this configuration, the RV_1 proportional valve is also controlled.

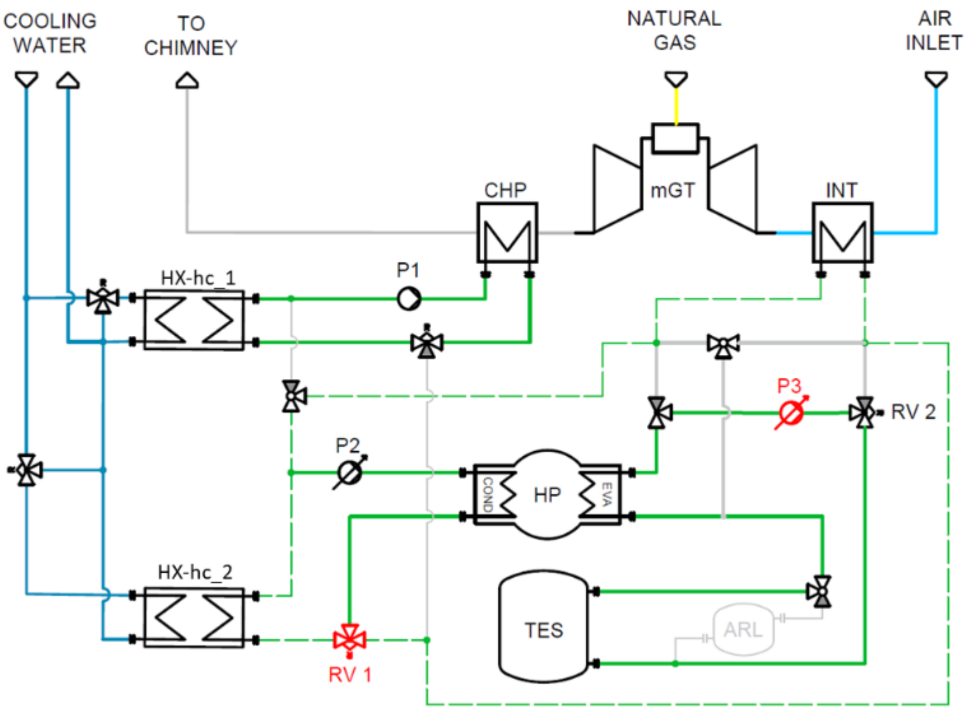

Figure 76 - TES charging configuration.

Varying the opening of this valve it is possible to regulate the mass flow entering the HE2 heat exchanger and the INT. This control action is necessary to keep the condenser temperature always under 47°C. This temperature is computed as the average between condenser inlet and outlet, with constant HTF mass flow on the hydraulic circuit side, corresponding to a condenser pressure of 4 bar(g) on the buthane side. When the condenser temperature is close to its limit, the RV_1 diverts part of the HTF flow through the HX-hc_2 to limit the temperature.

If the condenser were directly connected to the INT without the possibility of diverting part of the flow towards the HX-hc_2 exchanger, there could be situations in which the condenser temperature would exceed the operating limit (e.g. in the summer).

6.3 Control system

The control system is structured on four levels (Figure 77), operating on different sample times and time horizons, as explained in the following paragraphs.

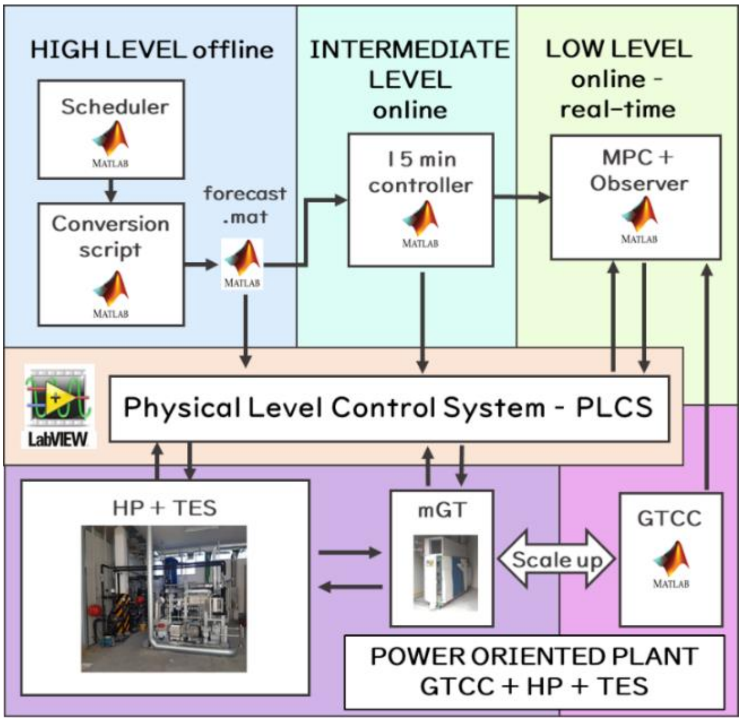

Figure 77 – Cyberphysical system: overall architecture and plant control system.

6.3.1 High Level Control System – SCHEDULER

The high-level controller is a scheduler that runs every 24 hours and optimizes the operation of the next day based on known electricity prices and forecasted ambient conditions.

The scheduler is a tool that determines the optimum operational modes of power plant for a time span of 24 hours, maximizing its operational profit. The optimum solution is found by solving an optimization problem formulated as a mixed-integer linear problem

(MILP)[110][111]. Such a problem contains several energy balances, physical and operational constraints, and linear correlations that simulate the performance of the upscaled GTCC plant (see Figure 72, top). For simplification purposes (i.e., computational time), it is assumed that the TES can absorb or release heat at a fixed rate, regardless of its temperature level. Similarly, the HP and the GTCC have been modeled with linear correlations that estimate their performance as a function of their temperature and part load operation. These correlations have been derived and verified by industrial and academic partners in the PUMP-HEAT project.

The working principle of the controller, as shown in Figure 78, consists of determining the best hourly dispatch of the GTCC (which then translates in a physical dispatch of mGT) and the operative configuration of the plant ("Outputs" in Figure 78), by optimizing the operational profits using the objective function presented in Eq. (10). This function is set to optimize the profits from selling electricity on the day-ahead market, considering electricity produced by GTCC, electricity consumed by the components of the inlet conditioning unit (ICU), cost of natural gas, carbon emission costs, O&M costs (including start-ups), hourly ambient temperature of the system location, and TES state of charge ("Inputs" in Figure 78). Table 4 summarizes the key parameters and variables defining optimisation objective function.

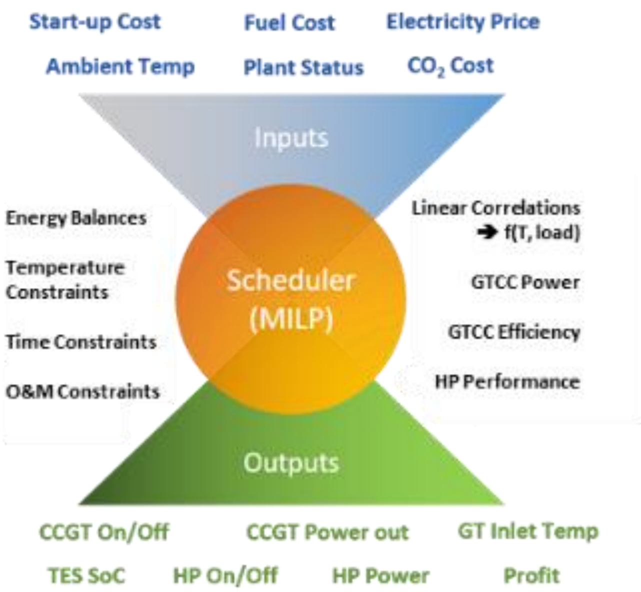

Figure 78 - Scheduler working principle

Table 4 – SCHEDULER: Key parameters for the optimisation objective function

Parameters and variables	Unit	Symbol
DAM electricity price a time t	€/MWh	pr_{el_t}
GTCC electricity production at time t	MWh	P_t^{out}
HP electricity consumption	MWh	P_t^{HP}
Gas price at time t	€/MWh	pr_{gas_t}
Fuel consumed at time t	MWh	Q_t^{fuel}
Plant hot start-up cost	€	C_{hs}
Hot start-up binary variable	-	V_t^h
Plant warm start-up cost	€	C_{ws}
Warm start-up binary variable	-	V_t^w
Cost of CO_2 emissions	€/tonCO_2	C_{CO2}
CO_2 emitted at time t	tonCO_2	CO_{2t}
Variable operating and maintenance cost	€/MWh	$O\&M_{var}$

$$\max \sum_{t=1}^{n\ hours} pr_{el_t}(P_t^{out} - P_t^{HP}) - pr_{gas_t}\left(Q_t^{fuel}\right) - C_{hs} V_t^h - C_{ws}V_t^w - C_{CO2}CO_{2_t} - O\&M_{var} \quad (10)$$

This scheduler is an adaptation of a model developed previously by the authors, presented in earlier publications [110], and used later in other studies [112]. The main difference between such a model and the one used for this study, is the scale of the components (MW vs. kW) and the presence of an mGT instead of a GTCC. The full set of constraints, as well as a detailed description of the model, lays outside the scope of this thesis but can be found in previous publications by the authors [110].

6.3.2 Intermediate Level Control System

This controller is executed every 15 minutes to correct the values of HP electric power P_{el} and plant operative condition (i.e., FLAG) determined by the high-level controller. This correction is performed by a simplex optimization algorithm [113], designed to maximize the profits of the GTCC. The simplex algorithm was developed following the methodology proposed in [114] and integrated with the GTCC dynamic model. The inputs of this algorithm are previous-day schedule, current T_{amb}, GTCC P_{el}, TES state of charge and FLAG.

6.3.3 Level Control System – MPC

The low-level control runs in real-time (1 s sample time) to regulate HP and TES at each time step (no direct interventions on the gas turbine or steam bottoming cycle are possible for the low level control). It is based on two functions: one for the model predictive control (MPC) and one for the observer. The MPC is a multi-input multi-output model-based control system, where a dynamic plant model is used to forecast the plant status along a moving predicting window, and the control outputs are obtained by minimizing a cost function J. In this case, J is based on a discrete linear quadratic regulator architecture and it has the form of Eq. (16),

$$J = \frac{1}{2} x^T Q x + u^T R u \qquad (16)$$

where Q and R are weight matrices, x is the system state and u is the control action.

The cost function is designed to minimize the error between HP electric power and its setpoint (determined by the intermediate level), and the GTCC electric power production mismatch. It forecasts the variation of GTCC power caused by HP and TES conditioning the compressor intake. The observer, on the other hand, is used to estimate the state of the system at each time step, to be fed back to the MPC dynamic model for the following iteration. The MPC algorithm of this work is based on velocity form as presented by Wang and Young [84].

6.3.4 Physical Level Control System - PLCS

The Physical Level Control System, which has been developed in NI Labview, is used to collect and elaborate all the physical signals from the plant and to control the equipment (e.g., three-way valves, proportional valves, pump inverter). It is also used to communicate with the higher control levels and translate their control signals into physical actions on the system actuators. It is also responsible for logging all the recorded data.

This control level includes many PID controllers, which are automatically activated or disabled, depending on the current plant configuration. The PID controllers were tuned using the Ziegler-Nichols [115] method, observing the response of the system to various step variations. Manual refinement was then performed to improve stability and responsiveness of each PID. The main controllers of the PLCS are described below:

- PID 1: activated for FLAG 4. It regulates the proportional valve RV_1 to send the maximum flow to INT, while keeping the HP condenser temperature at a proper value (internal SP).

For FLAG 2 this control is disabled, and RV_1 is fully open, to keep the condenser at the minimum feasible temperature and increase the machine COP.

- PID 2: activated for FLAG 4. It operates on the pump P3 speed, varying the HP load and following the SP determined by the MPC.
- PID 3: activated for FLAG 2. It operates on the RV_2 proportional valve to vary the HP load and follow the SP determined by the MPC.
- PID 4: activated for FLAG 3. It operates on the pump P3 speed to vary TES load and follow the thermal power SP provided by the MPC.

6.4 Model validation

Being based on the Iren Energia GTCC 2GT of Moncalieri, the GTCC model has been validated against historical data [88]. To ensure the proper validation of the model, a transient scenario different from the ones used to calibrate the model was selected. The information collected on 23rd April 2018 was used as input of the model (Figure 79).

The model results were compared to real data of temperature, pressure and mass flows in different sections of the plant, as well as to the power generated by the STs. For sake of brevity, only some of the most significant comparisons are included in this section. Figure 80 shows good agreement between the steam mass flow generated in the real plant and the one simulated by the GTCC model.

Observing the electric power generated by the ST (Figure 81), it is possible to verify that the model can reproduce the dynamic behavior of the ST well, despite some overestimation of the power at lower loads.

These results confirm that the time constants of the GTCC were computed correclty, and that the transient behavior of the plant can be simulated accurately. Compared to the real trend, the ST power trend shows some spikes, which are caused by noise in the input data and are expected to be reduced if the input noise is cancelled.

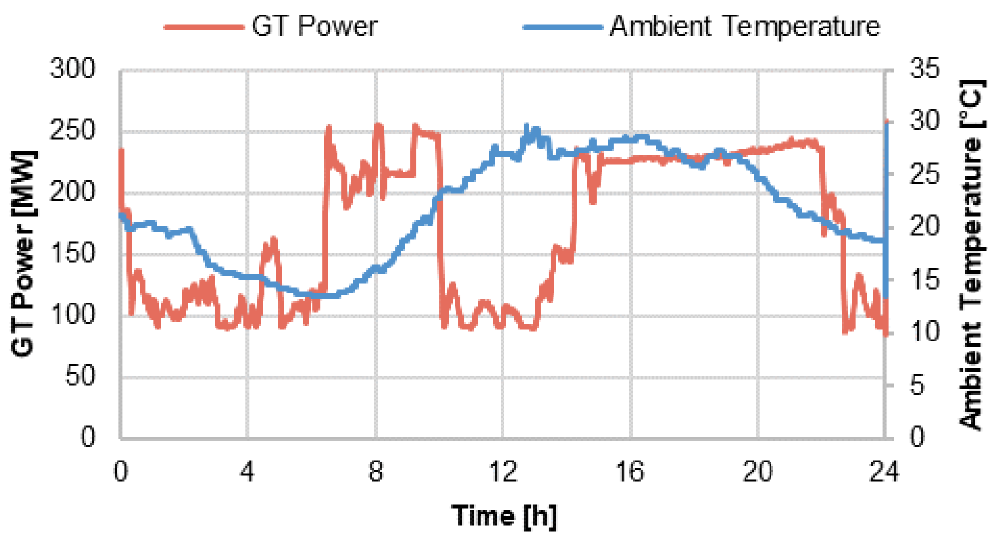

Figure 79 – Trends of GT power and T_{amb} for the 23rd of April 2018.

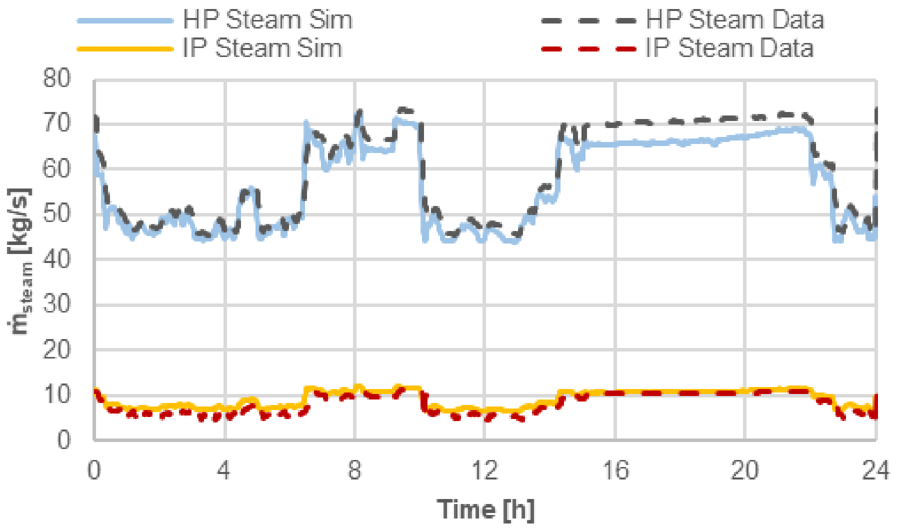

Figure 80 – Steam mass flow generated for the HPS and IPS lines, comparison between simulation results and real data.

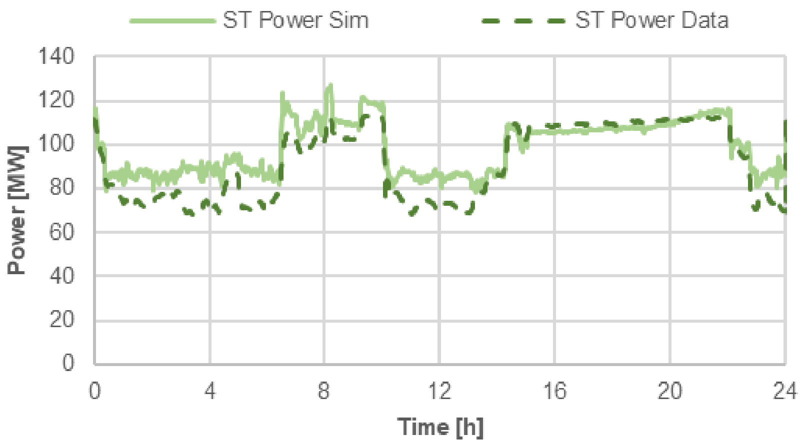

Figure 81 – Electric power generated by the ST, comparison between simulation results and real data.

It is possible to have a deeper understanding of the GTCC model precision from Table 5, which summarizes the relative errors of its most significant outputs.

Table 5 – relative errors of the most significant GTCC model outputs, averaged over time.

	SH HPS T	SH IPS T	SH LPS T	ST Pel
e [%]	0.44	0.90	2.22	4.93

	HPS $\dot{m}_{steam}$	HPS drum p	IPS $\dot{m}_{steam}$	IPS drum p
e [%]	3.66	6.20	9.02	3.71

6.5 Hardware in the loop results

To demonstrate the potential of the GTCC range extender, an 8 hour long test was designed and carried out on the test-rig.

All the measurements and uncertainties were evaluated relying on the experimental setup described in the first part of this study [51]. In this section the whole test scenario is described, and the effect of each different configuration is analyzed in details.

Figure 82 shows the full test, in terms of electric power demand, net electric power produced, scheduled and operative configuration (FLAGS).

The test starts with minimum power demand and the plant running under FLAG 1, where the GT is operated with no inlet conditioning. Due to a decrease of electric power demand, the control system changes the plant operation to FLAG 4, activating the HP. The HP condenser is connected to the INT heat exchanger to heat up the compressor intake, and effectively reduce the minimum load. Figure 83 shows the variation of electrical power absorbed by the HP, highlighting the responsiveness of the controller. During FLAG 4, the TES stores the cold energy generated by the HP; consequently, its SOC increases (Figure 84). FLAG 4 is active from 0.5 h to 2.5 h.

At the end of the TES Charge, the HP is switched off and the system is brought to full power, with a loading ramp performed entirely with no inlet conditioning, i.e., in FLAG 1. When maximum power is reached at 3.5 h, FLAG 1 is maintained for a further 0.75 h. Then, the control system activates TES Discharge (FLAG 3) at time 4.25 h. This phase demonstrates how the maximum power output of the GTCC can be increased by exploiting the cold energy that was previously stored in the TES. Figure 84 shows the trend of thermal power provided by the TES and its SOC.

When the TES is fully discharged (after 6.25 h), the FLAG automatically changes from 3 to 2, activating Continuous Cooling configuration and turning on the HP (Figure 83). FLAG 2 is a backup configuration, which can be used when the power demand is still high, but the TES is empty. This can be better understood looking at Figure 82, where the operative FLAG is not consistent anymore with the scheduled FLAG. FLAG 2 is maintained until the end of the test.

Figure 85 shows the direct impact of the FLAGS 4-3-2 in terms of inlet conditioning, highlighting the temperature increase and decrease with respect to the ambient temperature.

Figure 86 shows the different power contributions of the GTCC, displaying separately the power generated by the gas turbine and by the components of the steam bottoming cycle.

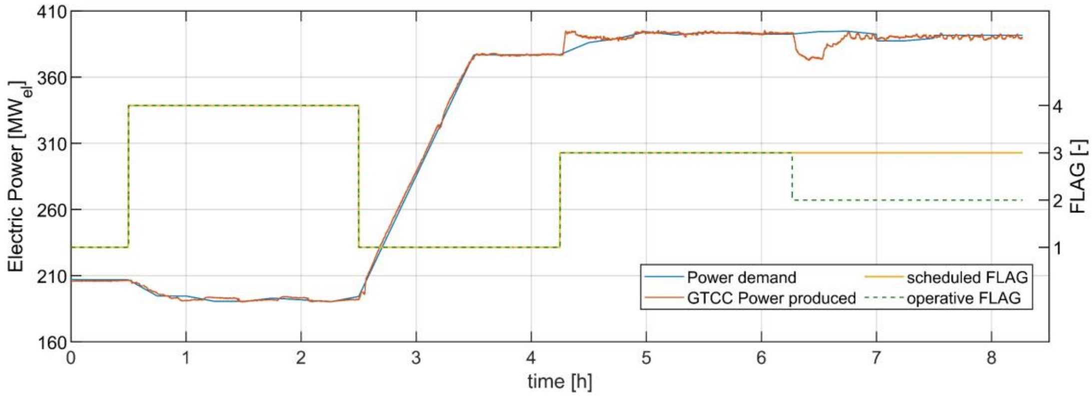

Figure 82 – GTCC Electric power TRENDS during the full day test.

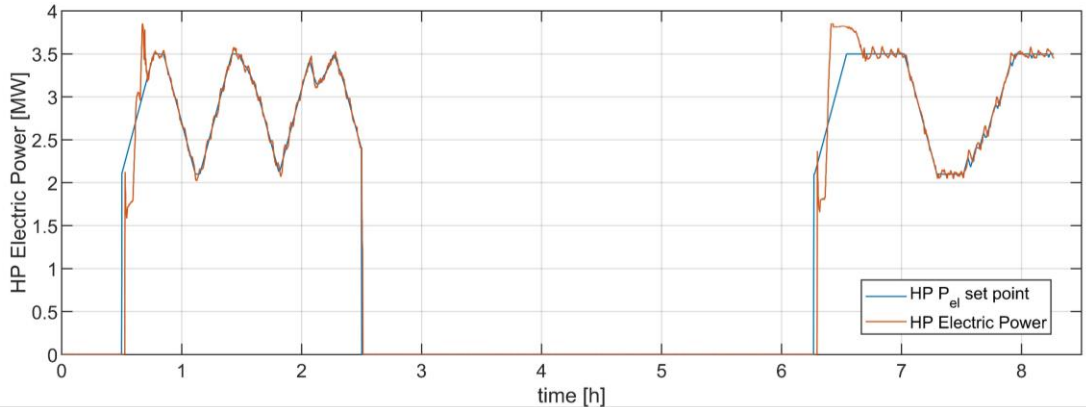

Figure 83 – HP Electric load TREND during the full day test.

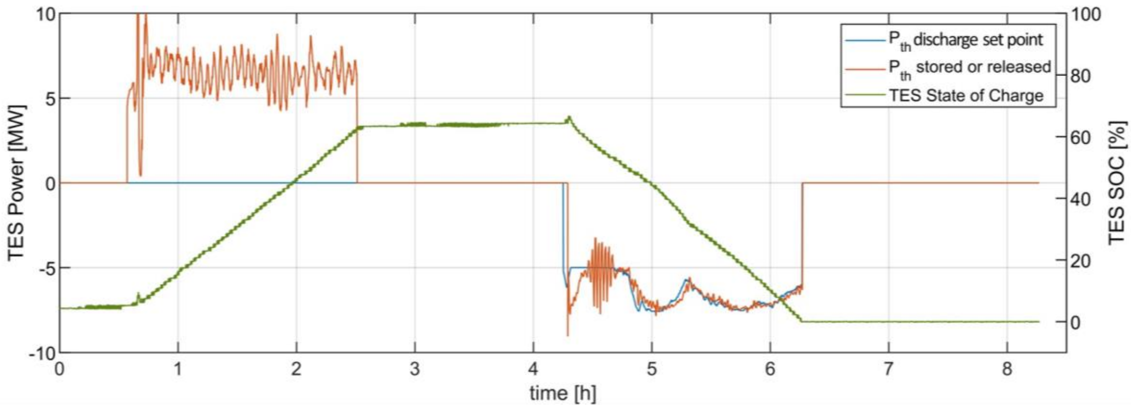

Figure 84 – TES thermal power TRENDS during the full day test.

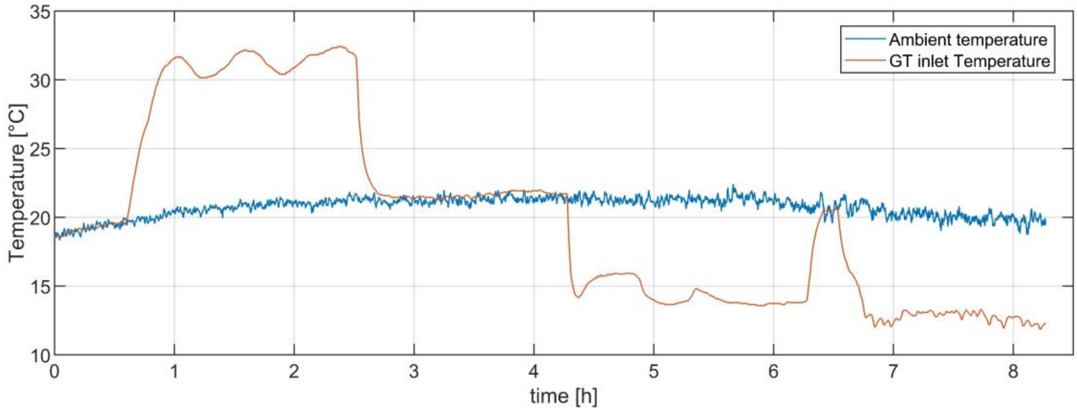

Figure 85 – Comparison between ambient temperature and compressor inlet temperature.

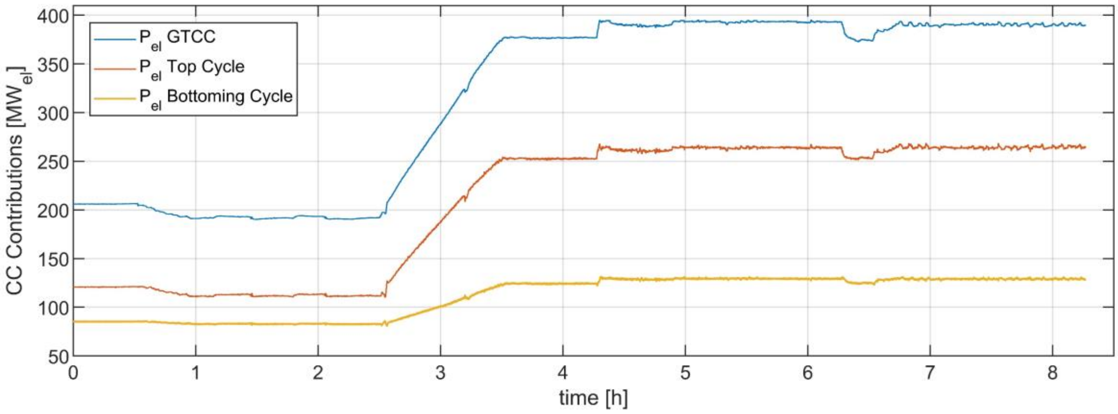

Figure 86 – Emulated GTCC POWER SHare during the full day test.

6.5.1 TES Charge – FLAG 4 analysis

As already introduced in the previous section, the first part of the test, between 0 h and 2.5 h, was designed to validate the range extension potential below the minimum environmental limit by turning on the HP to warm-up the compressor inlet. This is a very efficient configuration because all the energy flows converge for the same purpose, i.e., to reduce the GTCC load, and there are no parasitic effects as in the case of Continuous Cooling. In details, the heat flow leaving the condenser is introduced into the cycle, reducing the GT specific power, and consequently the GT load, while the electric power absorbed by the HP contributes to a further reduction of the net power of the plant. Moreover, the cold energy produced by the HP is not wasted, but stored in form of latent heat into the TES. Since the condenser is connected to INT, the ambient temperature indirectly influences its temperature (and thus its pressure), affecting the COP of the HP. However, the additional consumption of electric power by the HP to charge the TES occurs when the price of electrical energy is low, with minimum effect on the economic profitability of the plant.

Figure 87 shows a detail of the first hours of this test. During the first 30 minutes, the plant was operated at minimum load, around 206-207 MW, in accordance to [51] [85]. At 0.5 h, the electric power demand is reduced, and the control system changes plant configuration accordingly, switching from FLAG 1 to FLAG 4. The transition between FLAGs took some time because it was necessary to turn on valves, activate circulation pumps (around 2 minutes) and turn on the HP, which is the most critical and time-demanding process, requiring 12-15 minutes. In fact, before considering the FLAG 4 configuration as fully operative, the HP must reach a regulating condition, i.e., it is necessary to wait for the evaporator to reach -6°C and then to activate the dedicated PID (described in the first part of this study [3]).

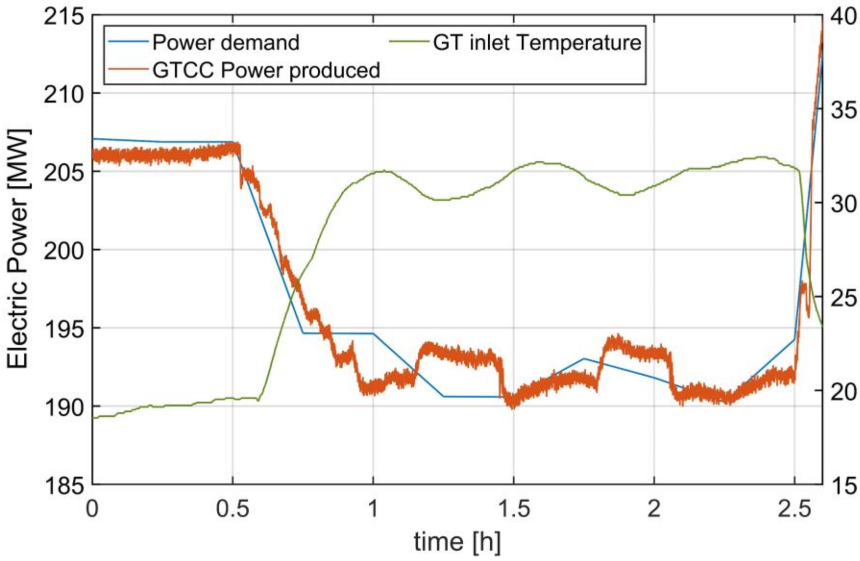

Figure 87 - net power produced with setpoint and GT inlet temperature during FLAG 4

This start-up process can be analyzed in Figure 88, where all the mismatches between HP electric load setpoint and the real HP load are concentrated between 0.5 h and 0.7 h, during a period of ~15 minutes corresponding to the configuration change and the HP start-up ramp. Except for this first part, the HP indirect controller described in [51] works properly and allows the HP to follow the load adequately, as shown in Figure 88.

Figure 89 shows the thermal power trend and the SOC of the TES. The variation of electrical power required by the HP is controlled indirectly by varying the HTF flow rate. For this reason, the power absorbed by the TES shows some oscillations, which are related to the flow rate variations made by the PID. The SOC grows linearly by about 60% in this first phase, and it is not significantly affected by thermal power fluctuations.

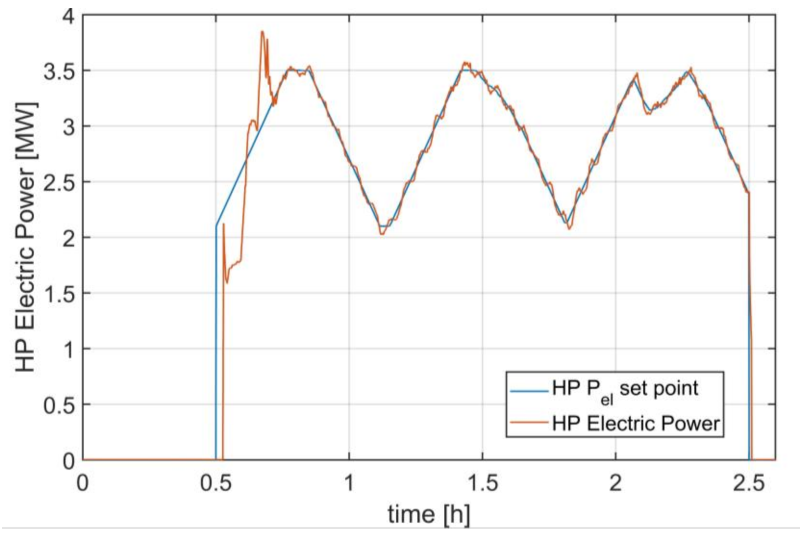

Figure 88 - HP Electric load and its setpoint during FLAG 4.

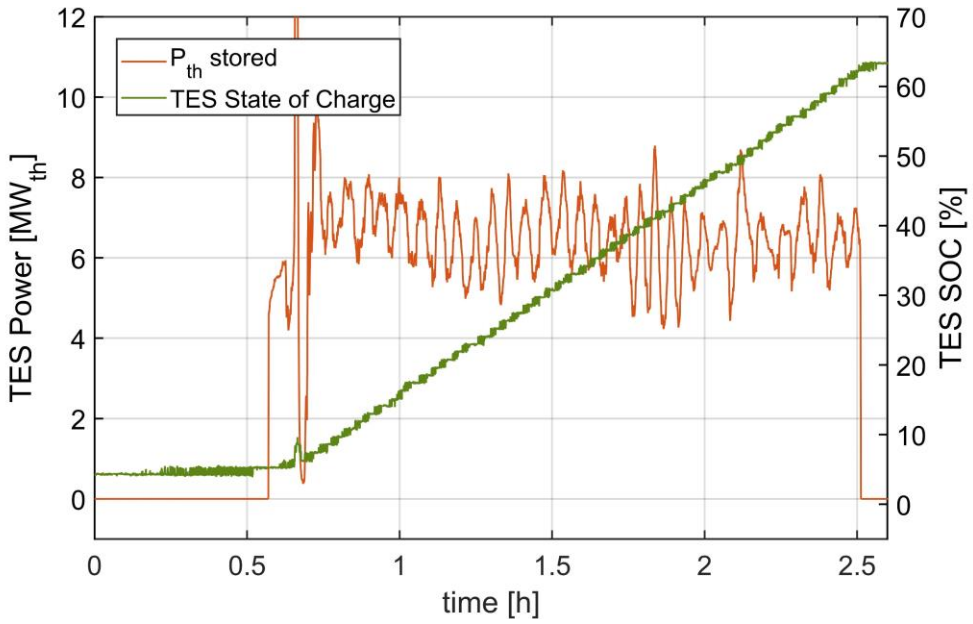

Figure 89 - TES SOC and thermal power during FLAG 4.

The hot thermal power generated at the HP condenser is transferred to the GT intake. The effect of temperature increase at the GT inlet is clearly visible in Figure 87, where the temperature increases from-20°C to-32°C. It can be noted that the plant was not able to perfectly match the demand. This is caused by the thermal capacitance of the physical components, in particular of the INT heat exchanger.

Moreover, the minimum load curve of the test-rig mGT was identified as the set of the operative points where the mGT internal controller switches from a constant speed logic to a $T_{T,out}$ constant logic. Therefore, varying the inlet temperature when the turbomachinery is close to this condition, the mGT changes for some minutes its control logic. Consequently, there are some sudden changes of the net power generated by the mGT, which can be observed at 1.1 h, 1.4 h, 1.8 h, 2.1 h in Figure 87. A possible way to avoid such disturbances would be to operate the mGT far from its lower limit.

From 1 h to 2.2 h, the mismatch between power demand and power produced by the GTCC had an average value of 0.715% (relative to power demand). The mismatch between HP set point and HP electric load was instead equal to 1.24% (relative to HP set point).

6.5.2 TES Discharge – FLAG 3 analysis

The TES Discharge phase is used to increase the maximum power output of the combined cycle, in order to exploit the cold thermal energy previously stored in the TES. As shown in Figure 90, right after 3.5 h, the system is operating under FLAG 1 and the GT is working at maximum load. In this condition, the GTCC is generating an electric power of 376 MW, in agreement with [3]. At time 4.25 h, the electric power demand increases, and the FLAG is changed from 1 to 3. This is possible because the TES is not fully discharged, otherwise FLAG 2 would have been set. The start-up phase of the TES power control goes up to about 4.5 h, taking about 15 minutes, as shown in Figure 91. The control takes quite a long time to increase the power provided by the TES because it reacts to changes in the HTF flow rate as a second order system. At 4.5 h the PID parameters were deliberately changed to make the control unstable, resulting in power fluctuations. This procedure was done to evaluate the influence of these oscillations on the plant power production. As shown in Figure 90, the fluctuations do not lead to changes in the power output of the combined cycle, probably because they are damped by the large thermal capacitance of the INT exchanger and its hydraulic circuit.

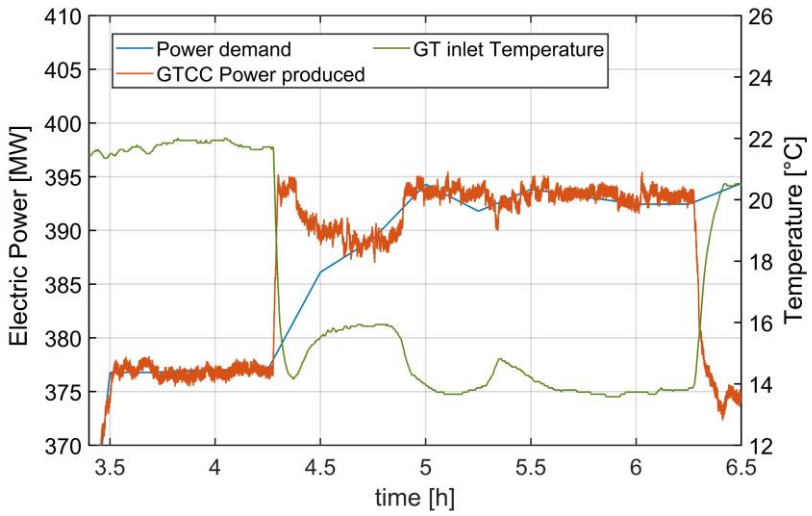

Figure 90 - net power produced with setpoint and compressor inlet temperature during FLAG 3.

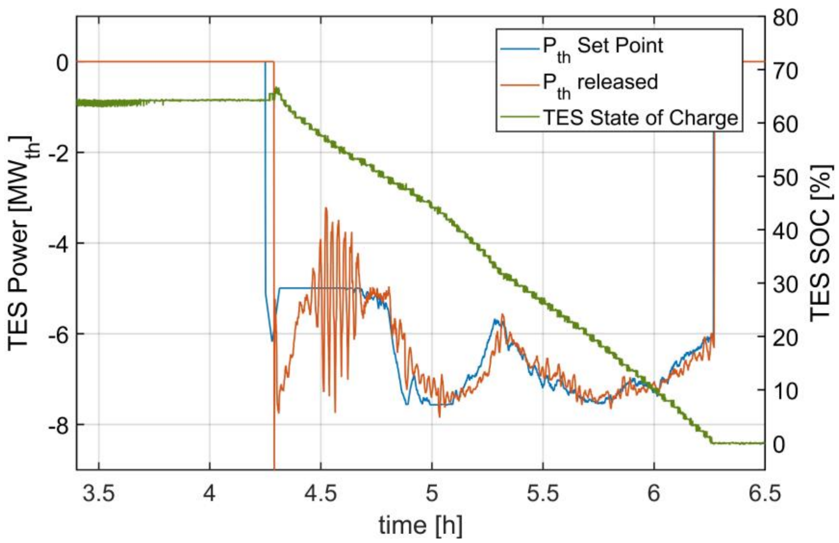

Figure 91 – TES SOC, TES thermal power Set Point and thermal power released during FLAG 3.

At 4.7 h the parameters of the controller were reset to their original values, and the TES power demand was again followed with good accuracy, showing only a small lag due to the complexity of the TES system. Figure 90 also shows the large temperature reduction at the

GT caused by the cold thermal power released by the TES. The compressor inlet temperature drops from 22°C in FLAG 1 to 14-16°C in FLAG 3, depending on the power required at the TES. The TES Discharge phase ends at 6.25 h, as soon as the minimum TES Charge level is reached (Figure 91). From 4.8 h to 6.2 h (after the initial TES power oscillations) the mismatch between power demand and power produced by the GTCC had an average value of 0.19% (relative to power demand). The average mismatch between TES thermal power and its set point was instead equal to 3.4% (relative to TES thermal power set point).

6.5.3 Continuous Cooling – FLAG 2 analysis

The Continuous Cooling phase is activated when the power demand is still high, but the TES is empty. In fact, this phase starts exactly at the end of the TES Discharge (6.25 h). As visible in Figure 82 and shown in Figure 92, the start-up of the HP takes approximately 15-20 minutes, because of the technical time required by the HP itself and the fact that the entire auxiliary resistive load (ARL) circuit must be pre-cooled. Since only one circulation pump (P3) is used to regulate TES and HP evaporator load, it was not possible to turn on the HP and let the ARL circuit reach the proper temperature before stopping draining cold energy from the TES. This highlights the necessity to include an additional circulating pump to serve exclusively the TES, in order to uncouple these two operative conditions (HP startup and TES Discharge).

In this configuration, the ARL is used as a thermal buffer, as explained in the first part of this study [51]. During this start-up phase, the HTF flow rate to the INT exchanger is zero and the HP is set to maximum power to speed up the cooling of the ARL circuit. As shown in Figure 93, during this period, the GTCC maximum power returns to its nominal value. Shortly after 6.5 h, the flow to the INT starts growing, cooling the air entering the GT. The cooling transient of the INT ends approximately at 6.75 h. When the HP is at maximum power, the power output of the combined cycle is less stable. This behavior is related to the physics of the system. In Continuous Cooling, a large variation of flow rate to the INT is required to change the outlet temperature of the HP evaporator. To reduce the HP load, the flow rate to the INT is reduced to almost zero, resulting in a temperature increase at the INT. To increase the HP load, the flow rate to the INT is increased significantly, causing a temperature reduction at the INT. This process causes the small fluctuations in GT inlet temperature and generated power shown in Figure 93. For higher ambient temperatures, a smaller flow rate variation would probably be required to achieve a similar variation in the HTF temperature at the evaporator outlet.

Figure 93 clearly shows that, regardless of these fluctuations, the power generated by the GTCC does not vary significantly, remaining always around 390 MW, while the HP power changes (Figure 92). In fact, both the electrical power absorbed by the HP and the power generated by the GT increase or decrease at the same time, causing minimum variations of the GTCC power output. The increase of COP when the HP is running at low power (i.e. low rotation speed, as described in [3]) should also be considered.

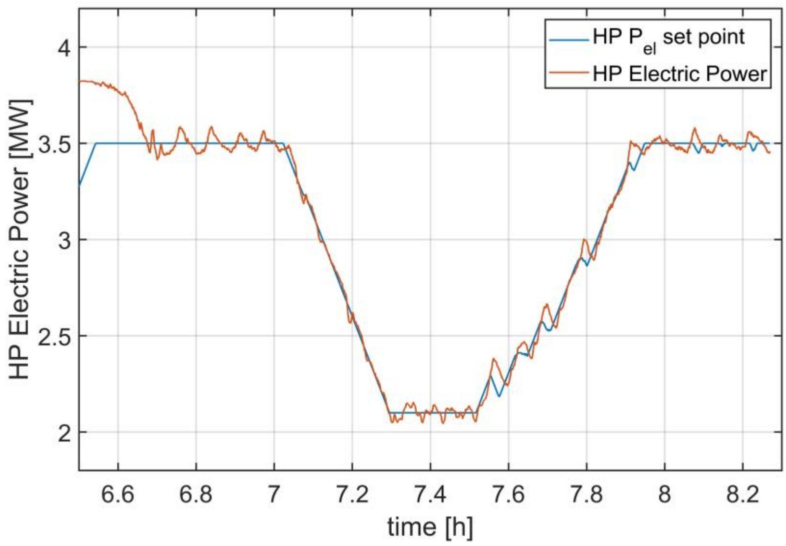

Figure 92 - Actual HP Electric load and its Setpoint during FLAG 2.

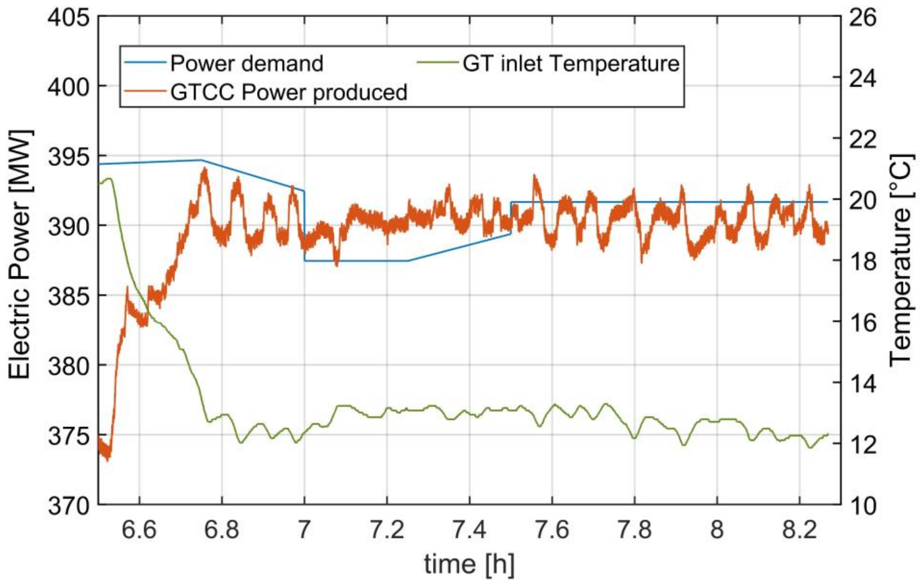

Figure 93 - net power produced with setpoint AND compressor INLET TEMPERATURE during FLAG 2.

In fact, this phenomenon is reason why the heat output at the evaporator does not vary significantly and so does the temperature at the GT inlet. The GT inlet temperature goes from 21°C to 12-13°C in this configuration, then remains approximately constant throughout the duration of the FLAG, despite the change in HP load.

An effective strategy for adopting Continuous Cooling could be to operate the HP at a fixed point, corresponding to its highest COP. However, it is possible that heat pumps with a wider operating range may give better results in regulation.

From 6.8 h to 8.2 h, the mismatch between power demand and power produced by the GTCC had an average value of 0.52% (relative to power demand). The average mismatch between HP set point and HP electric load was instead equal to 1.1% (relative to HP set point).

6.5.4 Comparison with Business as Usual

This section shows a comparison between the performance of a GTCC with and without the range enhancer proposed in this article. All the parameters are compared for inlet heating (TES Charge – FLAG 4), inlet cooling (TES Discharge – FLAG 3) and continuous cooling – FLAG 2).

Inlet heating

In Figure 87, it is possible to observe the effect of inlet heating comparing the behavior of the system before 0.5 h and between 1 h and 2 h. Inlet heating lowers the GTCC minimum environmental load and reduces its fuel consumption (-4.7%). When the price of electrical energy is low, this has a double beneficial effect, reducing the variable costs of the plant and its pollution emission [97].

Making an estimate of the different effects contributing to the minimum load reduction, about 80% is caused by inlet heating, while the remaining 20% is related to the power consumption of the HP (3 MWel on average).

Table 6 shows the comparison between the performance of the plant without and with inlet conditioning. The percentage difference with the business-as-usual configuration is displayed between brackets for each specific parameter.

Table 6 – Effect of the Inlet Heating+TES Charging at minimum load.

	Business as usual	Inlet Heating + TES Charge
Compressor intake temperature [°C]	20.9	32.1
Net power [MW_{el}]	205.5	190.4 (-7.4%)

Fuel consumption [kg/s]	8.5	8.1 (-4.7%)
Global efficiency [%]	50.4	49.0 (-2.7%)

Inlet cooling

The effect of the intake cooling is shown in Table 7. Also in this case, the percentage difference with the business-as-usual configuration is displayed between brackets for each specific parameter. Thanks to the reduction of intake temperature, the GTCC can generate an extra 17.5MW during TES discharge. When the HP is used for inlet cooling instead, the extra production is equal to 13.4 MW, with an auxiliary systems consumption of 2.2 MW. As already explained, the variation of the HP set point and load does not affect the net power produced by the plant. Consequently, a good operative strategy would be to keep the HP at minimum load in Continuous Cooling mode.

Table 7 – Effect of TES discharge and of continuous cooling at maximum load.

	Business as usual	Inlet cooling	
		TES Discharge	Continuous Cooling
Compressor intake temperature [°C]	21.2/ 20	13.8	12.9
Net power [Mw_{el}]	377.0	394.5 (+4.6%)	390.4 (+3.6%)

Fuel consumption [kg/s]	13.9	14.5 (+3.9%)	14.5 (+3.9%)
Global efficiency [%]	56.3	56.7 (+0.7%)	56.1 (-0.4%)

This impacts directly on the global efficiency of the GTCC, which gains 0.4 percentage points during TES discharge and loses 0.6 percentage points in Continuous Cooling.

6.5.5 GTCC enhance final conclusions

The cyber-physical GTCC emulator introduced in [51] was successfully operated in various conditions thanks to the high complex EMS, and its performance was deeply analyzed. Relying on scale-up equations, it was possible to create a relationship between the behavior of the devices in the laboratory (mGT, HP and TES) with the components of a simulated heavy-duty plant. The integration of the real components with a dynamic model of the bottoming cycle made it possible to emulate a full GTCC in a laboratory environment and to test the range enhancer on it.

The experimental campaign, which was designed to activate all the possible plant configurations, showed the effectiveness of the proposed four-levels control system. The proper FLAGs were scheduled for all the test duration, reducing the compressor intake temperature to increase the maximum power generation of the plant, while heating the intake when it was necessary to reduce the minimum environmental load of the GTCC. The control system also showed good adaptability to the current operative conditions, switching from TES discharge to inlet cooling in case of fully discharged TES.

The GTCC range extender developed for the PUMP-HEAT project could be easily adapted to other systems. In fact, it is regulated by an independent control system, and it requires minimum alterations of the pre-existent components. Thanks to these features, it could be tailored both for GTCCs and GTs, being included in the layout of new plants or integrated with existing facilities to improve their flexibility and provide a competitive advantage on the energy market.

The cyber-physical approach for the emulation of GTCCs could be adopted by other researchers, making it possible to study heavy duty plants in a laboratory environment. Hopefully this will help the development of technological solutions and control strategies aimed at increasing the flexibility of GTCCs, making them a key element towards decarbonization.

Analyzing the results presented for this study, and conducting additional experiments, it will be possible to characterize the real behavior of the devices installed in the laboratory, in particular mGT, HP and TES. The dynamic model will be then calibrated on the available data, in order to minimize the error between simulations and experimental tests. For this purpose, it will be necessary to determine the exact time constants of the main physical phenomena and to accurately model the effect of the various inlet conditioning strategies on the turbomachinery. Thanks to the high accuracy of the model, it will be possible to test the plant and its control system also in a a model-in-the-loop setup. In this way, the performance of the plant will be easily evaluated on multiple scenarios, providing a more deep understanding of the GTCC range enhancer.

7 Appendix 2 - EMS concept application for buildings thermal grid

To achieve the objectives set in the European Green Deal by 2050 [50] in terms of reduction of CO_2 emissions, ENVISION project proposed a new way to harvest solar energy from all building surfaces, integrating them in a polygeneration micro-grid having optimized EMS. Solar façade panels working by absorbing the invisible part of the solar radiation, the near infrared (NIR) one, constituting roughly the 50% of the solar energy spectrum have been realized in the framework of this project [116]. The panels have been installed at the Savona Campus which is the 'ENVISION' Southern Demosite and, to exploit in the best way the harvested energy, the NIR panels has been coupled with other components to give rise to an integrated system able of satisfying part of the thermal and electrical demand of the Campus. The system composed by façade panels, a micro-gas turbine, an innovative heat pump, two thermal energy storages and thermal dissipators, in fact, it is also connected to the Campus district heating network and to the Campus microgrid. The system dynamic model development and validation is a crucial point to be able to define the proper plant sizing and management depending on the site installation and its characteristics (e.g. square meters surface available, orientation, thermal demand etc.). A schematic representation of the system is reported in Figure 94 which shows the working principle: the integrated system configuration requires the solar façade panels to be connected to the heat pump that works as a temperature booster in order to guarantee the temperature required by the DHN. The heat pump is equipped with a Tesla turbine, installed in parallel with the isenthalpic valve allowing to operate in two possible configurations: the traditional one or the "high-efficiency" one in which the Tesla expander produces mechanical power increasing the HP COP [117]. A 5000 l thermal energy storage is also present to mitigate solar fluctuations on the heat pump and a CHP unit (100 kWe/160 kWth micro–Gas Turbine) to provide both electric and thermal power. Another 5000 l thermal energy storage is installed to guarantee one more degree of freedom in the management of both thermal and electric demand. Even more, thermal dissipators are present to allow tests to be conducted even when the plant is not connected to the DHN.

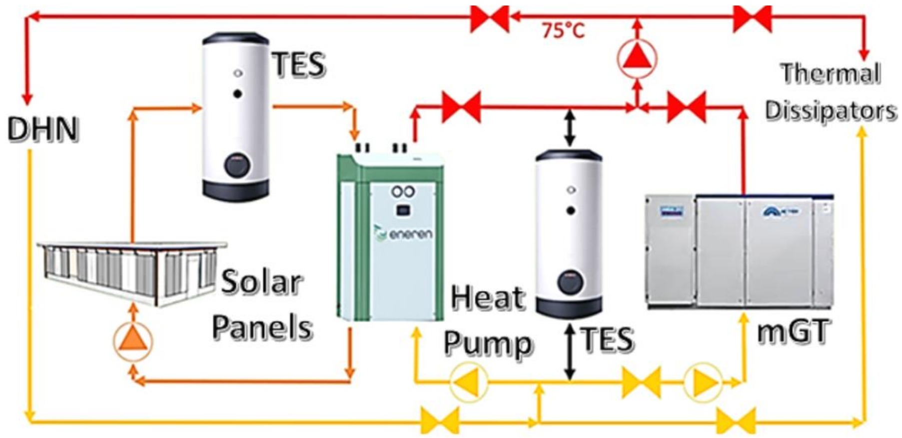

Figure 94 - *ENVISION Southern Demo simplified layout*

7.1 Experimental set-up

The performance of the realized novel integrated system has been evaluated trough a dedicated experimental campaign carried out on test-rig both in static and dynamic conditions. A simplified layout of the plant is shown in Figure 95, where all the main components and sensors are reported. The system has a double ring configuration which allows the connection to both the hot and cold side of the Campus DHN, but also to thermal dissipators to test the plant independently from the DHN constraints i.e., the fan coils can emulate different profile of thermal demand without the season constraints that, instead, characterize the DHN.

The aforementioned DHN has been developed in 1992 and, being a third generation one, requires hot water at about 75/80°C, whereas the return water temperature is ca. 50°C. The prototype panels have been designed to be installed in new buildings equipped with fourth generation DHN requiring significantly lower operating temperatures. The maximum water temperature coming out from the panels is about 45°C and, therefore, the integrated system configuration needs the NIR panels to be connected to the HP which works as a temperature booster to increase the water temperature to that required by the Campus DHN. Moreover, between the façade panels circuit and the HP, a Low-Temperature Thermal Energy Storage (L-TES) is present; L-TES is crucial to prevent sudden changes in the panels water outlet temperature due to solar fluctuations, force the HP to work in strong off-design conditions. The HP COP, in fact, is strictly related to the evaporator water inlet temperature (i.e., solar panels circuit outlet water temperature), the lower the temperature the lower the COP. The mGT is also integrated into the system, providing both electric and thermal energy when used in Combined Heat and Power (CHP) mode (100 kWe/160 kWth). Lastly, the High-Temperature Thermal Energy Storage (H-TES) is installed to ensure a better management of the system, limiting CO_2 emissions; the main aim of H-TES, in details, is to store the thermal energy produced in excess during the daytime, when the RESs are at peak, to satisfy the night thermal load avoiding further start-up of the mGT. H-TES is also used, in combination with the mGT, to cover the peak thermal load that usually occurs in the early morning when the buildings heating system is turning on.

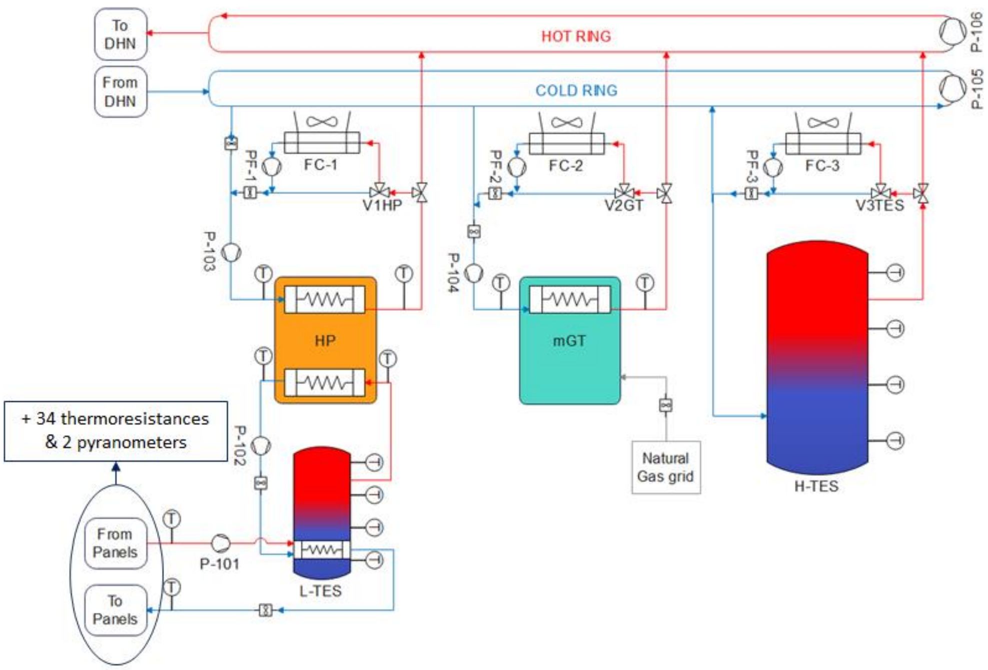

Figure 95 - ENVISION P&ID

The plant has been properly sensorized with the purpose of evaluate the thermal/electrical energy produced by the single component and the corresponding device efficiency: i) each panel couple has been equipped with two thermoresistance and one mass flow meter ii) two pyranometers have been installed to correlate the panels thermal power production with the corresponding incoming solar energy iii) for both TESs, four temperature measuring points at different heights have been foreseen to continuously evaluate their State Of Charge (SOC) together with inlet and outlet mass flow meters iv) on both HP evaporator and condenser, thermoresistances and mass flow meters to acquire water flow data have been placed, whereases the internal control system of the HP provides the data related to the refrigerant fluid (R134a) v) for the mGT, the measurement of rotational speed, Turbine Outlet Temperature (TOT) and electrical power produced are acquired by the machine control system whereas gas flow meter and thermoresistances have been installed to monitoring the fuel consumption and the inlet/outlet water temperature at the water-gas heat exchanger side respectively. The used sensors are summarized in Table 8.

Table 8 - List of Sensors

Physical quantity	Manufacturer and model	Accuracy
Thermoresistance	TC Direct PT100	±0.15 °C at 0°C
Pyranometer	Soluzione Solare PYR1-420	±0.2%
Mass flow meter	FLS F3.00.H	±0.5 %

7.2 Component modelling and validation

7.2.1 Solar façade panels

The novel solar façade panels have been developed with the aim of extending the absorption capacity of the collectors to the NIR field, which roughly cover the 50% of the total solar energy spectrum. The panels can be realized in different shapes and colors depending on the needs and, contrary to conventional panels, can have light and bright colors; for this reason, the 'ENVISION' panels are suitable to be applied to the whole building façade greatly increasing the available heat exchange surface and, in the meanwhile, maintaining a pleasant aesthetic appearance. Even more, the panels can be connected either in series or in parallel, depending on the temperature and the flow rate required, without any technical limitation imposed by the geometric configuration of the building.
In the test rig here investigated a total of 34 panels have been installed of which 24 grey and 10 white. Couples of panels of the same colors have been connected in series resulting in 17 panel couples. Then, each couple has been connected in parallel to be able to individually evaluate the performance depending on the color, the position, and the variation of solar radiation. In fact, since the surface color is the parameter that mostly affects the panel performance, it is fundamental to evaluate and compare the thermal energy produced by

both panels subjected to the same solar radiation profile. All the panel couples are connected to two manifolds: the inlet manifold at a low temperature and the outlet one at a higher temperature. The manifolds connect the panel circuit with the L-TES and the recirculation of the working fluid is guaranteed by a 0.55 kW pump.

The solar façade panels have been installed according to following orientation:

9 panels couples are South – West oriented.

3 panels couples are South oriented.

5 panels are South – East oriented.

The 5 panels couples that have been installed South – East oriented have been placed 2m far from the perimeter wall of the Campus which is a concrete wall about 2.5m high. This choice allows the panel performance related only to the NIR to be evaluated since, in that area, the panels are in shadow and never receive radiation in the visible field (with only the exception of 1h between 10 a.m. and 11 a.m.). The panels which have been installed in South and South – West position instead are directly exposed to the solar radiation and for this reason, a pyranometer on each side has been installed. In this way, it has been possible to correlate the increase in temperature between the inlet and outlet section of each panel couple with the corresponding solar radiation at a given time.

The technical configuration and operative data of the 'ENVISION' panels are summarized in Table 9.

Table 9 - Solar Façade Panels Data

Color		
Grey	Nr.	24
White	Nr.	10
Technical Data		
Material	Copper	/
Fluid Type	Water + 30% Glycol	/

Mass Flow Rate for Panel Couple	0.36	kg/s
Operating Pressure	1-2	Bar

Figure 96 - *'ENVISION' Solar Façade Panels*

The maximum electrical and thermal power production and the maximum efficiency as a function of the ambient temperature have been defined through the following equations:
If the ambient temperature is higher than 10°C:

$$\eta_{max} = poly1(1) * T_{ambient} + poly1(2) \tag{16}$$

$$Pel_{max} = poly2(1) * T_{ambient} + poly2(2) \tag{17}$$

$$Pth_{max} = poly3(1) * {T_{ambient}}^3 + poly3(2) * {T_{ambient}}^2 + poly3(4) * T_{ambient} + poly3(4) \tag{18}$$

If the ambient temperature is lower than 10°C:

$$Pel_{max} = 100 * 1.075 \text{ [kW]} \tag{19}$$

$$\eta_{max} = 1.025 * 0.3 \text{ [-]} \tag{20}$$

Where:

η_{max}[-]: mGT maximum efficiency.

Pel_{max}[kW]: mGT maximum electrical power.

Pth_{max}[kW]: mGT maximum thermal power.

$polyn(m)$[-]: m-th value of polynomial n.

$T_{ambient}$[K]: ambient temperature.

Considering the mGT maximum electrical power equal to the real power provided by the machine, the real efficiency (η), the real natural gas mass flow rate (m_{fuel}) and the real thermal power (Pth) are then calculated depending on Pel_{max} and $T_{ambient}$ by using again polynomial correlation keeping in consideration the correction factor provided by the manufacturer:

If $perc_{power}$ > 0.2:

$$m_{fuel} = perc_{power} * \frac{Pel_{max}}{LHV * \eta} \tag{21}$$

$$Pth = (poly3(1) * T_{ambient}{}^3 + poly3(2) * T_{ambient}{}^2 + poly3(3) * T_{ambient} + poly3(4)) * (poly4(1) * perc_{power} + poly4(2)) \tag{22}$$

$$\eta = \eta_{max} * poly5(1) * perc_{power}{}^3 + poly5(2) * perc_{power}{}^2 + poly5(3) * perc_{power} + poly5(4) \tag{23}$$

Where:

$perc_{power}$[kW]= $\frac{Pel_{max}}{100}$

LHV=natural gas lower heating value.

If $perc_{power}$ < 0.2 the equations are the same as before with $perc_{power} = 0.25$.

The validation of this model is reported in Fig. 12 where the blue line represents the model data and the black dotted one the experimental ones. Also in this case, the model can be considered successfully validated.

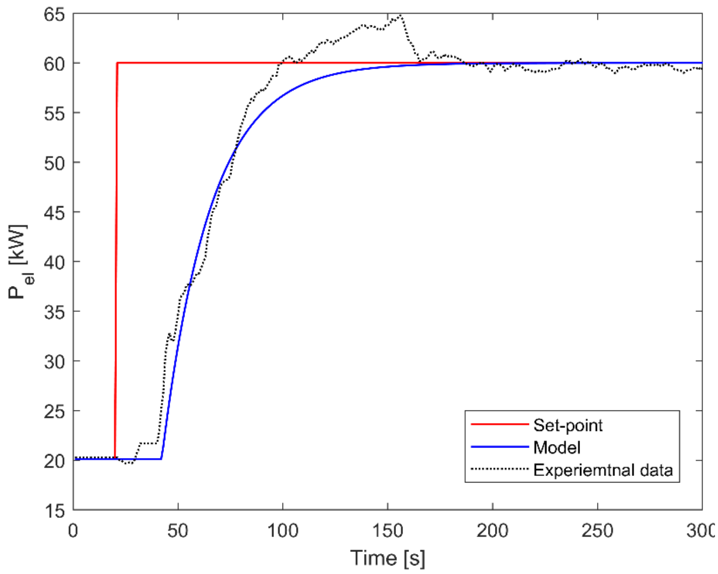

Figure 97 - mGT model validation

7.2.2 Heat pump

In the model, all the thermodynamic points are calculated, instant by instant, within MATLAB/Simulink with the help of the REFPROP tool [4]. The state of a thermodynamic system in equilibrium can be described with a finite number of parameters and REFPROP allows, starting from two parameters, to obtain the third state variable. The equations are solved within the model using ODE45 (Dormand-Prince) solver in variable-step approach using a relative tolerance equal to 0.001.

<u>CONDENSER</u>

To model this component a "two-step approach" has been developed: firstly, a static solution needs to be found, and then it is used as input in the dynamic equations.
The static solution includes two calculation loops: the first is simplified and provides the first guess to the second, which calculates the exact solution by solving a system of nonlinear equations as shown in Figure 98.

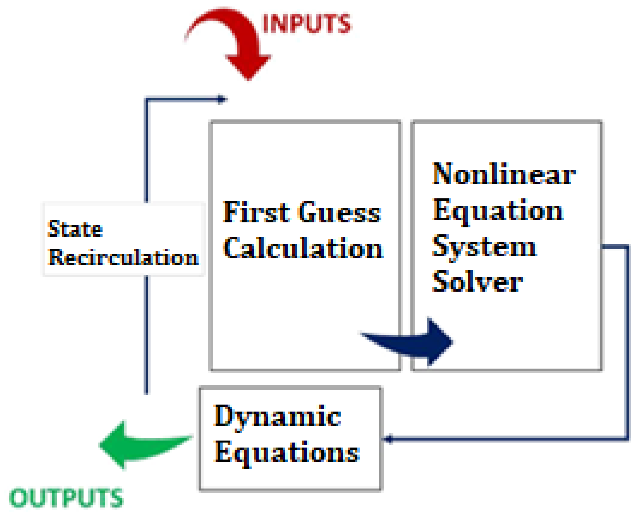

Figure 98 - Heat exchangers calculation logic

The condenser inputs are:

$T_{w,in}$ [K]: water condenser inlet temperature.

$\dot{m}_w$ [kg/s]: water mass flow rate.

$c_{p,w}$ [J/(kgK)]: water specific heat.

$h_{1,r}$ [J/kg]: refrigerant specific enthalpy at the condenser inlet.

$T_{1,r}$ [K]: refrigerant condenser inlet temperature.

$\dot{m}_r$ [kg/s]: refrigerant mass flow rate.

The characteristic parameters of this model are as follows:

L [m]: condenser length.

D [m]: condenser width.

K_s [W/(m^{2}K)]: global desuperheater heat transfer coefficient.

K_b *[W/(m²K)]: global two-phases heat transfer coefficient.*

K_l *[W/(m²K)]: global subcooling heat transfer coefficient.*

<u>Static solution:</u>

The first guess is calculated with the following equations, in bold text the unknown variables that provide the condenser outputs (Eqs24-31):

$$\dot{\boldsymbol{Q}}_{\boldsymbol{l}} = \dot{m}_r \left(h_{3,r} - h_{out}\right) \tag{24}$$

$$\dot{\boldsymbol{Q}}_{\boldsymbol{b,w}} = \dot{m}_r \left(h_{2,r} - h_{3,r}\right) \tag{25}$$

$$\dot{\boldsymbol{Q}}_{\boldsymbol{s}} = \dot{m}_r \left(h_{1,r} - h_{2,r}\right) \tag{26}$$

$$\boldsymbol{T}_{\boldsymbol{1,w}} = T_{w,in} + \frac{\dot{\boldsymbol{Q}}_{\boldsymbol{l}}}{\dot{m}_w \; c_{p,w}} \tag{27}$$

$$\boldsymbol{T}_{\boldsymbol{2,w}} = T_{1,w} + \frac{\dot{\boldsymbol{Q}}_{\boldsymbol{b,w}}}{\dot{m}_w \; c_{p,w}} \tag{28}$$

$$\boldsymbol{T}_{\boldsymbol{3,w}} = T_{2,w} + \frac{\dot{\boldsymbol{Q}}_{\boldsymbol{s}}}{\dot{m}_w \; c_{p,w}} \tag{29}$$

$$\boldsymbol{\lambda cond} = L\left[1 - \left(\frac{\dot{\boldsymbol{Q}}_{\boldsymbol{s}} + \dot{\boldsymbol{Q}}_{\boldsymbol{l}}}{\dot{\boldsymbol{Q}}_{\boldsymbol{b,w}} + \dot{\boldsymbol{Q}}_{\boldsymbol{s}} + \dot{\boldsymbol{Q}}_{\boldsymbol{l}}}\right)\right] \tag{30}$$

$$\boldsymbol{\lambda v} = L\left[1 - \left(\frac{\dot{\boldsymbol{Q}}_{\boldsymbol{b,w}} + \dot{\boldsymbol{Q}}_{\boldsymbol{l}}}{\dot{\boldsymbol{Q}}_{\boldsymbol{b,w}} + \dot{\boldsymbol{Q}}_{\boldsymbol{s}} + \dot{\boldsymbol{Q}}_{\boldsymbol{l}}}\right)\right] \tag{31}$$

Below, the nonlinear equations system that is solved by the MATLAB function *fsolve* is reported. It uses as a starting point the result of the aforementioned simplified calculation (Eqs.32-39):

$$\dot{\boldsymbol{Q}}_{\boldsymbol{b,w}} = K_b \, \boldsymbol{\lambda cond} \, D \, \frac{\left(T_{cond} - \boldsymbol{T}_{\boldsymbol{2,w}}\right) - \left(T_{cond} - \boldsymbol{T}_{\boldsymbol{1,w}}\right)}{\ln \frac{\left(T_{cond} - \boldsymbol{T}_{\boldsymbol{2,w}}\right)}{\left(T_{cond} - \boldsymbol{T}_{\boldsymbol{1,w}}\right)}} \tag{32}$$

$$\dot{\boldsymbol{Q}}_{\boldsymbol{b,w}} = \dot{m}_w \, c_{pw} \left(\boldsymbol{T}_{\boldsymbol{2,w}} - \boldsymbol{T}_{\boldsymbol{1,w}}\right) \tag{33}$$

$$\dot{\boldsymbol{Q}}_{\boldsymbol{b,w}} = \dot{m}_r \; (h_{2r} - h_{3r}) \tag{34}$$

$$\dot{\boldsymbol{Q}}_{\boldsymbol{s}} = K_s \, (\boldsymbol{\lambda v}) D \; \frac{\left(T_{1,r} - \boldsymbol{T}_{\boldsymbol{3,w}}\right) - \left(T_{cond} - \boldsymbol{T}_{\boldsymbol{2,w}}\right)}{\ln \dfrac{\left(T_{1r} - \boldsymbol{T}_{\boldsymbol{3,w}}\right)}{\left(T_{cond} - \boldsymbol{T}_{\boldsymbol{2,w}}\right)}} \tag{35}$$

$$\dot{\boldsymbol{Q}}_{\boldsymbol{s}} = \dot{m}_r \left(h_{1,r} - h_{2,r}\right) \tag{36}$$

$$\dot{\boldsymbol{Q}}_{\boldsymbol{s}} = \dot{m}_w \, c_{p,w} \left(\boldsymbol{T}_{\boldsymbol{3,w}} - \boldsymbol{T}_{\boldsymbol{2,w}}\right) \tag{37}$$

$$\dot{\boldsymbol{Q}}_{\boldsymbol{l}} = K_l (L - \boldsymbol{\lambda}_{\boldsymbol{v}} - \boldsymbol{\lambda}_{\boldsymbol{cond}}) D \cdot \; \frac{\left(T_{cond} - \boldsymbol{T}_{\boldsymbol{2,w}}\right) - \left(T_{cond} - \boldsymbol{T}_{\boldsymbol{1,w}}\right)}{\ln \dfrac{\left(T_{cond} - \boldsymbol{T}_{\boldsymbol{2,w}}\right)}{\left(T_{cond} - \boldsymbol{T}_{\boldsymbol{1,w}}\right)}} \tag{38}$$

$$\dot{\boldsymbol{Q}}_{\boldsymbol{l}} = \dot{m}_w \, c_{p,w} \left(\boldsymbol{T}_{\boldsymbol{1,w}} - T_{w,in}\right) \tag{39}$$

Where:

$\dot{Q}_s$ *[W]: desuperheater heating power.*

$\dot{Q}_{b,w}$ *[W]: two-phase heating power.*

$\dot{Q}_l$ *[W]: subcooling heating power.*

$\dot{m}_w$ *[kg/s]: water mass flow.*

$T_{1,w}$ *[K]: water temperature corresponding to the two-phase inlet region.*

$T_{2,w}$ *[K]: water temperature corresponding to the two-phase outlet region.*

$T_{3,w}$ *[K]: water outlet temperature.*

T_{cond} [K]: *refrigerant temperature during the change of isothermal state, from which the* p_{cond} *and the refrigerant-specific enthalpies are obtained at points 2r (*$\boldsymbol{h}_{2,r}$*) and 3r (*$\boldsymbol{h}_{3,r}$*).*

T_{out} *[K]: refrigerant outlet temperature.*

$c_{p,w}$ *[J/(kgK)]: specific heat capacity water.*

$\dot{m}_r$ *[kg/s]: refrigerant mass flow rate.*

h_{3r} *[J/kg] refrigerant-specific enthalpy in point 3.*

h_{2r} *[J/kg]: refrigerant-specific enthalpy in point 2.*

L *[m]: condenser length.*

$\lambda cond$ *[m]: two-phase heat exchange length.*

λv [m]: desuperheater heat exchange length.

Dynamic solution:

The water temperatures previously calculated enter through the ΔT_{ml} into the condenser energy balance, which takes as control volume the refrigerant fluid in condensation. Through these equations, the refrigerant condensation and outlet temperatures are known for each time interval (Eqs.40-43):

$$\Delta T_{ml,cond} = \frac{\left(T_{cond,old} - T_{2,w}\right) - \left(T_{cond,old} - T_{1,w}\right)}{\ln\frac{\left(T_{cond,old} - T_{2,w}\right)}{\left(T_{cond,old} - T_{1,w}\right)}} \tag{40}$$

$$T_{cond,new} = \frac{\dot{m}_r\left(h_{2,r} - h_{3,r}\right) - K_b\,\lambda cond\,D\,\Delta T_{ml,cond}}{M_{cond}\,c_{p,r,cond} + M_{s,cond}\,c_{p,s,cond}}\,\Delta t + T_{cond,old} \tag{41}$$

$$\Delta T_{ml,out} = \frac{\left(T_{cond,old} - T_{1,w}\right) - \left(T_{outcond,old} - T_{w,in}\right)}{\ln\frac{\left(T_{cond,old} - T_{1,w}\right)}{\left(T_{outcond,old} - T_{w,in}\right)}} \tag{42}$$

$$T_{outr,new} = \frac{\dot{m}_r\left(h_{3,r} - h_{outr,cond}\right) - K_l\,(L - \lambda_{cond} - \lambda_v)D\,\Delta T_{ml,out}}{M_{condout}\,c_{p,r,condout} + M_{s,cond}\,c_{p,s,cond}}\,\Delta t + T_{outrold} \tag{43}$$

EVAPORATOR

The evaporator has been simulated with the same condenser logic keeping in consideration that in this heat exchanger only the two-phase and the superheated regions are present.

COMPRESSOR

This component is responsible for the heat pump mass flow regulation. This compressor works at a fixed rotational speed and the main inputs are:

- the pressure from the evaporator model.
- the pressure from the condenser model.

The main outputs instead are:

- the compressor outlet temperature.
- the working fluid mass flow rate.

The compressor outlet temperature is depending on the compressor efficiency and, to be coherent with the datasheet provided by the manufacturer, has been set η =65.19%.

Therefore, the outlet compressor temperature is calculated starting from the outlet enthalpy calculation (Eq.44):

$$h_{out} = h_{in} + \frac{h_{out,s} - h_{in}}{\eta} \tag{44}$$

Where:

h_{out} [J/kg]: compressor outlet specific enthalpy.

h_{in} [J/kg]: compressor inlet specific enthalpy.

$h_{out,s}$ [J/kg]: compressor outlet isentropic specific enthalpy.

The compressor maps have been implemented in the Matlab-Simulink compressor model by using a 1D look-up table which takes as input the compression ratio $\beta = \frac{P_{cond,out}}{P_{eva,out}}$ and gives as output the refrigerant mass flow rate based on the data provided by the manufacturer.

A fluid dynamic delay has been implemented considering a first-order delay of 10s on the mass flow rate and enthalpy by implementing a Laplace Transfer Function as reported in Figure 99 [5].

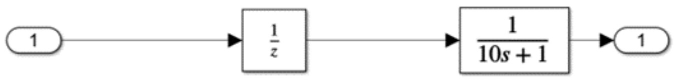

Figure 99 - Compressor dynamic

The compressor power P has been calculated as follows (Eq.45):

$$P = \dot{m}(h_{out} - h_{in}) \tag{45}$$

EXPANSION VALVE OR TESLA TURBINE

As already said if the HP works in a traditional way, an expansion valve is used to close the cycle through an iso-enthalpic expansion otherwise, to close the cycle, the expansion can be carried out by using the Tesla turbine [6] installed in series with an expansion valve. In this latter case the enthalpy difference will increase and so also the HP COP will be higher since the outlet temperature will be lower.

TRADITIONAL CONFIGURATION

The expansion valve is the component that, thanks to a reduced section passage, generates a pressure drop and brings the refrigerant fluid to the low pressures necessary for the evaporation at low temperature. In the model this component does not calculate the flow rate from the pressure information coming from the evaporator and the condenser, but only generates a delay of the flow information coming from the compressor.

The expansion valve inputs are:

P_{eva} [kPa]: expansion valve outlet pressure.

h_{in} [J/kg]: inlet specific enthalpy.

$\dot{m}$ [kg/s]: expansion valve mass flow rate.

h_{out}= h_{in} [J/kg]: isoenthalpy transformation.

The outgoing R134a title has been calculated as follows (Eq.46):

$$x = \frac{h_{out} - h_l}{h_v - h_l} \tag{46}$$

Where:

h_{out} [J/kg]: outgoing specific enthalpy.

h_l [J/kg]: saturated liquid specific enthalpy.

h_v [J/kg]: saturated steam specific enthalpy.

x [kgsteam/kg]: mass title, equal to the ratio between steam mass and liquid mass.

Analogously at the compressor, a delay is then defined in order to estimate the dynamic of the system which corresponds to a fluidynamic first order delay of 20 s which also takes into consideration the time required to filling and emptying the heat exchangers as a consequence of the inlet mass flow rate change [5].

TESLA TURBINE AND EXPANSION VALVE

In this case the expansion is performed by the Tesla turbine. To model the expander the inputs parameters are:

ε [-]: expansion ratio.

P_{in} [kPa]: Tesla expander inlet pressure.

T_{in} [kPa]: Tesla expander inlet temperature.

h_{in} [J/kg]: inlet specific enthalpy.

$\dot{m}$ [kg/s]: Tesla expander mass flow rate.

By using REFPROP it is possible to obtain the outlets:

P_{out} [kPa]: Tesla expander outlet pressure.

T_{out} [kPa]: Tesla expander outlet temperature.

h_{out} [J/kg]: outlet-specific enthalpy.

The electrical power produced is then calculated as (Eq.47):

$$P = \dot{m}(h_{out} - h_{in}) * \eta_{alternator} \tag{47}$$

The dynamic of this component has been implemented in a similar way as for the compressor and isenthalpic valve.
The following HP validation and the model results that will be presented in chapter 3 will be referred to the traditional HP configuration and so with the lamination valve after the condensation phase.

The model has been validated on the bases of the experimental data using the and thanks to the accurate approach used to model the heat pump it is possible to obtain data not only referred to the water circuit but also data of the internal section of the heat pump related to the refrigerant fluid circuit. In the following, the validation results are reported; the test has been conducted by varying the condenser water inlet mass flow rate at first reducing it from 0.38 kg/s to 0.22 kg/s, and then, after 1100 s, imposing a ramp increasing the mass flow rate from 0.22 kg/s to 0.57kg/s whereases the water mass flow rate at the evaporator side has been kept constant as reported in Figure 100.

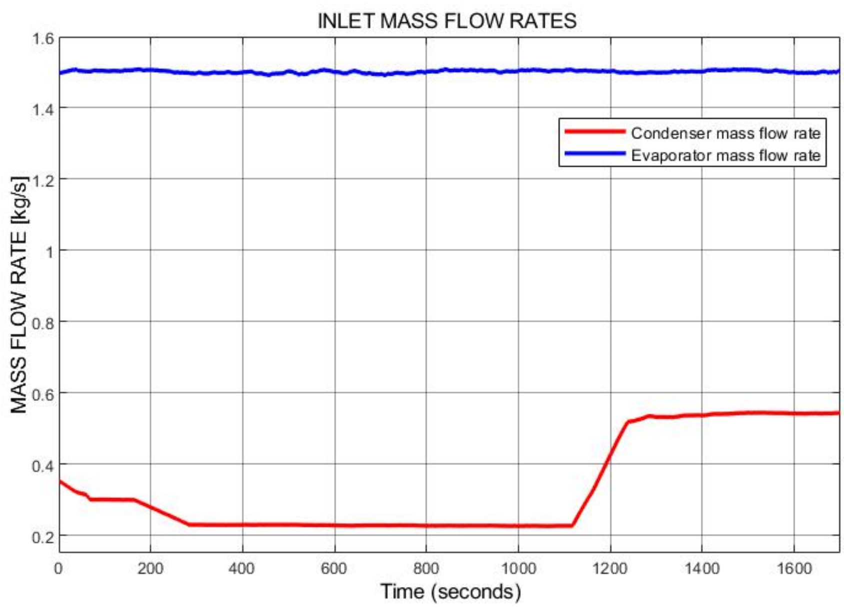

Figure 100 - HP water inlet mass flow rate

In Figure 101 the water outlet temperature at the condenser outlet is reported. The red line represents the model data whereas the blue one is referred to the data measured during the experiment. Figure 102 analogously reports the same data but referred to the evaporator side.

As the water mass flow rate variation has been performed on the condenser side the most relevant variation can be seen there. It is possible to state that the model is completely able to respect the real HP behavior giving a prompt response to the input change. In fact, as soon as the mass flow rate decreases, the increase in the water outlet temperature can be seen both from the experimental data and the model whereases the decrease in temperature starts after 1100 s due to the inlet water mass flow rate increase. The model is able to respect the real HP behavior presenting always an error lower than 4 K. Regarding the evaporator side, as no changes at the input side have been applied, the behavior of the water outlet temperature is almost constant, and, also in this case, the model shows good accuracy presenting always an error lower than 2 K.

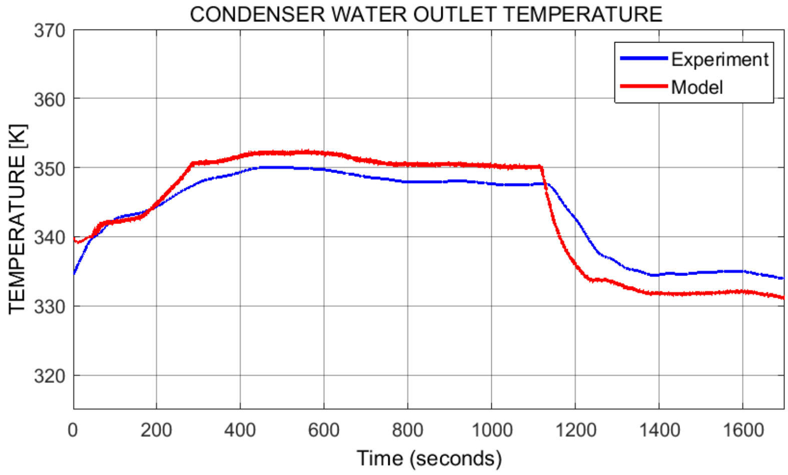

Figure 101 – Condenser water outlet temperature model validation

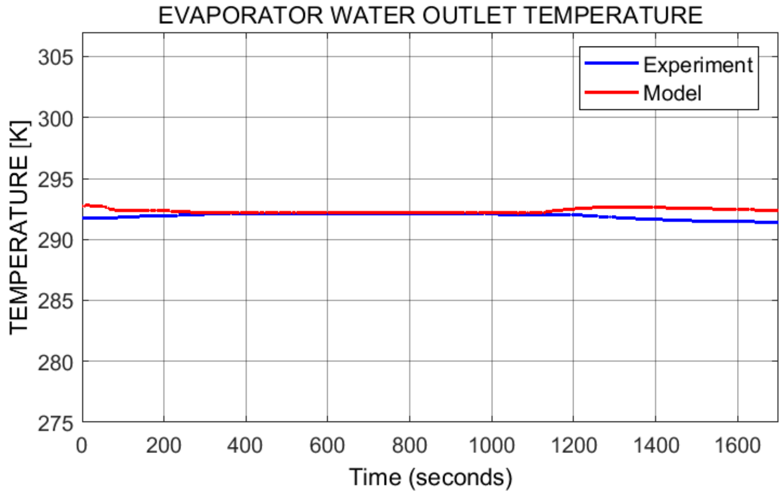

Figure 102 – Evaporator water outlet temperature model validation

Some data related to the R134a side has been compared (Figure 103, Figure 104). The Figure 103 reports the refrigerant compressor outlet temperature and the Figure 104 is related to the R134a evaporator outlet temperature (and so the condition at the inlet of the compressor). The considerations already made for the previous results are valid also in this case: the model is able to respect the real trend of the experimental data obtained during the test, the condenser side (outlet of the compressor) is influenced by the change in the input water mass flow rate whereases the evaporator side is not affected by any changes. The accuracy of the model is very high also in this case, presenting on the condenser side an error always lower than 6 K with the exception of a short transient section after the change in the condenser water flow rate.

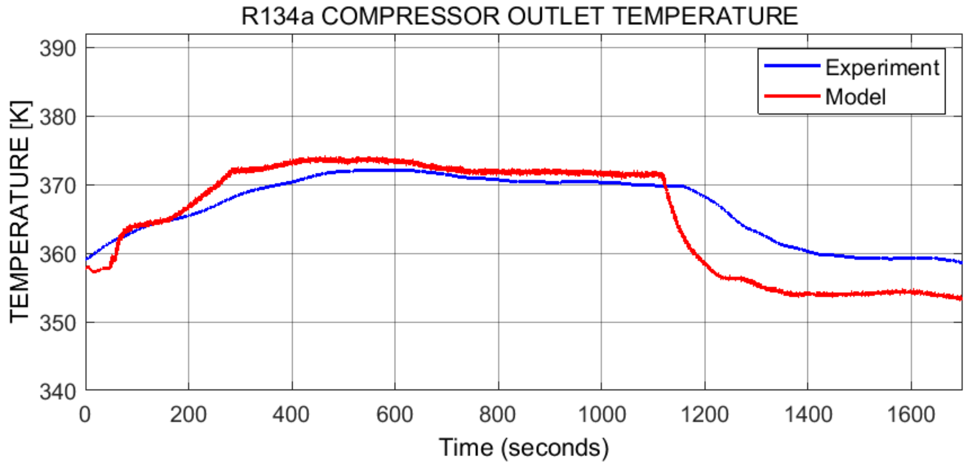

Figure 103 – Compressor outlet temperature model validation

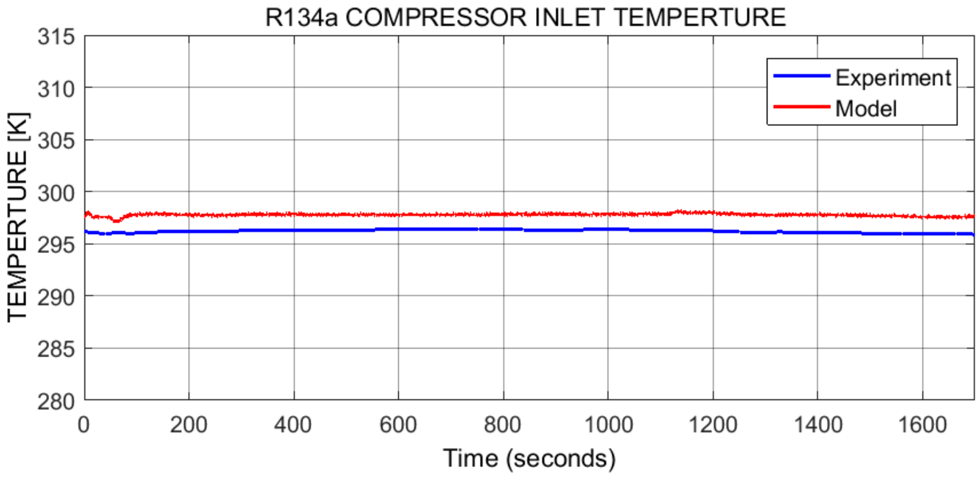

Figure 104 – Compressor inlet temperature model validation

7.2.3 Thermal energy storage

Both thermal energy storages have been modeled according to 1D model approach using TRANSEO, an in-house dynamic simulation tool developed by the Thermochemical Power Group [7],[8] and then implemented in Matlab/Simulink. In this case, the thermal storage tank has been modelled with a multi-nodal method, based on a numerical 1 D finite difference scheme. It consists of dividing the vessel into N sections (nodes) and solving an energy balance for each of them. Thus, a set of N differential equations is used to obtain the temperatures of the N nodes as a function of time. The problem domain was divided into N parts, spatially distributed in the z direction (Eq. 48).

$$\Delta z = \frac{H}{N-1} \tag{48}$$

N is the number of nodes predetermined by the user. It is a fundamental parameter of the system since it defines the model accuracy. H is the height of the tank. In this way, the whole storage is subdivided into N portions of water, each having the i-th mass (Eq. 49)

$$\dot{m}_i = A_i \rho_i \Delta z \tag{49}$$

The temperatures of these N masses are the outputs of the problem. Therefore, there are N unknown values to be calculated at each time step. To solve the mathematical problem, N differential equations are used, linking the temperatures with the model parameters, as well as taking into account the following different internal and external phenomena:

- heat conduction between the various water masses.
- heat losses between the masses and the outside.
- inlet or outlet water flow rate (positive or negative).
- Internal natural convection.

The energy balance considering different internal and external phenomena is reported in Eq. 50.

$$\frac{\rho v A \Delta z}{2} * \frac{dT_i}{dt} = q_{c,i} - q_{conv,i} + q_{s,i} + q_{m,i} \tag{50}$$

The mathematical time-dependent integration is performed through the implicit Crank-Nicolson method.

The most important parameter associated with the heat storage is the enthalpy content of the stored water (SoC parameter). The estimation of this parameter is affected by an error that increases with the decrease of the number of temperature nodes, since the theoretical exact value of the SoC could be obtained only with N tending to infinite. The objective is to improve the estimation accuracy of the stored heat amount (typical problems of system state identification) with a limited number of nodes and taking advantage of the field measurements.

The model implementation was carried out in Matlab-Simulink environment. The measurements of thermoresistances (four probes in the laboratory test case) were forced at the related i-th node, to take the advantage of experimental evidence: in such respect, the model can be regarded as a tool to physically interpolate between the temperature measurements. This approach is essential to avoid significant error accumulation and increase over time.

In Figure 105, an example of a graphical result of the model outputs in terms of temperature variation inside the storage is reported together with a simplified representation of the water stratification inside the tank.

The TES connected to the DHN is considered fully charged when the water temperature is 80°C whereas the one connected to the panels is fully charged as soon as the water temperature reaches 45°C.

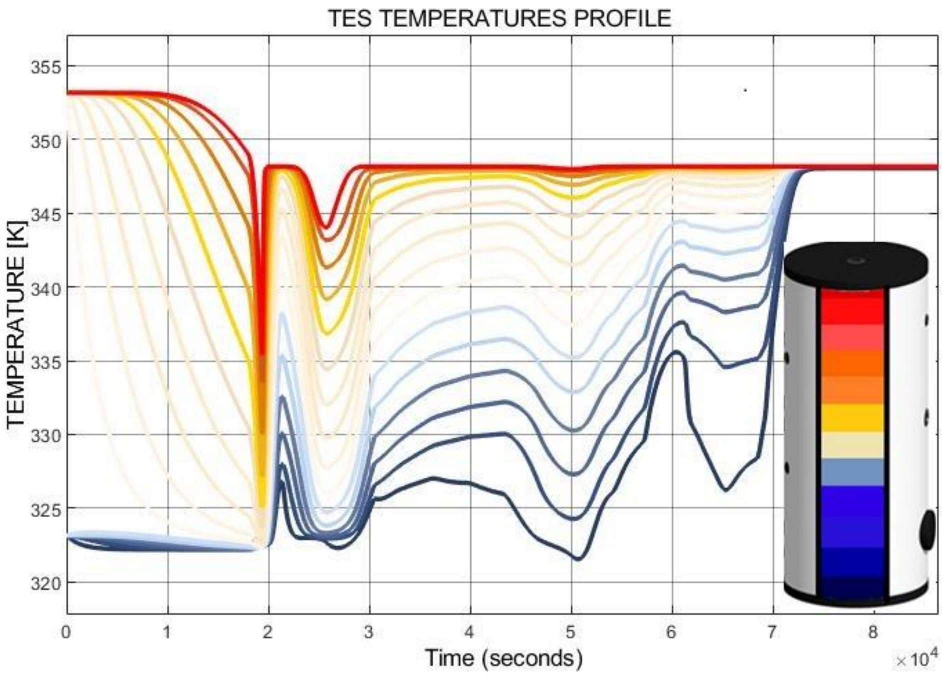

Figure 105 - TES water stratification

The model has been validated in previous works [9][10], showing really good accuracy.

7.3 Component integrations and interaction

In this section, the model component interaction is presented focusing on the input/output of each of them and the initialization procedure. A comparison between the model and the real environment has been carried out to highlight the main differences due to the technical constraints of the experimental plant.

7.3.1 Model vs facility

The ENVISION TEST RIG model provides the integration of different components. An initial state has been created for initializing the model; the initial state is of fundamental importance to allow the model to start from values in which each individual component works in stable conditions. The whole model has been developed in Matlab/Simulink environment and uses a fixed step type discrete solver. To guarantee stability a little sample time has been set equal to 0.25 s which is mainly required for the HP model convergence as a lot of nonlinear equations based on the use of the log mean temperature method have been implemented to be able to analyze variations of physical properties and operational parameters that would not be easily observable on the real HP such as the variation of condenser internal liquid mass.

With the model in Figure 106, several simulations have been carried out; at first, the real system behaviour has been simulated and then the number of solar façade panels has been increased to have greater exploitation of the solar energy but also to respect the technical requirement of the HP evaporator in terms of temperature: if the water temperature of the low-temperature storage (so the HP evaporator water inlet temperature) is lower than 13°C, the HP cannot operate properly and the HP control system developed by the manufacturer shut it down.

If this constrain is easily solved in the model by implementing a greater number of solar façade panels, in the real environment, an electrical heater has been installed between the low-temperature TES and the HP evaporator which acts as panel multiplier setting the water temperature at the exit of the TES equal to the one provided by the solar façade panels. In this way, the inlet temperature at the evaporator do not decrease as the test progresses ensuring to perform longer test avoiding interruptions due to technical constraints.

Regarding the objective of the model, the priority has been given to the satisfaction of a part of the Savona Campus thermal demand (specifically quarter of the total thermal demand has been set as a reference value for the Winter/Spring/Autumn seasons and the real demand for Summer according with the size of the ENVISION plant).

The components interact with each other as follows: the hot water and the mass flow rate coming from the solar façade panels are the inputs of the low-temperature TES which will be heated up as long as the solar radiation is higher than a minimum set point value set by the modeler and equal to 50 W/m^2. The TES has been modelled according to the water stratification method reported in 2.2.3. The hot water, coming from the solar façade panels, heats up the lower part of the TES and the mass flow rate required by the HP is taken from the upper part of it. The HP is then connected both to the cold side and to the hot side of the Campus DHN so the condenser low temperature is set equal to 50°C and the HP water output required is set at 75°C. If the thermal demand is lower than the HP thermal power production, the high-temperature TES will be charged. The mGT is also connected to both the hot and cold sides of the DHN and to the high-temperature TES which will be heated up following the MPC control that will be described in the next section.

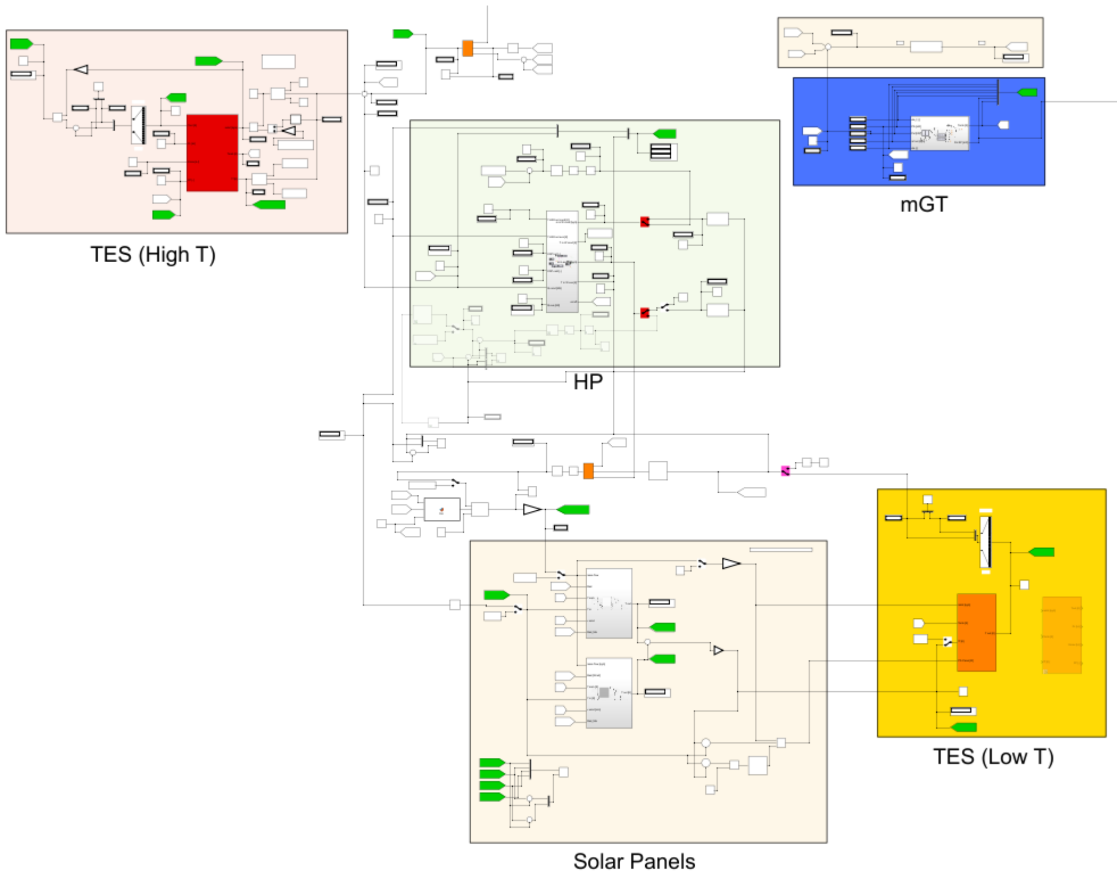

Figure 106 - ENVISION TEST RIG Matlab/Simulink model

The ENVISION test rig, thanks to a double ring configuration, can operate without the real connection with the DHN since a heat sink (fan cooler) is integrated to simulate the thermal demand as reported in the ENVISION P&ID in Figure 107; in this particular configuration the low temperature set at 50°C is ensured by the high-temperature TES which acts as a balancer: the lower part connected to the cold ring will be at 50°C whereases the higher part, connected to the hot ring is the one charged by the HP and the mGT at 75°C and which can be discharged to satisfy part of the thermal demand. This specific configuration is the main difference between the model and the real plant because in the model the high-temperature TES is used to store the exceeding thermal energy and to release it whenever required by varying its state of charge (SOC) between 1 (whole TES at 75°C) and 0 (whole TES at 50°C). In the real environment, instead, since this TES must act as a balancer to guarantee the 75°C of the hot ring and the 50°C of the cold ring, during the test and when the system is not physically connected to the district heating network of the Savona Campus, it is impossible to have the storage completely charged at 75°C otherwise the water condition at the inlet of the mGT and the HP wouldn't be respected; the water temperature difference inside the TES in the test rig is ensured by a dedicated fan coolers and recirculation lines. Whenever the mGT and the HP produce hot water at 75°C and the test rig is not connected to the Savona DHN, the high-temperature storage will be charged from the top with part of the hot mass flow rate whereas the remaining mass flow rate will be cooled down until 50°C and will enter into the TES from the bottom; the percentage of the mass flow rate that goes directly to the storage is determined in any time by a three-way valve that is controlled so that the water temperature at the fan cooler outlet is equal to 50°C.

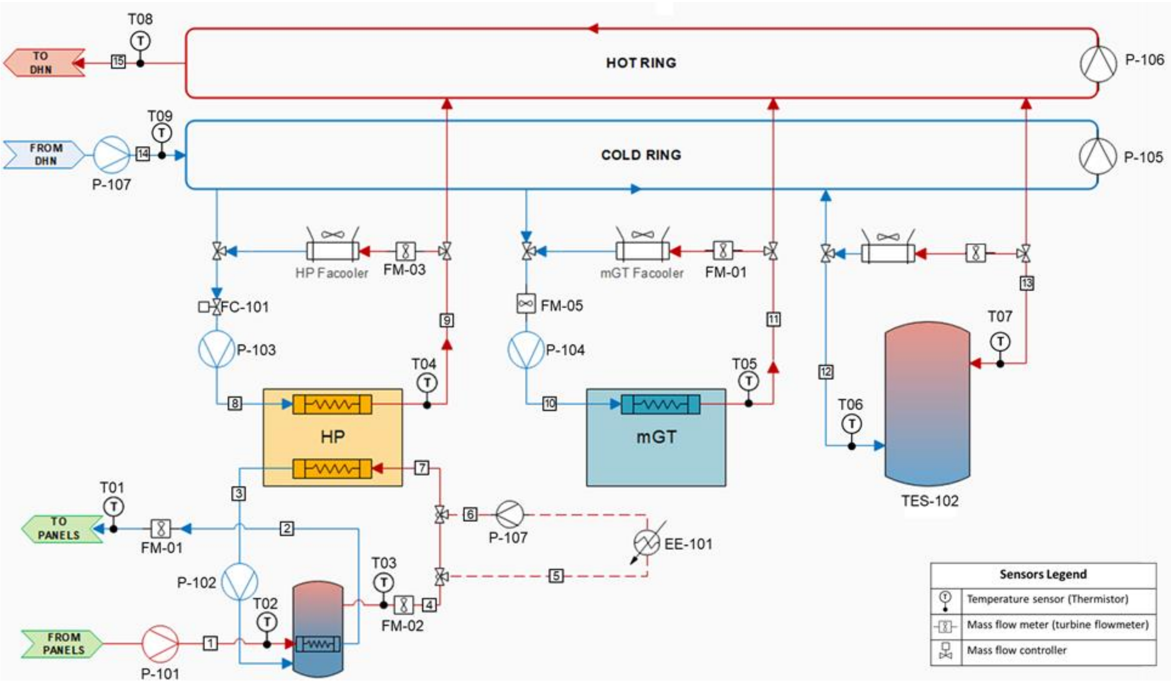

Figure 107 - *ENVISION P&Id*

7.4 ENVISION real-time control and management algorithm

In this section, a complete description of the model control system logic is performed, showing all the inputs required to make the proper decision to allow the best exploitation of the renewable energy sources minimizing the CO_2 production.

Considering that the ENVISION technologies installed in the Southern Demosite work in the direction of increasing the exploitation of the available building surface in order to harvest thermal energy, priority was given to satisfying the Campus thermal demand accepting that electricity demand is met by purchasing from the grid the difference between the electrical power demand and the mGT electrical power production.

7.4.1 ENVISION real-time control and management algorithm

The implemented control logic is based on different levels of optimization (Figure 108). The developed EMS takes decisions every 15 minutes based on the prediction of the thermal and the electrical demand with the goal of minimizing the CO_2 emissions. The EMS evaluates the target thermal demand to be satisfied and, in accordance with the thermal power estimation of the different system components, takes the proper decision regarding the startup/shut down/load of the components. If the thermal demand is sufficiently low to be covered by the HP and the TES, the mGT is never started up privileging in this way the exploitation of the renewable energy source. Instead, if the thermal demand is high, the startup of the mGT is necessary and it is operated so that the CHP can guarantee the match with the thermal demand operating at high-efficiency level also allowing the H-TES charge.

The MPC, instead, operates each second and, in this case, as the HP operates with constant rotational speed. It controls only the mGT receiving as inputs the measured values of the thermal power produced and the target one to give, as output, the calculated error and the correction to be applied which is automatically sent to the mGT. The developed MPC can be easily applied for further applications to the HPs which operate with different compressor rotational speeds.

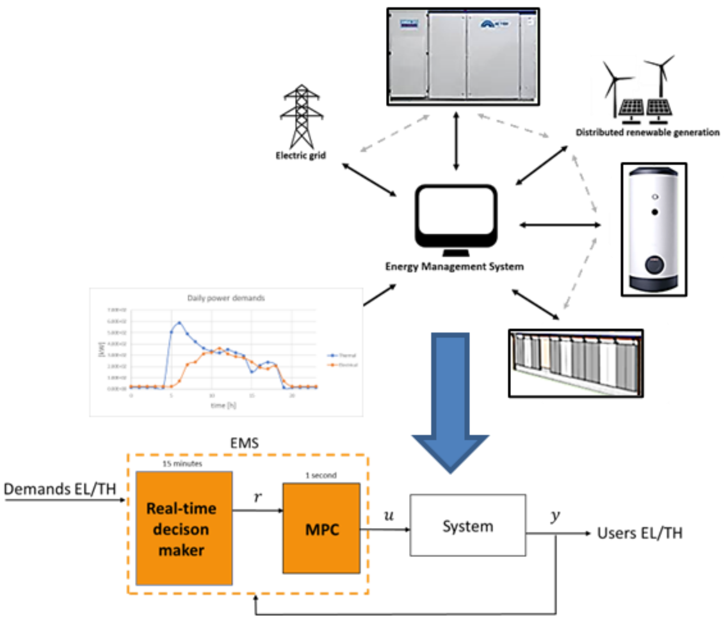

Figure 108 - *ENVISION control strategy*

The management of the solar façade panels circuit has been implemented imposing that if the solar radiation is higher than a minimum value, set equal to 50 W/m^2 , the recirculating pump of the corresponding circuit will be maintained ON whereas, if the solar radiation is under that value, the recirculated pump will be shut down to avoid the L-TES discharge.

The H-TES charge/discharge is controlled to ensure of the peak demand and the night demand to be satisfied. The SOC of the TESs is calculated in accordance with the temperature distribution inside it and depending on the TESs charge/discharge value. Inside the EMS a predictive control logic based on the analysis of the thermal demand gradient has been implemented: different decisions will be taken in accordance with that; if the gradient is negative the turn off of the mGT in case of low thermal demand will be privileged if the SOC of the storage is sufficiently high. Also, a particular case in which the gradient is negative and only TES and HP would not be able to satisfy the thermal demand has been kept into consideration: in this case, the target values of the mGT will be to meet the electrical power demand guaranteeing a surplus in the thermal energy production. This choice has a double benefit: the reduction of the electricity purchased from the grid and the H-TES charge. In this latter case, considering that the TES can be charged until reaching SOC equal to 1, also a bypass of the mGT exhaust gases has been implemented.

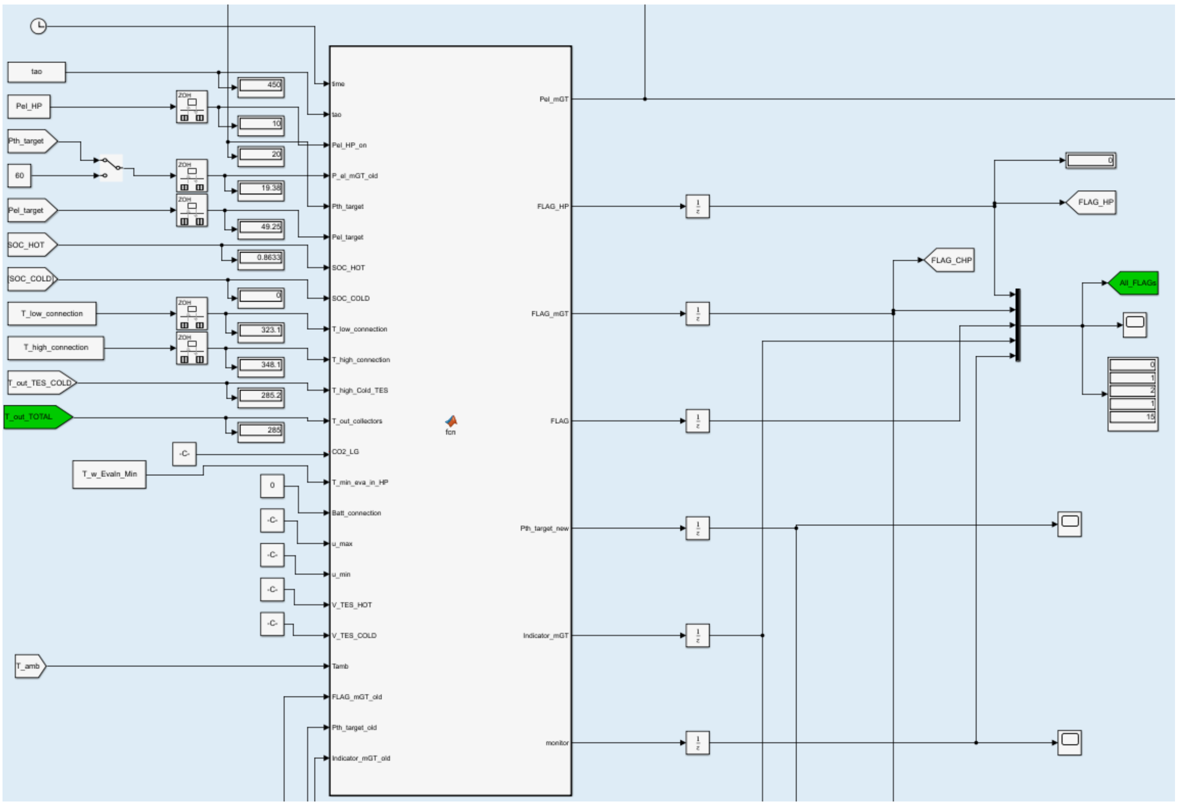

Figure 109 - ENVISON EMS model

The EMS that has been implemented in the ENVISION model is reported in (Figure 109). The MPC which controls the mGT instead is reported in Figure 110.

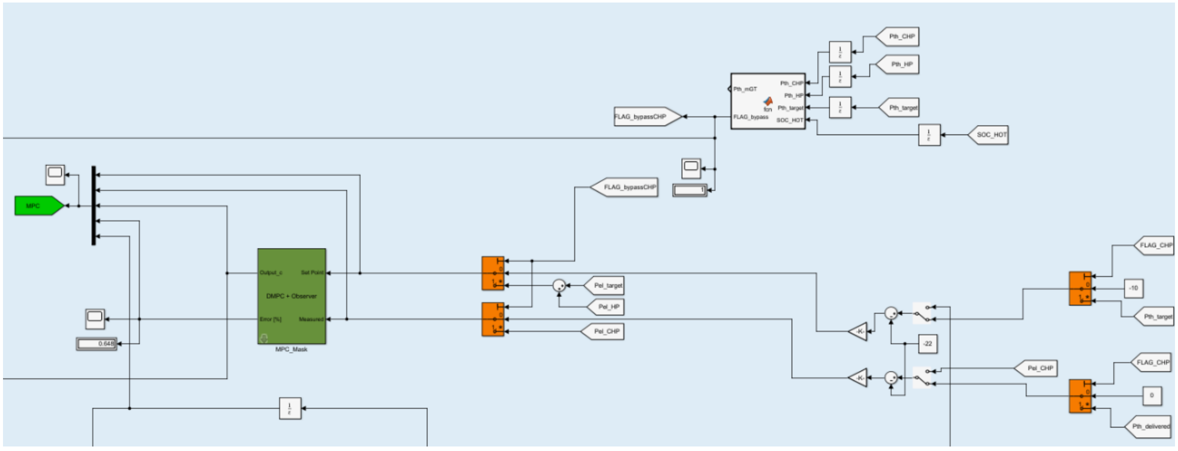

Figure 110 – Model Predictive control [83]

7.4.2 Input definition

All the inputs required by the EMS in order to take the proper decision every 15 minutes are listed in Table 10.

Table 10 - ENVISION EMS input

Tao	Sample time [s]
Pth target	User thermal demand [kW]
Pel target	User electrical demand [kW]
SOC COLD	State of Charge Panels TES [adim, 0-1]
SOC HOT	State of Charge rings TES [adim, 0-1]
T low connection	Temperature of the cold ring [K]
T high connection	Temperature of the hot ring [K]
T high Cold TES	Panel TES outlet Temperature [K]
T out collectors	Panel TES inlet Temperature [K]
CO_2 LG	CO_2 production for Local Grid Electricity [g/kWh]
Batt connection	Battery connection (0=off, 1 = on)
U max	Facility upper constraints [kW]
U min	Facility lower constraints [kW]
C TES HOT	Rings TES Capacity [kWh]
C TES COLD	Panel TES Capacity [kWh]
Tamb	Ambient Temperature [K]
FLAG HP old	ON/OFF HP Indicator at the previous decision [-]

FLAG mGT old	ON/OFF mGT Indicator at the previous decision [-]

The outputs instead are the decision taken from the EMS in terms of startup/shut down/ maintaining ON/OFF the components, the electrical power corresponding to the mGT set point value, the new thermal demand that has to be satisfied and, to be able to understand quickly, which scenario has been chosen by the EMS a general FLAG which at each decision shows which components are ON/OFF, the gradient of the thermal demand and the SOC of the H-TES.

Table 11 - ENVISION EMS output

Pel mGT	Set Point mGT
FLAG HP	ON/OFF HP Indicator
FLAG mGT	ON/OFF mGT Indicator
FLAG	Facility operating scenario
Pth target new	Thermal demand

7.5 ENVISION Model in the loop algorithm verification

The model algorithm validation based on the satisfaction of quarter of the Campus thermal energy demand has been carried out in all the months of the year. Different scenarios have been simulated by varying the solar façade panel number, and, only related to the summer period, the thermal demand imposing it equal to the real Campus demand. Positive results have been obtained in all the tested scenarios as the thermal demand has been always satisfied; In the following paragraphs, the model results referred to the different seasons and scenarios are reported and discussed. To analyse the different seasons of the year, the results related to specific months are reports: January, March, August, and October for winter, spring, summer, and autumn seasons, respectively.

7.5.1 Winter season simulation

Figure 111 shows the simulation results referred to a generic January day in the real ENVISION system configuration: 17 panels pairs, 5000 l L-TES, thermal demand to be satisfy equal to ¼ of the Campus demand.

The first graph shows in blue the thermal power production, in green the demand to be satisfied, and in red the power that is actually delivered to the Campus. At first glance, it can be immediately noticed that the supplied power is always equal to the demand. When the power produced by the plant is higher than the demand it corresponds to the H-TES charging phase that can be individuated in the second graph (red line): the TES is charging when the power is negative and discharging otherwise. The same behaviour can be seen for the instants in which the power production is lower than the demand: this phase in fact corresponds to the TES discharge. In the second graph, together with the H-TES power, are also reported the mGT (in green) and the HP (in blue) thermal power production. The third graph represents instead the state of charge of the H-TES during the whole day.
Analysing the second graph, it can be noted that the HP operates only during the first part of the day, this is because the initial temperature inside the L-TES (so the one connected to the HP and the solar panels) has been always set equal to 30°C. As a consequence, the HP will operate until the temperature inside the storage will be sufficiently high to overcame the constraint imposed by the HP manufacturer (>13°C) as already explained in the previous paragraph.
During January, it can be noted that the 17 solar panels pairs are not able to recharge the L-TES and for this reason, the HP never starts in the second part of the day. Even more,

considering also a simulation of the day after in which the L-TES wouldn't have an initial condition of 30°C, the HP will almost never operate.

Figure 111 instead reports (a) the solar irradiance of a generic sunny January day, (b) the water temperature difference between the inlet and outlet section of the grey and white solar façade panels which are subjected to the aforementioned solar radiation and (c) the temperature at the top and the bottom of the L-TES.

From the analysis of Figure 111, the previous considerations about the panels that are not able to considerably increase the temperature are confirmed.

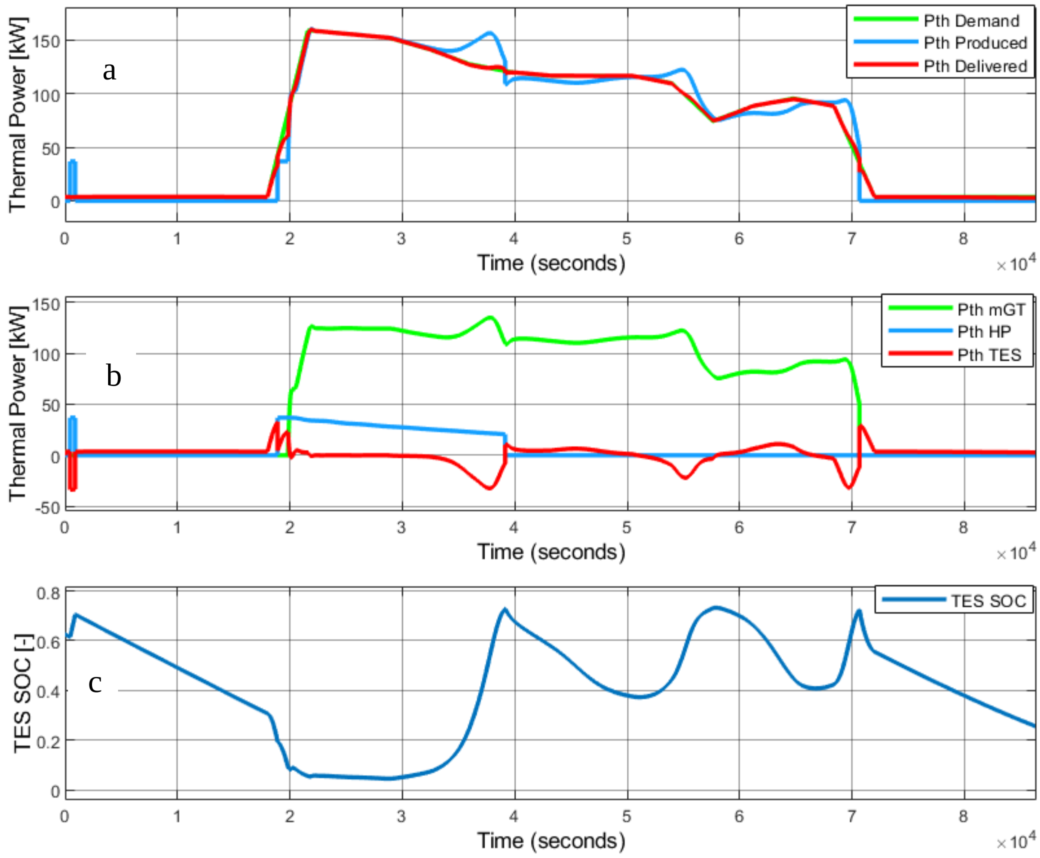

Figure 111 - January power production – 17 panels pair – (a) Demand Dispatchment – (b) Thermal Power Production – (c) H-TES SOC

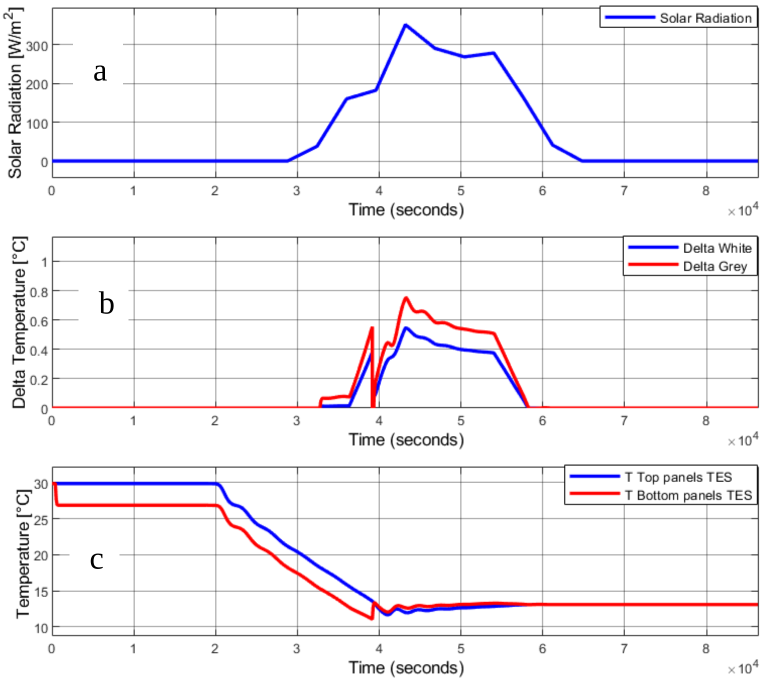

Figure 112 - January solar façade panels – 17 panels pair – (a) Solar Radiation – (b) Panels' Temperature Difference – (c) L-TES top and Bottom Temperatures

The same analysis has been performed by varying the solar façade panels number; 180 panels' couples have been implemented and the results are shown in Figure 113 and Figure 114.

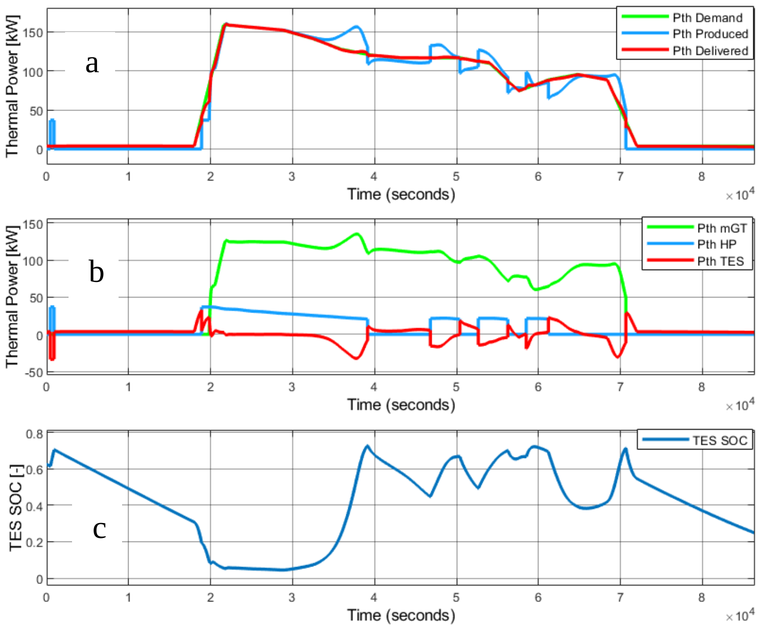

Figure 113 - January power production – 180 panels pair – (a) Demand Dispatchment – (b) Thermal Power Production – (c) H-TES SOC

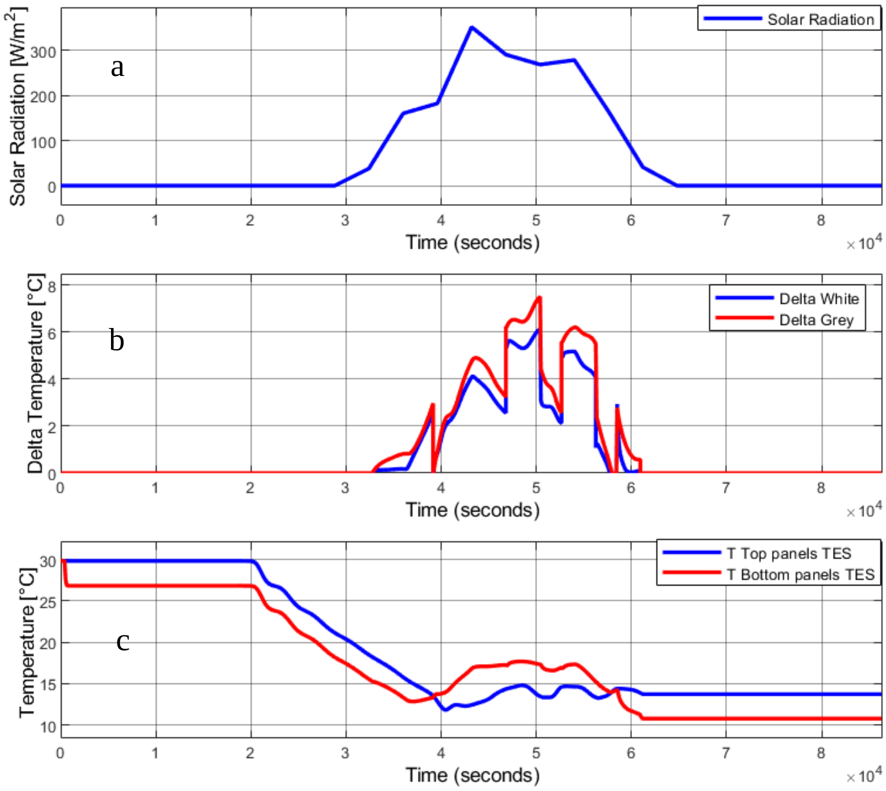

Figure 114 - January solar façade panels – 180 panels pair – (a) Solar Radiation – (b) Panels' Temperature Difference – (c) L-TES top and Bottom Temperatures

In 180 panels- case, it can be noted that the HP operates for a longer period also during the second part of the day and the panels are able to generate a considerably higher temperature difference. It must be said that the final state of charge of the L-TES is equal to zero as the case before but implementing a greater number of solar façade panels (and in particular a number that allows having the final SOC equal to the initial one) will be economically disadvantageous because it would imply oversizing the plant. So, a compromise between the thermal demand covered by the HP and the number of solar façade panels must be taken. It must also be underlined that January is the month with the lower solar radiation.

7.5.2 Summer season simulation

With the same logic already explained in the previous paragraph, the result referred to August considering to satisfy the total thermal demand of the Campus are here reported. Figure 115 and Figure 116 show the results concerning the simulation of the real plant whereas Figure 117 and Figure 118 report the simulation results of a plant with 180 panels pair.

From a comparison between the two scenarios, it can be noted that, even if in both cases the total demand is satisfied, in the second scenario the mGT power production is much lower leading to a greater reduction of the CO_2 emission. Even more, the final SOC of the storage-TES is almost equal to the initial one and the HP operates for the whole day maximizing in this way the best exploitation of the renewable energy source.

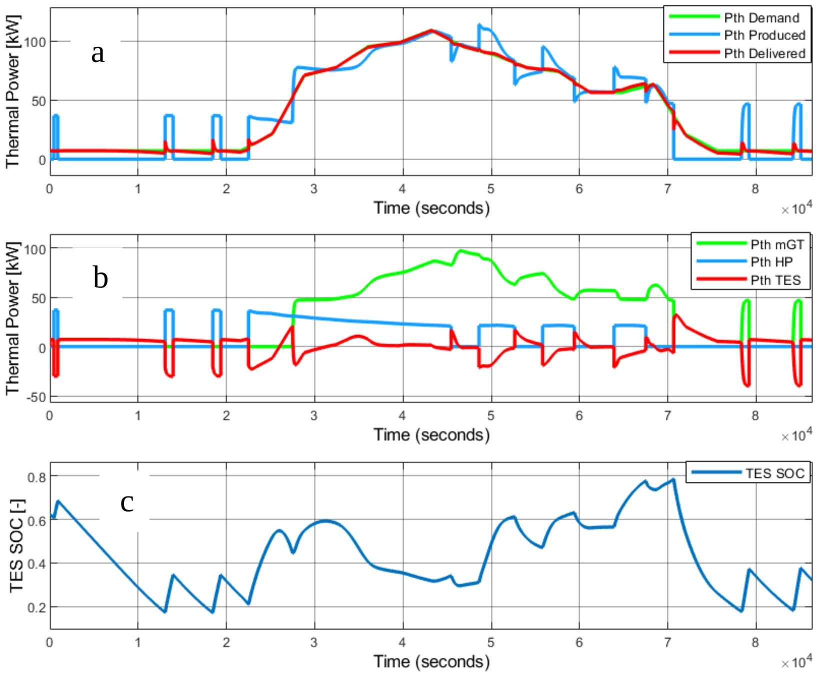

Figure 115 - August power production – 17 panels pair – (a) Demand Dispatchment – (b) Thermal Power Production – (c) H-TES SOC

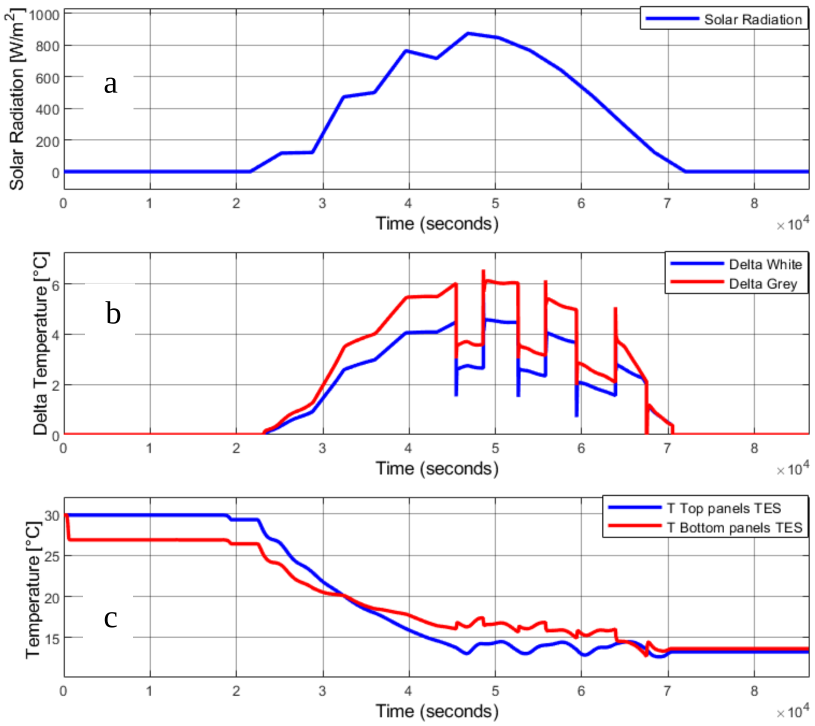

Figure 116 - August solar façade panels – 17 panels pair – (a) Solar Radiation – (b) Panels' Inlet/Outlet Temperature Difference– (c) L-TES top and Bottom Temperatures

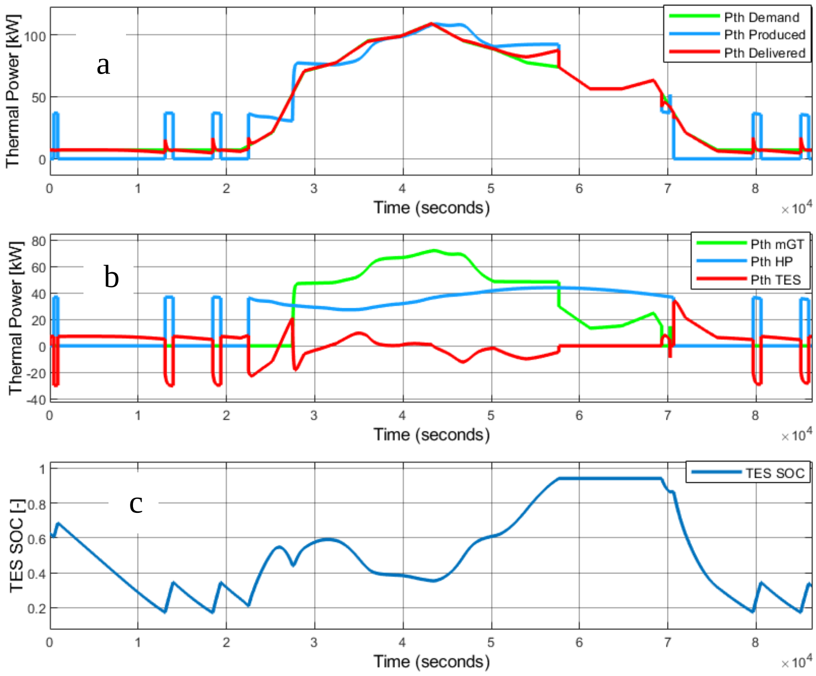

Figure 117 - August power production – 180 panels pair – (a) Demand Dispatchment – (b) Thermal Power Production – (c) H-TES SOC

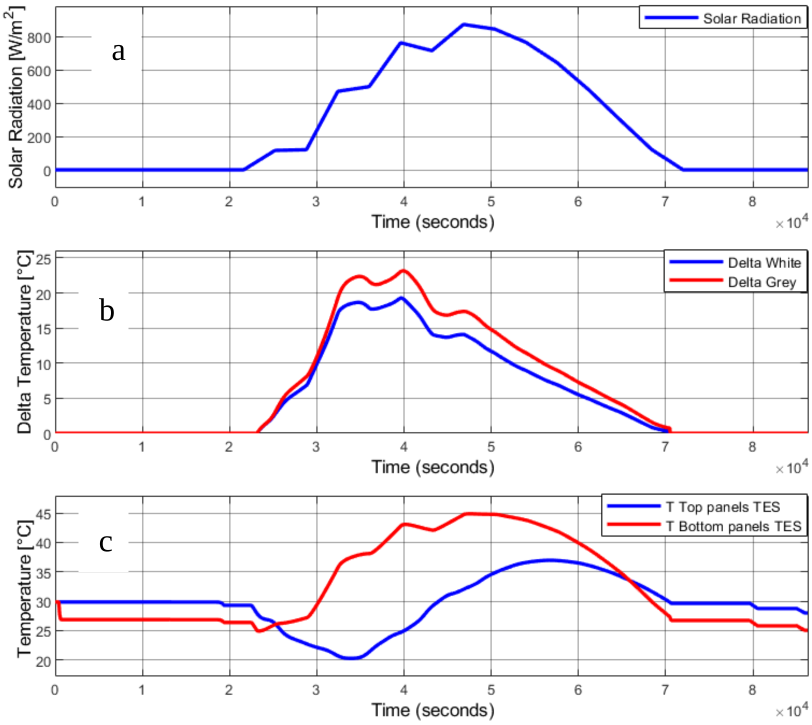

Figure 118 - August solar façade panels – 180 panels pair – (a) Solar Radiation – (b) Panel Temperature Difference – (c) L-TES top and Bottom Temperatures

7.5.3 Spring and Autumn season

Typical days of March and October have been simulated to report the results concerning Spring and Autumn seasons. Fig. 26 reports the power production of the real plant in March (left side) and in October (right side).

c

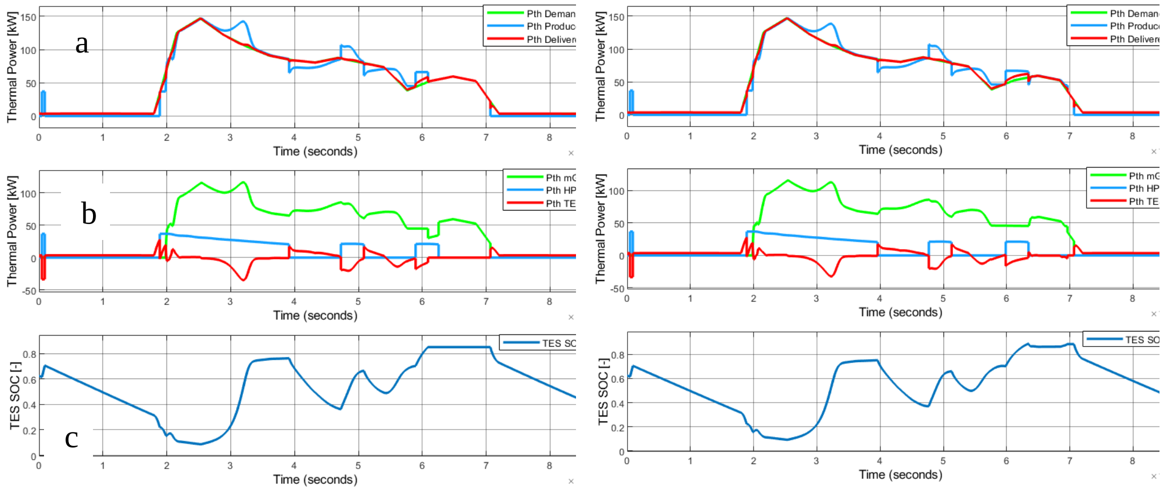

Figure 119 - March & October power production – 17 panels pair – (a) Demand Dispatchment March (left) & October (rigth) – (b) Thermal Power Production March (left) & October (rigth) – (c) H-TES SOC March (left) & October (rigth)

The power production is almost equal in the two analyzed cases as well as the final SOC of the H-TES. This is due to the fact that the solar irradiance is almost the same in the considered months.

Figure 120 reports a comparison between the power production of a typical October day with the real panel pair number (left side) and with 180 pairs (right side).

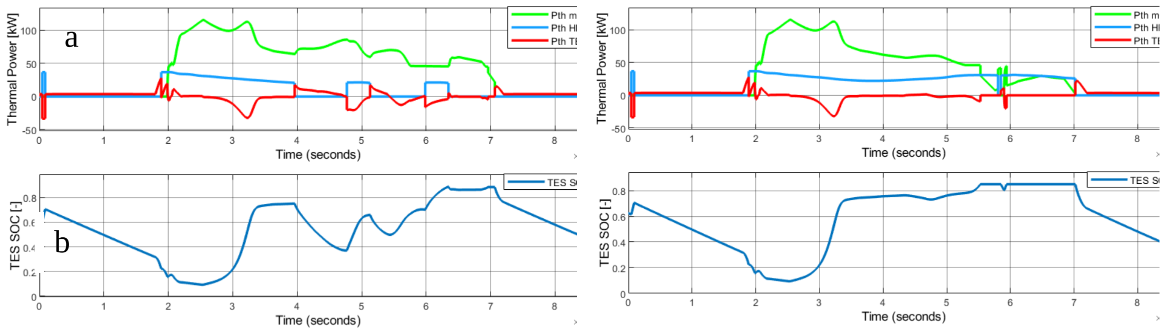

Figure 120 - October power production comparison – 17 vs 180 panels pair – (a) Demand Dispatchment 17 (left) & 180 (right) – (b) H-TES SOC 17 (left) & 180 (right)

With 180 panels pair the HP is able to operate for the whole day allowing for a lower mGT thermal power production; also the temperature difference that the panels are able to produce is different, having a peak of almost 4°C in the real configuration and of about 20°C in the configuration with a larger number of panels.

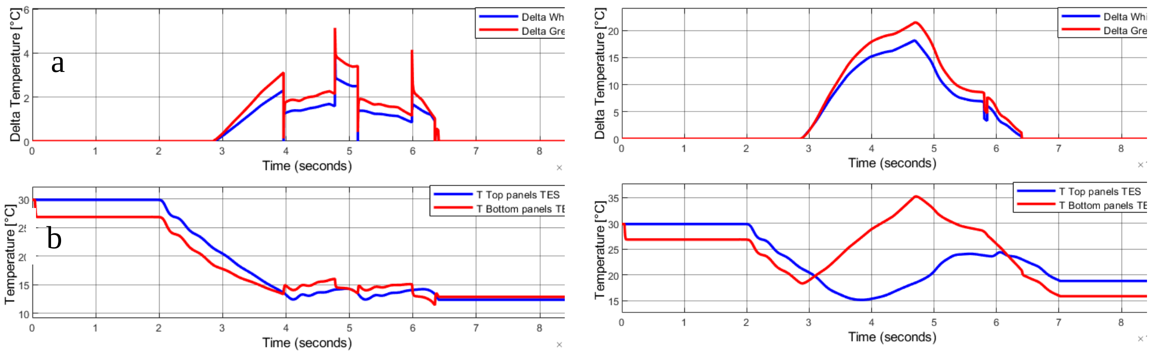

Figure 121 - October solar façade panels branch – 17 vs 180 panels pair – (a) Panels' Temperature Difference 17 (left) & 180 (right) – (b) L-TES top and Bottom Temperatures 17 (left) & 180 (right)

The final SOC of the storage-TES is 10°C lower than the initial one but simulating the next day (and so starting the next simulation with the temperature at the top of the panels TES equal to 19°C and the bottom one equal to 16°C) the HP is able to operate for most of the day and the final state of charge of the panels TES is equal to the initial one (Figure 122); so it can be stated that the configuration with 180 panels pair is able to satisfy the Campus thermal demand increasing the exploitation of the renewable energy sources and leading a great reduction in the CO_2 emissions. Even more, with this configuration, the total building area required for the installation of the solar panels will be 432 m^2 . Considering that a single building façade of the Savona Campus has a total opaque lateral surface higher than 700 m^2 a single building would be enough to allocate the 180 panels couple. If the panels couple must be subjected to the same solar radiation profile, in this case two building surfaces will be required.

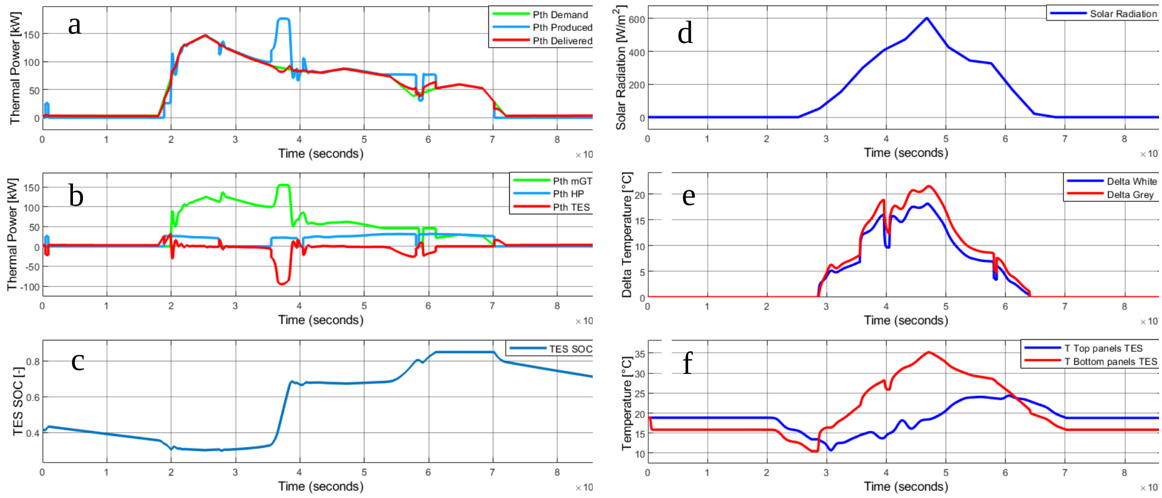

Figure 122 - October day 2 with 180 panels pair – (a) Demand Dispatchment – (b) Thermal Power Production – (c) H-TES SOC – (d) Solar Radiation – (e) Panels' Temperature Difference – (f) L-TES top and Bottom Temperatures

7.6 Physical control system in southern demo site

The EMS and the MPC developed in Matlab/Simulink environment have been integrated into the LabVIEW environment which allows the control of the real plant. It must be specified that there are differences between the real environment and the model; the main ones are reported below. During the test, the fan coolers (thermal dissipators) are properly controlled in such a way to simulate the thermal demand but a limitation related to their size must be considered; it is not possible to emulate a thermal demand higher than 150 kWth.

Due to the necessity of dissipating the produced thermal power, a recirculation lines between the mGT, the HP, and the H-TES are installed to connect the components at the thermal dissipators and, on each branch, three-way valves are installed, and controlled to guarantee 50°C at the inlet side of each machine.

The turbine recirculating pump is properly controlled to set the water outlet temperature equal to 75°C and so the water mass flow rate will change according to the rotational speed of the recirculation pump.
HP recirculating pump has a fixed rotational speed (the inverter is not present on this pump) and so the set point outlet temperature is guaranteed by the internal control of the machine and, in a strong off design condition, can be controlled by opening/closing a manual valve located on the condenser line.
Solar façade panels recirculating pump is instead controlled according to the solar radiation that is measured by the pyranometer as already explained in the other chapter.

7.6.1 Physical control system in Southern demo site

The EMS and the MPC that have been implemented in LabVIEW have been tested in the real environment. The test data have been acquired with a sample time of 1s and in Fig. 30 the power production of the mGT, the HP, and the H-TES is reported. The blue line represents the thermal demand, the yellow one the thermal power produced by the mGT, the light blue the power produced by the HP, and the green one the power associated with the TES; the TES is in the charging phase when the power is negative and in discharging phase when it is positive.
The test in the real environment has been successful considering that the implemented control system strategy properly managed the thermal demand, satisfying it at each time interval and properly managing the interconnection of the whole harvesting package with the thermal dissipators (which emulates the DHN demand) and the Campus electrical grid. It is possible to note that as soon as the gradient of the thermal demand was strongly negative the EMS chose to shut down the mGT starting the TES discharge and so, covering the demand only with the HP and the TES. The change in the HP thermal power production along the test has been caused by changing the mass flow rate inside the HP passing from

strongly OFF design conditions (at the beginning of the test) to the manufacturer design condition.

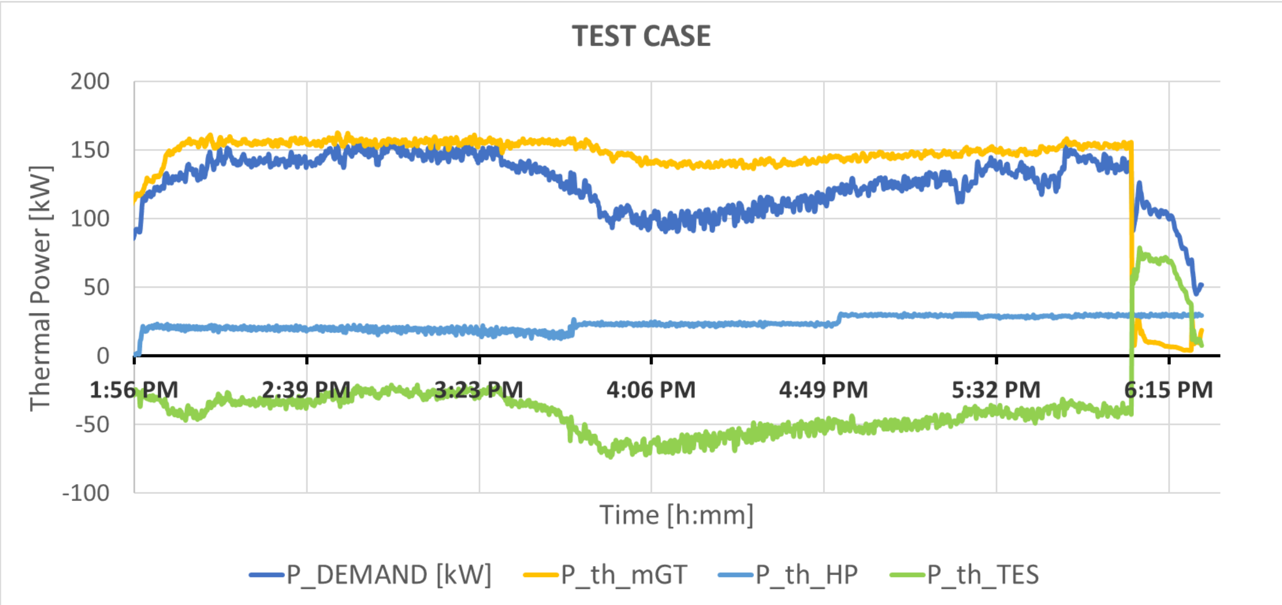

Figure 123 - Test in the real environment - thermal power profile

The two different phases related to TES charge and discharge can be better visualised in Figure 123 which compares the total power produced by the plant with the demand that needs to be satisfied.

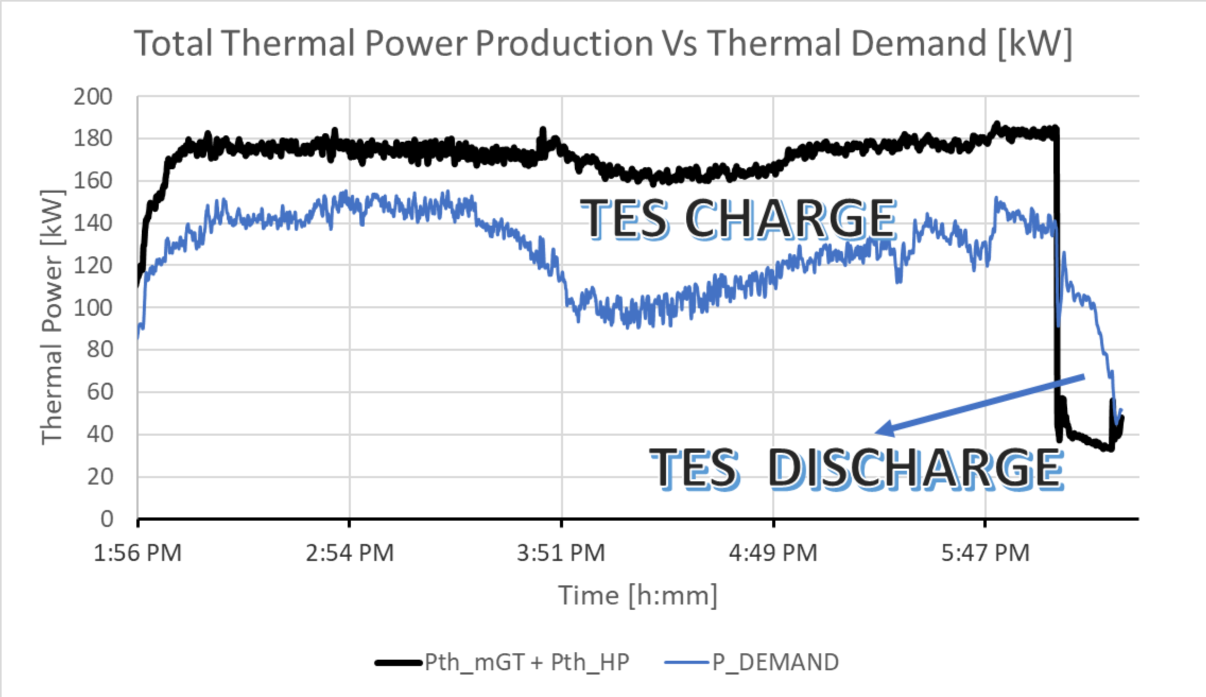

Figure 124 - Test in the real environment – TES charge/discharge

Moreover, the constraints related to the inlet and the outlet section of the mGT and the HP have been satisfied throughout the whole test. Figure 124 shows the water temperature related to the turbine. As it possible to see, the constraints imposed by the DHN of maintaining the water outlet temperature at about 75°C and the inlet at 50°C is completely respected.

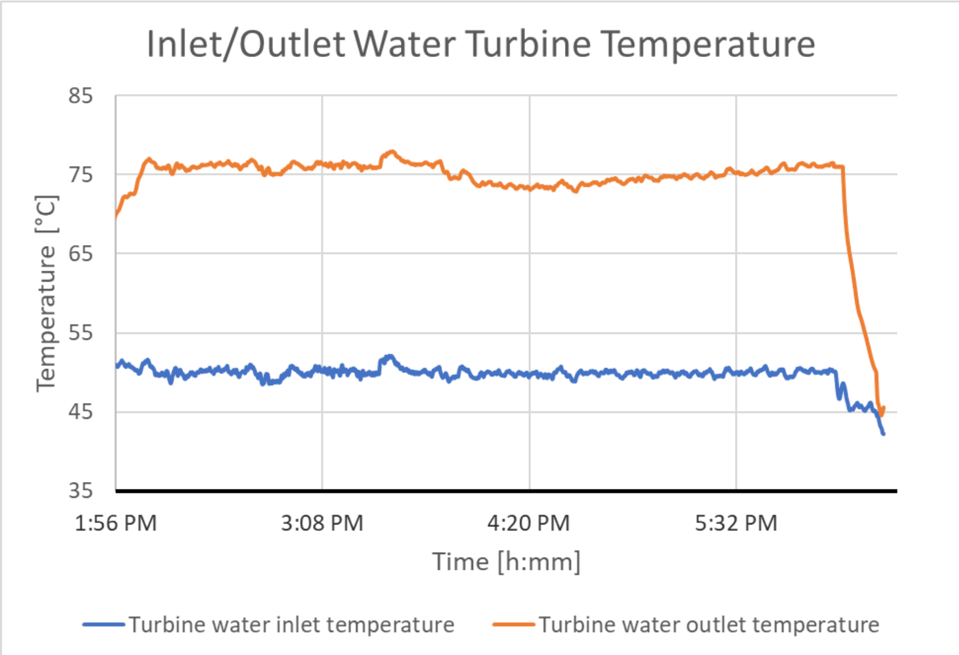

Figure 125 - Test results in the real environment – turbine water inlet/outlet temperature

Referring to the electrical power produced by the mGT, it has been supplied to Savona Campus. The power supplied to the Campus grid during the test is reported in Figure 126.

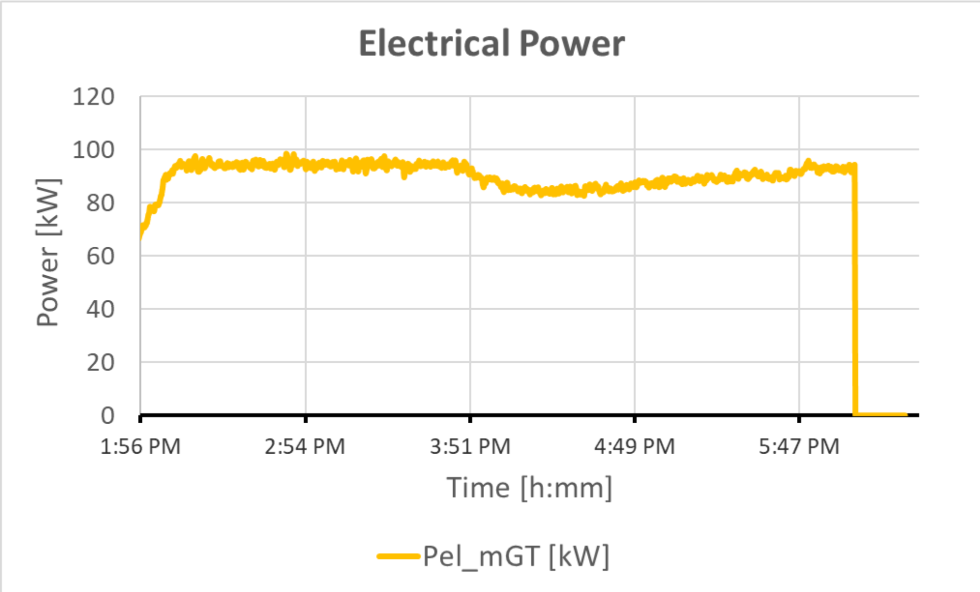

Figure 126 - Test in the real environment - electrical power profile

7.7 Summary conclusions for buildings thermal grid optimization

All the models of the ENVISION system components have been successfully validated through experimental data obtained during a test campaign in 2022.

The HP dynamic model includes all the components of the HP closed loop, making it possible to simulate its performance and monitor all the main process parameters. Moreover, this model can be used to simulate the HP in various conditions following the input changes, and thanks to the moving boundary approach used to model the condenser and the evaporator it is possible to compute pressure and temperature also in the internal sections of the heat exchangers. The developed HP model is very flexible and allows effortlessly to emulate the behavior of other heat pumps of different sizes and working fluid.

Concerning the solar façade panels model, the realized model presents always an error lower than 1.5 K and thanks to that it is possible to simulate with a high level of accuracy different scenarios varying the number of grey and white solar façade panels pairs.

The Combined Heat and Power AE-T100 mGT model that has been developed implementing the off-design manufacture correlations and the experimental data obtained during the test campaign allows for the integration with the MPC with a short running time making possible to control the micro gas turbine to have the best exploitation of the produced thermal and electrical energy.

Both the thermal energy storage models, that have been treated with a multi-nodal method based on a numerical 1D finite difference scheme, allow reproducing the water stratification phenomena making possible the precise calculation of the SOC at each time instant.

The EMS was developed to control the ENVISION system and properly manage the whole system minimizing the CO_2 emission and allowing for the best exploitation of the RES. The system, which is controlled by giving priority to the thermal demand, in fact, always privileges the use of the HP which is connected to the solar façade panels branch using the mGT only to cover the difference between the thermal demand and the power produced by the renewables having the foresight to use the H-TES to cover the night thermal demand.

The system which has been tested in Matlab-Simulink environment ensures the possibility to cover quarter of the Savona Campus total thermal demand during winter and the total demand during summer.

The model, equipped with the advanced control system, has been tested in all the months and, even for January, which is the month with the lower amount of solar radiation, shows that the power produced by the Southern Demosite ENVISION plant is enough to cover the demand.

With the developed ENVISION integrated system model it was possible to simulate different scenarios by varying the number of ENVISION solar façade panels finding a configuration that is able to strongly reduce the mGT contribution and consequently the natural gas consumption.

The control system has been also tested in the real environment, and so at the district level, implementing it on the LabVIEW interface from which is possible to control the real system and to perform data acquisition. During the tests in the real environment, the control system properly manages the ENVISION system component exploiting the RES, performing TES charging when a large quantity of solar radiation is available and TES discharging as soon as the thermal demand decreases consistently. Also, the electrical power produced by the mGT has been properly managed and exchanged with the Savona Campus electrical grid.